

Electronic Thesis and Dissertation Repository

---

7-13-2017 11:15 AM

## Investigating Brown Dwarf Atmospheres: Gravity, Dust Content, Cloud Structure and Metallicity

Kendra Kellogg, *The University of Western Ontario*

Supervisor: Prof. Stanimir Metchev, *The University of Western Ontario*

A thesis submitted in partial fulfillment of the requirements for the Doctor of Philosophy degree in Astronomy

© Kendra Kellogg 2017

Follow this and additional works at: <https://ir.lib.uwo.ca/etd>



Part of the [Other Astrophysics and Astronomy Commons](#)

---

### Recommended Citation

Kellogg, Kendra, "Investigating Brown Dwarf Atmospheres: Gravity, Dust Content, Cloud Structure and Metallicity" (2017). *Electronic Thesis and Dissertation Repository*. 4857.  
<https://ir.lib.uwo.ca/etd/4857>

This Dissertation/Thesis is brought to you for free and open access by Scholarship@Western. It has been accepted for inclusion in Electronic Thesis and Dissertation Repository by an authorized administrator of Scholarship@Western. For more information, please contact [wlsadmin@uwo.ca](mailto:wlsadmin@uwo.ca).

## ABSTRACT

Brown dwarfs are the lowest mass products of star formation. Their low masses don't allow them to sustain, or sometimes even begin, the thermonuclear processes that provide stars with internal energy and the thermal pressure necessary to maintain hydrostatic equilibrium. Thus, their radii and effective temperatures decrease as they age, continually changing their spectral classification. However, it is now a well-known fact that the spectral appearance of ultra-cool dwarfs is governed by more than just temperature. Factors such as gravity, metallicity and cloud distribution play an important role in the structure and composition of ultra-cool dwarf atmospheres and ultimately their spectra.

Pinning down the effects of some of the contributing factors to the structure and evolution of brown dwarf atmospheres has been the goal of my thesis research. Through a joint positional and colour cross-match of optical, near-infrared and mid-infrared all-sky surveys, I have identified 20 new brown dwarfs with "peculiar photometric colours which are candidates for having unusual atmospheric properties. I have determined that a number of these objects have atypical surface gravities and/or atmospheric dust content using near-infrared spectroscopic observations. I have also determined the timescales for the various peculiarities by comparing these objects to the population of "normal" objects. In addition, I have studied in detail a few of the most peculiar objects in order to understand how conditions on individual objects affect their atmospheric structure and composition.

**Keywords:** Astrophysics, brown dwarf, atmospheres, binary, survey

The following authors contributed to Chapter 1: Stanimir Metchev, Kerstin Geissler, Shannon Hicks, J. Davy Kirkpatrick, Radostin Kurtev. Stanimir Metchev provided the initial setup and much guidance. Kerstin Geissler contributed to the initial data and analysis. Shannon Hicks contributed to part of the initial setup. J. Davy Kirkpatrick contributed to part of the initial setup. Radostin Kurtev contributed to the taking of part of the data.

The following authors contributed to Chapter 2: Stanimir Metchev, Paulo Miles-Páez, Megan Tannock. Stanimir Metchev provided guidance. Paulo Miles-Páez provided very insightful comments. Megan Tannock helped in part of the observations.

The following authors contributed to Chapter 3: Stanimir Metchev, Jonathan Gagné, Jacqueline Faherty. Stanimir Metchev provided part of the analysis and guidance. Jonathan Gagné contributed to the data reduction and part of the analysis. Jacqueline Faherty took the observations for us.

The following authors contributed to Chapter 4: Stanimir Metchev, Aren Heinze, Jonathan Gagné, Radostin Kurtev. Stanimir Metchev provided part of the analysis and guidance. Aren Heinze contributed to the initial observations. Jonathan Gagné contributed to the data reduction and part of the analysis. Radostin Kurtev took the observations for us.

The following authors contributed to Chapter 5: J. Davy Kirkpatrick, Jonathan Gagné, Jacqueline Faherty. J. Davy Kirkpatrick provided part of the preceding data and guidance. Jonathan Gagné contributed to the data reduction and part of the analysis. Jacqueline Faherty took the observations for us.

# Acknowledgments

I would like to thank my supervisor, Prof. Stanimir Metchev, for helping me throughout my degree and encouraging me to take on extra projects beyond my main thesis work. It helped me grow much more as a scientist than I would have otherwise. I would also like to thank Stan for encouraging me to participate in the IPAC Graduate Fellowship at IPAC/Caltech. It exposed me to a completely different environment than I was used to and gave me a new set of experiences to draw from in the future.

I would also like to thank my supervisor at IPAC, Dr. J. Davy Kirkpatrick, for encouraging me to come up with my own project ideas and allowing me to take that important step as a scientist.

None of this work would have been possible without the invaluable contributions from my collaborators. I would like to thank all of them for all of their hard work and insight they provided on my papers.

I would also like to sincerely thank my parents, Del and Teri Kellogg, for giving me support during my undergraduate degree so that I could pursue some auspicious opportunities in my early research career.

Finally, I would like to thank my friends who have kept me sane throughout my graduate degree. Without them, I would not have been able to maintain a positive outlook on life through the grueling years of graduate school.

# Contents

LISTING OF TABLES	<b>ix</b>
LISTING OF FIGURES	<b>x</b>
<b>1 BACKGROUND MATERIAL</b>	<b>1</b>
1.1 Introduction . . . . .	1
1.2 Evolution . . . . .	2
1.3 Atmospheres . . . . .	8
1.3.1 Classification . . . . .	8
1.3.2 Effect of Clouds . . . . .	9
1.3.3 Evolution of Opacity Sources . . . . .	13
1.3.4 Modeling the L–T Transition . . . . .	18
1.3.5 Observational Evidence . . . . .	20
1.3.6 Effect of Gravity and Metallicity . . . . .	21
1.4 Outstanding Problems Addressed in My Thesis . . . . .	25
1.5 Summary . . . . .	27
<b>2 A TARGETED SEARCH FOR PECULIARLY RED L AND T DWARFS IN SDSS, 2MASS, AND WISE: DISCOVERY OF A POSSIBLE L7 MEMBER OF THE TW HYDRAE ASSOCIATION</b>	<b>32</b>
2.1 Introduction . . . . .	32
2.2 Candidate Selection . . . . .	34
2.2.1 Selection Criteria . . . . .	35
2.2.2 Prioritization of Peculiar Objects . . . . .	37
2.3 Spectroscopic Observations and Data Reduction . . . . .	37
2.3.1 IRTF/SpeX . . . . .	39
2.3.2 Magellan/FIRE . . . . .	41
2.3.3 Synthetic Photometry . . . . .	43
2.4 Spectral Classification Results . . . . .	44
2.4.1 Normal Ultra-cool Dwarfs . . . . .	49
2.4.2 Peculiar L Dwarfs . . . . .	50
2.4.2.1 2MASS J11193254–1137466 (L7) . . . . .	52
2.4.2.2 2MASS J17081563+2557474 (L5) . . . . .	53

2.4.2.3	2MASS J16135698+4019158 (L5)	54
2.4.2.4	2MASS J17251557+6405005 (L2)	54
2.4.3	Brown Dwarfs with Composite Spectral Types	55
2.4.3.1	2MASS J13043568+1542521 (L6+T6?)	56
2.4.3.2	2MASS J14025564+0800553 (L8+T5?)	57
2.4.3.3	2MASS J17373467+5953434 (L4+T5?)	57
2.4.3.4	2MASS J23322678+1234530 (L5+T5?)	57
2.4.3.5	2MASS J10020752+1358556 (L7+T8?)	58
2.4.3.6	2MASS J22153705+2110554 (T0+T2?)	58
2.5	Discussion	59
2.6	Conclusions	60
3	A STATISTICAL SURVEY OF PECULIAR L AND T DWARFS IN SDSS, 2MASS, AND WISE	<b>72</b>
3.1	Introduction	72
3.2	Candidate Selection	75
3.2.1	Candidate Ultra-cool Dwarfs	75
3.2.2	Peculiarly Red Candidates	76
3.2.3	Candidate T Dwarfs or L+T Binaries	76
3.3	Spectroscopic Observations and Data Reduction	77
3.3.1	IRTF/SpeX	77
3.3.2	Gemini/GNIRS	80
3.4	Spectral Classification Results	82
3.4.1	Peculiar L Dwarfs	85
3.4.1.1	2MASS J00133470+1109403 (L1)	96
3.4.1.2	2MASS J00440332+0228112 (L7)	96
3.4.1.3	2MASS J03302948+3910242 (L7)	97
3.4.1.4	2MASS J03530419+0418193 (L6)	97
3.4.1.5	2MASS J10265851+2515262 (L5)	98
3.4.1.6	2MASS J10524963+1858151 (L5)	98
3.4.1.7	2MASS J14313545−0313117 (L6)	99
3.4.2	Brown Dwarfs with Composite Spectral Types	99
3.4.2.1	2MASS J00132229−1143006 (T3.5+T4.5?)	102
3.4.2.2	2MASS J00452972+4237438 (M8+L7?)	102
3.4.2.3	2MASS J09240328+3653444 (L2+T3)	103
3.4.3	Normal Ultra-cool Dwarfs	103
3.4.4	False-Positive Ultra-cool Dwarfs	105
3.5	Population Statistics	108

3.5.1	Efficacy of the Survey . . . . .	109
3.5.2	Unusually Red Objects . . . . .	111
3.5.3	Candidate Binaries . . . . .	112
3.5.4	WISE Colours . . . . .	113
3.6	Conclusions . . . . .	113
4	THE NEAREST ISOLATED MEMBER OF THE TW HYDRAE ASSOCIATION IS A GIANT PLANET ANALOG	<b>120</b>
4.1	Introduction . . . . .	120
4.2	Observations and Data Reduction . . . . .	121
4.3	Confirmation of Youth . . . . .	122
4.4	Kinematics . . . . .	123
4.5	TWA Membership . . . . .	126
4.6	Conclusion . . . . .	130
5	CHARACTERIZING THE CLOUD DECKS OF LUHMAN 16AB WITH MEDIUM- RESOLUTION SPECTROSCOPIC MONITORING	<b>134</b>
5.1	Introduction . . . . .	134
5.2	Observations and Data Reduction . . . . .	137
5.3	Analysis and Results . . . . .	140
5.3.1	Light Curve Calibration . . . . .	140
5.3.2	Creation of Representative Bright and Faint State Spectra . . . . .	142
5.3.3	Variability and Absorption Strength Changes . . . . .	146
5.4	Discussion . . . . .	148
5.4.1	Spectral Type Changes . . . . .	149
5.4.2	Cloud Tomography . . . . .	154
5.5	Conclusions . . . . .	157
6	DISCOVERY OF A POSSIBLE EARLY-T THICK-DISK/HALO SUBDWARF FROM THE ALLWISE 2 MOTION SURVEY	<b>161</b>
6.1	Introduction . . . . .	161
6.2	Candidate Selection . . . . .	163
6.3	Spectroscopic Observations and Data Reduction . . . . .	167
6.4	Spectral Classification and Kinematics . . . . .	169
6.4.1	Late-L/Early-T Subdwarf . . . . .	169
6.4.2	Unresolved Binary? . . . . .	173
6.4.3	Kinematics . . . . .	175
6.5	Halo/Thick-Disk Brown Dwarfs . . . . .	177
6.6	Conclusions . . . . .	178

7 CONCLUSION	<b>183</b>
7.1 Timescales of Atmospheric Phenomena . . . . .	184
7.2 Atmospheres of Individual Objects . . . . .	185
7.3 Summary . . . . .	187
APPENDIX A PERMISSIONS	<b>189</b>
CURRICULUM VITAE	<b>191</b>

# Listing of tables

2.1	SpeX Observations . . . . .	40
2.2	FIRE Observations . . . . .	42
2.3	Results from Spectroscopic Classification and Synthetic Photometry	47
3.1	SpeX Observations . . . . .	77
3.2	GNIRS Observations . . . . .	82
3.3	Results from Spectroscopic Classification and Synthetic Photometry	91
3.4	Unknown object photometry . . . . .	107
3.5	Summary of object types . . . . .	109
4.1	Characteristics of 2MASS J11193254–1137466 . . . . .	127
6.1	AllWISE2 Motion Candidates Lacking 2MASS Counterparts . . . .	165
6.2	Object Properties . . . . .	167
6.3	Inferred Properties of WISE J0711–5736 . . . . .	177

# Listing of figures

1.1	Luminosity vs Age . . . . .	3
1.2	Radius vs Age . . . . .	4
1.3	Central Temperature vs Age . . . . .	5
1.4	Rotation Period vs Age . . . . .	6
1.5	Effective Temperature vs Age . . . . .	8
1.6	Effective Temperature vs Spectral Type . . . . .	10
1.7	Relative Flux Contributions . . . . .	11
1.8	Brightness Temperature Spectra . . . . .	12
1.9	Condensation Curves . . . . .	13
1.10	Near-Infrared Spectral Type Sequence . . . . .	15
1.11	$J$ -band Spectral Type Sequence . . . . .	16
1.12	$M_J$ and $T_{eff}$ vs $J - K$ Color . . . . .	17
1.13	Wavelength Dependent Brightness Temperatures . . . . .	18
1.14	Theoretical $M_J$ vs $J - K$ Color . . . . .	22
1.15	L0 Dwarf Gravity Spectral Sequence . . . . .	23
1.16	L3 Dwarf Gravity Spectral Sequence . . . . .	24
2.1	Photometric colour-colour diagram of all L and T dwarf candidates . . . . .	38
2.2	Difference in synthetic vs photometric $J - K_s$ and $z - J$ colours . . . . .	46
2.3	Spectra of candidates . . . . .	49
2.4	Spectra continued . . . . .	50
2.5	Spectra of the four peculiar objects . . . . .	62
2.6	2MASS J1119-1137 spectra comparison . . . . .	63
2.7	Spectra of three candidate unresolved binaries . . . . .	64
2.8	Spectra of remaining three candidate unresolved binaries . . . . .	65
2.9	WISE photometric colour-colour diagrams . . . . .	66
3.1	Synthetic $z - J$ vs $J - K_s$ diagram of all objects . . . . .	81
3.2	Spectra of candidates . . . . .	83
3.3	Spectra continued . . . . .	84
3.4	Spectra continued . . . . .	85
3.5	Spectra continued . . . . .	86
3.6	Spectra continued . . . . .	87

3.7	Synthetic $J - K_s$ colour vs spectral type . . . . .	88
3.8	Spectra of the peculiar objects . . . . .	100
3.9	Peculiar object spectra continued . . . . .	101
3.10	Spectra of the candidate unresolved binaries . . . . .	104
3.11	Non-ultracool dwarf spectra . . . . .	106
3.12	$z - J$ vs $J - K_s$ diagram of recovered objects . . . . .	110
3.13	$H - W2$ and $W1 - W2$ vs $J - K_s$ diagrams . . . . .	115
4.1	2MASS J1119–1137 spectra comparison . . . . .	124
4.2	Forward model fitting to the observed spectra of 2MASS J1119–1137	125
4.3	Galactic position and space velocity of 2MASS J1119–1137 . . . . .	128
5.1	Luhman 16AB FIRE spectra . . . . .	139
5.2	Luhman 16AB continuum variations . . . . .	141
5.3	Luhman 16B continuum variations . . . . .	143
5.4	Luhman 16B/A spectra ratios . . . . .	145
5.5	Telluric variability . . . . .	147
5.6	Template fitting $\chi^2$ values . . . . .	152
5.7	Best fitting templates . . . . .	153
6.1	Co-added images from WISE . . . . .	167
6.2	Telluric correction comparison . . . . .	169
6.3	WISE 0711–5736 spectra comparison . . . . .	170
6.4	Subdwarf comparison . . . . .	172
6.5	Theoretical spectra comparison . . . . .	174
6.6	Peculiar spectra comparison . . . . .	176

# 1

## Background Material

### 1.1 INTRODUCTION

Phase transitions are always good places to discover new and exciting physics. The mass region between low-mass stars and planets is no different. In this case, the transition is occupied by objects called brown dwarfs.

Brown dwarfs are so called “failed stars” because they don’t have enough mass to ever reach the main sequence and achieve stable hydrogen fusion in their core. The hydrogen burning minimum mass (HBMM) is  $\sim 0.072 M_{\odot}$  ( $\sim 75 M_{Jup}$ ; Hayashi et al., 1963) and sets the upper limit for the definition of a brown dwarf. The mass at which an object can achieve lithium burning is  $\sim 0.060 M_{\odot}$  ( $\sim 63 M_{Jup}$ ) and is  $\sim 0.012 M_{\odot}$  ( $\sim 13 M_{Jup}$ ) for deuterium burning (Dantona et al., 1985). The deuterium burning limit is sometimes set as the defining line between brown dwarfs and planets, however, the delineator is sometimes ambiguous.

In fact when it comes to their atmospheres, it is a boon that brown dwarfs and giant planets are so similar. Since direct imaging and spectroscopy of extra-solar giant planets are difficult to obtain (due to the flux contrast between the planet and host star), understanding the properties of free-floating brown dwarfs

will aid in the understanding of exoplanets.

The relatively cool effective temperatures of brown dwarfs ( $\sim 250\text{--}2500\text{ K}$ ) enable the formation of a multitude of molecular species in their atmospheres. As brown dwarfs age and cool, the structure and composition of their atmospheres undergo significant changes which manifest themselves in their spectra. The exact atmospheric evolutionary sequence depends on a number of factors and is still an area of keen interest in brown dwarf research. A brief overview of the evolution of low-mass stars and substellar objects is presented in § 1.2 and a detailed discussion of the atmospheric properties is given in § 1.3.

Pinning down the effects of some of the contributing factors to the structure and evolution of brown dwarf atmospheres is the goal of my thesis research. This work, in addition to contributing to the development of a multipronged classification — which considers temperature, gravity, and metallicity — provides further observational constraints to atmospheric models through investigations of so-called “peculiar” brown dwarfs.

## 1.2 EVOLUTION

As with stars, the fate of a brown dwarf is predetermined by its initial mass and chemical composition. In an evolutionary context, whether an object is a brown dwarf or a planet is irrelevant; the same physics and chemistry apply to both.

**Luminosity:** Unless an object has enough mass to eventually begin stellar nucleosynthesis, it will cool and fade throughout its lifetime. Figure 1.1 (Burrows et al., 2001) shows the evolutionary tracks of luminosity for solar-metallicity objects. The colours of the tracks only serve to guide the eye and represent masses that will eventually stably burn hydrogen on the main sequence (blue;  $75\text{--}211 M_{Jup}$ ), can burn deuterium (green;  $15\text{--}73 M_{Jup}$ ) or will never be able to burn anything (red;  $0.3\text{--}13 M_{Jup}$ ). The gold and magenta dots represent the ages at which a given mass object will have burned half of its deuterium and lithium, respectively. The bumps at early times along the green tracks result from the complete depletion of deuterium. The bifurcation of low-mass stars and brown dwarfs only manifests itself at late times when stars begin

thermonuclear burning which compensates for the photon losses at the surface.

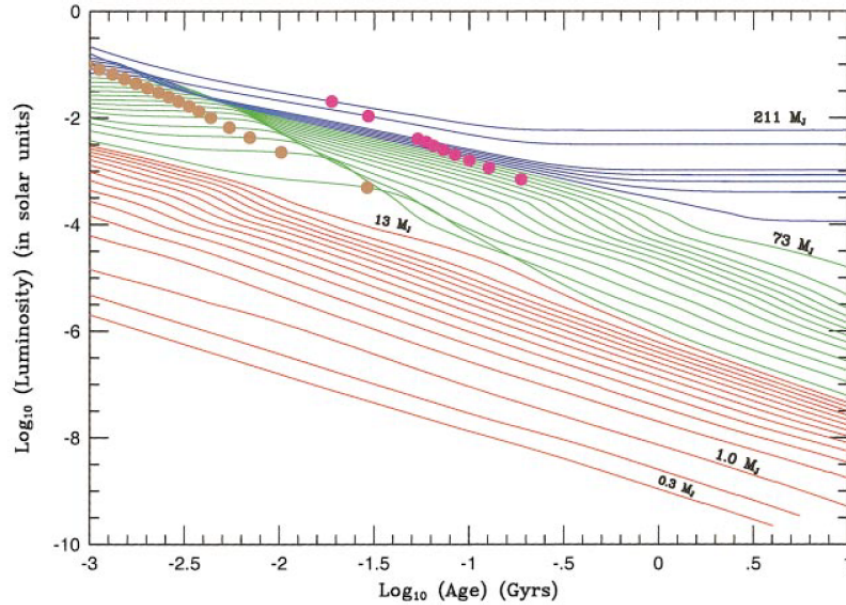


Figure 1.1: Evolution of the luminosity (in  $L_{\odot}$ ) of isolated solar-metallicity red dwarf stars and substellar-mass objects versus age (Burrows et al., 2001). The stars are shown in blue, brown dwarfs above  $13 M_{Jup}$  are shown in green, and brown dwarfs/giant planets of mass equal to or below  $13 M_{Jup}$  are shown in red. The masses of the substellar objects/stars portrayed range from  $0.3 M_{Jup}$  to  $0.2 M_{\odot}$  ( $211 M_{Jup}$ ). For a given object, the gold dots mark when 50% of the deuterium has burned and the magenta dots mark when 50% of the lithium has burned. Note that the lithium sequence penetrates into the brown dwarf regime near  $0.065 M_{\odot}$ , below the hydrogen burning minimum mass.

**Radius and Central Temperature:** Figure 1.2 (Burrows et al., 2001) depicts the evolutionary tracks for the radius of substellar and the lowest mass stellar objects. The colours of the tracks are for the same masses as those in Fig. 1.1. While a brown dwarf burns deuterium, the collapse is somewhat stabilized by the nuclear fusion in the core. Once the deuterium is completely depleted, the substellar object rapidly collapses. The resulting compression of interior material increases the central temperature until collapse is halted by electron degeneracy pressure. Figure 1.3 (Burrows et al., 2001) demonstrates the evolution of the central temperature with age. Once the interior becomes electron degenerate, the central temperature inexorably decreases. It is evident that

at later times, radii are roughly independent of mass. This behaviour is the result of the competition between Coulomb and electron degeneracy effects. The Coulomb barrier sets a fixed interparticle distance and, hence, a fixed density which leads to the relation  $R \propto M^{1/3}$  but electron degenerate matter has the relation  $R \propto M^{-1/3}$ . These two effects essentially cancel and render the radius constant over approximately two orders of magnitude in mass (e.g. Burrows et al., 1993; Marley et al., 1996). In the case of the lowest mass stars, both the radius and central temperature plateau once hydrogen burning begins.

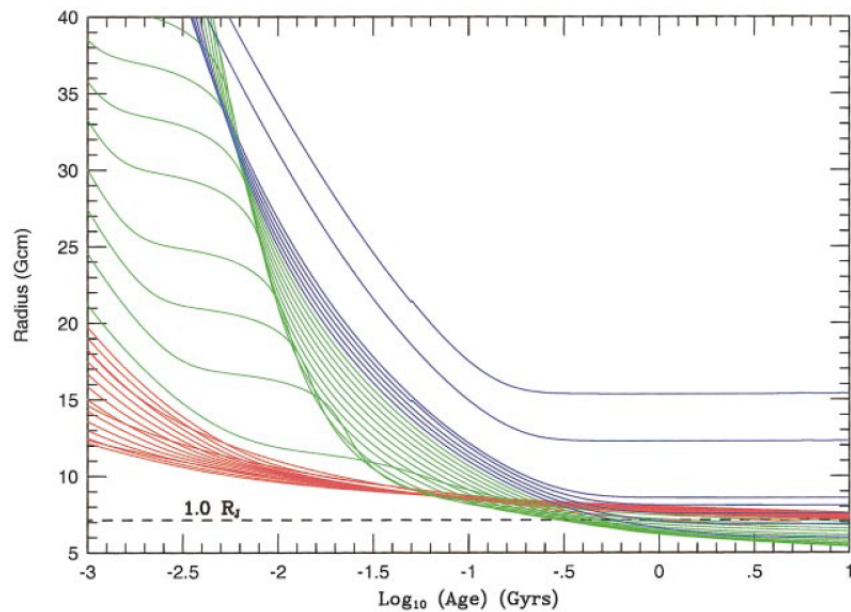


Figure 1.2: The radius (in units of  $10^9$  cm) of substellar-mass objects with the masses given in Fig. 1.1 vs the  $\log_{10}$  of the age (in Gyr; Burrows et al., 2001). The same colour scheme that was used in Fig. 1.1 is used here. Also shown is the radius of Jupiter. Note that the radii are not monotonic with mass and that they cluster near the radius of Jupiter at late times, despite the wide range of masses from  $0.3 M_{Jup}$  to  $0.2 M_{\odot}$  represented.

**Rotation:** The rotation rate of a brown dwarf also changes over its lifetime. As a brown dwarf ages and contracts, its rotation rate increases due to a conservation of angular momentum. Figure 1.4 (Bouvier et al., 2014) shows periods for brown dwarfs that are  $\sim 1$  Myr,  $\sim 3$  Myr and field age along with models for a medium sized brown dwarf ( $0.05 M_{\odot}$ ) with and without angular momentum

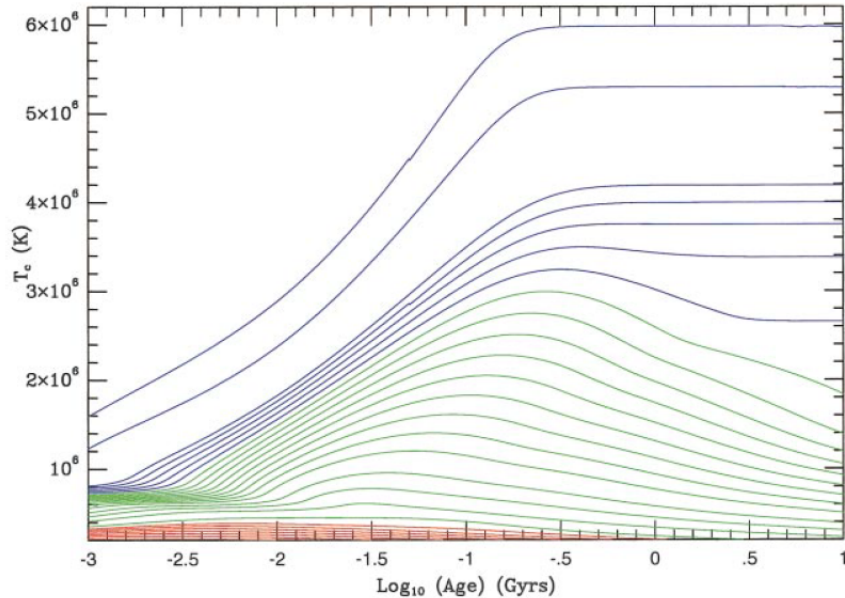


Figure 1.3: The central temperature ( $T_c$ ) in K vs the logarithm (base ten) of the age (in Gyr) for the same mass set of substellar objects presented in Fig. 1.1 (Burrows et al., 2001).

loss. Studies have shown that in star-forming regions such as the Orion Nebula Cluster, the median rotation period ranges from 5 days for  $M > 0.4M_\odot$  to 2 days for  $M < 0.08M_\odot$  (Rodríguez-Ledesma et al., 2009) and that there is very little angular momentum loss. By  $\sim 1$  Gyr, the rotation periods have decreased to just a few hours. Figure 1.4, however, shows that the best fit to the observational constraints is obtained with models that do have some angular momentum loss, albeit  $\sim 10,000\times$  less than that seen in solar-type stars (Bouvier et al., 2014) and on a timescale of a few Gyr. The cause of such inefficient braking is currently unknown but could be due to the lack of a significant disk or stellar winds.

One way to determine the rotation rates of brown dwarfs is through photometric monitoring and seeking periodic variability. Brown dwarfs have a non-uniform distribution of atmospheric clouds which produces varying amounts of flux (e.g. Apai et al., 2013; Karalidi et al., 2016; Marley et al., 2002; Morley et al., 2014). These clouds tend to be stable on the timescale of several rota-

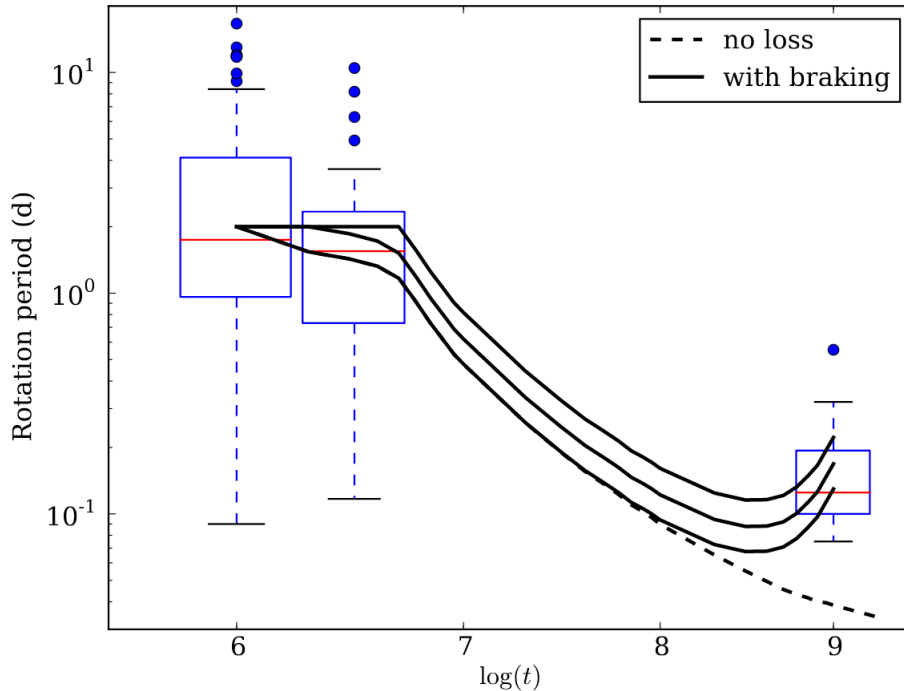


Figure 1.4: The rotation period in days for brown dwarfs as a function of age (Bouvier et al., 2014). Periods for brown dwarfs that are  $\sim 1$  Myr,  $\sim 3$  Myr and field age (all shown at 1 Gyr for convenience). The boxes show the upper and lower quartile at each age and the red line shows the median rotation period. The ‘whiskers’ indicate the range that is  $1.5\times$  the quartile ranges and outliers are indicated by individual points. The dashed line represents evolution model for a  $0.05M_{\odot}$  object without angular momentum loss and the solid lines correspond to models with saturated angular momentum loss and disk locking phases that last for 1, 2 and 5 Myr.

tion periods. Thus, the flux variability of these objects is modulated by their rotation (e.g. Artigau et al., 2009; Buenzli et al., 2015). Recently studies have focused on characterizing the variability of brown dwarfs and looking for correlations between age, spectral type, and variability amplitude (Heinze et al., 2013; Metchev et al., 2015; Miles-Páez et al., 2017). Radigan, 2014 and Metchev et al., 2015 have found that photometric variability, and therefore patchy or non-uniform clouds, are ubiquitous from early-L to late-T dwarfs. They, and others, have concluded that as a brown dwarf transitions from a relatively warm L dwarf to a cooler T dwarf, the clouds break up and sink (e.g. Burgasser et al., 2002a). Clouds and their effects are discussed more in § 1.3.

Another way to determine rotation rates is to obtain  $v \sin i$  measurements from high-resolution spectra. The absorption features in a spectrum will be broadened by the rotation of the brown dwarf. Determining how much they are doppler broadened on top of the spectral resolution will give the projected rotational velocity of the object. Together with the rotational period, the  $v \sin i$  measurement gives a more accurate estimate of the radius of the object within a factor of the sine of the inclination relative to the line of sight.

**Effects of Initial Conditions:** Burrows et al., 2001 note that several properties, including the luminosity and effective temperature are functions of metallicity, helium fraction and opacity. Therefore, changing any of these quantities has an effect on the evolutionary sequence of substellar objects. For example, increasing the opacity steepens the temperature gradient and decreases the rate at which energy is lost (luminosity) resulting in a higher central temperature, making it easier to achieve a main-sequence power balance at lower masses. These properties are a direct consequence of how the substellar object was formed and serve as the initial conditions to the evolutionary models. While composition may have a significant influence on the fate of a brown dwarf, Baraffe et al., 2002 conclude that other initial conditions such as convection efficiency and mixing length affect evolution models only at ages  $\lesssim 1$  Myr. After this time, different evolutionary models converge to a single track.

**Effective Temperature:** One of the most easily observable properties of stellar and substellar objects is their effective temperature. Figure 1.5 (Kirkpatrick, 2005) shows the evolution of effective temperature with age. In this diagram, low-mass stars that can eventually burn hydrogen are indicated by red tracks and substellar objects that can never reach the main-sequence are indicated by blue tracks (in units of solar masses). The orange line marks the boundary at which half of the initial lithium is depleted. Approximate temperature ranges for the spectral types are marked by shaded grey regions. These theoretical tracks suggest that the early- to mid-L dwarfs are a mix of old, low-mass stars and young, brown dwarfs. Since no observational way to determine whether or not an object is fusing hydrogen yet exists, we refer to objects with spectral types later than M7 as ultra-cool dwarfs. The criteria for the spectral

classifications is discussed in the next section.

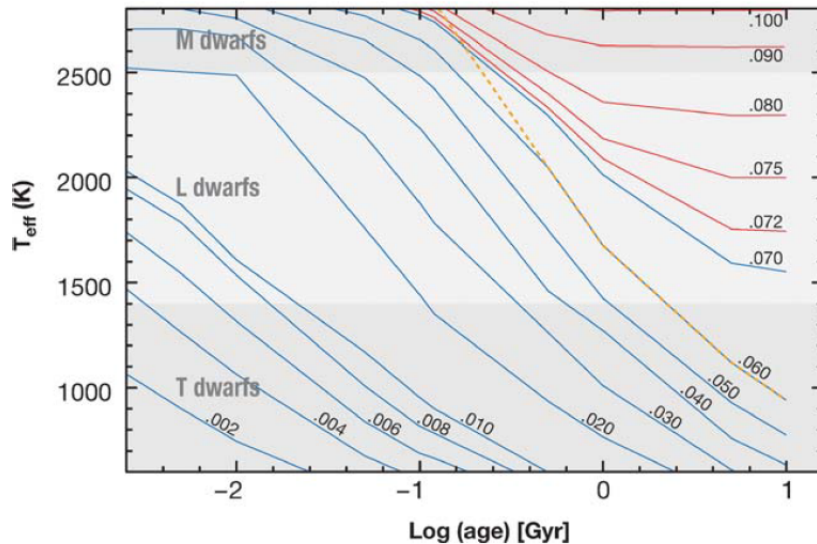


Figure 1.5: Theoretical tracks showing the evolution of effective temperature with age for low-mass stars (red) and brown dwarfs (blue; Kirkpatrick, 2005). The masses of each evolutionary track indicated are in units of solar masses. Grey areas delineate the approximate temperature ranges for the optical L and T dwarf sequences. The tracks warmer than 1500 K come from Chabrier et al. (2000, using the AMES-dusty models of Allard et al., 2001) and the tracks cooler than 1500 K come from Baraffe et al. (2003, using the AMES-cond models of Allard et al., 2001). The line marking the boundary at which lithium is 50% depleted is shown by the orange dotted line (see Chabrier et al., 2000). Objects to the right of this orange dotted line will have burned their primordial stock of lithium; objects to the left will not have burned their lithium.

## 1.3 ATMOSPHERES

### 1.3.1 CLASSIFICATION

Classification is used as a tool to uncover the underlying reasons why objects are in the forms we see. The Morgan-Keenan (MK or MKK) stellar spectral type classification scheme is essentially a temperature and luminosity sequence and prior to the discovery of brown dwarfs, it did not reach into the substellar mass regime and ended with M-type stars. Therefore, a new set of spectral types was needed. First proposed at a conference in 1997, the letters “L” and

“T” were decided upon as the new spectral types for substellar objects. More recently, a third spectral type has been added — the “Y” classification.

As with stars, brown dwarfs are classified based on their spectra. The defining characteristics of each spectral type for stars (except for M-dwarfs) are relatively simple — there are few atomic and molecular absorption lines. For brown dwarfs, however, the story is much more complicated. Brown dwarf spectra are riddled with neutral alkali lines and oxide, hydride, and water bands. There are currently two classification schemes based on spectra in the optical and near-infrared. As Figure 1.6 (Bailey, 2014) shows, the near-IR classification scheme is not perfectly correlated with temperature. This means that we have to be careful when defining spectral types. It also means that more than temperature governs atmospheric characteristics. A multi-dimensional optical classification scheme was proposed by Cruz et al., 2009 and extended into the infrared by Allers et al., 2013. This system primarily adds a gravity component to the classification but the authors recognize that more dimensions are needed. A separate classification scheme already exists to characterize objects with varying metallicities (Burgasser et al., 2005). So far, however, the two classification schemes have not been combined and have not expanded to include other parameters such as binarity, cloud properties and potentially others that we have not yet identified. Classifications will continue to be improved as new objects are observed with unique qualities.

### 1.3.2 EFFECT OF CLOUDS

The red-optical and near-infrared are the spectral regions that have been used to develop the spectral classifications schemes. Kirkpatrick et al., 1999 used psuedo-continuum slopes and the strengths of various absorption features in the optical to classify L dwarfs. Geballe et al., 2002 used the strengths of molecular absorption bands in the near-infrared to classify L and T dwarfs and noted that there were some inconsistencies between their classification of L dwarfs and the Kirkpatrick et al., 1999 classification. Knapp et al., 2004 suggest that there is an inherent difference between the optical and near-infrared regimes of L dwarfs as the near-IR classification of T dwarfs developed by Burgasser et al., 2002b

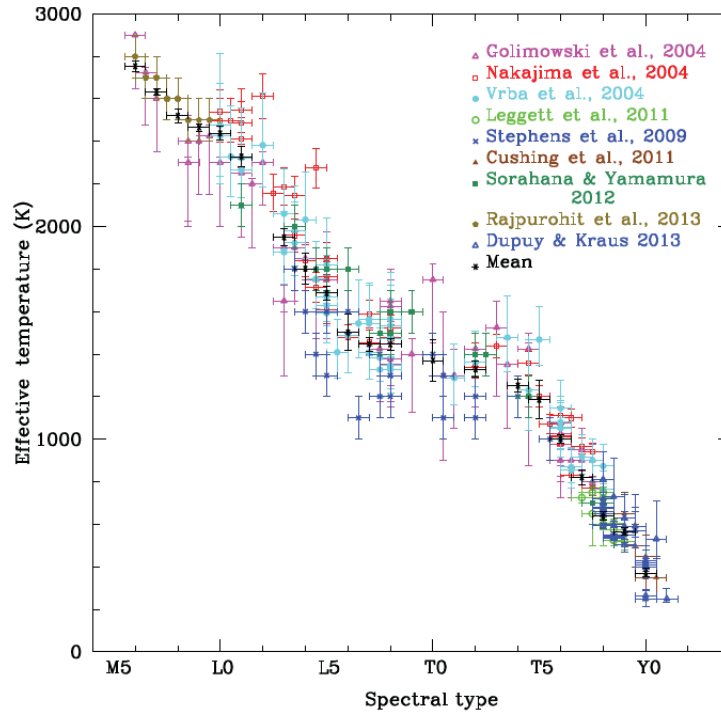


Figure 1.6: Effective temperature plotted against near-infrared spectral type (Bailey, 2014) compiled from various literature sources.

closely matches that of Geballe et al., 2002 and the differences in the optical and infrared spectral types are not random.

The difference comes from the location of the emergent flux at each wavelength and the effect that condensate clouds in the atmospheres of ultra-cool dwarfs have on that emergent flux. At warmer temperatures corresponding to the earliest L dwarfs, the deepest layers observed in the red-optical are located below the cloud deck. At these temperatures, the clouds are optically thin and have little effect on the emergent spectra. As temperature decreases towards later L dwarfs, clouds become thicker and obscure the deeper layers but most of the emergent flux originates above the cloud deck due to the large opacity from refractory diatomics, water, Na I and K I. Thus in the red-optical to near-IR region ( $0.7\text{--}1.0\ \mu\text{m}$ ), changes in the cloud profile have little effect on the emergent spectrum (Knapp et al., 2004).

In the near-IR, however, the windows between the water bands and other opacity sources allow flux to emerge from very deep in the atmosphere throughout the L sequence. This can be seen in Figure 1.7 which shows the schematic of the relative flux contribution from 0.8 to 2.4  $\mu\text{m}$  of a  $T_{\text{eff}}=1300$  K object (Karalidi et al., 2016). From this figure we see that in the 1.30–1.45  $\mu\text{m}$  and 1.70–1.95  $\mu\text{m}$  water bands, the flux that contributes to the spectrum originates from high in the atmosphere. Outside of these bands, however, the flux originates from deeper in the atmosphere (higher pressures). Thus in the near-IR, any clouds that are present alter the source function in atmosphere and changes in the cloud deck optical depth can significantly affect the spectra.

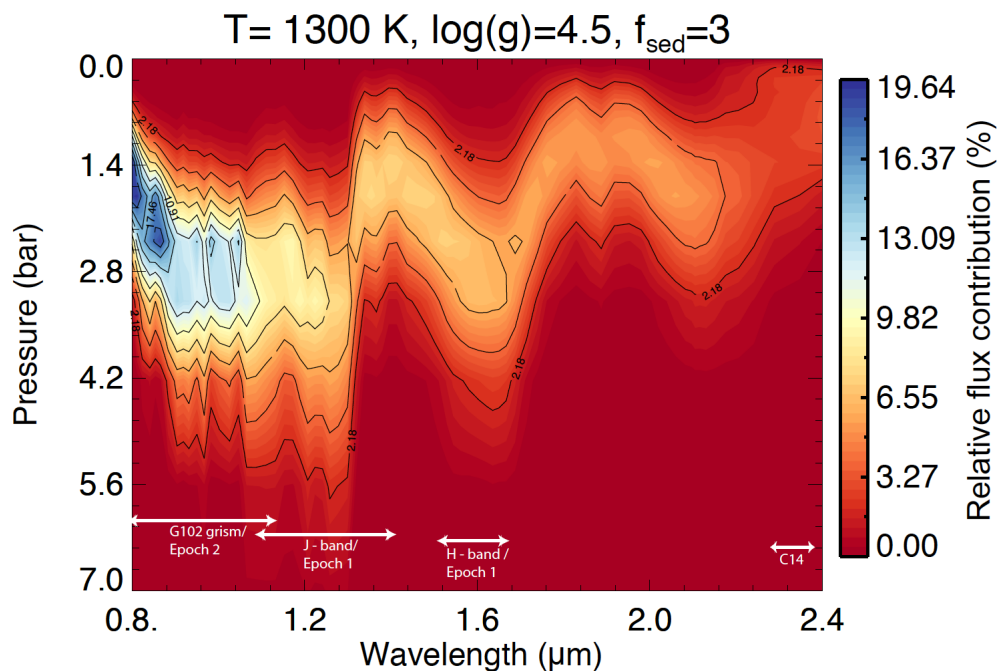


Figure 1.7: Relative flux contributions of every pressure level in a model atmosphere of a  $T_{\text{eff}}=1300$  K object (Karalidi et al., 2016).

This is also demonstrated in theoretical brightness temperature spectra from the red-optical to mid-infrared for early-L, late-L, and early-T dwarfs from early work by Marley et al., 2002 (Figure 1.8). The brightness temperature is the temperature for which a corresponding blackbody distribution,  $\pi B_{\lambda}(T)$ , pro-

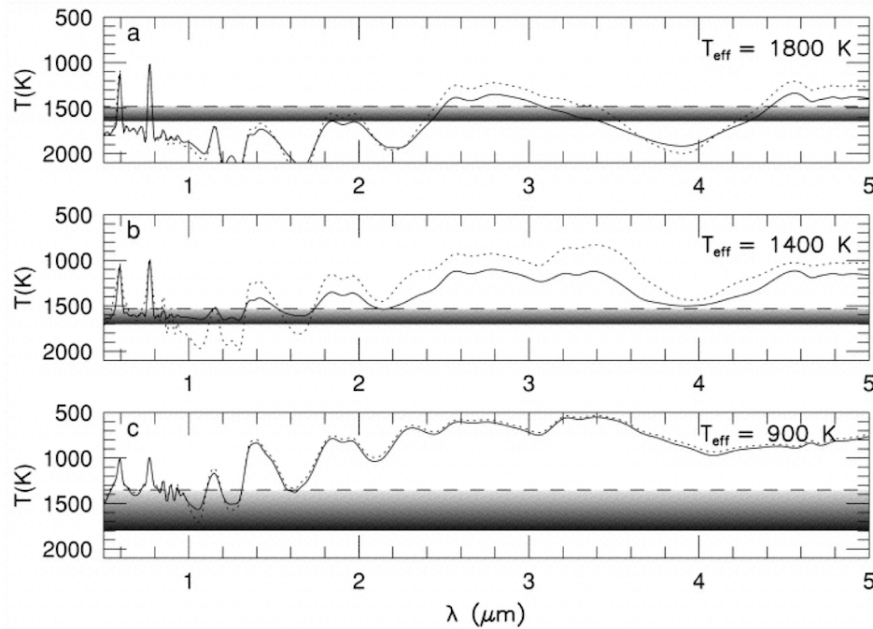


Figure 1.8: Theoretical brightness temperature spectra for an early-L, late-L and early-T dwarf (top to bottom) from Marley et al., 2002. The solid lines represent cloudless models and the dotted lines represent models with clouds included. The shaded regions indicate the locations of silicate clouds with the solid line depicting the base of the cloud, the dashed line indicating where the column extinction optical depth reaches 0.1 and the shading depicts the decreasing cloud extinction with altitude.

duces the same intensity as the theoretical surface flux density at each wavelength given an assumed radius ( $\sim 1R_{\text{Jup}}$ ). Using a pressure-temperature profile for a given  $T_{\text{eff}}$  model (e.g. Figure 1.9; Morley et al., 2012), one can calculate the pressure level in the atmosphere from which the flux originates at each wavelength. Condensation curves for each condensate species are also indicated in Figure 1.9 and will be discussed more in the next section.

The different originating locations of the flux at different wavelengths implies that spectral typing schemes for the mid- to late-L dwarfs that are determined from red-optical spectra (e.g. Kirkpatrick et al., 1999) are less sensitive to cloud thickness and location than schemes that use near-IR spectra or spectral indices (e.g. Geballe et al., 2002). In fact, Stephens, 2002, 2003 found that the flux from the bandpasses used to calculate the spectral indices from Geballe et al.,

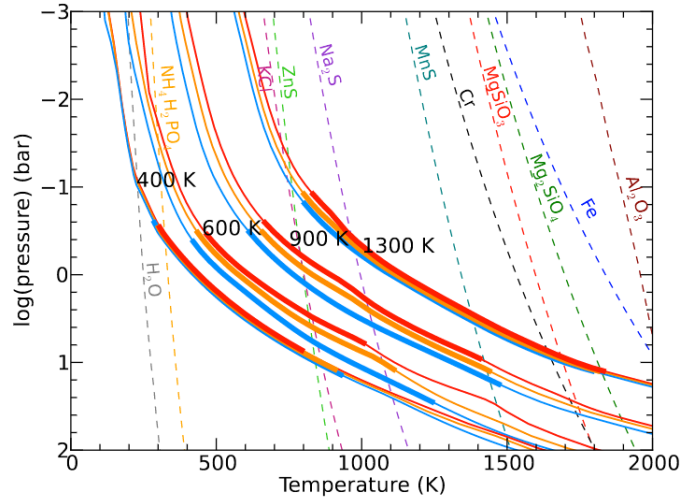


Figure 1.9: Example pressure-temperature profiles for different  $T_{\text{eff}}$  models from Morley et al., 2012. Colours indicate cloudless (blue) to cloudy (red) models and the thick portions of the curves show the 1–6  $\mu\text{m}$  region of the atmosphere. Condensation curves for each condensate species are also indicated.

2002 originates from within the cloud decks so will always be sensitive to the vertical distribution of condensates in the atmosphere.

### 1.3.3 EVOLUTION OF OPACITY SOURCES

Ultra-cool dwarf atmospheres, and thus their spectra, are demonstrably complex. One example of the complexity can be seen in the chemical reactions of several oxides as temperature decreases throughout the L to T spectral sequence. The beginning of the L dwarf sequence is characterized by the disappearance of TiO and VO molecules. As the atmosphere cools, these molecules begin combining with oxygen atoms or condensing to form much more complex molecules such as perovskite ( $\text{CaTiO}_3$ ). The removal of these molecules robs the photosphere of its two main absorbers resulting in a large change in appearance of the spectra. The weakening of the opacity of these molecules increases the contrast of the alkali lines and hydride bands against the continuum so Na I and K I (most abundant of alkali metals at solar metallicity) become the dominant absorbers in the mid- to late-L dwarfs (Burrows et al., 2003).

Of course, TiO and VO are not the only molecules that will be affected by the change in temperature. More refractory elements such as calcium and aluminum will be removed at higher temperatures than TiO which has a direct consequence on the rate at which perovskite is formed, thus, the rate at which TiO is removed from the atmosphere (Lodders et al., 2002). Furthermore, if Al and Si were not lost to condensate clouds at higher temperatures, they would have combined with O and K to form orthoclase ( $\text{KAlSi}_3\text{O}_8$ ) and removed K as a major absorber in late-L and T dwarfs.

These are only a couple examples of the myriad of reactions and possible reactions that occur in the atmospheres of ultra-cool dwarfs. We begin to see the complexity of molecular species that can affect the emergent spectra of these objects, making classifying them difficult work and understanding them even more difficult.

Throughout the L sequence, hydride molecules are strong absorbers and have a significant influence on the spectra. The most dominant of these is FeH. The strength of this feature increases towards mid-L then weakens by late-L. Burgasser et al., 2002a, however, noticed that the Wing-Ford band at 9896 Å increases in strength again in the early-T dwarfs before completely disappearing by mid-T. Water also becomes a dominant absorber by the late-L dwarfs as it is created in increasing amounts by the conversion of carbon monoxide into methane via the reaction  $\text{CO} + 3\text{H}_2 \rightarrow \text{CH}_4 + \text{H}_2\text{O}$  (Kirkpatrick, 2005). Figures 1.10 and 1.11 (Kirkpatrick, 2005) show the sequence of full near-IR and J-band spectra, respectively, from the warmest (late-M) ultra-cool dwarfs to coolest (late-T).

One of the defining characteristics of T dwarfs is  $\text{CH}_4$  absorption in the  $H$ - and  $K_s$ -bands. Methane is first seen at 3.3  $\mu\text{m}$  (the fundamental band; Cushing et al., 2005; Noll et al., 2000) in mid-L dwarfs but the unambiguous detection of the overtone bands at 1.6 and 2.2  $\mu\text{m}$  signals the start of the T sequence. As temperatures continue to decrease, more CO and  $\text{H}_2$  is turned into  $\text{CH}_4$  and  $\text{H}_2\text{O}$  so the water bands become increasingly strong along with methane. Although they are being converted into other molecules, CO and  $\text{H}_2$  are still important absorbers in the spectra of T dwarfs. At such low temperatures,  $\text{H}_2$

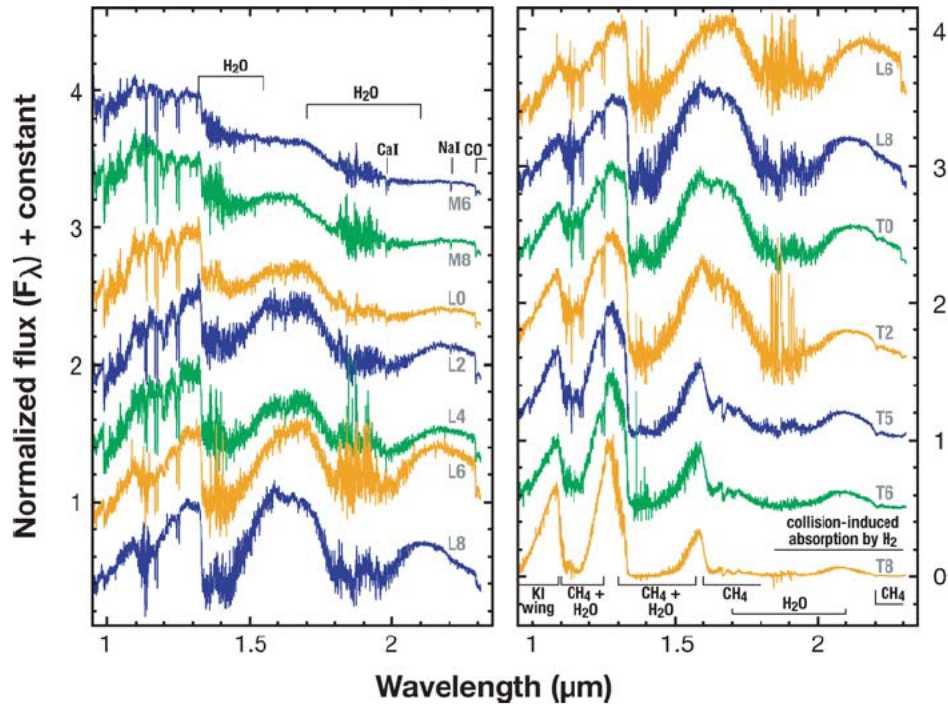


Figure 1.10: A sequence of mid-M through late-T spectra between 0.95 and 2.3  $\mu\text{m}$  (Kirkpatrick, 2005). Feature identifications within the  $H$ - and  $K_s$ -band windows are marked. The feature-rich  $J$ -band spectra are shown on an expanded scale in Figure 1.11. The spectra in this spectral sequence from Kirkpatrick, 2005 come from the Brown Dwarf Spectroscopic Survey archive (<http://www.astro.ucla.edu/~mclean/BDSSarchive/>; McLean et al., 2003).

is a very abundant molecule and the high pressures of L and T dwarfs ensure that there is a high collision rate. These collisions induce dipole moments in the molecules causing nearly continuous absorption in the infrared (Borysow et al., 1990) and bluer  $J - K_s$  and  $H - K_s$  colours (central wavelengths:  $J$  - 1.248  $\mu\text{m}$ ;  $H$  - 1.633  $\mu\text{m}$ ;  $K_s$  - 2.146  $\mu\text{m}$ ). The changing colours through the L and T sequences is shown in Figure 1.12.

Condensates also have significant influence on the T spectral type sequence. They are the dusty component of the photosphere that contributes to the very red near-infrared colours of the latest L dwarfs ( $J - K_s \approx 2$  mag; Tsuji, 2000). The gravitational settling of these condensates also explains the mid- to late-T colours ( $J - K_s \approx 0$  mag) but simple presence or absence of these molecules can-

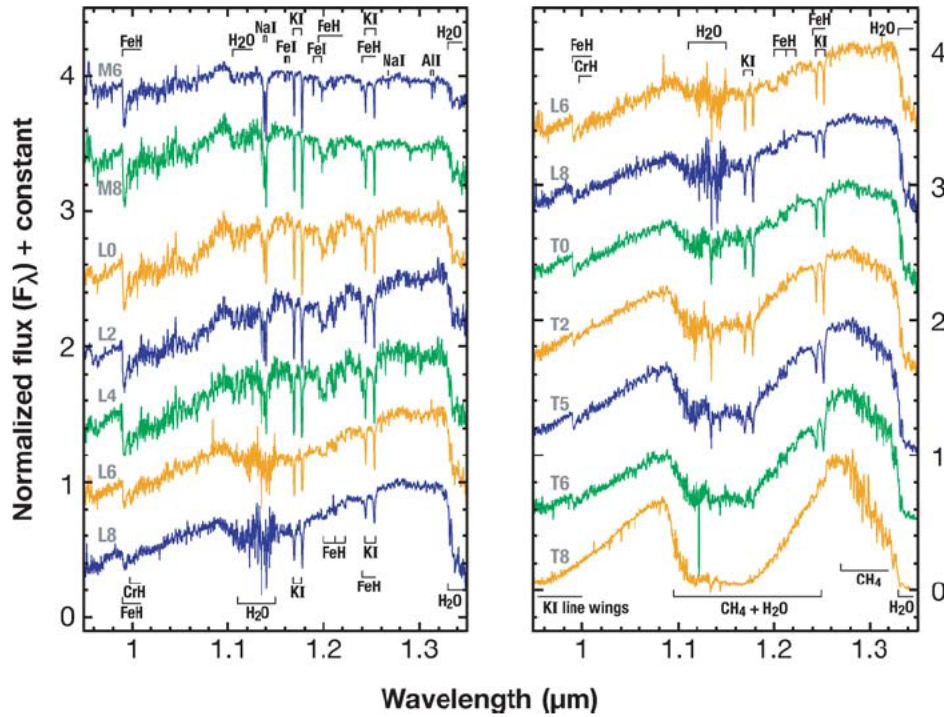


Figure 1.11: A 0.95–1.35  $\mu\text{m}$  detail of the mid-M through late-T spectral sequence shown in Figure 1.10 (Kirkpatrick, 2005). Feature identifications are marked.

not explain the behaviour of the early-T dwarfs. In order to understand their behaviour, cloud and dust settling physics must be employed. These extra parameters are discussed in the next section.

The condensation curves for a number of the condensate species can be seen in Figure 1.9 (Morley et al., 2012). These condensation curves indicate the temperatures, for a given pressure, at which each of the species condenses into clouds and become more important contributors to the opacity. Figure 1.13 shows theoretical wavelength-dependent brightness temperatures based on these curves for  $T_{\text{eff}}=1300$  K (late-L/early-T), 900 K (mid-T), 600 K (late-T), and 400 K (early-Y) objects. The relative amount of clouds in each model is given by the  $f_{\text{sed}}$  parameter which defines the efficiency of sedimentation relative to the turbulent mixing. Each panel shows cloudless (blue;  $f_{\text{sed}} = \infty$ ), partially cloudy (orange;  $f_{\text{sed}}=4$ ), and cloudy (red;  $f_{\text{sed}}=2$ ) models and the location of the dom-

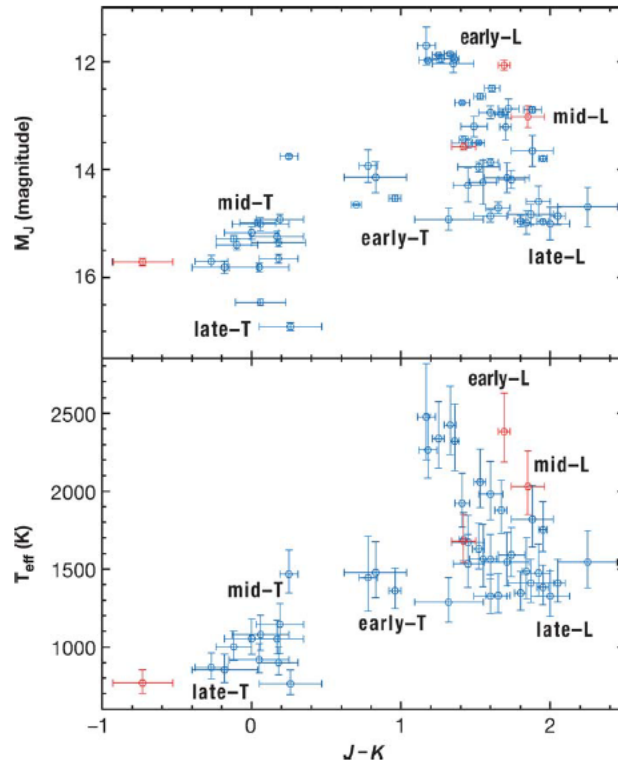


Figure 1.12: (Top panel) Absolute  $J$ -band magnitude versus  $J - K$  colour for L and T dwarfs (Kirkpatrick, 2005). (Bottom panel) Effective temperature versus  $J - K$  colour for the same data set. The colours come from data tabulated in Vrba et al., 2004 supplemented with data from 2MASS. Approximate locations of early-L through late-T dwarfs are shown in black. The spectroscopically peculiar objects from Figure 1.6 are again noted in red and represent, from left to right, 2MASS J09373487+2931409, SDSS J042348.57-041403.5, Kelu-1, and 2MASSW J1841086+311727 (not shown in previous figure).

inant cloud species for each type of object. We can see that in the  $T_{\text{eff}}=900$  K object, the flux at most wavelengths originates from within the clouds so the thickness of the clouds has a large impact on the flux density. In the cooler objects, the clouds are thicker but have sunk below the emergent flux regions at all wavelengths except those in the optical, therefore, only the optical wavelengths are affected by cloud variations at these temperatures. In the warmest model ( $T_{\text{eff}}=1300$  K), the atmosphere is too hot for most condensate species to form so there is little to no cloud variation occurring.

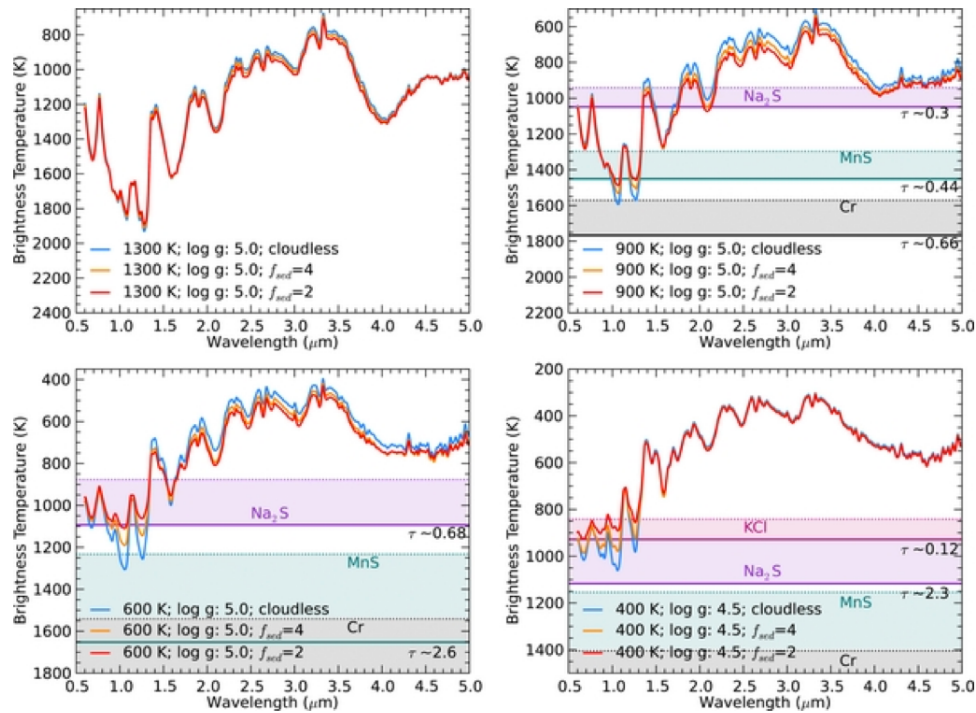


Figure 1.13: Model brightness temperature spectra from Morley et al., 2012. Colours indicate models with no clouds (blue), thin clouds (orange) and thick clouds (red). The solid horizontal line indicates the base of the dominant species of clouds and the dashed horizontal line denotes where the column extinction optical depth of the cloud reaches 0.1.

As evidenced by the dramatic difference in spectral appearance between L and T dwarfs, the transition between these two spectral types is a region where atmospheric composition changes drastically. This is also a region where atmospheric models can be put to the test and our understanding of the underlying physics can be refined.

#### 1.3.4 MODELING THE L–T TRANSITION

Relatively early in brown dwarf atmosphere theory, several models were produced to try to explain the rapid reversal of the near-infrared colours at the transition from L to T dwarfs. The bottom panel of Figure 1.12 (Kirkpatrick, 2005) shows that the reversal of colour from red to blue occurs over a temper-

ature range of only  $\sim 200$  K–  $300$  K. Depending on the mass of the object, this change could take place over a timescale of anywhere from a few Myr to a few Gyr (Figure 1.6). In the Tsuji, 2002 models, this reversal occurs over a range of  $>600$  K. These models say that the clouds start at an optically thin region of the photosphere where the temperature is  $>1600$  K. As the temperature decreases, the clouds thicken and start falling deeper into the atmosphere. When the dust moves into the optically thick region of the atmosphere ( $T_{eff} < 1400$  K), the upper atmosphere cools rapidly and begins the CO to CH<sub>4</sub> conversion along with the reversal of near-infrared colours. This seems to be a nice description of the physical process but the colour reversal is too slow.

Marley et al., 2002 attempted to incorporate the effect of clouds in their models by introducing the  $f_{sed}$  parameter which defines the efficiency of sedimentation relative to the turbulent mixing. To simulate an atmosphere with efficient sedimentation with little mixing (latest L dwarfs), they set their  $f_{sed}$  parameter to between 0 and 3. The early-T dwarfs can be fit by  $f_{sed} > 3$  and the cloud-free mid- to late-T dwarfs can be fit with  $f_{sed} \approx \infty$ . These models, however, also fail to reproduce the rapid reversal of near-infrared colours.

Knapp et al., 2004 expanded on this model by suggesting that around  $T_{eff} = 1300$  K,  $f_{sed}$  gradually increases from  $\sim 3$  to infinity at roughly a fixed effective temperature. This is the equivalent of saying that there is a “sudden downpour” of condensed iron and silicates. The rapid increase in sedimentation efficiency creates a “torrential rain” of these condensed molecules.

Burgasser et al., 2002a expanded on an idea that was first suggested in Ackerman et al., 2001 that instead of treating the clouds as uniform, perhaps they should be treated as patchy as seen on Jupiter and Saturn. Holes in the clouds allows flux from the deeper, warmer layers to emerge. Brown dwarfs with fewer clouds will have bluer  $J - K_s$  colours and fainter  $M_J$  than ultra-cool dwarfs of the same temperature with more clouds. The unexpected increase in strength of the Wing-Ford FeH band at  $0.99\mu\text{m}$  can also be explained with this scenario. The iron has been condensed out of the cool, optically thin layers of the atmosphere above the clouds by the late-L dwarfs. When the clouds start to become patchy in the early-T dwarfs due to the same physical process described

in the Tsuji, 2002 models, the light from the warmer, deeper layers emerges. In these layers, the FeH has not been depleted by the condensation of iron, thus the strength of the FeH band increases again until the mid- to late-T dwarfs where the atmosphere has cooled enough so that none of the observable layers contain FeH.

Marley et al., 2010 also adopt a patchy cloud scenario by incorporating a cloud coverage parameter  $h$  into their models. In this way they can model both the cloud thickness and patchiness in a single profile. With their models, they have been able to provide good spectral matches to a number of blue and variable objects.

A different solution was posed by Tsuji et al., 2003 and further developed by Burrows et al., 2006 which suggests that a single evolutionary sequence should not be attributed to the observational  $M_J$  vs  $J - K$  diagram (top panel of Fig. 1.12). Instead, the authors say that we should interpret the diagram as seeing objects along different evolutionary sequences according to their gravities. In this scenario, the brightest of the objects between mid-L to mid-T have the lowest gravity (i.e. lowest mass) and the faintest objects in this range have the highest gravity since a high gravity object would lose its cloud deck at a lower temperature and dimmer  $M_J$  than a low gravity object.

### 1.3.5 OBSERVATIONAL EVIDENCE

Knapp et al., 2004 point out that all of the transition models will have predictions that are testable. One of the largest differences between the models that is observable is gravity. Knapp et al., 2004 note that the gravity tests for the late-L dwarfs are fairly subtle as all the models predict that the faintest and reddest L dwarfs will have higher masses. The downpour model predicts that higher masses turn to the blue later than the lower masses. The authors note, however, that the turn off at the lower masses happens at later spectral types than the Tsuji et al., 2003 model.

In the early-T region, however, the gravity tests are much more effective. The downpour model of Knapp et al., 2004 predicts that low mass (low gravity) ultra-cool dwarfs will turn to bluer near-infrared colours earlier than higher

mass (higher gravity) objects since a high gravity object would lose its cloud deck at a lower temperature and dimmer  $M_J$  than a low gravity object. Figure 1.14 shows the evolutionary tracks of theoretical objects with different gravities and sedimentation efficiencies. The authors use as an example the T3.5 dwarf — SDSS J175032.96+175903.9 — in Figure 1.14 to demonstrate how different models predict different gravities. This T3.5 dwarf lies near the highest gravity track of the downpour model so they estimate  $\log g \sim 5.4$ . The patchy cloud model would predict a slightly lower gravity of  $\log g = 5$  because the evolutionary tracks curve downward at blue  $J - K_s$ . Tsuji et al., 2003, on the other hand, predict that this object would have an even lower gravity ( $\log g \sim 4$ ) because it is such a bright object that has already turned to a bluer  $J - K_s$  colour. Determining the gravity of this object could help determine which of the models is the most likely to be correct.

Gravity is not the only diagnostic. The resurgence of the the FeH absorption is also an observation that needs to be reproduced in the models. The patchy-cloud model straightforwardly accounts for the trend in FeH, as discussed above, but it is uncertain if the other models do.

### 1.3.6 EFFECT OF GRAVITY AND METALLICITY

As previously discussed, ultra-cool dwarfs can have a wide range of masses and ages for any given temperature (Fig. 1.5). Generally, objects from low-mass stars to the lowest-mass ultra-cool dwarfs have the same radii so the surface gravities simply depend on mass. At a given temperature (spectral type), however, the oldest ultra-cool dwarfs will have already contracted into their final configuration while the youngest will still be enlarged, making them bigger than their older counterparts. This enhances the gravity difference between the old (high mass) and young (low mass) ultra-cool dwarfs (Kirkpatrick, 2005).

Fortunately, approximate surface gravities can be determined from the low-resolution ( $R \sim 75-150$ ), near-IR spectra from the SpeX instrument on the Infrared Telescope Facility that are commonly used for classification of ultra-cool dwarfs. Pressure broadening caused by collisions depends on the temperature and the density (gravity) in the atmosphere. Therefore, an ultra-cool dwarf with

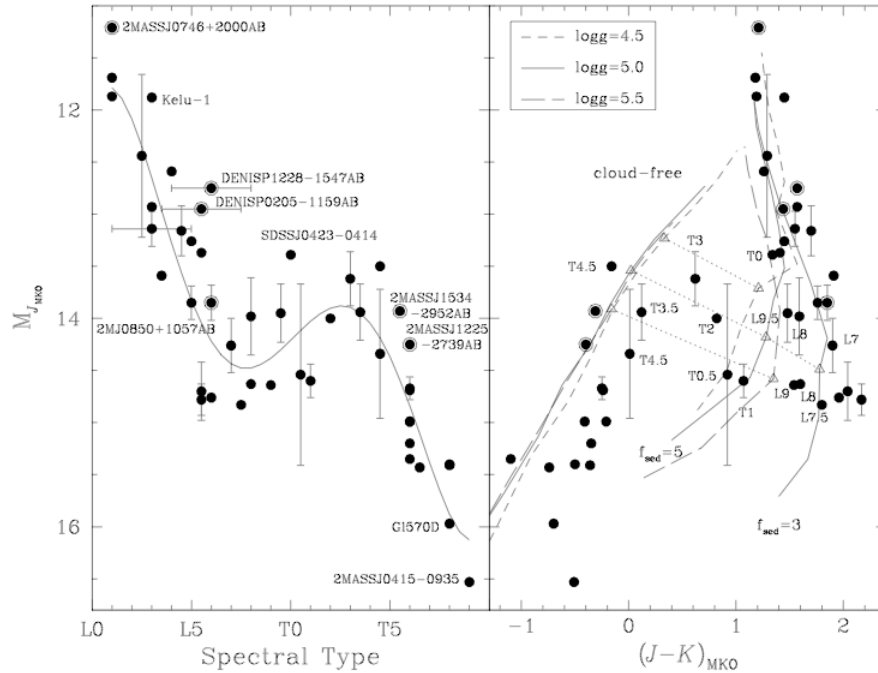


Figure 1.14:  $M_J$  as a function of spectral type and  $J - K$  colour (Knapp et al., 2004). Error bars are shown where the distance modulus is uncertain by 0.1 mag and where type is uncertain by  $>1$  subclass. Known binaries are indicated by ringed symbols. In the left panel the known binaries and other apparently superluminous dwarfs are labelled, as well as the two faintest dwarfs. A 5th order polynomial fit to  $M_J$  is shown. In the right panel all objects with types between L7 and T4.5 are identified. Model  $M_J$  against  $J - K$  sequences are shown for  $f_{sed} = 3$ ,  $f_{sed} = 5$  and cloud-free models from Marley et al., 2002. The dotted lines between the triangles connect the  $T_{eff} = 1300$  K points on each model sequence.

a given temperature and lower gravity than another ultra-cool dwarf with the same temperature, will have less pressure-broadened absorption lines. Gorlova et al., 2003 found that the K I ( $1.25 \mu\text{m}$ ), Na I ( $2.21 \mu\text{m}$ ) and possibly FeH ( $1.20 \mu\text{m}$ ) lines are the most gravity sensitive. As seen in Figure 1.15 (Allers et al., 2013), ultra-cool dwarfs with lower gravity have weaker absorption lines than objects of typical field ages ( $> 1$  Gyr) with higher gravities. These features are still easily recognizable in the low-resolution spectra that are commonly obtained (Fig. 1.16; Allers et al., 2013).

The most recognizable identifier of low surface gravity is an extremely red

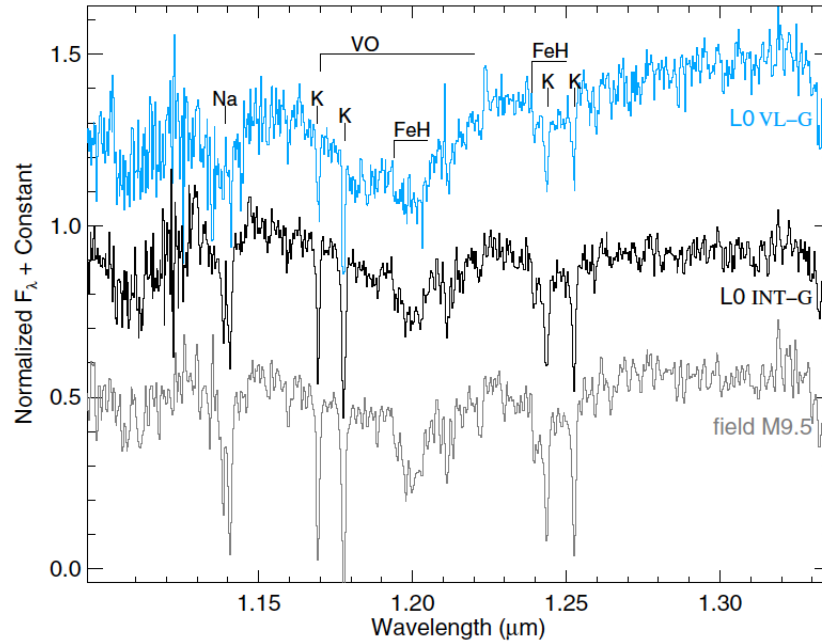


Figure 1.15: Moderate-resolution ( $R \approx 2000$ ) spectra comparing the gravity (age) sensitive features in the  $J$ -band spectra of objects classified as L0 in the near-IR (Allers et al., 2013). The L0 very low-g spectrum is 2MASS J01415823-4633574 (blue; Kirkpatrick et al., 2006) and the intermediate-g spectrum is 2MASS J15474719-2423493 (black; Allers et al., 2013). For comparison, the spectrum of a field M9.5 (BRI 0021-0214; gray; Cushing et al., 2005) is displayed. Young, low-gravity L0s have weaker Na I, K I, and FeH features than normal field L0 dwarfs.

$J - K_s$  colour for the spectral type (e.g. Barman et al., 2011; Kirkpatrick et al., 2008). The lower pressure at a given temperature reduces the collision-induced absorption (CIA) by  $H_2$  which leads to less suppression of the K-band flux (Faherty et al., 2013). The flux in the  $H$ -band is also affected by this phenomenon but to a lesser extent. This region takes on a triangular shape as only part of the  $H$ -band is subject to CIA by  $H_2$ . Because young ultra-cool dwarfs have not yet contracted into their final configurations and their gravities are low, many of the condensates are suspended high in their atmospheres and provide a larger column depth of extinction. These thicker, dusty clouds obscure a greater portion of the flux from the deeper layers, reducing the amount of emergent flux at the shorter wavelength end of the near-IR. This leads to fainter absolute  $J$ -band magnitudes (e.g. Burgasser et al., 2010) and redder  $J - K_s$  colours. Burgasser

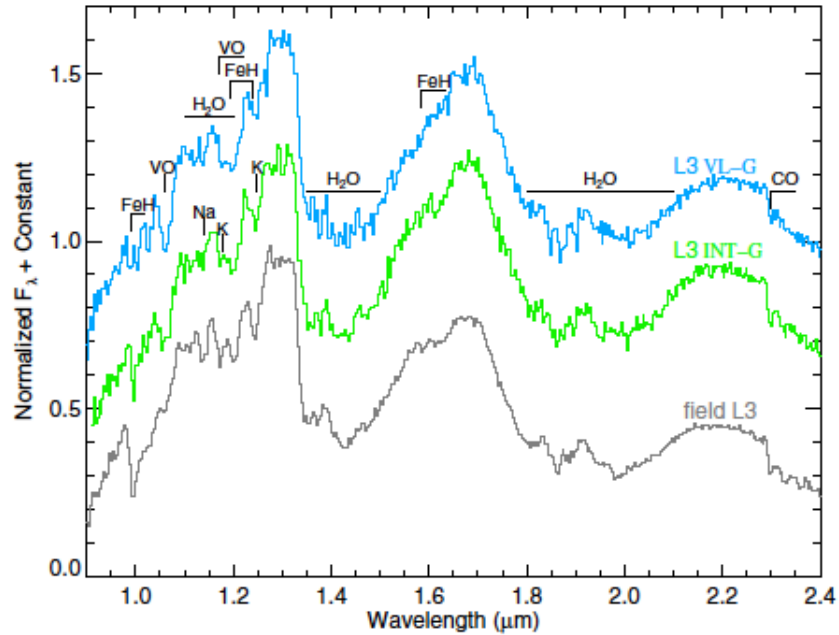


Figure 1.16: Low-resolution ( $R \approx 100$ ) spectra comparing the gravity (age) sensitive features for objects classified as L3 in the near-IR (Allers et al., 2013). The very low-g object is 2MASS J22081363+2921215 (blue; Allers et al., 2013), the intermediate-g object is 2MASS J17260007+1538190 (green; Allers et al., 2013) and the field dwarf is the L3 standard 2MASS J15065441+1321060 (gray; Burgasser et al., 2007). FeH, Na I, and K I features are weaker at lower gravities and VO is stronger. The  $H$ -band continuum shows a distinct triangular shape at low gravities.

et al., 2010 note that models have predicted that particle sizes in low-gravity atmospheres are larger and therefore are more visible and scatter more efficiently than their older, more massive counterparts, further reducing the emergent flux from the deeper layers.

Metallicity also plays a role in shaping the spectra and the evolutionary sequence of ultra-cool dwarfs. Burrows et al., 1993 show that the star to ultra-cool dwarf transition occurs at a much higher mass and temperature in a zero-metallicity environment than for solar metallicity objects. The dominant opacity sources in zero-metallicity ultra-cool dwarfs are bound-free and free-free absorption by  $H^-$ , Rayleigh scattering by  $H_2$  and H and collision-induced  $H_2$  absorption which gives rise to very blue  $J - K$  colours. These low-metallicity

ultra-cool dwarfs would have been produced in the earliest epochs of star formation in the galaxy and the lack of metals would be readily distinguishable in their spectra.

#### 1.4 OUTSTANDING PROBLEMS ADDRESSED IN MY THESIS

There are still many outstanding issues in understanding the atmospheres of brown dwarfs. Determining how long we can detect the signatures of low gravity in the spectra of ultra-cool dwarfs, for instance, would allow us to put constraints on the exact timescale of the contraction phase and help us to understand the effects of this phase on atmospheric properties. In Chapters 2 and 3, I present a survey that identified peculiarly red objects in a cross-match of the Sloan Digital Sky Survey (SDSS), 2-Micron All Sky Survey (2MASS), and Wide-field Infrared Survey Explorer (WISE) databases. Our goal was to determine the frequency of young objects compared to all other field-age objects. We used various colour selection criteria to select objects with peculiarly red colours which included young ultra-cool dwarfs and objects that had unusually high dust contents but no signatures of youth. Since there have not been many of the latter kinds of objects found before my work, the cause of their dustiness is still unknown. The frequency of their occurrence could be the key to understanding them. We have determined this frequency and speculate on the nature of their high dust content in Chapter 2.

From the survey, I have identified one of the brightest, planetary-mass free-floating brown dwarfs known to date — the L7 dwarf 2MASS J11193254–1137466. In Chapter 4, I present how we confirmed that this object is part of the 10 Myr-old TW Hydrae Association and determine that it is actually the closest member. At 27 pc, it is also one of the closest very low mass brown dwarfs known and is an excellent place to study the atmosphere of an object that is considered an exoplanet analogue. Exoplanets are inherently difficult to study due to the proximity to their very bright host star. Free-floating planetary-mass brown dwarfs offer the unique opportunity to study objects that are very similar to many of the directly imaged extrasolar giant planets without being washed out

by a bright host star. Further observations of 2M 1119–1137 will potentially reveal more about the atmospheric composition and cloud structure of this interesting object.

To really understand the atmospheres of brown dwarfs, we need to study individual objects in detail. Understanding how cloud structures change and how those changes affect observables such as broad-band photometric colours and individual spectral features will help in the understanding of the population as a whole. In Chapter 5, I present our study of the variability of one of the closest systems to the sun — Luhman 16AB — from a two night spectroscopic monitoring campaign. Luhman 16B is known to have a very large amplitude flux variability. We obtained spectra of the system continuously over two nights with the goal of determining how the flux at each wavelength changed over the course of its rotation period (5hrs). We were also able to determine how the variability — most likely due to changes in the optical depth of the clouds — affected individual absorption features in the spectra and thus which absorbers are affected the most in the changing atmosphere.

Finally in Chapter 6, I present the potential discovery of a rare L/T transition dwarf that is most likely part of the low-metallicity thick-disk or halo — the oldest populations of objects in the Milky Way. Only  $\sim 6\%$  of the objects in the solar neighbourhood are part of either of these populations and even more rare are the members that are late-L or early-T dwarfs due to the nature of the L/T transition. This transition from L to T dwarfs is very quick and only a handful of thin-disk objects with this spectral type have been found. This makes thick-disk/halo L/T transition dwarfs very difficult to find. We have potentially found one such object in our search for all objects in the solar neighbourhood. Further observations of this objects will shed light on an extremely rare type of ultra-cool dwarf, and help us understand what role metallicity plays in the evolution of brown dwarf atmospheres.

## 1.5 SUMMARY

Brown dwarfs are unique and complex objects. Their low masses don't allow them to sustain, or sometimes even begin, the thermonuclear processes that provide stars with internal energy and the thermal pressure necessary to maintain hydrostatic equilibrium. Thus, their radii, luminosities and effective temperatures decrease as they age. They eventually stop collapsing when they reach the point where electron degeneracy pressure takes over. However, they continue to fade and cool for the rest of their lives due to the lack of internal energy generation. Their inexorable cooling means their spectral classification continually changes as well.

It is now a well known fact that the spectral appearance of ultra-cool dwarfs is governed by more than just temperature. Factors such as gravity, metallicity and cloud distribution play an important role in the structure and composition of ultra-cool dwarf atmospheres and ultimately their spectra. Understanding exactly how these properties affect the observable spectra gives us insight into their effects on the underlying physics. Having a better picture of the physical process inside brown dwarfs helps put constraints on evolutionary and atmospheric models, eventually allowing us to fully understand every aspect of these unique objects.

The goal of my work has been to identify objects with unusual characteristics such as decreased gravity, high atmospheric dust content, and unresolved binarity in large all-sky surveys. By comparing the population of objects with such properties to the population of "normal" objects, we can determine the timescales of each atmospheric phenomenon and how they play into the evolution of ultra-cool dwarfs. Another piece of the puzzle is understanding how conditions on individual objects affect their structure and composition. With this goal in mind, we have studied in detail one of the closest systems to the sun — Luhman 16AB. The secondary component, Luhman 16B is also known to have large degrees of varying cloud structure. Finally, old, low-metallicity objects in the Milky Way are remnants from the early galactic environment and we have found one such potential object. By studying these objects we can gain a bet-

ter understanding of conditions in the young Milky Way and figure out the role that metallicity plays on the evolution of these lowest mass objects.

#### REFERENCES

- Ackerman, A. S. and Marley, M. S. (2001). *ApJ* 556, pp. 872–884. DOI: [10 . 1086/321540](https://doi.org/10.1086/321540).
- Allard, F., Hauschildt, P. H., Alexander, D. R., et al. (2001). *ApJ* 556, pp. 357–372. DOI: [10.1086/321547](https://doi.org/10.1086/321547).
- Allers, K. N. and Liu, M. C. (2013). *ApJ* 772, 79, p. 79. DOI: [10 . 1088/0004-637X/772/2/79](https://doi.org/10.1088/0004-637X/772/2/79).
- Apai, D., Radigan, J., Buenzli, E., et al. (2013). *ApJ* 768, 121, p. 121. DOI: [10 . 1088/0004-637X/768/2/121](https://doi.org/10.1088/0004-637X/768/2/121).
- Artigau, É., Bouchard, S., Doyon, R., et al. (2009). *ApJ* 701, pp. 1534–1539. DOI: [10.1088/0004-637X/701/2/1534](https://doi.org/10.1088/0004-637X/701/2/1534).
- Bailey, J. (2014). *PASA* 31, e043, e043. DOI: [10.1017/pasa.2014.38](https://doi.org/10.1017/pasa.2014.38).
- Baraffe, I., Chabrier, G., Allard, F., et al. (2002). *A&A* 382, pp. 563–572. DOI: [10.1051/0004-6361:20011638](https://doi.org/10.1051/0004-6361:20011638).
- Barman, T. S., Macintosh, B., Konopacky, Q. M., et al. (2011). *ApJ* 735, L39, p. L39. DOI: [10.1088/2041-8205/735/2/L39](https://doi.org/10.1088/2041-8205/735/2/L39).
- Borysow, A. and Frommhold, L. (1990). *ApJ* 348, pp. L41–L43. DOI: [10.1086/185626](https://doi.org/10.1086/185626).
- Bouvier, J., Matt, S. P., Mohanty, S., et al. (2014). *Protostars and Planets VI*, pp. 433–450. DOI: [10.2458/azu\\_uapress\\_9780816531240-ch019](https://doi.org/10.2458/azu_uapress_9780816531240-ch019).
- Buenzli, E., Saumon, D., Marley, M. S., et al. (2015). *ApJ* 798, 127, p. 127. DOI: [10.1088/0004-637X/798/2/127](https://doi.org/10.1088/0004-637X/798/2/127).
- Burgasser, A. J., Marley, M. S., Ackerman, A. S., et al. (2002a). *ApJ* 571, pp. L151–L154. DOI: [10.1086/341343](https://doi.org/10.1086/341343).
- Burgasser, A. J., Kirkpatrick, J. D., Brown, M. E., et al. (2002b). *ApJ* 564, pp. 421–451. DOI: [10.1086/324033](https://doi.org/10.1086/324033).

- Burgasser, A. J., Kirkpatrick, J. D., and Lépine, S. (2005). *13th Cambridge Workshop on Cool Stars, Stellar Systems and the Sun*. Ed. by F. Favata, G. A. J. Hussain, and B. Battrick. Vol. 560. ESA Special Publication, p. 237.
- Burgasser, A. J., Cruz, K. L., and Kirkpatrick, J. D. (2007). *ApJ* 657, pp. 494–510. DOI: [10.1086/510148](https://doi.org/10.1086/510148).
- Burgasser, A. J., Cruz, K. L., Cushing, M., et al. (2010). *ApJ* 710, pp. 1142–1169. DOI: [10.1088/0004-637X/710/2/1142](https://doi.org/10.1088/0004-637X/710/2/1142).
- Burrows, A., Hubbard, W. B., Saumon, D., et al. (1993). *ApJ* 406, pp. 158–171. DOI: [10.1086/172427](https://doi.org/10.1086/172427).
- Burrows, A., Hubbard, W. B., Lunine, J. I., et al. (2001). *Reviews of Modern Physics* 73, pp. 719–765. DOI: [10.1103/RevModPhys.73.719](https://doi.org/10.1103/RevModPhys.73.719).
- Burrows, A. and Volobuyev, M. (2003). *ApJ* 583, pp. 985–995. DOI: [10.1086/345412](https://doi.org/10.1086/345412).
- Burrows, A., Sudarsky, D., and Hubeny, I. (2006). *ApJ* 640, pp. 1063–1077. DOI: [10.1086/500293](https://doi.org/10.1086/500293).
- Chabrier, G., Baraffe, I., Allard, F., et al. (2000). *ApJ* 542, pp. 464–472. DOI: [10.1086/309513](https://doi.org/10.1086/309513).
- Cruz, K. L., Kirkpatrick, J. D., and Burgasser, A. J. (2009). *AJ* 137, pp. 3345–3357. DOI: [10.1088/0004-6256/137/2/3345](https://doi.org/10.1088/0004-6256/137/2/3345).
- Cushing, M. C., Rayner, J. T., and Vacca, W. D. (2005). *ApJ* 623, pp. 1115–1140. DOI: [10.1086/428040](https://doi.org/10.1086/428040).
- Dantona, F. and Mazzitelli, I. (1985). *ApJ* 296, pp. 502–513. DOI: [10.1086/163470](https://doi.org/10.1086/163470).
- Faherty, J. K., Rice, E. L., Cruz, K. L., et al. (2013). *AJ* 145, 2, p. 2. DOI: [10.1088/0004-6256/145/1/2](https://doi.org/10.1088/0004-6256/145/1/2).
- Geballe, T. R., Knapp, G. R., Leggett, S. K., et al. (2002). *ApJ* 564, pp. 466–481. DOI: [10.1086/324078](https://doi.org/10.1086/324078).
- Gorlova, N. I., Meyer, M. R., Rieke, G. H., et al. (2003). *ApJ* 593, pp. 1074–1092. DOI: [10.1086/376730](https://doi.org/10.1086/376730).
- Hayashi, C. and Nakano, T. (1963). *Progress of Theoretical Physics* 30, pp. 460–474. DOI: [10.1143/PTP.30.460](https://doi.org/10.1143/PTP.30.460).

- Heinze, A. N., Metchev, S., Apai, D., et al. (2013). *ApJ* 767, 173, p. 173. DOI: [10.1088/0004-637X/767/2/173](https://doi.org/10.1088/0004-637X/767/2/173).
- Karalidi, T., Apai, D., Marley, M. S., et al. (2016). *ApJ* 825, 90, p. 90. DOI: [10.3847/0004-637X/825/2/90](https://doi.org/10.3847/0004-637X/825/2/90).
- Kirkpatrick, J. D. (2005). *ARA&A* 43, pp. 195–245.
- Kirkpatrick, J. D., Reid, I. N., Liebert, J., et al. (1999). *ApJ* 519, pp. 802–833. DOI: [10.1086/307414](https://doi.org/10.1086/307414).
- Kirkpatrick, J. D., Barman, T. S., Burgasser, A. J., et al. (2006). *ApJ* 639, pp. 1120–1128. DOI: [10.1086/499622](https://doi.org/10.1086/499622).
- Kirkpatrick, J. D., Cruz, K. L., Barman, T. S., et al. (2008). *ApJ* 689, 1295–1326, pp. 1295–1326. DOI: [10.1086/592768](https://doi.org/10.1086/592768).
- Knapp, G. R., Leggett, S. K., Fan, X., et al. (2004). *AJ* 127, pp. 3553–3578. DOI: [10.1086/420707](https://doi.org/10.1086/420707).
- Lodders, K. and Fegley, B. (2002). *Icarus* 155, pp. 393–424. DOI: [10.1006/icar.2001.6740](https://doi.org/10.1006/icar.2001.6740).
- Marley, M. S., Saumon, D., Guillot, T., et al. (1996). *Science* 272, pp. 1919–1921. DOI: [10.1126/science.272.5270.1919](https://doi.org/10.1126/science.272.5270.1919).
- Marley, M. S., Seager, S., Saumon, D., et al. (2002). *ApJ* 568, pp. 335–342. DOI: [10.1086/338800](https://doi.org/10.1086/338800).
- Marley, M. S., Saumon, D., and Goldblatt, C. (2010). *ApJ* 723, pp. L117–L121. DOI: [10.1088/2041-8205/723/1/L117](https://doi.org/10.1088/2041-8205/723/1/L117).
- McLean, I. S., McGovern, M. R., Burgasser, A. J., et al. (2003). *ApJ* 596, pp. 561–586. DOI: [10.1086/377636](https://doi.org/10.1086/377636).
- Metchev, S. A., Heinze, A., Apai, D., et al. (2015). *ApJ* 799, 154, p. 154. DOI: [10.1088/0004-637X/799/2/154](https://doi.org/10.1088/0004-637X/799/2/154).
- Miles-Páez, P. A., Metchev, S. A., Heinze, A., et al. (2017). *ArXiv e-prints*.
- Morley, C. V., Fortney, J. J., Marley, M. S., et al. (2012). *ApJ* 756, 172, p. 172. DOI: [10.1088/0004-637X/756/2/172](https://doi.org/10.1088/0004-637X/756/2/172).
- Morley, C. V., Marley, M. S., Fortney, J. J., et al. (2014). *ApJ* 789, L14, p. L14. DOI: [10.1088/2041-8205/789/1/L14](https://doi.org/10.1088/2041-8205/789/1/L14).
- Noll, K. S., Geballe, T. R., Leggett, S. K., et al. (2000). *ApJ* 541, pp. L75–L78. DOI: [10.1086/312906](https://doi.org/10.1086/312906).

- Radigan, J. (2014). *ApJ*, *in press*, <http://arxiv.org/abs/1408.5919>.
- Rodríguez-Ledesma, M. V., Mundt, R., and Eisloffel, J. (2009). *A&A* 502, pp. 883–904. DOI: [10.1051/0004-6361/200811427](https://doi.org/10.1051/0004-6361/200811427).
- Stephens, D. C. (2002). PhD thesis. NEW MEXICO STATE UNIVERSITY.
- (2003). *Brown Dwarfs*. Ed. by E. Martín. Vol. 211. IAU Symposium, p. 355.
- Tsuji, T (2000). *Very Low-Mass Stars and Brown Dwarfs*. Ed. by R. Rebolo and M.R. Zapatero-Osorio. Cambridge Contemporary Astrophysics. Cambridge University Press, pp. 156–168.
- Tsuji, T. (2002). *ApJ* 575, pp. 264–290.
- Tsuji, T. and Nakajima, T. (2003). *ApJ* 585, pp. L151–L154. DOI: [10.1086/374388](https://doi.org/10.1086/374388).
- Vrba, F. J., Henden, A. A., Luginbuhl, C. B., et al. (2004). *AJ* 127, pp. 2948–2968. DOI: [10.1086/383554](https://doi.org/10.1086/383554).

# 2

## A Targeted Search for Peculiarly Red L and T Dwarfs in SDSS, 2MASS, and WISE: Discovery of a Possible L7 Member of the TW Hydrae Association

### 2.1 INTRODUCTION

Compared to main sequence stars, ultra-cool dwarfs display a wide range of near-infrared colours, even among objects at the same effective temperature or spectral type. The diversity is diagnostic of the unique processes taking place in their molecule- and condensate-rich atmospheres. Effective temperature is the main factor that governs the photospheric appearance of field-aged brown dwarfs, with current understanding pointing to a monotonic correspondence between effective temperature and optical spectral type (Golimowski et al., 2004;Looper et al., 2008a; Vrba et al., 2004).

Cruz et al. (2009) proposed a dimensional extension to the classification scheme

---

A version of this chapter has been published (Kellogg et al., 2015).

for brown dwarfs, by incorporating surface gravity as a second parameter. They adopt a qualitative description of surface gravities—intermediate, low, and very low—based on optical spectral line strengths. Allers et al. (2013) expanded the classification scheme to the near-IR by adding continuum index measures to classify the absorption strengths of volatile molecules.

Low surface gravities generally contribute to higher dust content in the upper atmospheres of brown dwarfs, making them redder. Analyses of the L and T dwarf population have shown that the optical and near-infrared colours of low-surface gravity objects are readily distinguishable from those of “normal” objects (e.g., Allers et al., 2013; Cruz et al., 2009; Faherty et al., 2012; Knapp et al., 2004). However, there is also evidence of red brown dwarfs with high dust content without any signatures of youth (Kirkpatrick et al., 2010;Looper et al., 2008b). Their near-IR colours are very similar to those of the young, low-surface gravity objects but their spectra do not have any of the characteristics of youth. That is, peculiarly red brown dwarfs may not necessarily be low-gravity and hence young, but could instead be unusually dusty. As there have not been many unusually red old L dwarfs found, the cause of such dustiness is not well established.

Finding the cause for the enhanced dust content is undoubtedly of interest for understanding the evolution of substellar objects, and the processes that affect the sedimentation and/or condensation of atmospheric dust. It is also crucial for revealing the ages and properties of directly imaged extrasolar planets, most of which exhibit spectral energy distribution (SED) characteristics of both youth and high dust content (e.g., Bonnefoy et al., 2013; Marley et al., 2012). Because isolated brown dwarfs can be scrutinized much more readily than directly imaged extrasolar planets, we stand to potentially learn more about ultra-cool atmospheres from brown dwarfs than we can from exoplanets.

Our understanding of the nature of brown dwarfs with unusual SEDs is presently hindered by the relatively small numbers of such peculiar objects. Until recently, there have been no colour-selected searches for peculiar brown dwarfs. Discoveries have been serendipitous, usually a by-product of searches for T dwarfs (Burgasser et al., 2004;Looper et al., 2008a,b; McLean et al., 2007, etc.). Only

over the past few years have targeted searches been performed on large-area surveys to specifically seek unusually red objects (e.g., Aller et al., 2013; Gagné et al., 2015).

In view of this, we are conducting an independent program to purposefully seek L and T dwarfs with unusual optical/near-infrared (near-IR) colours. The goal is to substantially expand the sample of peculiar L and T dwarfs in order to map the full range of their photospheric properties, and to better understand the evolution and content of their atmospheres. We cross-correlated the SDSS, 2MASS, and WISE survey databases to seek candidate peculiar brown dwarfs based solely on photometric criteria. Our first pass through the databases focused mainly on identifying unusually red objects. Most notable among these is one of the reddest L dwarfs ever found (2MASS J11193254-1137466; 2MASS  $J - K_s = 2.62 \pm 0.15$  mag). While peculiar L and T dwarfs have until now been found mostly serendipitously in large-scale photometric surveys, we have implemented a systematic approach to find these objects by design. We discuss the selection and prioritization of candidates in Section 2, and their follow-up observations in Section 3. The spectroscopic characterization of the new L and T dwarfs is presented in Section 4. In Section 5 we assess the significance of the findings from our systematic search of peculiar objects in the context of the presently known sample of L and T dwarfs.

## 2.2 CANDIDATE SELECTION

We employ a photometric search for peculiar L and T dwarfs using combined optical (SDSS), near-IR (2MASS) and mid-IR (WISE) fluxes. Our candidate selection expands on the procedure presented in Metchev et al., 2008 and Geißler et al., 2011, which applied joint positional and colour constraints to search for T dwarfs in the overlap area of 2MASS and SDSS DR1 (2099 deg<sup>2</sup>). We use the ninth Data Release (DR9) from SDSS (Ahn et al., 2012), which has a 14555 deg<sup>2</sup> footprint, encompassing an area 6.9 times larger than the DR1 footprint. The >10-year observational epoch difference between 2MASS and SDSS DR9 prompts us to choose a much larger cross-match radius than was used in the

first two studies. We use the Virtual Astronomical Observatory catalog cross-comparison tool\* and chose a cross-match radius of  $16''.5$  to maintain sensitivity to objects with proper motions as high as  $1''.5 \text{ yr}^{-1}$ .

### 2.2.1 SELECTION CRITERIA

Our magnitude and colour selection criteria are summarized below. In the following, all *griz* magnitudes are on the SDSS photometric scale (Lupton et al., 2002), and the 2MASS and WISE magnitudes are on the Vega scale:

1.  $z - J > 2.5 \text{ mag}$ ;
2.  $i - z > 1.5 \text{ mag}$ ;
3.  $J > 14 \text{ mag}$ ;
4.  $z \leq 21 \text{ mag}$  and  $z_{err} \leq 0.2 \text{ mag}$ ;
5. no  $g, r < 23 \text{ mag}$  detection within  $1''.3$  of the 2MASS coordinate;
6. SDSS object flag setting type = 6 or 3 (point or extended source);
7. 2MASS object flag setting mp\_flg = 0 (i.e., not marked as a known minor planet), gal\_contam = 0 (i.e., not contaminated by a nearby 2MASS extended source), and ext\_key = NULL (i.e., not extended in 2MASS);
8.  $H - W2 > 1.2 \text{ mag}$ ;
9.  $z - J > -0.75(J - K_s) + 3.8 \text{ mag}$  (criterion used only to prioritize follow-up of red outliers).

Our  $z - J$  and  $i - z$  colour cuts (criteria 1 and 2) were chosen to ensure sensitivity to L and T dwarfs, all of which have a steep red optical slope. The  $J > 14$  magnitude cutoff was imposed to minimize the large number of candidates representing the cross-identification of a bright star artifact in SDSS (e.g., a filter glint or a diffraction spike, especially near saturated stars) with the (unsaturated) image of the same star in 2MASS. Criterion 4 was chosen to ensure detection in SDSS with at least a moderate SNR.

Our  $16''.5$  matching radius commonly resulted in multiple matches of nearby faint SDSS objects to the same, brighter 2MASS object. Each of these individ-

---

\*<http://vao-web.ipac.caltech.edu/applications/VAOSCC/>. This link, however, no longer works.

ual matches would nominally satisfy the colour and magnitude selection criteria, since the faint SDSS photometry would be paired with the brighter 2MASS photometry. However, visual inspection clearly demonstrated that the SDSS and 2MASS objects were distinct, and that the actual object in SDSS that positionally matched the 2MASS object was not nearly as red, and so did not satisfy the  $z - J > 2.5$  mag criterion. Therefore, we discarded any object that had a  $g$ -band detection (i.e.  $g \leq 23$  mag and likely a star) in the SDSS catalog within  $1''.3$  (the angular resolution of SDSS) of the original 2MASS coordinates (criterion 5). This removed  $\sim 86\%$  of the candidate sample.

The SDSS object flag restrictions (criterion 6) ensure that the identified candidates are not known artifacts or flux measurements of the blank sky in SDSS. The SDSS morphological star-galaxy separation is  $< 97\%$  accurate for  $r \geq 21$  mag (Yasuda et al., 2001) so we include both star and galaxy object types in this criterion in case our faint brown dwarfs were mis-classified. We also wanted to ensure that they are not known minor planets, extended or contaminated by nearby extended sources in 2MASS (criterion 7).

To make sure that all of the objects in our candidate list were real objects, we cross-matched our list with the WISE All-Sky Data Release using the SDSS coordinates. Our objects are expected to be detected in the WISE  $W1$  band because outside of the galactic plane the  $W1$  SNR = 5 level corresponds to  $\lesssim 16.8$  mag.<sup>†</sup> This matches the 2MASS  $K_s$  flux limit at high galactic latitude, especially since L and T dwarfs have positive  $K_s - W1$  colours. A radius of  $16''.5$  was again chosen for this cross-match. An additional colour cut was applied on  $H - W2$  (criterion 8) in order to select only L and T dwarfs (based the colour-spectral type relations from Kirkpatrick et al., 2011). This removed  $\sim 74\%$  of the remaining sample.

Finally, we visually inspected the images of remaining candidates using the Infrared Science Archive Finder Chart service<sup>‡</sup> and removed objects that were contaminated by nearby extended sources in SDSS. This eliminated approximately 22% of the remaining candidate sample leaving us with 314 candidates

---

<sup>†</sup>[http://wise2.ipac.caltech.edu/docs/release/allsky/expsup/sec6\\_3a.html](http://wise2.ipac.caltech.edu/docs/release/allsky/expsup/sec6_3a.html)

<sup>‡</sup><http://irsa.ipac.caltech.edu/applications/FinderChart/>

(Figure 2.1a).

### 2.2.2 PRIORITIZATION OF PECULIAR OBJECTS

Since our goal was to select unusually red brown dwarfs in the absence of spectral type information, an additional colour criterion (9) was set in order to prioritize red objects. To decide the form of the colour criterion, we first analyzed the spectra of L and T dwarfs in the SpeX Prism Archive<sup>§</sup> by forming synthetic photometry over various red-optical and near-IR bandpasses. These L and T dwarfs with archival SpeX data formed our control sample, based on which we designed our  $z - J$  vs.  $J - K_s$  criterion 9 (Figure 2.1b).

Given available spectral type information, the unusually red objects in the control sample were set to be those for which the  $J - K_s$  colour was  $>2\sigma$  redder than the median for the spectral subtype. The medians and standard deviations of the  $J - K_s$  colours of M8-T8 dwarfs were adopted from Faherty et al. (2009; M8-M9 and T0-T9) and from Faherty et al. (2013; L0-L9). The unusually red objects in the control sample are shown with red symbols in Figure 2.1b. The number of objects from our sample that passed this criteria was 178.

The colour prioritization did not streamline our observational follow-up strategy significantly, as the scatter in colours among spectral types is larger than the scatter at any given spectral type. Nonetheless, we did observe the reddest candidates whenever possible, and included observations of lower-priority targets only as necessary.

## 2.3 SPECTROSCOPIC OBSERVATIONS AND DATA REDUCTION

Once our candidates were selected, we performed follow-up spectroscopic observations of 40 of the objects ( $\sim 13\%$  of the total candidate sample; 22 high priority and 18 lower priority) using the SpeX instrument (Rayner et al., 2003) on the NASA Infrared Telescope Facility (IRTF) and the Folded-port InfraRed Echellette (FIRE) instrument (Simcoe et al., 2008) on the Magellan Baade telescope. Conditions were photometric on most nights, except on August 3, 2011,

---

<sup>§</sup><http://pono.ucsd.edu/~adam/browndwarfs/spexprism/>

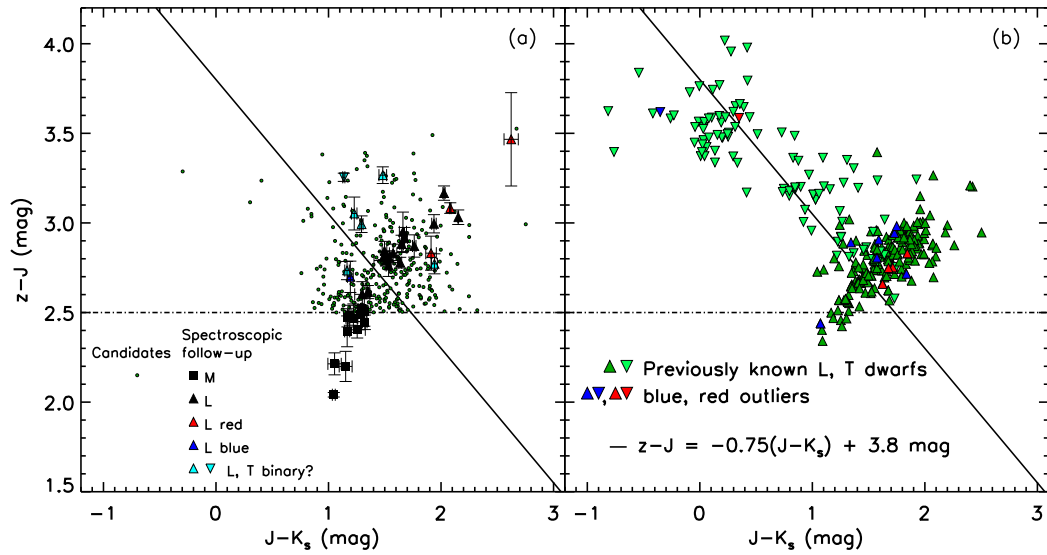


Figure 2.1: (a) Photometric colour-colour diagram of all L and T dwarf candidates redder than  $z - J = 2.5$  mag (green dots) identified in our SDSS-2MASS-WISE cross-match. All other symbols (squares - M dwarfs; upwards triangles - L dwarfs; downwards triangle - T dwarf) represent the synthetic colours of the candidates followed up with spectroscopic observations so far. The black symbols are “normal” objects and the red and blue symbols are objects that we have identified as peculiar or binary. Objects redder than the  $z - J = -0.75(J - K_s) + 3.8$  mag line are candidate peculiarly red L and T dwarfs and were prioritized for spectroscopic follow-up.

(b) SDSS/2MASS synthetic colour-colour diagram of L and T dwarfs from the SpeX Prism Archive (upwards and downwards triangles, respectively). The  $z - J$ , and  $J - K_s$  colours were formed synthetically from the SpeX spectra. Two-sigma red and blue photometric colour outliers are indicated by red and blue symbols, respectively. The  $z - J = -0.75(J - K_s) + 3.8$  mag line was designed to select the photometric red outliers.

April 18, 2012, April 19, 2012, and July 14, 2012, when there was scattered cirrus. All reduction of the low-resolution spectra (SpeX and FIRE LD) was done in Interactive Data Language (IDL).

### 2.3.1 IRTF/SPEX

The majority of our follow-up observations were taken using the SpeX spectrograph on the IRTF. The broad, simultaneous wavelength coverage (0.8–2.5  $\mu\text{m}$ ) of SpeX and its location in the northern hemisphere are ideal for follow-up of SDSS-identified candidates. These spectra were obtained between 2011 August and 2013 June. The observations were taken in prism mode either with the  $0''.8 \times 15''.0$  or with the  $1''.6 \times 15''.0$  slit, resulting in resolutions of  $R \sim 150$  and  $\sim 75$ , respectively. The slit orientation was maintained to within  $20^\circ$  of the parallactic angle for all targets. We used a standard A-B-B-A nodding sequence along the slit to record object and sky spectra. Individual exposure times were either 60 s or 180 s per pointing. The shorter exposure times allowed us to better subtract the sky-glow under changing atmospheric conditions. Standard stars were used for flux calibration and telluric correction. Flat-field and argon lamps were observed immediately after each set of target and standard star observations for use in instrumental calibrations. Observation epochs and instrument settings for each science target are given in Table 2.1.

All reductions of the data taken with SpeX were carried out with the SPEX-TOOL package version 3.4 (Cushing et al., 2004; Vacca et al., 2003), using a weighted profile extraction approach (Horne, 1986; Robertson, 1986). The aperture widths were set to be the radius at which the spatial profile dropped to  $\sim 5\%$  of the peak flux value to ensure no contamination from background noise; the background regions were chosen to begin at the edge of the PSF radius (i.e., beyond 2.5 pixels =  $0''.375$ ). A constant value was fit to the background and subtracted from the spectrum. The individual extracted and wavelength calibrated spectra from a given sequence of observations, each with their own A0 standard, were then scaled to a common median flux and median-combined using X\_COMBSPEC. The combined spectra were corrected for telluric absorption and flux-calibrated using the respective telluric standards with X\_TELLCOR.

All calibrated sets of observations of a given object were median combined to produce the final spectrum. The reduced spectra were smoothed to the instrumental resolution corresponding to the chosen slit width, using the Savitzky-Golay smoothing kernel (Press et al., 1992).

Table 2.1: SpeX Observations

Identifier (J2000)	Date (UT)	2MASS J (mag)	Slit Width (arcsec)	Exposure (min)	A0 Calibrator
2MASS J08095903+4434216	2011 Dec 31	16.44	0.8	24	HD 75135
2MASS J09572983+4624177	2013 Jun 06	16.25	1.6	24	HIP 53735
2MASS J10020752+1358556	2013 Jun 07	17.19	1.6	32	HIP 35735
2MASS J11193254-1137466	2013 Jun 06	17.29	1.6	16	HIP 53735
... <sup>a</sup>	2013 Jun 07	17.29	1.6	8	HIP 54815
2MASS J11260310+4819256	2013 Jun 07	17.20	1.6	24	HIP 54815
2MASS J13043568+1542521	2013 Jun 06	17.32	1.6	70	HIP 68209
2MASS J13431670+3945087	2011 Dec 31	16.16	0.8	16	HD 125798
2MASS J14025564+0800553	2013 Jun 07	16.84	1.6	160	HIP 68868
2MASS J16005759+3021571	2011 Aug 02	16.97	0.8	54	HD 153650
2MASS J16094569+1426422	2011 Aug 03	16.84	0.8	60	HD 152531
2MASS J16091143+2116584	2011 Aug 02	16.96	0.8	60	HD 153650
2MASS J16135698+4019158	2012 Apr 19	17.05	0.8	48	HD 151353
2MASS J16231308+3950419	2012 Apr 18	16.97	0.8	60	HD 165623
2MASS J16242936+1251451	2011 Aug 03	16.26	0.8	36	HD 152531
2MASS J16304999+0051010	2012 Jul 14	16.00	0.8	12	HD 157359
2MASS J16322360+2839567	2012 Apr 18	16.63	0.8	48	HD 158261
2MASS J16360752+2336011	2012 Jul 14	16.88	0.8	12	HD 157359
2MASS J16370238+2520386	2011 Aug 03	16.50	0.8	36	HD 157359
2MASS J16403870+5215505	2012 Apr 19	17.22	0.8	60	HD 155838
2MASS J16410015+1335591	2011 Aug 03	16.90	0.8	48	HD 157359
2MASS J16470847+5120088	2012 Apr 19	17.03	0.8	48	HD 155838
2MASS J16592987+2055298	2012 Jul 15	16.33	1.6	90	HD 164728
2MASS J17081563+2557474	2011 Aug 02	16.42	0.8	48	HD 164728
2MASS J17145224+2439024	2012 Jul 14	16.84	0.8	12	HD 165623
2MASS J17161258+4125143	2011 Aug 03	16.75	0.8	36	HD 165623
... <sup>a</sup>	2012 Jul 15	16.75	1.6	36	HD 165623
2MASS J17251557+6405005	2012 Jul 15	16.81	1.6	24	HD 165622
2MASS J17373467+5953434	2012 Apr 19	16.88	0.8	60	HD 166639
2MASS J21050130-0533505	2011 Aug 03	16.42	0.8	36	HD 209051
2MASS J21111559-0543437	2011 Aug 03	16.09	0.8	36	HD 209051
2MASS J21115335-0644172	2011 Aug 02	16.90	0.8	60	HD 209051
2MASS J21203483-0747378	2011 Aug 02	16.82	0.8	60	HD 210253
2MASS J21243864+1849263	2013 Jun 06	17.03	1.6	56	HIP 53735

Continued on Next Page...

Table 2.1 – Continued

Identifier (J2000)	Date (UT)	2MASS J (mag)	Slit Width (arcsec)	Exposure (min)	A0 Calibrator
2MASS J21392224+1124323	2011 Aug 03	16.49	0.8	48	HD 210265
... <sup>a</sup>	2011 Dec 31	16.49	0.8	36	HD 210265
... <sup>a</sup>	2012 Jul 15	16.49	0.8	48	HD 210265
2MASS J22153705+2110554	2013 Jun 07	16.00	1.6	72	HIP 116886
2MASS J22483513+1301453	2011 Dec 31	16.82	0.8	28	HD 220184
... <sup>a</sup>	2012 Jul 14	16.82	1.6	36	HD 220184
... <sup>a</sup>	2012 Jul 15	16.82	0.8	24	HD 210265
2MASS J23023319-0935188	2012 Jul 15	16.80	0.8	60	HD 222903
2MASS J23322678+1234530	2013 Jun 06	16.89	1.6	42	HIP 68868
2MASS J23443744-0855075	2011 Aug 02	16.77	0.8	60	HD 2717

<sup>a</sup> Repeat observations of the same object, combined with the previous data.

### 2.3.2 MAGELLAN/FIRE

Two of the 40 total candidates were observed using the FIRE spectrograph on the 6.5 m Magellan telescope. The observations of these objects were taken in the low-dispersion (LD) mode with the  $0''.6 \times 50''.0$  longslit resulting in a resolution of  $\sim 400$ . We used a standard A-B-B-A nodding sequence along the slit to record object and sky spectra. Individual exposure times ranged from 31.7–126.8 s per pointing, depending on the brightness of the object. Standard stars were used for flux calibration and telluric correction. We used optimal gain settings of  $1.2 \text{ e}^-/\text{DN}$  and  $3.8 \text{ e}^-/\text{DN}$  for the science targets and  $3.8 \text{ e}^-/\text{DN}$  for the standards as suggested in the FIRE observing manual<sup>¶</sup>. Illumination and appropriate pixel flats were observed either at the beginning or the end of the night and a neon-argon lamp was observed immediately after each set of target and standard star observations for use in instrumental calibrations. All science and telluric observations were taken using the sample-up-the-ramp (SUTR) readout mode whereas all calibration observations were taken in Fowler 1 mode due to the shortness of exposure times. Observation epochs and instrument settings for each target are given in Table 2.2.

<sup>¶</sup>[http://web.mit.edu/~rsimcoe/www/FIRE/ob\\_manual.htm](http://web.mit.edu/~rsimcoe/www/FIRE/ob_manual.htm)

Table 2.2: FIRE Observations

Identifier (J2000)	Date (UT)	J (mag)	Dispersion Mode	Slit Width (arcsec)	Gain ( $e^-$ /DN)	Exposure (min)	A0 Calibrator
2MASS J07483864+1743329	2012 Mar 21	16.27	Long Slit	0.60	3.8	4.2	HD 57450
2MASS J16110632+0025469	2012 Mar 21	17.02	Long Slit	0.60	1.2	16.9	HD 153940

The FIRE low-dispersion spectra were reduced using the FIREHOSE Low Dispersion package which evolved from the optical echelle reduction software package MASE (Bochanski et al., 2009). The spectra were extracted using the optimal extraction approach with the aperture radius being the PSF radius (usually  $\sim 3$  pixels =  $0''.45$ ) which was then masked to prevent biasing to the sky model. A local background was modeled using a basis spline (i.e., piecewise polynomial) fit to the masked profile and subtracted from the spectra which were subsequently extracted using a weighted profile extraction approach (Horne, 1986). The extracted spectra were wavelength-calibrated and each set of observations were median-combined. The combined spectra were corrected for telluric absorption and flux-calibrated with their associated A0 calibration star. All calibrated sets of observing sequences of a given object were median combined to produce a final spectrum. The reduced spectra were smoothed, using the IDL Savitzky-Golay smoothing algorithm, to the same resolution as the SpeX standards for comparison.

### 2.3.3 SYNTHETIC PHOTOMETRY

While comparing the 2MASS colours of our L and T dwarf candidates to their spectra, we noticed that in a significant fraction of cases the 2MASS colours were too red compared to the spectra. All of our objects were flux-calibrated with A0 stars with known  $B - V$  colours, observed at similar airmasses, so we had no reason to suspect a chromatic effect in our flux calibration. Instead, the reason for the discrepancy was traced to flux over-estimation bias at low SNR in 2MASS.

Our objects are faint and often near the  $\text{SNR} = 5$  detection limit of 2MASS in the  $J$ -band filter. The greater noise near the detection limit means that objects that would normally be below the limit have a finite chance of appearing brighter because of statistical variations. The effect enhances the number of faint objects with low SNR in a flux-limited survey, becoming increasingly important at  $\text{SNR} < 10$  (Cutri, 2006). Because all of our objects are faint and red, their 2MASS  $J$ -band magnitudes preferentially suffer from this bias, resulting in redder than expected  $z - J$  colours. This effect is particularly large in the case

of the few faint M-dwarfs that entered our sample because of their biased photometric colours (section 4.1). Figure 2.2 shows how the synthetic colours compare to the photometric colours as a function of the photometric  $J$ -band SNR for both  $z - J$  and  $J - K_s$ . Indeed, at lower SNR, the  $z - J$  photometric colours are on average redder than their synthetic colours while the  $J - K_s$  photometric colours are on average slightly bluer.

For the remainder of our analysis we use only synthetic SDSS  $z$  and 2MASS  $JHK_s$  magnitudes for our candidates and for previously known objects with SpeX Prism Archive spectra. The errors on the synthetic photometry in Table 2.3 are standard errors derived from the scatter among the continuum slopes of the individual 60 s or 180 s-exposure spectra of our targets and their corresponding standard stars. These errors incorporate systematic uncertainties from potential chromatic slit losses should the targets have been imperfectly positioned on the slit.

## 2.4 SPECTRAL CLASSIFICATION RESULTS

We estimate spectral types for our objects by comparing them to spectra of brown dwarfs available from the SpeX Prism Archive<sup>‡</sup>. When our spectra don't match any of the normal brown dwarf spectra, we compare to other unusual spectra. In this way, we are able to assess potential spectroscopic peculiarities that may not be evident from the colours alone. Finally, following the approach of Burgasser, 2007 and Burgasser et al., 2010, we form combination templates from the standards to assess whether any of our objects might be best fit as unresolved binaries. For spectral comparison to standard L and T dwarfs we used  $\chi^2$  minimization over the 0.95-1.35  $\mu\text{m}$  wavelength range. To assess candidate binarity we compare our spectra to combinations of L and/or T dwarf doubles over the entire 0.8-2.5  $\mu\text{m}$  range, as detailed in Section 4.3. Table 2.3 lists the determined spectral types, the characteristics of each object, and the peculiarities of our objects determined from both colours and a detailed analysis of their

---

<sup>‡</sup>Kirkpatrick et al., 2010, Burgasser et al., 2010, Burgasser et al., 2008, Burgasser et al., 2007, Loper et al., 2007, Burgasser et al., 2006b, Chiu et al., 2006, Reid et al., 2006, and Burgasser et al., 2004

spectra. All of our spectra are shown in Figures 2.3–2.4.

We determined that our candidate list of 40 observed objects includes 13 M dwarfs, 26 L dwarfs, and 1 T dwarf. Of these, 10 were previously known and suspected to be L dwarfs but did not have any published near-IR spectra. The remaining 30 are new, including the T dwarf. Ten of the 27 L and T dwarfs are either peculiar (4) or possible unresolved binaries (6).

The newly classified M, L, and T dwarfs are plotted on the  $z - J$  vs.  $J - K_s$  colour-colour diagram in Figure 2.1a, where we have used the synthetic colours integrated from the spectra. We find that in a few cases the synthetic  $z - J$  colours are bluer than 2.5 mag. As discussed in Section 3.3, this is likely the result of flux over-estimation bias for these faint targets, mostly in the 2MASS  $J$ -band. We discuss the normal, peculiar, and candidate binary ultra-cool dwarfs in our sample below.

A handful of objects have synthetic colours that are bluer than the  $z - J = 2.5$  mag colour selection criterion. The SDSS and 2MASS photometry had suggested that they were redder than  $z - J = 2.5$  mag. However, their photometric SNRs from 2MASS and/or SDSS were low (see §3.3), and the synthetic photometry indicates that they are in fact bluer.

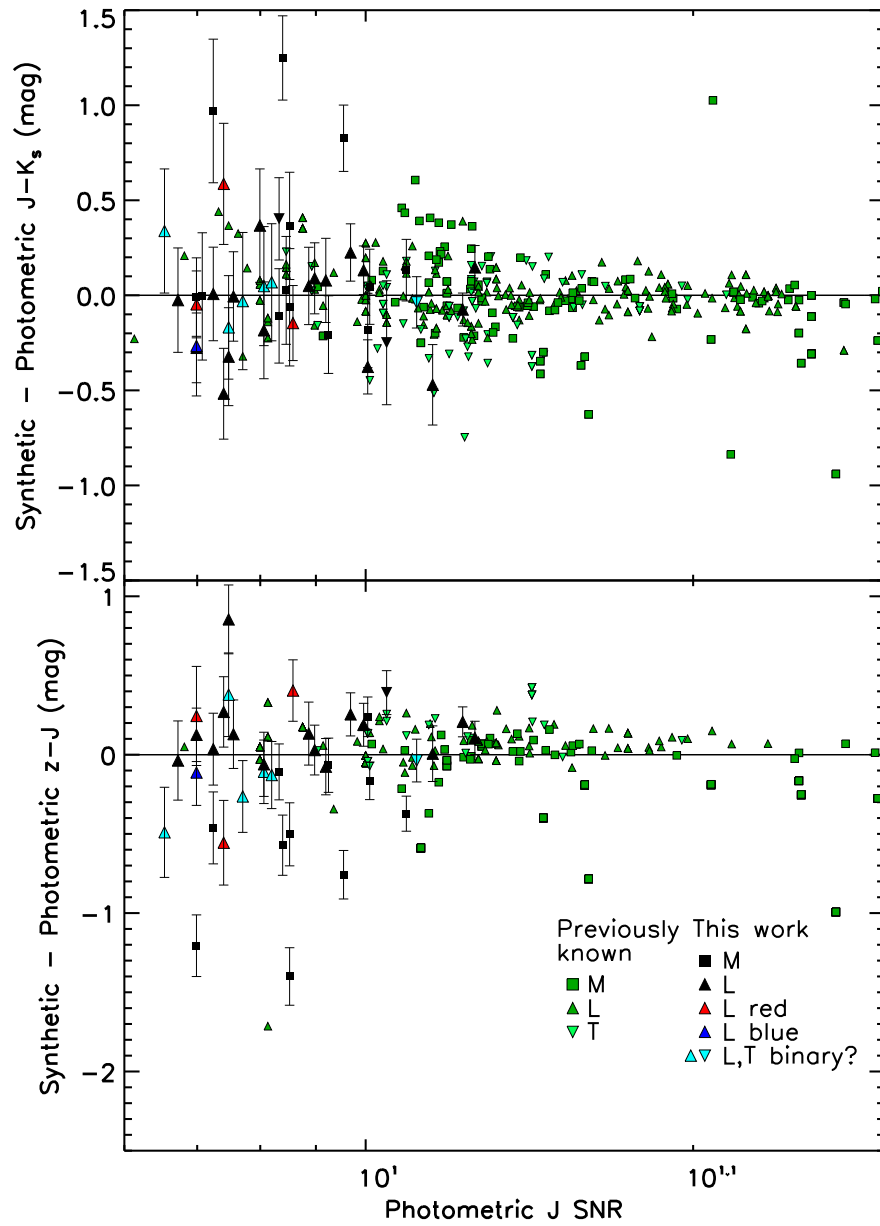


Figure 2.2: Difference in synthetic vs photometric  $J - K_s$  and  $z - J$  colours for M, L and T dwarfs from the SpeX Prism Archive (green symbols) and for objects from this work (all other coloured symbols). The black symbols are “normal” objects and the blue and red symbols are objects that we have identified as peculiar or binary. Fewer objects appear in the  $z - J$  comparison figure (lower panel) because not all SpeX Archive objects are in the SDSS database.

Table 2.3: Results from Spectroscopic Classification and Synthetic Photometry

2MASS ID (J2000)	IR SpT	Interpretation (from spectrum)	$z$ (mag)	$J$ (mag)	$H$ (mag)	$K_s$ (mag)	Disc. Pub.	$>1\sigma$ Colour Outlier	$>2\sigma$ Colour Outlier
High Priority									
07483864+1743329	L5		... <sup>a</sup>	... <sup>b</sup>	...	...	1		
08095903+4434216	L7		19.25 ± 0.09	16.22 ± 0.05	14.94 ± 0.05	14.07 ± 0.05	2	+	
09572983+4624177	L6		19.78 ± 0.08	16.62 ± 0.06	15.39 ± 0.06	14.59 ± 0.06	7	+	
10020752+1358556	L7 pec	L7+T8?	20.49 ± 0.10	17.72 ± 0.08	16.56 ± 0.06	15.78 ± 0.07			
11193254-1137466	L7 red	young	20.69 ± 0.30	17.23 ± 0.12	15.70 ± 0.08	14.60 ± 0.10			+
11260310+4819256	L5		20.07 ± 0.11	17.20 ± 0.07	16.14 ± 0.06	15.44 ± 0.06			
13043568+1542521	T0 pec	L6+T6?	20.50 ± 0.09	17.24 ± 0.08	16.37 ± 0.06	15.76 ± 0.08			
13431670+3945087	L5		19.02 ± 0.10	16.02 ± 0.08	14.84 ± 0.07	14.08 ± 0.07	3		
14025564+0800553	T2 pec	L8+T5?	20.30 ± 0.09	17.31 ± 0.07	16.51 ± 0.04	16.01 ± 0.06	5	+	
16005759+3021571	L5		20.25 ± 0.10	17.33 ± 0.07	16.30 ± 0.06	15.66 ± 0.07			
16094569+1426422	L4		19.70 ± 0.08	16.92 ± 0.06	15.93 ± 0.06	15.28 ± 0.06			
16091143+2116584	L2		20.02 ± 0.10	17.19 ± 0.09	16.25 ± 0.08	15.62 ± 0.09	1		
16135698+4019158	L5 red	old/dusty	20.29 ± 0.13	17.46 ± 0.10	16.30 ± 0.06	15.54 ± 0.10		+	
16470847+5120088	M9		19.58 ± 0.10	17.10 ± 0.05	16.36 ± 0.06	15.91 ± 0.06			
16592987+2055298	M9		20.14 ± 0.13	17.75 ± 0.08	17.06 ± 0.06	16.58 ± 0.07			
17081563+2557474	L5 red	young	20.00 ± 0.08	16.92 ± 0.04	15.68 ± 0.05	14.84 ± 0.04		+	
17161258+4125143	L4		19.77 ± 0.16	16.82 ± 0.09	15.83 ± 0.09	15.16 ± 0.08			
17373467+5953434	L5 pec	L4+T5?	20.80 ± 0.14	17.75 ± 0.08	16.97 ± 0.07	16.52 ± 0.07	6		-
21203483-0747378	L2		19.97 ± 0.08	17.17 ± 0.06	16.24 ± 0.05	15.68 ± 0.05	6		
21243864+1849263	L9		20.15 ± 0.09	17.27 ± 0.05	16.18 ± 0.05	15.62 ± 0.06			
22153705+2110554	T1 pec	T0+T2?	19.48 ± 0.07	16.22 ± 0.07	15.45 ± 0.06	15.09 ± 0.05			
23322678+1234530	T0 pec	L5+T5?	19.66 ± 0.10	16.92 ± 0.08	16.20 ± 0.07	15.76 ± 0.06			-
Lower Priority									
16110632+0025469	M9		...	...	...	...	4		
16231308+3950419	L3		20.16 ± 0.08	17.35 ± 0.06	16.42 ± 0.06	15.81 ± 0.05			
16242936+1251451	M9		19.20 ± 0.06	16.68 ± 0.06	15.88 ± 0.04	15.39 ± 0.06	5		
16304999+0051010	L2		18.40 ± 0.11	15.64 ± 0.07	14.74 ± 0.06	14.11 ± 0.07			
16322360+2839567	L1		19.90 ± 0.12	17.30 ± 0.12	16.50 ± 0.10	16.00 ± 0.10			

Continued on Next Page...

Table 2.3 – Continued

2MASS ID (J2000)	IR SpT	Interpretation (from spectrum)	$z$ (mag)	$J$ (mag)	$H$ (mag)	$K_s$ (mag)	Disc. Pub.	$>1\sigma$ Colour Outlier	$>2\sigma$ Colour Outlier
16360752+2336011	L1		19.61 ± 0.08	17.00 ± 0.07	16.16 ± 0.06	15.65 ± 0.06	5		
16370238+2520386	L4		19.95 ± 0.10	17.10 ± 0.08	16.18 ± 0.07	15.61 ± 0.06		–	
16403870+5215505	M9		20.37 ± 0.09	17.97 ± 0.11	17.19 ± 0.08	16.72 ± 0.11			
16410015+1335591	L2		20.27 ± 0.08	17.48 ± 0.14	16.56 ± 0.10	15.97 ± 0.14			
17145224+2439024	M9		19.17 ± 0.12	16.67 ± 0.08	15.86 ± 0.07	15.35 ± 0.07			
17251557+6405005	L2 pec	blue	20.10 ± 0.13	17.40 ± 0.08	16.66 ± 0.07	16.20 ± 0.07	1		–
21050130-0533505	M7		18.36 ± 0.06	16.32 ± 0.06	15.65 ± 0.06	15.28 ± 0.06			
21111559-0543437	M9		18.94 ± 0.09	16.46 ± 0.08	15.67 ± 0.08	15.17 ± 0.07			
21115335-0644172	M9		19.83 ± 0.08	17.38 ± 0.06	16.60 ± 0.06	16.06 ± 0.07			
21392224+1124323	M8		19.74 ± 0.13	17.54 ± 0.10	16.81 ± 0.08	16.39 ± 0.10			
22483513+1301453	M9		19.61 ± 0.12	17.14 ± 0.09	16.38 ± 0.07	15.92 ± 0.08			
23023319-0935188	M7		19.63 ± 0.10	17.41 ± 0.10	16.75 ± 0.07	16.36 ± 0.10			
23443744-0855075	M9		19.43 ± 0.10	16.96 ± 0.06	16.24 ± 0.04	15.79 ± 0.05			

Determination of colour outliers came from comparing synthetic  $J - K_s$  colours to average  $J - K_s$  colours for M8-M9 and T0-T8 spectral types from Faherty et al., 2009 and for L0-L9 spectral types from Faherty et al., 2013. Positives and negatives indicated whether the object was above or below the average, respectively. <sup>1</sup>Zhang et al., 2009, <sup>2</sup>Knapp et al., 2004, <sup>3</sup>Kirkpatrick et al., 2000, <sup>4</sup>Schmidt et al., 2010, <sup>5</sup>Chiu et al., 2006, <sup>6</sup>Geißler et al., 2011, <sup>7</sup>Luhman et al., 2014.

<sup>a</sup> FIRE spectra do not cover the entire SDSS  $z$ -band.

<sup>b</sup> Target and standard observations were taken with different gain settings so individual JHK<sub>s</sub> magnitudes are not reported.

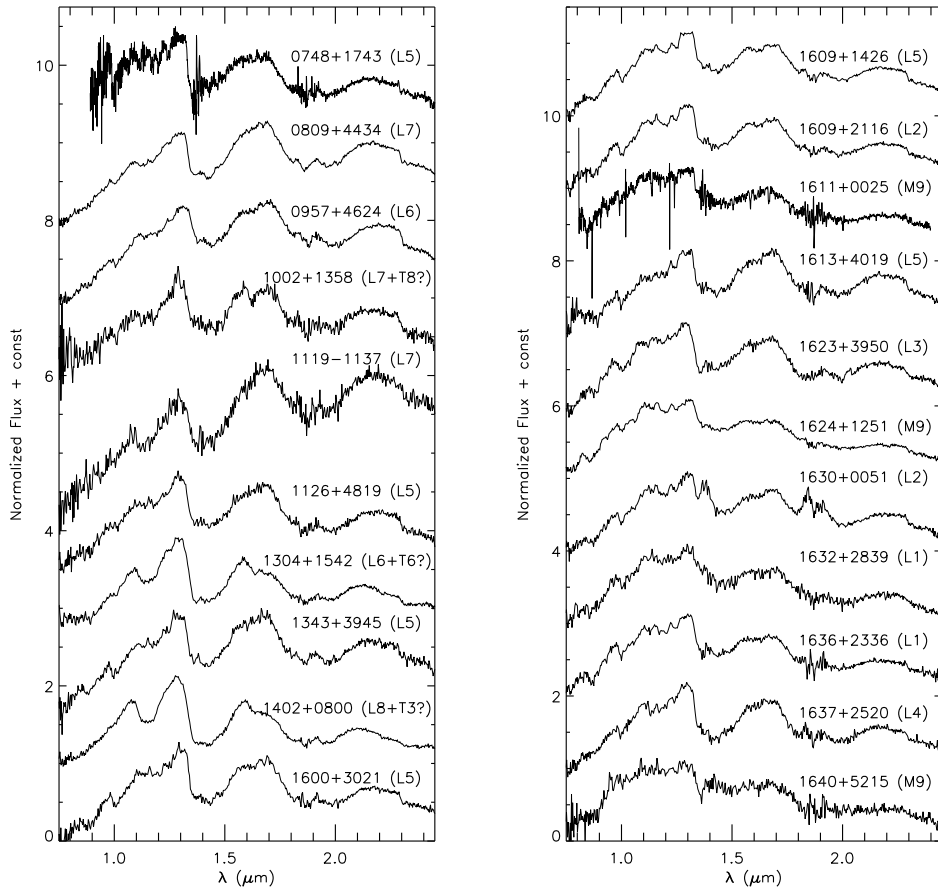


Figure 2.3: FIRE (0748+1743, 1611+0025;  $R \sim 400$ ) SpeX (all the rest;  $R \sim 75$ -150) spectra of all of our reported ultra-cool dwarfs in order of right ascension. Spectral types are given in parentheses.

#### 2.4.1 NORMAL ULTRA-COOL DWARFS

We classify 17 of our candidates as normal L dwarfs, i.e., they do not have any readily apparent peculiarities based on their comparison to SpeX spectral standards. These objects are presented as black upward-triangles in Figure 2.1a. We find that a further 13 candidates are M7–M9 dwarfs. These were included in our program likely because the  $i - z$  and  $z - J$  colours of late-M dwarfs are close to the limits of our colour selection criteria (Section 2.2.1), and because they may

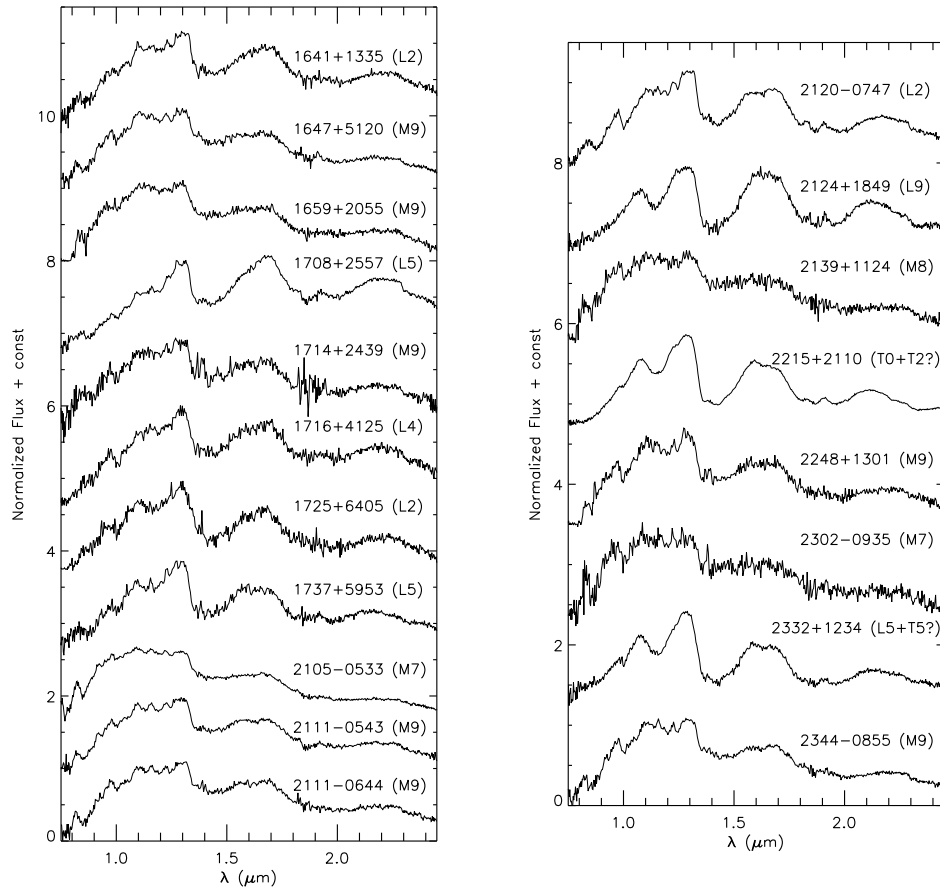


Figure 2.4: Spectra continued

have been subject to flux-overestimation bias at  $J$  band (Section 2.3.3).

#### 2.4.2 PECULIAR L DWARFS

Various absorption features in the near-infrared are gravity-sensitive, hence, the low-gravity of young brown dwarfs will result in line strengths that differ from those in older objects (e.g., Allers et al., 2007, 2013; Gorlova et al., 2003; Lodieu et al., 2008; Lucas et al., 2001; McGovern et al., 2004; Rice et al., 2010). Some of these features include the Na I (1.138 and 1.141  $\mu\text{m}$ ) and K I (1.169 and 1.178  $\mu\text{m}$ , 1.244 and 1.253  $\mu\text{m}$ ) doublets, FeH (bandheads at 0.990  $\mu\text{m}$  and

1.194  $\mu\text{m}$ ), and VO (1.05–1.08  $\mu\text{m}$  and 1.17–1.22  $\mu\text{m}$ ). Alkali lines are weaker at low gravity because of decreased pressure broadening. In low-resolution spectra these lines are often blended with other molecular features so we can not obtain accurate measurements of their strengths. Metal hydride molecular features are also weaker at low gravity because of decreased opacity from these refractory species, while VO bands are stronger (see, e.g., Kirkpatrick et al., 2006). The 1.17 $\mu\text{m}$  VO band is not used as a gravity indicator at low resolution because it is blended with K I, FeH and H<sub>2</sub>O (Allers et al., 2013). Collision-induced absorption from molecular hydrogen (H<sub>2</sub> CIA) also changes as a function of gravity, with lower collision rates in low-gravity objects imparting a triangular shape to the *H* band.

Several prior analyses have introduced broad-band measures to discern low-gravity from field-gravity objects. Allers et al., 2013 design several near-IR indices to measure the changing strengths of FeH, VO, and K I absorption and the slope of the *H*-band continuum as a function of gravity by comparing  $\sim$ 1–100 Myr M5–L7 members of young moving associations with field dwarfs. Canty et al., 2013 analyzed M9–L0 dwarfs to design an  $H_2(K)$  index that measures the contribution of H<sub>2</sub> CIA on the slope of the *K*-band continuum; Schneider et al., 2014 expand this index to the L dwarfs. Indices have the potential to offer a quantitative gravity classification, analogous to spectral classification. However, index measures depend on the spectral resolution of the data used to calibrate them, and our spectra are sufficiently distinct from those used in prior studies. In addition, most of the indices do not extend into the late-L dwarfs, and so are inadequate to classify some of our most interesting objects. Therefore, we do not adopt spectral indices as a default gravity classification scheme. However, we do check for consistency with applicable spectral indices whenever we note peculiarities in the spectra of our L and T candidates.

We note that some of the spectral features, in particular the strength of the FeH bands, the peakiness of the *H*-band continuum, and the redness of the near-IR SED, may also be attributable to high atmospheric dust content or thicker clouds, as discussed inLooper et al. (2008b) and Allers et al. (2013). High dust content itself may be linked to low gravity, so a clear distinction may

not always be possible, especially at low spectral resolution.

Our assessment of peculiarity is based on two factors: (1) the deviation from the median  $J$ - $K_s$  colours for objects of the same spectral type, with  $>2\sigma$  outliers considered peculiar, or (2) high spectral similarity to objects that have previously been classified as peculiar. In two cases below (2MASS J17081563+2557474 and 2MASS J16135698+4019158), we find similarities to the spectra of objects previously classified as peculiar because of being young and/or dusty. In the remaining two cases (2MASS J11193254–1137466 and 2MASS J17251557+6405005) the assessment of peculiarity is based on the comparison to spectra of previously classified peculiar objects as well as the  $J - K_s$  colours.

#### 2.4.2.1 2MASS J11193254–1137466 (L7)

The most interesting object uncovered by our cross-correlation is 2M 1119–1137. This object is one of the reddest objects published to date with a synthetic  $J - K_s = 2.62 \pm 0.15$  mag. Only the L7 dwarfs PSO J318.5338–22.8603 (Liu et al., 2013) and ULAS J222711–004547 (Marocco et al., 2014) among free-floating brown dwarfs are known to be redder. From its low-resolution spectrum (Figure 2.5), we classify this object as an L7. The low signal-to-noise prevents us from unambiguously determining if this object has low gravity. The peak of the  $H$ -band continuum — thought to be sharpened at low surface gravity (e.g., Allers et al., 2013; Lucas et al., 2001) — is not very sharp. We measured the  $H$ -cont index of Allers et al., 2013 and found a value of 0.907, which is  $1.5\sigma$  above the median for L7 dwarfs, and similar to the  $H$ -cont indices of low gravity objects. The authors note that very red L dwarfs with no youth signatures can still exhibit a triangular  $H$ -band shapes and similarly high  $H$ -cont indices. In summary, the  $H$ -cont index of 2M 1119–1137 is consistent with it being a low-gravity object, but we can not conclude from the index alone that it is definitely young.

In Figure 2.6 we compare 2M 1119–1137 to the known very low-gravity dwarfs 2MASSW J224431.67+204343.3 (L7.5; Looper et al., 2008a), WISE J174102.78–464225.5

(L7; Schneider et al., 2014), and WISEP J004701.06+680352.1 (L7.5; Gizis et al., 2012). We see that 2M1119–1137 most closely matches W0047+6803 and also matches the redness of W1741–4642 but has a less peaked  $H$ -band and a shallower slope in the  $K$ -band. Although it is slightly redder, the shape of the  $H$ - and  $K$ -band of 2M 1119–1137 also matches that of 2M 2244+2043. The agreement with the spectra of other young L7–L7.5 dwarfs also indicate that 2M 1119–1137 may be young. A decisive classification will require higher-SNR and/or higher-resolution spectra than we presently have.

Further evidence that 2M 1119–1137 may be young comes from its proper motion and photometric distance. By comparing the 2MASS and AllWISE positions, we estimate an annual proper motion of  $-155 \pm 20$  mas in right ascension and  $-101 \pm 17$  mas in declination. Given a  $K_s$  absolute magnitude of  $12.6 \pm 0.4$  mag for young L7 dwarfs or  $12.5 \pm 0.4$  mag for field-age L7 dwarfs (calculated from the empirically determined  $L_{\text{bol}}$ -SpT relationship and  $K_s$  bolometric corrections from Filippazzo et al., 2015), the photometric parallax of 2M 1119–1137 is  $40 \pm 12$  mas or  $38 \pm 12$  mas. The BANYAN II space motion estimation algorithm (Gagné et al., 2014; Malo et al., 2013) gives 2M 1119–1137 between 39% and 69% probability of being a TW Hydrae moving group member, depending on whether an arbitrary age or a  $<1$  Gyr age is chosen as an input prior with the respective photometric parallax estimates. Confirmation of the association with the TW Hydrae group will require radial velocity and trigonometric parallax measurements.

Should 2M 1119–1137 be confirmed as a member of the 7–13 Myr (Bell et al., 2015) TW Hydrae association (Webb et al., 1999), it will be its coolest and lowest-mass ( $5\text{--}6 M_{\text{Jup}}$ , based on evolutionary models by Allard et al., 2012) free-floating member. Only the planetary-mass companion 2M 1207b (Chauvin et al., 2004, 2005) is likely cooler.

#### 2.4.2.2 2MASS J17081563+2557474 (L5)

This object is determined to be a young L5 brown dwarf based on the decreased absorption of K I and FeH and the increased absorption of H<sub>2</sub>O in the  $J$ -band. Calculations of the spectral indices from Allers et al., 2013 and Schneider et

al., 2014 also suggest that this object is a low gravity brown dwarf. As seen in Figure 2.5, the strengths of the gravity sensitive features in the  $J$ -band and the shape of the  $H$ -band are more similar to the young L5 2MASS J23174712-4838501 (Kirkpatrick et al., 2010), although the observed spectrum is still slightly redder than the comparison spectrum.

#### 2.4.2.3 2MASS J16135698+4019158 (L5)

While this object is peculiarly red, it does not exhibit the features of a low-gravity object. As seen in Figure 2.5, the object has normal absorption strengths, aside from  $H_2O$ , and is more similar to the red L5 dwarf 2M 2351+3010 published in Kirkpatrick et al., 2010. There is also strong FeH absorption. The authors speculate that 2M 2351+3010 is actually an older object that simply has a higher dust content. Since our object seems very similar in nature, we adopt this explanation as well.

#### 2.4.2.4 2MASS J17251557+6405005 (L2)

2M 1725+6405 is a peculiarly blue L2 dwarf (Fig. 2.5). This object was found in our cross-correlation but it was not part of our high-priority sample. Peculiarly blue L dwarfs have often been classified as metal-poor (e.g., Burgasser, 2004; Burgasser et al., 2003), with their blue near-IR colours dictated by increasingly strong collision-induced hydrogen absorption over 1.5–2.5  $\mu\text{m}$ . Metal-poor L dwarfs, or L subdwarfs, also show strong metal-hydride absorption. However, the FeH Wing-Ford band at 0.99  $\mu\text{m}$  in 2M 1725+6405 is weak compared to the standard, which suggests that the 2M 1725+6405 is blue likely because it is unusually dust-poor.

It is also possible that 2M 1725+6405 may be an unresolved L + T dwarf binary, with the  $J$  band flux enhanced by the T dwarf component. We consider unresolved binarity in the next Section (2.4.3). Unlike all of the candidate binaries discussed in Section 2.4.3, we actually do not find a better binary template fit for 2M 1725+6405. We therefore conclude that this L2 dwarf is intrinsically blue.

### 2.4.3 BROWN DWARFS WITH COMPOSITE SPECTRAL TYPES

Several of the objects show peculiarities that do not readily match those found in other individual objects. Instead, they more closely resemble combination spectra of L and T dwarfs. Burgasser, 2007 and Burgasser et al., 2010 developed a technique that enables one to infer the spectral types of the individual components of a candidate unresolved binary by a goodness-of-fit comparison to a library of spectral template combinations. We adopt this technique in a simple form, by creating combination templates from the set of single L and T dwarf standards from the SpeX Prism Library. Unlike Burgasser et al. (2010), we do not create a large list of templates built on the entire population of L and T dwarfs with available SpeX spectra. Nonetheless, we find that our simple approach gives sufficient indication whether a brown dwarf displays a composite spectral signature, and produces approximate spectral types for the components.

Our composite template spectra are constructed by normalizing all of the standard single brown dwarfs over the same wavelength range (1.2-1.3  $\mu\text{m}$ ; chosen because it is relatively free of absorption features), scaling them to their absolute spectral-type dependent magnitudes given by the polynomials in Table 14 of Dupuy et al., 2012, and summing the pairs of resulting spectra. We compute the  $\chi^2$  over most of the 0.8-2.5  $\mu\text{m}$  region, excluding ranges of strong water absorption (1.35-1.45 and 1.8-2.0  $\mu\text{m}$ ). In all cases, the  $\chi^2$  is greater than one but this is to be expected as we are only testing the fit to templates created from one object of each spectral type. We have classified an object as a likely spectral type composite – a potential binary – if the  $\chi^2$  of the dual-template spectral fit is significantly lower than the  $\chi^2$  of the single-template fit. Each of the  $\chi^2$  values have been calculated over the entire 0.8-2.5  $\mu\text{m}$  region, minus the water absorption bands.

In addition to template fitting, we have analyzed the spectral indices defined specifically for SpeX prism spectra in Burgasser et al., 2010 for all our binary candidates and we report the strength of their candidate binarity. We have also analyzed the SpeX prism spectral indices from Bardalez Gagliuffi et al., 2014

but because the binary index selection criteria in that work were not designed for late-L to early-T dwarfs, we only report the results where applicable.

We note that while brown dwarfs displaying combination spectral signatures have until recently been considered to all be unresolved binaries, they can also be highly variable brown dwarfs with photospheres that display two distinct temperature components. Recent examples include the T1.5 dwarf 2MASS J21392676+0220226, suggested as a strong L8.5 + T3.5 spectral binary candidate by Burgasser et al. (2010), but identified as a *J*-band variable that is unresolved in *HST* images (Radigan et al., 2012), or the T dwarfs 2MASS J13243559+6358284 (T2.5) and SDSS J151114.66+060742.9 (T2), identified as binary candidates (Burgasser et al., 2010; Geißler et al., 2011), but that are also unresolved in *HST* and are variable (Metchev et al., 2015). Therefore, while the objects discussed in this section are considered candidate unresolved binaries, they are also strong candidates for photometric variables.

#### 2.4.3.1 2MASS J13043568+1542521 (L6+T6?)

This object is one of several that is best fit by a binary combination template. As seen in Figure 2.7, the best fit single brown dwarf (T0) does not match the features of 2M 1304+1542. The *Y*-/*J*-band ratio is lower than any of the closest standard objects and the *H*-band has a dip at  $\sim 1.65 \mu\text{m}$ . The *K*-band does not have differences that are as pronounced as in the other bands though it is slightly redder than the standard object. In fitting this object with a binary template, we find that the best fit is a combination of an L6 and a T6 brown dwarf. The *Y*-/*J*-band ratio and the *K*-band flux more closely resemble the object spectrum. The contribution of the methane break in the cooler brown dwarf at  $1.6 \mu\text{m}$  also reproduces the dip in the *H*-band well. Further evidence that this object is a binary comes from the analysis of spectral indices identified in Burgasser et al., 2010 and Bardalez Gagliuffi et al., 2014. 2M 1304+1542 satisfies four of the six binary index selection criteria given in Table 5 of Burgasser et al., 2010 and ten of the twelve selection criteria in Table 4 of Bardalez Gagliuffi et al., 2014, making this a strong binary candidate.

#### 2.4.3.2 2MASS J14025564+0800553 (L8+T5?)

The spectrum of 2M 1402+0800 also shows distinctive composite characteristics. While the  $Y$ -/ $J$ -band ratio is not significantly dissimilar from the closest single brown dwarf spectrum, the  $H$ - and  $K$ -bands are more similar to an L8+T5 binary. Figure 2.7 shows that the shape and relative flux of all three 2MASS bandpasses are very well reproduced by the L/T binary template. Most importantly, the dip in the  $H$ -band is well reproduced by the contribution of the methane in the T dwarf. This object passes all six of the binary index selection criteria of Burgasser et al., 2010 which makes it a strong binary candidate.

#### 2.4.3.3 2MASS J17373467+5953434 (L4+T5?)

This object is classified as having an L4+T5 composite spectrum. As seen in Figure 2.7, an L5 spectrum matches 2M 1737+5953 well in the  $Y$ - and  $J$ -bands but is a very poor match to the  $H$ - and  $K$ -bands. The observed spectrum shows signs of methane absorption at 1.6 and 2.2  $\mu\text{m}$  which is indicative of having a T dwarf secondary component. The binary index selection criteria from Burgasser et al., 2010 were not designed for mid-L dwarfs so we analyzed the spectral indices from Bardalez Gagliuffi et al., 2014 instead. Because this object only passes four of the twelve selection criteria from Bardalez Gagliuffi et al., 2014, it is only a weak binary candidate.

#### 2.4.3.4 2MASS J23322678+1234530 (L5+T5?)

While 2M 2332+1234 is best fit in the  $J$ -band by a scaled T0 spectrum, the  $H$ - and  $K$ -bands clearly do not appear to belong to a T0 dwarf. The  $H$ -band shows evidence of methane absorption at 1.6-1.8  $\mu\text{m}$  but there is less presence of  $\text{CH}_4$  in the  $K$ -band. This points to a composite L/T spectrum similar to SDSS J151114.66+060742.9 presented in Burgasser et al., 2010. The methane absorption features are best fit by an L5+T5 template, however, the continuum of our observed spectrum is still slightly bluer at the longer wavelengths. This object passes four of the binary index selection criteria of Burgasser et al., 2010 which makes it a strong binary candidate.

#### 2.4.3.5 2MASS J10020752+1358556 (L7+T8?)

This object is tentatively classified as having a composite spectrum. As seen in Figure 2.7, 2M 1002+1358 has a large dip in flux in the  $H$  band at the location of the  $\text{CH}_4$  absorption feature that is usually present in a T dwarf, and has much more water and methane absorption in the  $J$ -band than a typical L dwarf. The  $K$ -band, however, seems to be similar to an L4–L6 dwarf. These suggest a composite spectral type. There is a much greater difference between L and T dwarfs in the  $J$ - and  $H$ -band features than there is in the  $K$ -band features, therefore, the  $K$ -band of a combined binary spectrum can look like it belongs to an L dwarf whereas the  $J$ - and  $H$ -bands will appear to have a contribution from both binary components. The large dip in  $H$ -band flux may also be the result of an extraneous signal in the raw spectrum of the object as it has an atypical shape compared to that of a feature usually associated with  $\text{CH}_4$ . However, the spectrum of the telluric calibration star does not exhibit the same behavior, while the feature is apparent in most of the individual spectra of this object, even if at low SNR. This suggests that the feature may be real, even if we can not fully exclude a random variation due to noise. Analyzing the spectral indices does not shed any light on the true nature of this object as it only passes four of the twelve binary index selection criteria from Bardalez Gagliuffi et al., 2014, making it a weak binary candidate.

#### 2.4.3.6 2MASS J22153705+2110554 (T0+T2?)

The T dwarf 2M 2215+2110 is a new discovery in the SDSS footprint. Some of the features in the spectrum of 2M 2215+2110 are ambiguous as to their origin. While the  $J$ - and  $K$ -bands more closely resemble an early T dwarf, the  $H$ -band has a clear dearth of flux. The overall shape of this band might be explained by a presence of a slightly later-type T dwarf secondary component than the primary, but the lack of flux still persists in the binary template spectrum. Several features, such as the FeH feature at  $0.99 \mu\text{m}$ , do match a T0+T2 composite spectrum. However, the  $\text{H}_2\text{O} + \text{CH}_4$  absorption between  $1.1\text{--}1.2 \mu\text{m}$  is much stronger in the binary composite template than in the observed spec-

trum. The spectral indices also do not help us with this object – only two of the index selection criteria from Burgasser et al., 2010 are passed which makes this object a weak binary candidate.

## 2.5 DISCUSSION

Our search was aimed at discovering peculiar L or T dwarfs, with priority in this first iteration placed on unusually red objects. Overall, we have observed and identified 10 peculiar or binary L dwarfs, 16 normal L dwarfs, one T dwarf, and 13 M dwarfs. The latter had been mis-identified as candidate L or T dwarfs because of low-SNR photometry.

The total fraction of objects in an unbiased sample of brown dwarfs with  $J - K_s$  colours  $>2\sigma$  from the mean colour at a given spectral type — the criterion used for detecting photometrically peculiar L and T dwarfs in Faherty et al., 2009 — is expected to be 4.6%. Faherty et al., 2009 report a somewhat larger fraction, 5.8%, of peculiar objects among the 1268 M7–T8 dwarfs in their sample. The small discrepancy arises from an apparent non-gaussianity of the  $J - K_s$  colour distribution: they have nearly twice as many red outliers than blue outliers.

Only three of our L dwarfs are peculiarly red or dusty, and an equal number of our discoveries are in fact peculiarly blue. While at face value this does not indicate a higher success rate in finding peculiarly red objects than in a random sample of field brown dwarfs, we have at present followed up only a small number (40) of our total candidate sample (314). The 40 objects presented here comprise roughly equal numbers of high- (22) and low-priority (18) objects: a circumstance of weather and observational constraints. It is possible that the larger high-priority sample (178 candidates) will reveal a higher incidence rate of unusually red objects.

We do find, however, that our present prioritization strategy reveals a larger fraction of unusual objects — including not only peculiar L dwarfs but also candidate unresolved binaries that are not colour outliers in  $J - K_s$  but are unusually red in  $z - J$  — among the high-priority candidates. Eight of the 22 objects

in the high-priority sample are peculiar or candidate binaries vs. two of the 18 in the low-priority sample. The difference between the two is statistically significant at the 96% level. It indicates that combinations of optical and infrared colours, such as employed here, can successfully discern even moderate peculiarities in ultra-cool dwarfs. Table 2.3 summarizes the peculiarities of each object — from spectral comparison and synthetic colours.

Because L and T dwarfs are brighter in the 3–5  $\mu\text{m}$  wavelength range, we investigated whether the  $J - K_s$  colour outliers also have unusual colours at these wavelengths. We find that L dwarfs with the very reddest  $J - K_s$  colours are clearly distinguishable from the locus of L dwarfs on a  $J - K_s$  vs.  $H - W2$  and  $J - K_s$  vs.  $W1 - W2$  diagram (Fig. 2.9) mainly because of their red near-IR colours. They stand out in their  $J - K_s$  and  $H - W2$  colours but not significantly in their  $W1 - W2$  colours. T dwarfs with peculiarly red  $J - K_s$  colours are only marginally redder in  $H - W2$  and  $W1 - W2$ , and the peculiarly blue L or T dwarfs are not distinguishable from the normal population with the exception of the blue L dwarf discovered in this work (2MASS J17251557+6405005).

## 2.6 CONCLUSIONS

We performed a colour-selected search for peculiar L and T dwarfs, focusing primarily on the peculiarly red objects, and demonstrated that with the proper selection criteria, we can identify unusual L and T dwarf candidates in large photometric surveys in the absence of spectral type information. With follow-up spectroscopy, we can verify the unusual properties and begin to discern their underlying cause. This is particularly advantageous for finding isolated objects that are analogous to the typically very red directly imaged extrasolar planets in order to study their atmospheric characteristics at higher fidelity. We had a high success rate in discovering either peculiar L dwarfs or candidate unresolved binaries in our prioritized sample, and discovered one of the reddest L dwarfs known to date. This new red L7 dwarf is a potential TW Hydrae member, and if confirmed, would make it the coolest and least massive free-floating object in the association. We note that even after many searches for T dwarfs

in the SDSS and 2MASS catalogs, we still uncovered a new T dwarf among the  $\sim 13\%$  fraction of candidates that we have spectroscopically characterized so far. These discoveries attest to the power of simultaneous positional and colour cross-correlations across photometric databases — as performed here, in Metchev et al., 2008, in Geißler et al., 2011, and now enabled with the Virtual Astronomical Observatory — over colour-only searches on individual databases that are then positionally compared to other databases. At the same time, the discovery of only a single new T dwarf in our characterized sample indicates the census of T dwarfs (132) in SDSS is nearly complete.

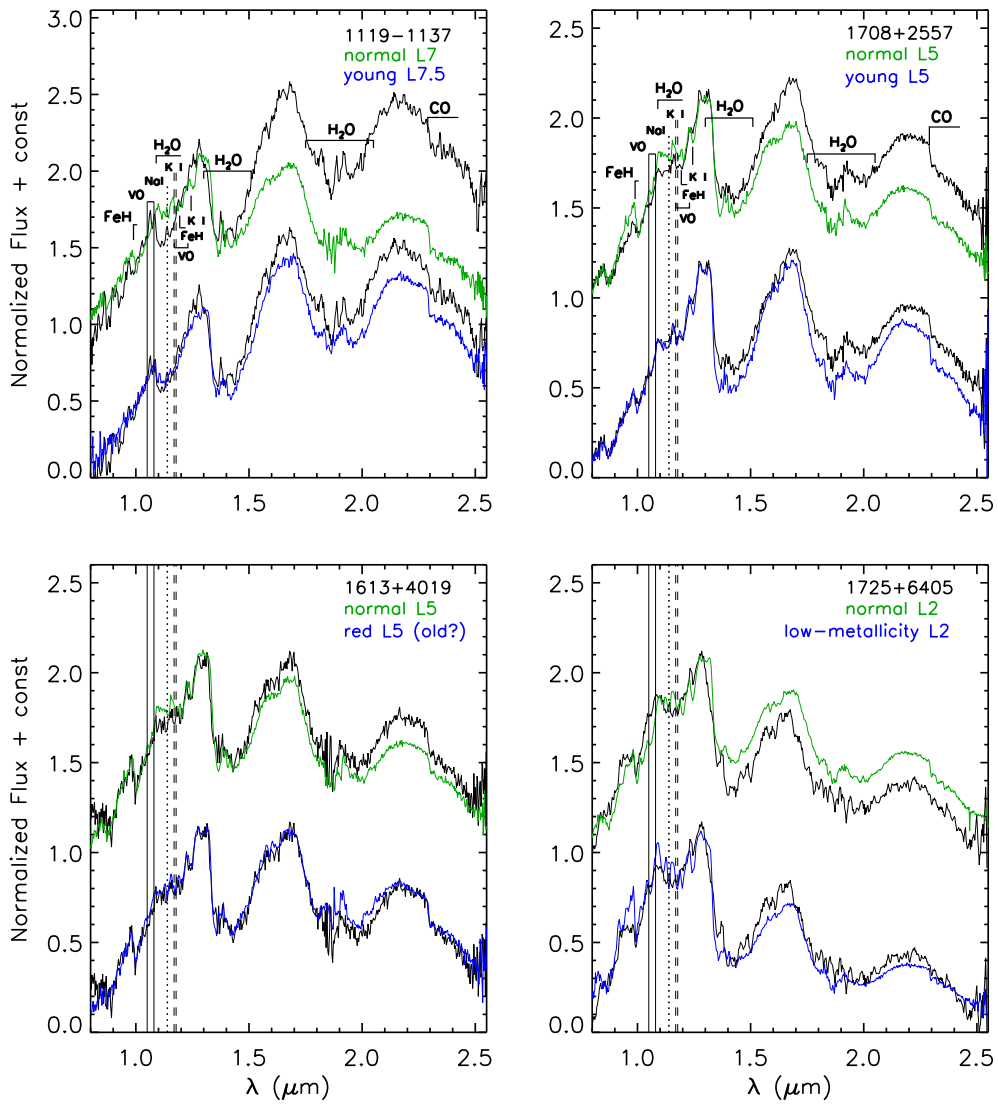


Figure 2.5: Spectra of the four peculiar objects identified in this work. In each case, the spectrum of the candidate is compared to the spectrum of a normal object of the same spectral type, and to the spectrum of a peculiar object of the nearest spectral type. The comparison spectra from left to right and top to bottom are L7 (2MASS J0028208+224905; Burgasser et al., 2010) and L7.5 young (2MASS J22443167+2043433; Looper et al., 2008a); L5 (2MASS J01550354+0950003; Burgasser et al., 2010) and L5 pec (2MASS J23174712-4838501; Kirkpatrick et al., 2010); L5 (2MASS J01550354+0950003; Burgasser et al., 2010) and L5 pec (2MASS J23512200+3010540; Kirkpatrick et al., 2010); L2 (2MASS J13054019-2541059; Burgasser et al., 2007) and L2 pec (2MASS J14313097+1436539; Sheppard et al., 2009).

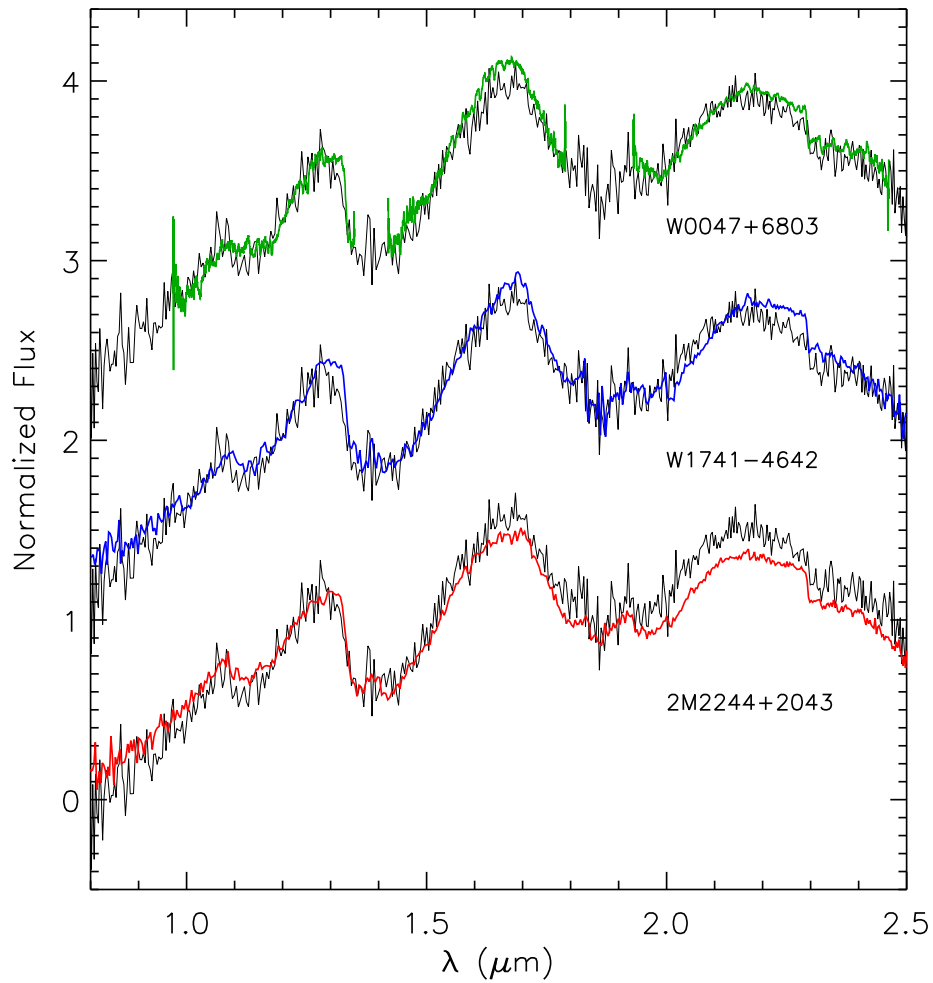


Figure 2.6: A comparison of the SpeX prism spectrum of 2M 1119–1137 (black) with low-resolution spectra of other young L7–L7.5 dwarfs: WISEP J004701.06+680352.1 (L7.5 (pec), Gizis et al., 2012), WISE J174102.78–464225.5 (L7 (pec), Schneider et al., 2014) and 2MASSW J224431.67+204343.3 (L7.5 (pec), Kirkpatrick et al., 2010).

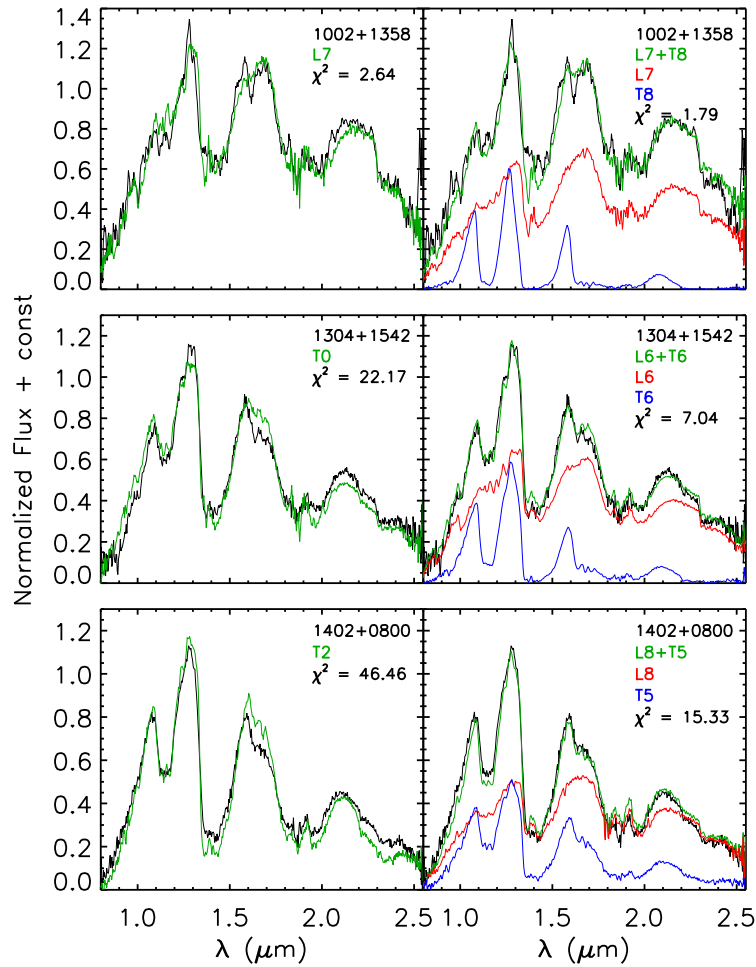


Figure 2.7: Spectra of three of the objects identified as candidate unresolved binaries (or photometric variables). The left panels show comparisons to the spectra (in green) that fit the 0.95–1.35  $\mu\text{m}$  continuum best: i.e., as done for spectral typing of the individual objects in Sections 4.1–4.2. The right panels show the two-component templates (also in green) that fit best over 0.8–2.5  $\mu\text{m}$ ; the individual component contributions are shown in red and blue. The quoted  $\chi^2$  values are the smallest ones for, respectively, single- and binary-template fits over the entire 0.8–2.5  $\mu\text{m}$  range, as done in Section 4.3. The comparison spectra from left to right and top to bottom are: L7 (2MASS J0028208+224905; Burgasser et al., 2010) and T8 (2MASS J04151954-0935066; Burgasser et al., 2004); T0 (2MASS J12074717+0244249;Looper et al., 2007), L6 (2MASS J10101480-0406499; Reid et al., 2006) and T6 (2MASS J16241436+0029158; Burgasser et al., 2006a); T2 (2MASS J12545393-0122474; Burgasser et al., 2004), L8 (2MASS J16322911+1904407; Burgasser, 2007) and T5 (2MASS J15031961+2525196; Burgasser et al., 2004).

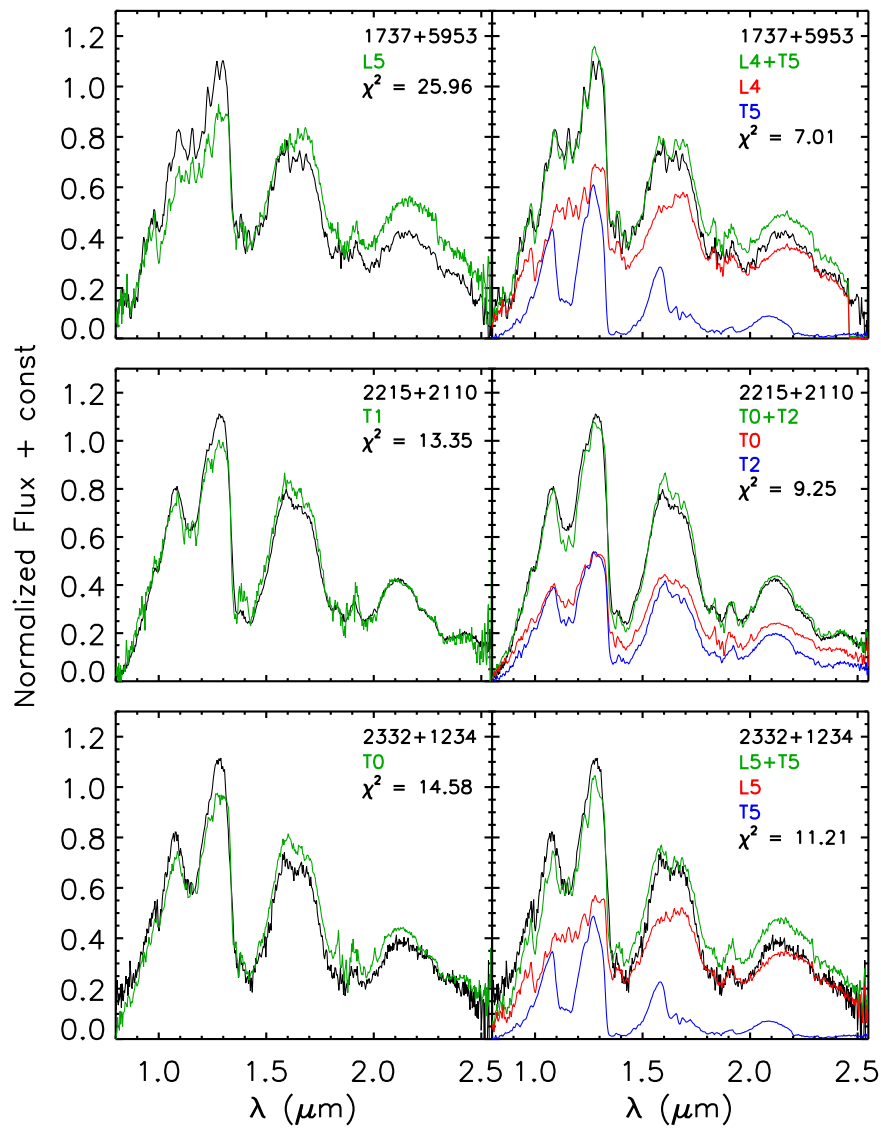


Figure 2.8: Spectra of the remaining three objects identified as candidate unresolved binaries (or photometric variables). The comparison spectra from left to right and top to bottom are: L5 (2MASS J08350622+1953050; Chiu et al., 2006), L4 (2MASS J21580457-1550098; Kirkpatrick et al., 2010) and T5 (2MASS J15031961+2525196; Burgasser et al., 2004); T1 (2MASS J01514155+1244300; Burgasser et al., 2004), T0 (2MASS J12074717+0244249;Looper et al., 2007) and T2 (2MASS J12545393-0122474; Burgasser et al., 2004). L5 (2MASS J08350622+1953050; Chiu et al., 2006) and T5 (2MASS J15031961+2525196; Burgasser et al., 2004).

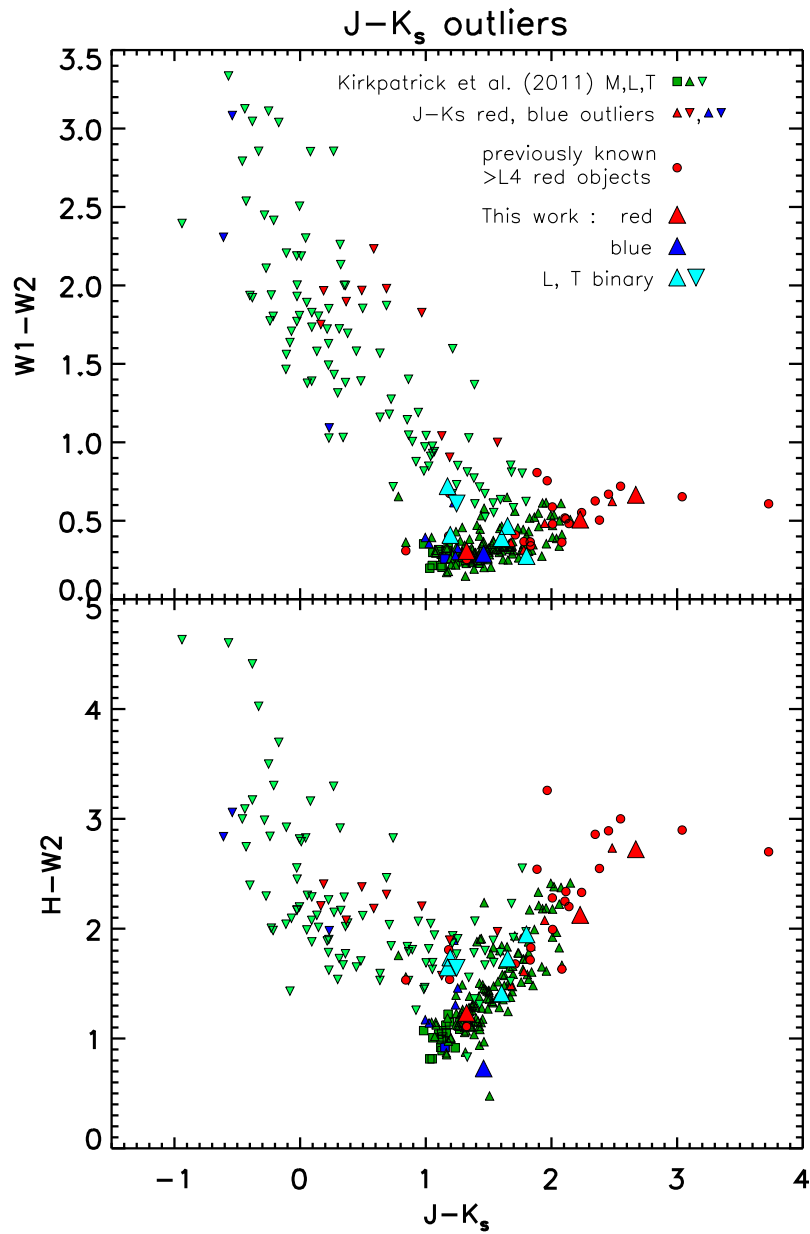


Figure 2.9: Photometric colour-colour diagrams of objects from Kirkpatrick et al., 2011. Upwards and downwards triangles denote L and T dwarfs, respectively. Red symbols denote objects with  $J - K_s$  colours  $>2\sigma$  redder than the mean for their spectral type Faherty et al., 2009, 2013. Blue symbols denote objects that are  $>2\sigma$  bluer. Large symbols represent peculiar objects identified in this work. Red circles indicate the previously known red brown dwarfs with spectral types of L4 and later.

## REFERENCES

- Ahn, C. P., Alexandroff, R., Allende Prieto, C., et al. (2012). *ApJS* 203, 21, p. 21. DOI: [10.1088/0067-0049/203/2/21](https://doi.org/10.1088/0067-0049/203/2/21).
- Allard, F., Homeier, D., and Freytag, B. (2012). *Philosophical Transactions of the Royal Society of London Series A* 370, pp. 2765–2777. DOI: [10.1098/rsta.2011.0269](https://doi.org/10.1098/rsta.2011.0269).
- Aller, K. M., Kraus, A. L., Liu, M. C., et al. (2013). *ApJ* 773, 63, p. 63. DOI: [10.1088/0004-637X/773/1/63](https://doi.org/10.1088/0004-637X/773/1/63).
- Allers, K. N., Jaffe, D. T., Luhman, K. L., et al. (2007). *ApJ* 657, pp. 511–520. DOI: [10.1086/510845](https://doi.org/10.1086/510845).
- Allers, K. N. and Liu, M. C. (2013). *ApJ* 772, 79, p. 79. DOI: [10.1088/0004-637X/772/2/79](https://doi.org/10.1088/0004-637X/772/2/79).
- Bardalez Gagliuffi, D. C., Burgasser, A. J., Gelino, C. R., et al. (2014). *ApJ* 794, 143, p. 143. DOI: [10.1088/0004-637X/794/2/143](https://doi.org/10.1088/0004-637X/794/2/143).
- Bell, C. P. M., Mamajek, E. E., and Naylor, T. (2015). *MNRAS* 454, pp. 593–614. DOI: [10.1093/mnras/stv1981](https://doi.org/10.1093/mnras/stv1981).
- Bochanski, J. J., Hennawi, J. F., Simcoe, R. A., et al. (2009). *PASP* 121, pp. 1409–1418. DOI: [10.1086/648597](https://doi.org/10.1086/648597).
- Bonnefoy, M., Boccaletti, A., Lagrange, A.-M., et al. (2013). *A&A* 555, A107, A107. DOI: [10.1051/0004-6361/201220838](https://doi.org/10.1051/0004-6361/201220838).
- Burgasser, A. J. (2004). *ApJ* 614, pp. L73–L76. DOI: [10.1086/425418](https://doi.org/10.1086/425418).
- (2007). *ApJ* 659, pp. 655–674. DOI: [10.1086/511027](https://doi.org/10.1086/511027).
- Burgasser, A. J., Kirkpatrick, J. D., Burrows, A., et al. (2003). *ApJ* 592, pp. 1186–1192. DOI: [10.1086/375813](https://doi.org/10.1086/375813).
- Burgasser, A. J., McElwain, M. W., Kirkpatrick, J. D., et al. (2004). *AJ* 127, pp. 2856–2870. DOI: [10.1086/383549](https://doi.org/10.1086/383549).
- Burgasser, A. J., Burrows, A., and Kirkpatrick, J. D. (2006a). *ApJ* 639, pp. 1095–1113. DOI: [10.1086/499344](https://doi.org/10.1086/499344).
- Burgasser, A. J., Geballe, T. R., Leggett, S. K., et al. (2006b). *ApJ* 637, pp. 1067–1093. DOI: [10.1086/498563](https://doi.org/10.1086/498563).

- Burgasser, A. J., Looper, D. L., Kirkpatrick, J. D., et al. (2007). *ApJ* 658, pp. 557–568. DOI: [10.1086/511518](https://doi.org/10.1086/511518).
- Burgasser, A. J., Liu, M. C., Ireland, M. J., et al. (2008). *ApJ* 681, pp. 579–593. DOI: [10.1086/588379](https://doi.org/10.1086/588379).
- Burgasser, A. J., Cruz, K. L., Cushing, M., et al. (2010). *ApJ* 710, pp. 1142–1169. DOI: [10.1088/0004-637X/710/2/1142](https://doi.org/10.1088/0004-637X/710/2/1142).
- Canty, J. I., Lucas, P. W., Roche, P. F., et al. (2013). *MNRAS* 435, pp. 2650–2664. DOI: [10.1093/mnras/stt1477](https://doi.org/10.1093/mnras/stt1477).
- Chauvin, G., Lagrange, A.-M., Dumas, C., et al. (2004). *A&A* 425, pp. L29–L32. DOI: [10.1051/0004-6361:200400056](https://doi.org/10.1051/0004-6361:200400056).
- (2005). *A&A* 438, pp. L25–L28. DOI: [10.1051/0004-6361:200500116](https://doi.org/10.1051/0004-6361:200500116).
- Chiu, K., Fan, X., Leggett, S. K., et al. (2006). *AJ* 131, pp. 2722–2736. DOI: [10.1086/501431](https://doi.org/10.1086/501431).
- Cruz, K. L., Kirkpatrick, J. D., and Burgasser, A. J. (2009). *AJ* 137, pp. 3345–3357. DOI: [10.1088/0004-6256/137/2/3345](https://doi.org/10.1088/0004-6256/137/2/3345).
- Cushing, M. C., Vacca, W. D., and Rayner, J. T. (2004). *PASP* 116, pp. 362–376. DOI: [10.1086/382907](https://doi.org/10.1086/382907).
- Cutri, Roc (2006). [http://www.ipac.caltech.edu/2mass/releases/allsky/doc/seca2\\_1c.html](http://www.ipac.caltech.edu/2mass/releases/allsky/doc/seca2_1c.html). [Online; accessed 26-October-2013].
- Dupuy, T. J. and Liu, M. C. (2012). *ApJS* 201, 19, p. 19. DOI: [10.1088/0067-0049/201/2/19](https://doi.org/10.1088/0067-0049/201/2/19).
- Faherty, J. K., Burgasser, A. J., Cruz, K. L., et al. (2009). *AJ* 137, pp. 1–18. DOI: [10.1088/0004-6256/137/1/1](https://doi.org/10.1088/0004-6256/137/1/1).
- Faherty, J. K., Burgasser, A. J., Walter, F. M., et al. (2012). *ApJ* 752, 56, p. 56. DOI: [10.1088/0004-637X/752/1/56](https://doi.org/10.1088/0004-637X/752/1/56).
- Faherty, J. K., Rice, E. L., Cruz, K. L., et al. (2013). *AJ* 145, 2, p. 2. DOI: [10.1088/0004-6256/145/1/2](https://doi.org/10.1088/0004-6256/145/1/2).
- Filippazzo, J. C., Rice, E. L., Faherty, J., et al. (2015). *ApJ* 810, 158, p. 158. DOI: [10.1088/0004-637X/810/2/158](https://doi.org/10.1088/0004-637X/810/2/158).
- Gagné, J., Lafrenière, D., Doyon, R., et al. (2014). *ApJ* 783, 121, p. 121. DOI: [10.1088/0004-637X/783/2/121](https://doi.org/10.1088/0004-637X/783/2/121).
- (2015). *ApJ* 798, 73, p. 73. DOI: [10.1088/0004-637X/798/2/73](https://doi.org/10.1088/0004-637X/798/2/73).

- Geißler, K., Metchev, S., Kirkpatrick, J. D., et al. (2011). *ApJ* 732, 56, p. 56.  
DOI: [10.1088/0004-637X/732/1/56](https://doi.org/10.1088/0004-637X/732/1/56).
- Gizis, J. E., Faherty, J. K., Liu, M. C., et al. (2012). *AJ* 144, 94, p. 94. DOI: [10.1088/0004-6256/144/4/94](https://doi.org/10.1088/0004-6256/144/4/94).
- Golimowski, D. A., Leggett, S. K., Marley, M. S., et al. (2004). *AJ* 127, pp. 3516–3536. DOI: [10.1086/420709](https://doi.org/10.1086/420709).
- Gorlova, N. I., Meyer, M. R., Rieke, G. H., et al. (2003). *ApJ* 593, pp. 1074–1092. DOI: [10.1086/376730](https://doi.org/10.1086/376730).
- Horne, K. (1986). *PASP* 98, pp. 609–617. DOI: [10.1086/131801](https://doi.org/10.1086/131801).
- Kellogg, K., Metchev, S., Geißler, K., et al. (2015). *AJ* 150, 182, p. 182. DOI: [10.1088/0004-6256/150/6/182](https://doi.org/10.1088/0004-6256/150/6/182).
- Kirkpatrick, J. D., Reid, I. N., Liebert, J., et al. (2000). *AJ* 120, pp. 447–472. DOI: [10.1086/301427](https://doi.org/10.1086/301427).
- Kirkpatrick, J. D., Barman, T. S., Burgasser, A. J., et al. (2006). *ApJ* 639, pp. 1120–1128. DOI: [10.1086/499622](https://doi.org/10.1086/499622).
- Kirkpatrick, J. D., Looper, D. L., Burgasser, A. J., et al. (2010). *ApJS* 190, pp. 100–146. DOI: [10.1088/0067-0049/190/1/100](https://doi.org/10.1088/0067-0049/190/1/100).
- Kirkpatrick, J. D., Cushing, M. C., Gelino, C. R., et al. (2011). *ApJS* 197, 19, p. 19. DOI: [10.1088/0067-0049/197/2/19](https://doi.org/10.1088/0067-0049/197/2/19).
- Knapp, G. R., Leggett, S. K., Fan, X., et al. (2004). *AJ* 127, pp. 3553–3578. DOI: [10.1086/420707](https://doi.org/10.1086/420707).
- Liu, M. C., Magnier, E. A., Deacon, N. R., et al. (2013). *ApJ* 777, L20, p. L20. DOI: [10.1088/2041-8205/777/2/L20](https://doi.org/10.1088/2041-8205/777/2/L20).
- Lodieu, N., Hambly, N. C., Jameson, R. F., et al. (2008). *MNRAS* 383, pp. 1385–1396. DOI: [10.1111/j.1365-2966.2007.12676.x](https://doi.org/10.1111/j.1365-2966.2007.12676.x).
- Looper, D. L., Kirkpatrick, J. D., and Burgasser, A. J. (2007). *AJ* 134, pp. 1162–1182. DOI: [10.1086/520645](https://doi.org/10.1086/520645).
- Looper, D. L., Gelino, C. R., Burgasser, A. J., et al. (2008a). *ApJ* 685, pp. 1183–1192. DOI: [10.1086/590382](https://doi.org/10.1086/590382).
- Looper, D. L., Kirkpatrick, J. D., Cutri, R. M., et al. (2008b). *ApJ* 686, pp. 528–541. DOI: [10.1086/591025](https://doi.org/10.1086/591025).

- Lucas, P. W., Roche, P. F., Allard, F., et al. (2001). MNRAS 326, pp. 695–721.  
DOI: [10.1046/j.1365-8711.2001.04666.x](https://doi.org/10.1046/j.1365-8711.2001.04666.x).
- Luhman, K. L. and Sheppard, S. S. (2014). ApJ 787, 126, p. 126. DOI: [10.1088/0004-637X/787/2/126](https://doi.org/10.1088/0004-637X/787/2/126).
- Lupton, R. H., Ivezić, Z., Gunn, J. E., et al. (2002). *Survey and Other Telescope Technologies and Discoveries*. Ed. by J. A. Tyson and S. Wolff. Vol. 4836. Society of Photo-Optical Instrumentation Engineers (SPIE) Conference Series, pp. 350–356. DOI: [10.1117/12.457307](https://doi.org/10.1117/12.457307).
- Malo, L., Doyon, R., Lafrenière, D., et al. (2013). ApJ 762, 88, p. 88. DOI: [10.1088/0004-637X/762/2/88](https://doi.org/10.1088/0004-637X/762/2/88).
- Marley, M. S., Saumon, D., Cushing, M., et al. (2012). ApJ 754, 135, p. 135.  
DOI: [10.1088/0004-637X/754/2/135](https://doi.org/10.1088/0004-637X/754/2/135).
- Marocco, F., Day-Jones, A. C., Lucas, P. W., et al. (2014). MNRAS 439, pp. 372–386. DOI: [10.1093/mnras/stt2463](https://doi.org/10.1093/mnras/stt2463).
- McGovern, M. R., Kirkpatrick, J. D., McLean, I. S., et al. (2004). ApJ 600, pp. 1020–1024. DOI: [10.1086/379849](https://doi.org/10.1086/379849).
- McLean, I. S., Prato, L., McGovern, M. R., et al. (2007). ApJ 658, pp. 1217–1235. DOI: [10.1086/511740](https://doi.org/10.1086/511740).
- Metchev, S. A., Kirkpatrick, J. D., Berriman, G. B., et al. (2008). ApJ 676, pp. 1281–1306. DOI: [10.1086/524721](https://doi.org/10.1086/524721).
- Metchev, S. A., Heinze, A., Apai, D., et al. (2015). ApJ 799, 154, p. 154. DOI: [10.1088/0004-637X/799/2/154](https://doi.org/10.1088/0004-637X/799/2/154).
- Press, W. H., Teukolsky, S. A., Vetterling, W. T., et al. (1992).
- Radigan, J., Jayawardhana, R., Lafrenière, D., et al. (2012). ApJ 750, 105, p. 105.  
DOI: [10.1088/0004-637X/750/2/105](https://doi.org/10.1088/0004-637X/750/2/105).
- Rayner, J. T., Toomey, D. W., Onaka, P. M., et al. (2003). PASP 115, pp. 362–382. DOI: [10.1086/367745](https://doi.org/10.1086/367745).
- Reid, I. N., Lewitus, E., Burgasser, A. J., et al. (2006). ApJ 639, pp. 1114–1119.  
DOI: [10.1086/499484](https://doi.org/10.1086/499484).
- Rice, E. L., Barman, T., Mclean, I. S., et al. (2010). ApJS 186, pp. 63–84. DOI: [10.1088/0067-0049/186/1/63](https://doi.org/10.1088/0067-0049/186/1/63).
- Robertson, J. G. (1986). PASP 98, pp. 1220–1231. DOI: [10.1086/131925](https://doi.org/10.1086/131925).

- Schmidt, S. J., West, A. A., Hawley, S. L., et al. (2010). *AJ* 139, pp. 1808–1821.  
DOI: [10.1088/0004-6256/139/5/1808](https://doi.org/10.1088/0004-6256/139/5/1808).
- Schneider, A. C., Cushing, M. C., Kirkpatrick, J. D., et al. (2014). *AJ* 147, 34,  
p. 34. DOI: [10.1088/0004-6256/147/2/34](https://doi.org/10.1088/0004-6256/147/2/34).
- Sheppard, S. S. and Cushing, M. C. (2009). *AJ* 137, pp. 304–314. DOI: [10.1088/0004-6256/137/1/304](https://doi.org/10.1088/0004-6256/137/1/304).
- Simcoe, R. A., Burgasser, A. J., Bernstein, R. A., et al. (2008). *Society of Photo-Optical Instrumentation Engineers (SPIE) Conference Series*. Vol. 7014. Society of Photo-Optical Instrumentation Engineers (SPIE) Conference Series.  
DOI: [10.1117/12.790414](https://doi.org/10.1117/12.790414).
- Vacca, W. D., Cushing, M. C., and Rayner, J. T. (2003). *PASP* 115, pp. 389–409. DOI: [10.1086/346193](https://doi.org/10.1086/346193).
- Vrba, F. J., Henden, A. A., Luginbuhl, C. B., et al. (2004). *AJ* 127, pp. 2948–2968. DOI: [10.1086/383554](https://doi.org/10.1086/383554).
- Webb, R. A., Zuckerman, B., Platais, I., et al. (1999). *ApJ* 512, pp. L63–L67.  
DOI: [10.1086/311856](https://doi.org/10.1086/311856).
- Yasuda, N., Fukugita, M., Narayanan, V. K., et al. (2001). *AJ* 122, pp. 1104–1124. DOI: [10.1086/322093](https://doi.org/10.1086/322093).
- Zhang, Z. H., Pokorny, R. S., Jones, H. R. A., et al. (2009). *A&A* 497, pp. 619–633. DOI: [10.1051/0004-6361/200810314](https://doi.org/10.1051/0004-6361/200810314).

# 3

## A Statistical Survey of Peculiar L and T Dwarfs in SDSS, 2MASS, and WISE

### 3.1 INTRODUCTION

Ultra-cool dwarf atmospheres are complex: L-type dwarf atmospheres host a wide variety of atomic and molecular gases and mineral condensates, while the appearance of cooler T-type dwarfs is dominated by several molecular gas species and other more volatile elements. The change in spectral appearance from early- to late- L dwarfs follows an approximate monotonic trend with decreasing temperature throughout the spectral type sequence. However, across the L/T transition a drastic change in the appearance of the spectra takes place over only a narrow range of effective temperatures and luminosities (Burgasser, 2007; Golimowski et al., 2004; Kirkpatrick et al., 2000).

A number of brown dwarf atmosphere models have been able to reproduce the observed characteristics of this transition by confining the condensate species to cloud layers (e.g., Ackerman et al., 2001; Burgasser, 2002; Burrows et al.,

---

A version of this chapter has been accepted to The Astronomical Journal (Kellogg et al. 2017b).

2006; Marley et al., 2002; Tsuji, 2002). As a brown dwarf cools and transitions from an L dwarf to a T dwarf, the optically thick clouds originally residing in the upper atmosphere sink and disappear below the photosphere. These clouds can vary in composition, height, structure and thickness.

The clouds themselves are affected by a number of conditions. There have been numerous pieces of evidence to show that surface gravity is a contributing factor in the structure of clouds (e.g., Cruz et al., 2009; Faherty et al., 2012, 2013, 2016; Knapp et al., 2004). In young ultra-cool dwarfs, low surface gravity means that the clouds extend a greater range of altitudes in the atmosphere. This leads to redder near-infrared colours than their older counterparts at similar effective temperatures. There has also been evidence of unusually red brown dwarfs with high dust content that do not have signatures of youth (Kirkpatrick et al., 2010; Liu et al., 2016;Looper et al., 2008). As there have not been many of these older red objects found, the cause of such dustiness is not well established.

Settling the ambiguity in the underlying cause of unusually dusty atmospheres is undoubtedly of interest for understanding the evolution of substellar objects, and the processes that affect the sedimentation and/or condensation of atmospheric dust. It is also crucial for revealing the ages and properties of directly imaged extrasolar planets, most of which exhibit spectral energy distribution (SED) characteristics of both youth and high dust content (e.g., Faherty et al., 2013). Because isolated brown dwarfs can be scrutinized much more readily than directly imaged extrasolar planets, we stand to potentially learn more about ultra-cool atmospheres from brown dwarfs than we can from exoplanets.

Observations of L+T binaries are also important for understanding the evolution of condensates and clouds in brown dwarf atmospheres across the L/T transition. Their coevality removes many of the uncertainties due to the distribution of initial conditions normally incorporated into evolutionary models. These types of systems also exhibit unusual near-infrared colours. In the  $J$ -band, the contributions from the L and T dwarf components are roughly equal — the “ $J$ -band bump” phenomenon in early T dwarfs (Tinney et al. 2003) — while the contribution from the T dwarf is much less in the far-optical, resulting

in slightly redder  $z - J$  colours than for normal L dwarfs. The  $J - K_s$  colours, however, are much bluer than normal L dwarfs because in the  $K$ -band, the contribution from the T dwarf is much fainter, while in the  $J$ -band the binary can be twice as bright as a single L dwarf. A number of such unresolved binaries have already been identified (e.g., Bardalez Gagliuffi et al., 2014; Burgasser et al., 2010; Cruz et al., 2004) but the completeness of that set is unknown. The observations of L+T binaries have already shed light on several mysteries surrounding the L/T transition (Burgasser et al., 2006a; Liu et al., 2006;Looper et al., 2008) and the role that clouds play in ultra-cool dwarf atmospheres (e.g. Ackerman et al., 2001; Apai et al., 2013; Burgasser et al., 2002; Kellogg et al. 2017d, submitted).

In view of our limited understanding of the evolution of substellar objects and the processes that affect condensation and sedimentation in the atmospheres of brown dwarfs, we carried out a dedicated search for L and T dwarfs with unusual optical/near-infrared colours. The goal was to substantially expand the sample of peculiar L and T dwarfs and L+T binaries in order to map the full range of their photospheric properties, and to better understand the evolution and content of L and T type atmospheres. We cross-correlated the SDSS, 2MASS and WISE catalogs to seek candidate peculiarly red brown dwarfs based solely on photometric criteria. From the first batch of candidates, presented in Kellogg et al. (2015, hereafter Paper 1 or P1), we discovered one of the brightest and least massive free-floating planetary-mass objects known to date, 2MASS J11193254–1137466 (Kellogg et al., 2016; TWA 42), which was recently resolved into a planetary-mass binary system where each object is  $\sim 3M_{\text{Jup}}$  (Best et al., 2017b). With this new survey, we determine the occurrence rate of various kinds of ultra-cool dwarfs by comparing our sample of peculiar L and T dwarfs to our full sample of ultra-cool dwarfs.

We discuss our candidate selection technique in §3.2 and our follow-up spectroscopic observations in §3.3. We present our results and discuss the characteristics of all the objects we have identified as peculiar in §3.4. In §3.5 we discuss the totality of our results and put them into a brown dwarf evolutionary context and we present our conclusions in §3.6.

### 3.2 CANDIDATE SELECTION

We implemented a photometric search for peculiar L and T dwarfs using combined optical (Sloan Digital Sky Survey; SDSS), near-infrared (2-Micron All-Sky Survey; 2MASS) and mid-infrared (Wide-Field Infrared Survey Explorer; WISE) fluxes. We applied joint positional and colour criteria to the full SDSS DR9 and 2MASS point source catalogs to identify L and T dwarfs with unusual photometric colours. Our criteria included selecting objects with steep red optical slopes ( $i - z > 1.5$  mag;  $z - J > 2.5$  mag) and no counterparts in SDSS at wavelengths shorter than the  $z$ -band. We then cross-matched the results against the AllWISE catalog to confirm our ultra-cool dwarf candidates were detected in the mid-infrared where most brown dwarf energy distributions peak and had colours consistent with other ultra-cool dwarfs ( $H - W2 > 1.2$  mag). We identified sub-samples of potentially interesting candidates using criteria that selected objects with peculiar optical/near-infrared colours. Our full candidate selection process is detailed in P1 and we briefly discuss the various selection criteria in the following sections.

#### 3.2.1 CANDIDATE ULTRA-COOL DWARFS

In P1, we reported a sample of 314 objects that passed all of our selection criteria and visual verification. We had obtained spectra of a first set of 45 of these candidates and 5 of them turned out to be false positives, i.e. their spectra were not like those of ultra-cool dwarfs. The first 40 bonafide ultra-cool dwarfs were reported in P1. We reviewed the finder charts of the 5 false-positives and determined that these objects indeed did not look like the bonafide ultra-cool dwarfs (e.g. were more diffuse than point-like). After refining our visual verification, as informed by our re-analysis of the 5 false-positives, our total candidate L and T dwarf list was cut to 156 objects including 104 new candidates, the 40 candidates reported in P1, the original 5 false positives, and 7 new false positives. For this paper we will focus on the remaining 104 candidates that we verified to be ultra-cool dwarfs via spectroscopy and only briefly discuss the 12 total false positives in §3.4. We also recovered 276 ultra-cool dwarfs that were previously

known. We discuss these in §3.5 where we analyze the statistics of the whole survey.

### 3.2.2 PECULIARLY RED CANDIDATES

The priority of our survey was to identify peculiarly red ultra-cool dwarfs in the cross section of the SDSS, 2MASS and WISE catalogs. We designed an appropriate selection criterion from the sample of L and T dwarfs in the SpeX Prism Archive. We formed synthetic photometry from their spectra by convolving with the 2MASS filter transmission profiles and integrating over the filter band-passes. We identified objects that had  $J - K_s$  colours that were  $>2\sigma$  redder than the median for the spectral type (red symbols in Figure 3.1a). The medians and standard deviations of the  $J - K_s$  colours were taken from Faherty et al. (2009; M7–M9 and T0–T8) and Faherty et al. (2013; L0–L9). All of the red colour outliers in the SpeX Prism Archive lie above the  $z - J = -0.75(J - K_s) + 3.8$  mag line in Figure 3.1a. We then applied this criterion to our 156 ultra-cool dwarf candidates and ended up with a sample of 88 peculiarly red candidates, 22 of which were already reported in P1. The synthetic colours of all of the candidates are presented in Figure 3.1b with different plotting colours used to represent objects with various spectroscopic peculiarities (discussed in §3.4). Our selection criteria were based on the photometric colours of the candidates so there are a number of objects whose synthetic colours do not appear to pass the initial colour-selection criteria (discussed more in §3.4).

### 3.2.3 CANDIDATE T DWARFS OR L+T BINARIES

In addition to selecting unusually red objects, our prioritization criterion from §3.2.2 also efficiently identified candidate unresolved L+T binary brown dwarfs. Figure 3.1b shows that they also stand out from the locus of objects on a  $z - J$  vs  $J - K_s$  diagram. Late-L and early-T dwarfs are similar in brightness in the  $J$ -band but are fainter in the  $z$ - and  $K$ -bands resulting in moderate or blue  $J - K_s$  colours but red  $z - J$  colours. To fully include all potential unresolved L+T binaries, we created a second independent criterion to select these. Any object that satisfied the criterion  $z - J > 0.95(J - K_s) + 1.45$  mag was either a candidate

L+T binary or a candidate T dwarf as the latter also have the same red-optical and near-infrared colours. This criterion selected 13 objects that were candidate binary or T dwarfs. Twenty objects satisfied both selection criteria, i.e., they were red in  $z - J$  but moderate in  $J - K_s$  (top centre of Fig. 3.1b).

### 3.3 SPECTROSCOPIC OBSERVATIONS AND DATA REDUCTION

We obtained near-infrared spectroscopic observations of the remaining 104 objects in our survey — 66 peculiarly red, 13 candidate binary and 25 general ultra-cool dwarf candidates — using the SpeX instrument (Rayner et al., 2003) on the NASA Infrared Telescope Facility (IRTF) and the Gemini Near-Infrared Spectrograph (GNIRS) instrument (Elias et al., 2006) on the Gemini North telescope. All reduction of the SpeX spectra was done in Interactive Data Language (IDL). The GNIRS spectra were reduced using the Gemini package version 1.13.1 in Image Reduction and Analysis Facility (IRAF; Cooke et al., 2005).

#### 3.3.1 IRTF/SPEX

We obtained the majority of our follow-up observations (91 of 104) with the SpeX spectrograph on the IRTF in prism mode ( $0.75\text{--}2.5\ \mu\text{m}$ ;  $R\sim 75\text{--}150$ ), between 2014 October and 2016 April. Observing sequences and instrument settings were the same as those in P1. Table 3.1 gives observation epochs and SpeX instrument settings for each science target. We reduced all the SpeX data in the same way as in P1. Figure 3.2 shows all reduced spectra in order of increasing spectral type (see § 3.4) and within each spectral type in order of increasing RA.

Table 3.1: SpeX Observations

Identifier (J2000)	Date (UT)	2MASS J (mag)	Slit Width (arcsec)	Exposure (min)	A0 Calibrator
2MASS J00065552+0236376	2015 Oct 08	16.75	1.6	26	BD+02 66
2MASS J00062250+1300451	2015 Nov 30	16.96	1.6	24	BD+12 5
2MASS J00082822+3125581	2015 Jul 06	15.61	1.6	24	HD 3925

Continued on Next Page...

Table 3.1 – Continued

Identifier (J2000)	Date (UT)	2MASS J (mag)	Slit Width (arcsec)	Exposure (min)	A0 Calibrator
2MASS J00100480-0930519	2015 Jul 07	16.33	1.6	12	HIP 115119
2MASS J00132229-1-143006	2014 Oct 12	16.35	0.8	40	HIP 5899
2MASS J00133470+1109403	2015 Sep 08	15.72	1.6	26	BD+10 102
2MASS J00150673+3006004	2014 Oct 12	16.10	0.8	20	HIP 2969
2MASS J00435012+0928429	2014 Oct 12	16.18	0.8	40	HIP 10441
2MASS J00440332+0228112 <sup>a</sup>	2015 Jul 01	17.00	1.6	38	HD 9538
2MASS J00452972+4237438	2015 Nov 30	17.06	1.6	60	HIP 10559
2MASS J00501561+1012431	2015 Jun 30	16.78	1.6	32	HD 7353
2MASS J00550564+0134365	2015 Jul 05	16.44	1.6	28	HD 9538
2MASS J01001471-0301494	2015 Jun 29	16.32	1.6	24	HD 9716
2MASS J01114355+2820024	2015 Jul 06	16.34	1.6	24	HD 10681
2MASS J01145788+4318561	2015 Jul 07	14.51	1.6	12	HD 10773
2MASS J01141304+4354287	2015 Nov 29	16.81	1.6	36	HIP 13917
2MASS J01165802+4333081	2015 Jul 07	16.88	1.6	36	HD 10499
2MASS J01183399+1810542	2015 Sep 08	15.72	1.6	34	HD 10982
2MASS J01194279+1122427	2014 Oct 12	15.97	0.8	20	HIP 9965
2MASS J01343635-0145444	2015 Nov 29	16.64	1.6	56	HIP 13917
2MASS J01341675-0546530	2015 Sep 08	16.17	1.6	34	HD 7194
2MASS J01352531+0205232	2015 Sep 08	16.62	1.6	34	HD 7194
2MASS J01392388-1845029	2015 Nov 30	16.55	1.6	60	HIP 10185
2MASS J01394906+3427226	2015 Oct 08	17.13	1.6	24	HIP 10559
2MASS J01414428+2227409	2015 Sep 08	16.81	1.6	50	HD 14334
2MASS J01442482-0430031	2015 Nov 29	17.25	1.6	60	HIP 10512
2MASS J01453520-0314117 <sup>a</sup>	2015 Oct 08	17.12	1.6	36	HIP 10512
2MASS J02151451+0453179	2015 Nov 30	16.60	1.6	24	HIP 13917
2MASS J02314893+4521059	2015 Nov 30	16.55	1.6	32	HIP 15925
2MASS J03315828+4130486	2015 Nov 30	16.86	1.6	32	HIP 18769
2MASS J03511847-1149326	2015 Feb 24	16.35	0.8	44	HIP 19053
2MASS J03530419+0418193	2014 Oct 12	16.47	0.8	20	HD 29838
2MASS J04214620-0025072	2015 Oct 08	16.34	1.6	20	HIP 22435
2MASS J04232191-0803051	2015 Nov 29	16.27	1.6	20	HIP 22435
2MASS J04234652+0843211	2014 Dec 30	16.18	0.8	40	HIP 22923
2MASS J04510592+0014394	2015 Nov 30	16.78	1.6	40	HIP 25121
2MASS J07244848+2506143	2014 Dec 30	16.48	0.8	48	HIP 38722
2MASS J07552723+1138485	2015 Feb 25	17.26	0.8	40	HIP 43018
2MASS J08270185+4129191	2014 Dec 30	15.91	0.8	68	HIP 41798
2MASS J08443811+2226161	2014 Dec 30	16.80	0.8	36	HIP 50459
2MASS J09053247+1339138	2015 Feb 24	17.26	0.8	76	HIP 48414
2MASS J09083688+5526401	2015 Nov 29	16.46	1.6	24	HIP 50459
2MASS J09194512+5135149	2015 Feb 25	16.72	0.8	40	HIP 53735
2MASS J09325053+1836485	2015 Nov 29	17.46	1.6	60	HIP 50459
2MASS J09393078+0653098 <sup>b</sup>	2015 Nov 30	16.78	1.6	44	HIP 45167

Continued on Next Page...

Table 3.1 – Continued

Identifier (J2000)	Date (UT)	2MASS J (mag)	Slit Width (arcsec)	Exposure (min)	A0 Calibrator
2MASS J09481259+5300387	2015 Nov 29	15.59	1.6	16	HIP 53735
2MASS J10271549+5445175	2016 Apr 24	16.15	1.6	26	HIP 53735
2MASS J10551343+2504028	2016 Apr 17	17.06	1.6	50	HIP 55627
2MASS J10592523+5659596	2016 Apr 24	15.51	1.6	34	HIP 56147
2MASS J11060459-1907025	2016 Apr 17	16.76	1.6	30	HIP 56746
2MASS J11213919-1053269	2016 Apr 24	16.44	1.6	30	HD 97516
2MASS J11220855+0343193	2016 Apr 17	16.65	1.6	10	HIP 54849
2MASS J11285958+5110202	2016 Apr 24	16.19	1.6	26	HIP 52478
2MASS J11282763+5934003	2016 Apr 24	16.37	1.6	36	HD 97516
2MASS J12023885+5345384	2016 Apr 24	17.56	1.6	68	HD 108346
2MASS J12232570+0448277 <sup>b</sup>	2016 Apr 16	16.33	1.6	18	HIP 62745
2MASS J12352675+4124310	2016 Apr 16	16.71	1.6	34	HIP 65280
2MASS J12453705+4028456	2016 Apr 17	16.75	1.6	26	HIP 65280
2MASS J12492272+0310255	2016 Apr 17	16.36	1.6	18	HIP 62745
2MASS J13042886-0032410	2016 Apr 16	17.03	1.6	26	HIP 65599
2MASS J13064517+4548552	2016 Apr 24	17.01	1.6	52	HD 116405
2MASS J13170488+3447513	2016 Apr 17	16.50	1.6	34	HIP 61534
2MASS J13184567+3626138 <sup>a</sup>	2016 Apr 17	17.21	1.6	34	HIP 65280
2MASS J13264464+3627407	2016 Apr 17	16.44	1.6	34	HIP 65280
2MASS J13451417+4757231	2016 Apr 24	16.50	1.6	26	HIP 68767
2MASS J14124574+3403074	2016 Apr 17	16.55	1.6	34	HIP 71172
2MASS J14154242+2635040	2016 Apr 24	16.37	1.6	34	HIP 77111
2MASS J14313545-0313117	2016 Apr 17	16.09	1.6	26	HIP 73200
2MASS J14554511+3843329	2016 Apr 24	16.70	1.6	34	HIP 77111
2MASS J15102256-1147125	2016 Apr 16	15.66	1.6	10	HIP 78436
2MASS J15163838+3333576	2016 Apr 16	16.79	1.6	42	HIP 77111
2MASS J15442544+0750572	2016 Apr 16	16.75	1.6	34	HIP 79332
2MASS J15500191+4500451	2016 Apr 17	17.33	1.6	66	HD 141930
2MASS J15525579+1123523	2016 Apr 17	15.92	1.6	18	HIP 79332
2MASS J15543602+2724487	2015 Sep 08	16.19	1.6	22	HIP 77111
2MASS J15565004+1449081	2015 Sep 08	17.31	1.6	38	HIP 77111
2MASS J16123860+3126489	2016 Apr 24	16.64	1.6	34	BD+34 2755
2MASS J17120142+3108217	2015 Jul 01	16.18	1.6	40	HD 161259
2MASS J17153111+1054108	2015 Jul 05	17.11	1.6	12	HD 161259
2MASS J17440969+5135032	2015 Jul 07	16.92	1.6	16	HIP 82884
2MASS J17570962+4325139	2015 Sep 14	16.73	1.6	50	HD 170560
2MASS J21123034+0758505	2015 Jul 06	16.26	1.6	32	HD 207073
2MASS J22035781+0713492	2015 Jun 19	16.68	1.6	28	HIP 116886
2MASS J22191282+1113405 <sup>b</sup>	2015 Oct 08	16.74	1.6	20	HIP 109452
2MASS J22295358+1556180	2015 Jul 01	16.46	1.6	32	HD 116886
2MASS J22355244+0418563	2014 Oct 12	15.37	0.8	20	HIP 116886
2MASS J22545900-0330590	2015 Nov 29	16.84	1.6	40	HIP 116886

Continued on Next Page...

Table 3.1 – Continued

Identifier (J2000)	Date (UT)	2MASS J (mag)	Slit Width (arcsec)	Exposure (min)	A0 Calibrator
2MASS J22582325+2906484	2015 Nov 29	16.77	1.6	36	HIP 116886
2MASS J23004298+0200145	2014 Oct 12	16.40	0.8	40	HIP 116886
2MASS J23053808+0524070	2014 Oct 12	16.43	0.8	40	HIP 116886
2MASS J23313131+2041273	2015 Jul 05	16.06	1.6	40	HD 3347

<sup>a</sup> Independently reported by Schneider et al., 2017.

<sup>b</sup> Independently reported by Best et al., 2017a.

### 3.3.2 GEMINI/GNIRS

We followed-up the remaining 13 objects in our candidate list using GNIRS on Gemini North (0.9–2.5  $\mu\text{m}$ ). We observed these objects in queue mode between 2015 October and 2017 May. We took the observations in cross-dispersed mode with the short-blue camera, 32 l/mm grating and  $1''.0 \times 7''.0$  slit resulting in a resolution of  $R \sim 500$ . We used a standard A-B-B-A nodding sequence along the slit to record object and sky spectra. Individual exposure times were 120s per pointing. Standard stars were used for flux calibration and telluric correction. Flat-field and argon lamps were taken immediately after each set of target and standard star observations for use in instrumental calibrations. Table 3.2 gives Gemini/GNIRS observation epochs for each science target.

We reduced the cross-dispersed spectra by straightening the traces, rectifying them to the vertical, and then wavelength calibrating before extracting. We extracted the spectra using the variance weighted sum of the flux within the aperture with the aperture radius equal to the PSF radius (usually  $\sim 4$  pixels =  $0''.60$ ). We modeled a local background using a linear fit to a specified background region (usually  $\sim 8$  pixels =  $1''.2$  wide on either side of the PSF  $\sim 2$  pixels =  $0''.30$  away from the PSF) and subtracted it from the spectra which we subsequently extracted. Each set of extracted spectra were median-combined, corrected for telluric absorption and flux-calibrated with their associated A0 calibration star. We median combined all calibrated sets of observing sequences to produce a final spectrum. The reduced spectra were smoothed, using the IDL

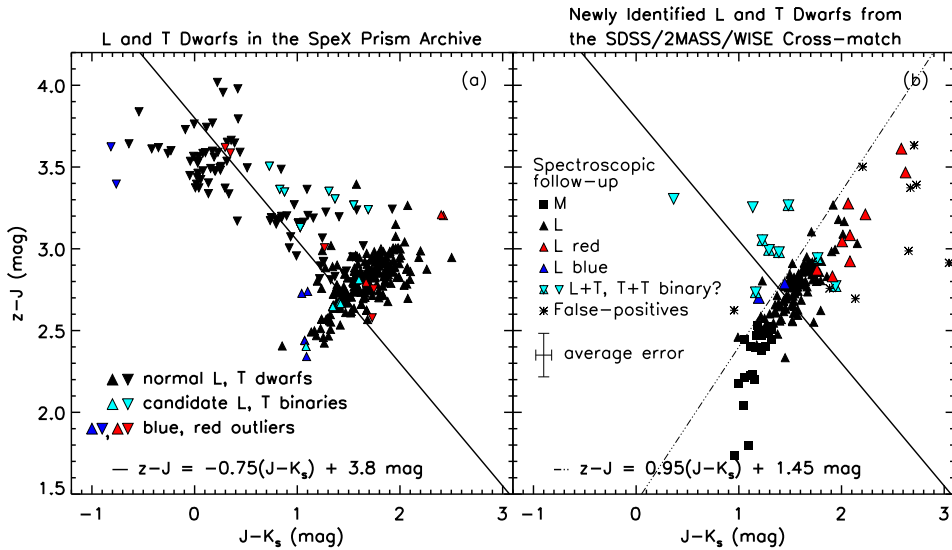


Figure 3.1: (a) SDSS/2MASS synthetic colour-colour diagram of L and T dwarfs from the SpeX Prism Archive (upwards and downwards triangles, respectively). The  $z - J$ , and  $J - K_s$  colours were formed synthetically from the SpeX spectra. Two-sigma red and blue photometric colour outliers within each spectral type are indicated by red and blue symbols, respectively. The  $z - J = -0.75(J - K_s) + 3.8$  mag line was designed to select the red outliers based on their photometric SDSS/2MASS colours. (b) colour-colour diagram of all of our L and T dwarf survey candidates with photometric colours redder than  $z - J = 2.5$  mag identified from the SDSS-2MASS-WISE cross-match. All symbols (squares - M dwarfs; upwards triangles - L dwarfs; downwards triangles - T dwarfs) represent the synthetic colours of the candidates from their spectra. The GNIRS spectra do not cover the entire  $z$ -band so for objects observed with GNIRS, the  $z - J$  colours are their photometric colours. The black symbols are “normal” objects and the red and blue symbols are objects that we have identified as peculiar or binary. Objects to the right of the  $z - J = -0.75(J - K_s) + 3.8$  mag line are candidate peculiarly red L and T dwarfs and objects to the left of the  $z - J = 0.95(J - K_s) + 1.45$  mag line are candidate unresolved L+T binaries or T dwarfs. Both sets of peculiar objects were prioritized for spectroscopic follow-up. The photometric colours of the 12 false-positives (§3.4.4) are shown by asterisks.

interpolation algorithm with a least squares quadratic fit, to the same resolution as the SpeX standards for comparison in §3.4. The reduced Gemini/GNIRS spectra are included in Figures 3.2–3.6, where they are shown prior to smoothing.

Table 3.2: GNIRS Observations

Identifier (J2000)	Date (UT)	2MASS J (mag)	Exposure (min)	A0 Calibrator
2MASS J01412651+1001339	2015 Oct 21	17.05	44	HIP 7353
2MASS J02022917+2305141 <sup>a</sup>	2015 Nov 04	17.22	48	HD 9071
2MASS J03302948+3910242	2016 Jan 05	17.12	60	HIP 18769
2MASS J09240328+3653444	2015 Nov 04	17.09	64	HIP 41798
2MASS J10265851+2515262	2016 Jan 25	17.36	56	HIP 50459
2MASS J10524963+1858151	2016 Jan 25	17.30	56	HIP 56736
2MASS J12260640+1756293	2015 Apr 02	16.85	40	HIP 56736
2MASS J14193789+3333326	2017 Feb 01	16.30	120	HIP 68767
2MASS J15025475+5044252	2017 Apr 12	16.16	48	HIP 67848
2MASS J15202471+2203340	2017 May 23	16.67	124	HIP 68767
2MASS J15552840+5918155	2017 Apr 15	15.96	120	HIP 78017
2MASS J16194822-0425366	2017 Apr 18	16.57	68	HIP 81584
2MASS J17164469+2302220	2015 Apr 02	17.02	56	HIP 79102

<sup>a</sup> Independently reported by Schneider et al., 2017.

### 3.4 SPECTRAL CLASSIFICATION RESULTS

We estimate spectral types for our candidates by comparing them to ultra-cool dwarf spectral standards in the SpeX Prism Archive<sup>\*</sup>. Our spectral type classifications have an average uncertainty of  $\pm 1$  spectral type.

The newly classified M, L, and T dwarfs are plotted on the  $z - J$  vs.  $J - K_s$  colour-colour diagram in Figure 3.1b, where we have used the synthetic colours integrated from the spectra. The spectral types and synthetic colours are presented in Table 3.3. The GNIRS spectra do not cover the entire  $z$ -band so the

<sup>\*</sup>Standards used for comparison are from Burgasser, 2004, 2007; Burgasser et al., 2006a,b, 2007, 2008; Chiu et al., 2006; Cruz et al., 2004; Kirkpatrick et al., 2010; Reid et al., 2006

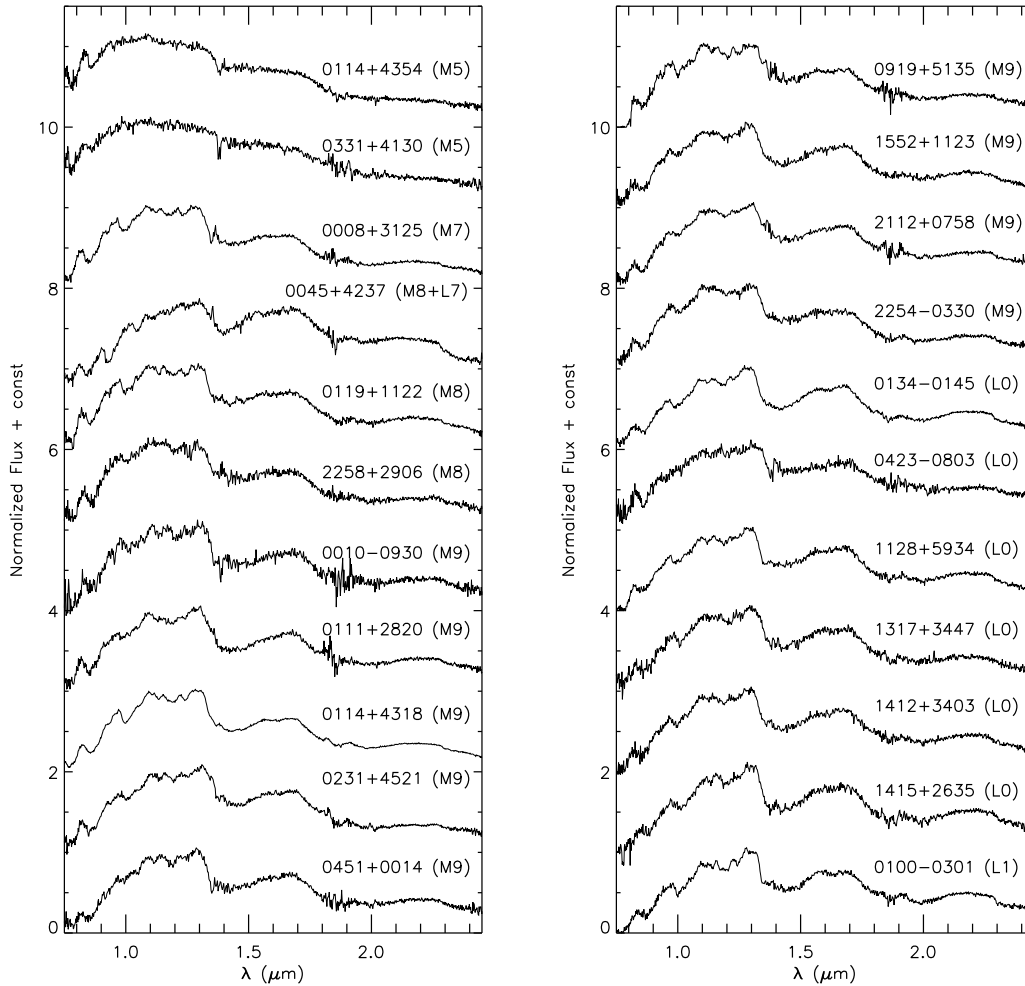


Figure 3.2: SpeX (0.75–2.5  $\mu\text{m}$ ;  $R \sim 75\text{--}150$ ) and GNIRS (0.9–2.5  $\mu\text{m}$ ;  $R \sim 500$ ) spectra of the 104 newly discovered ultra-cool dwarfs in order of spectral type. Spectral types are given in parentheses.

$z - J$  colours for the objects taken with GNIRS are their photometric colours. A number of objects have synthetic  $z - J$  colours that are bluer than  $z - J > 2.5$  mag. Many of the photometric magnitudes may have been subject to flux-overestimation bias at  $J$ -band (Section 3.3 of P1) and their colours are close to or below the limits of our  $z - J > 2.5$  mag colour selection criteria (Section 3.2). This is likely the reason why the synthetic and photometric colours are not the

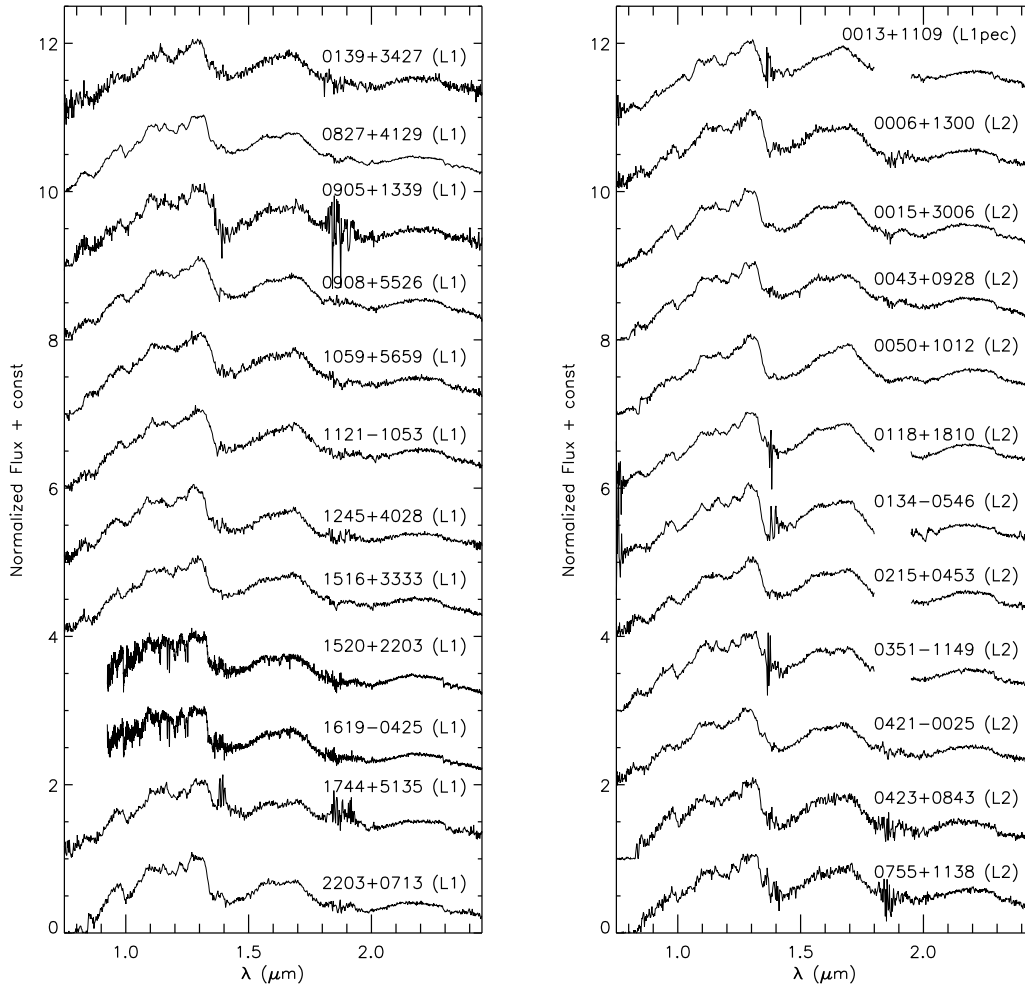


Figure 3.3: Spectra continued

same and why some objects no longer satisfy the photometric selection criteria with their synthetic colours (Fig. 3.1b). We check that the synthetic colours of our normal L and T dwarfs correctly represent those of the field L and T population by comparing to the L and T near-infrared colour compendium of Faherty et al. (2009; 2013). Figure 3.7 shows that there is a very good match. Therefore, we are confident that our procedure of adopting synthetic colours to correct the low-SNR SDSS and 2MASS photometry can be used to also identify

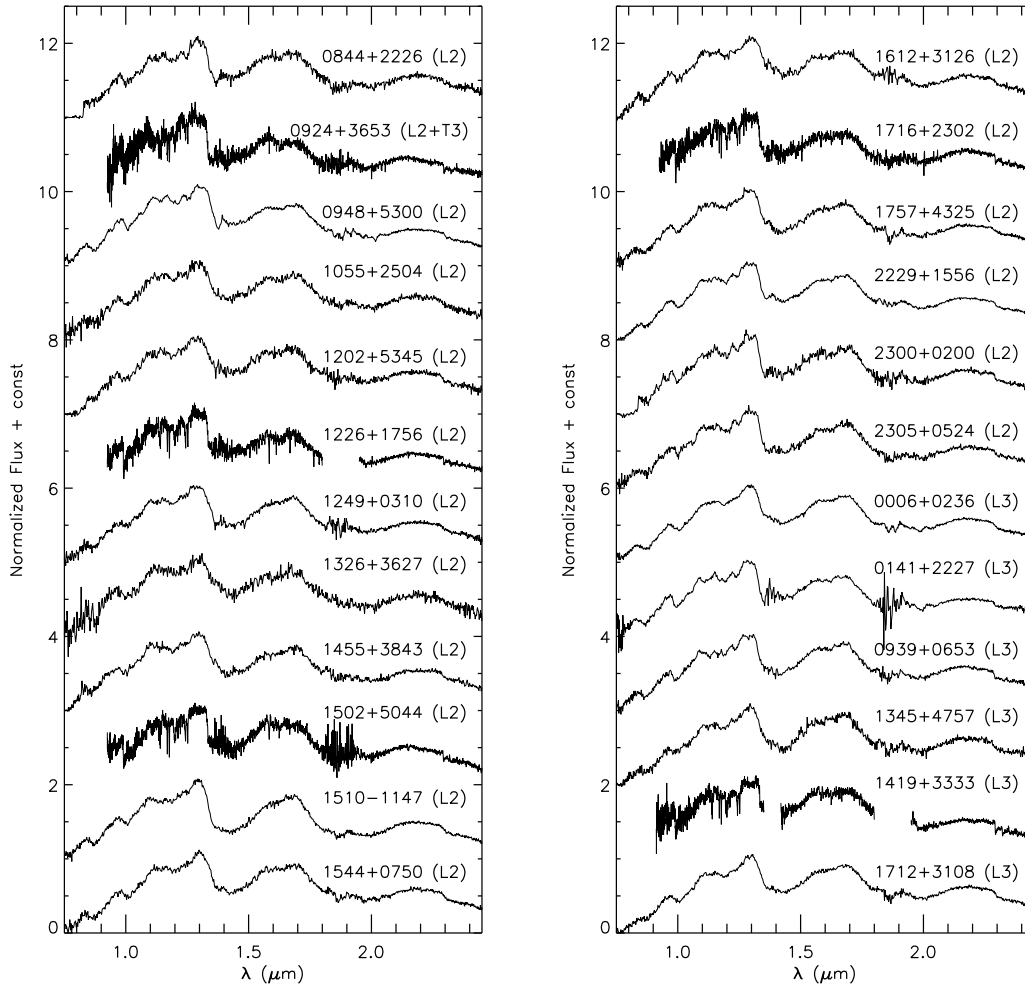


Figure 3.4: Spectra continued

colour outliers: candidate peculiar objects.

We discuss the peculiar (§3.4.1), candidate binary (§3.4.2), and normal (§3.4.3) ultra-cool dwarfs, and false-positives (§3.4.4) in our sample below.

### 3.4.1 PECULIAR L DWARFS

We classify seven objects as unusual based on their spectroscopic peculiarities. Our assessment of peculiarity is determined by high spectral similarity to ob-

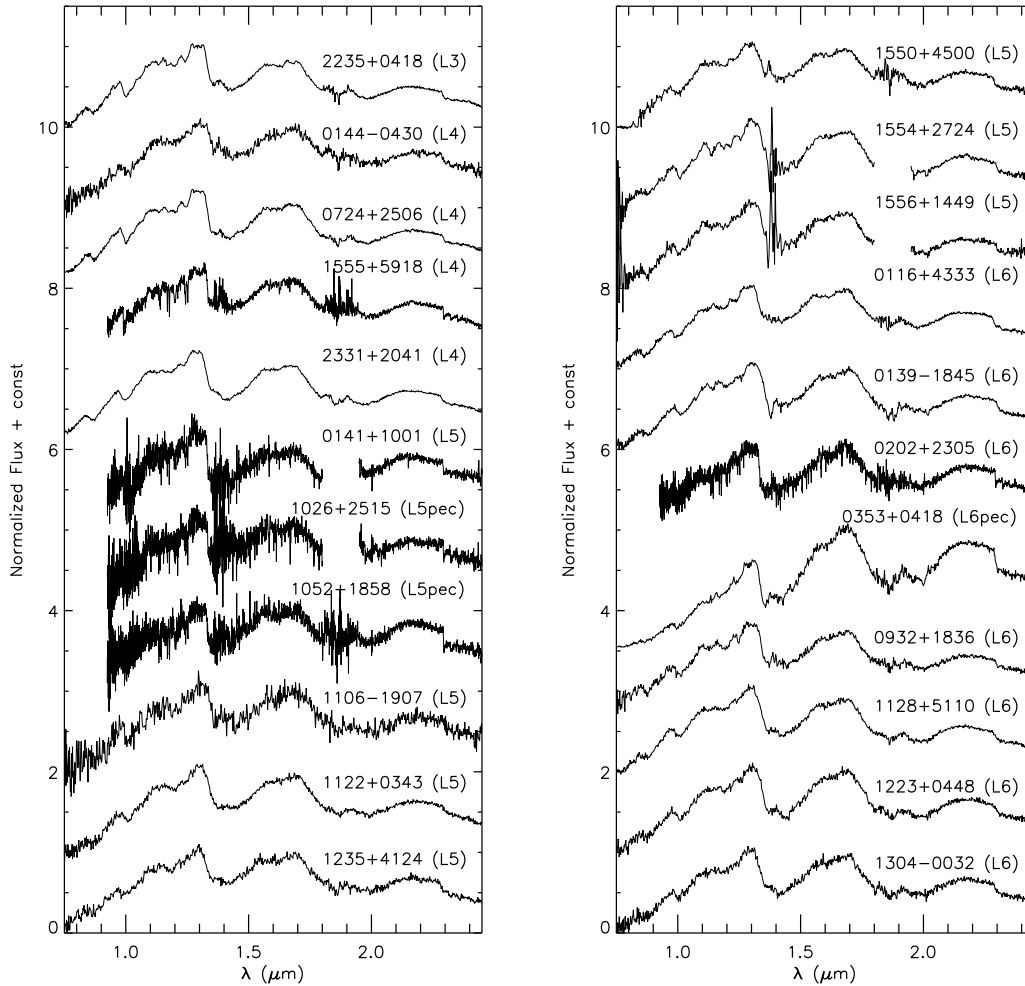


Figure 3.5: Spectra continued

jects that have previously been classified as peculiar. The peculiar characteristics of our objects can be produced by youth, large amounts of atmospheric dust, or low-metallicity. The most interesting objects from this portion of the survey are the young, planetary-mass L7 dwarf 2MASS J00440332+0228112 (§3.4.1.2), the very red L6 dwarf 2MASS J03530419+0418193 (§3.4.1.4), and the candidate young L1 dwarf 2MASS J00133470+1109403 (§3.4.1.1).

Young ultra-cool dwarfs have low surface gravity, hence, the line strengths of

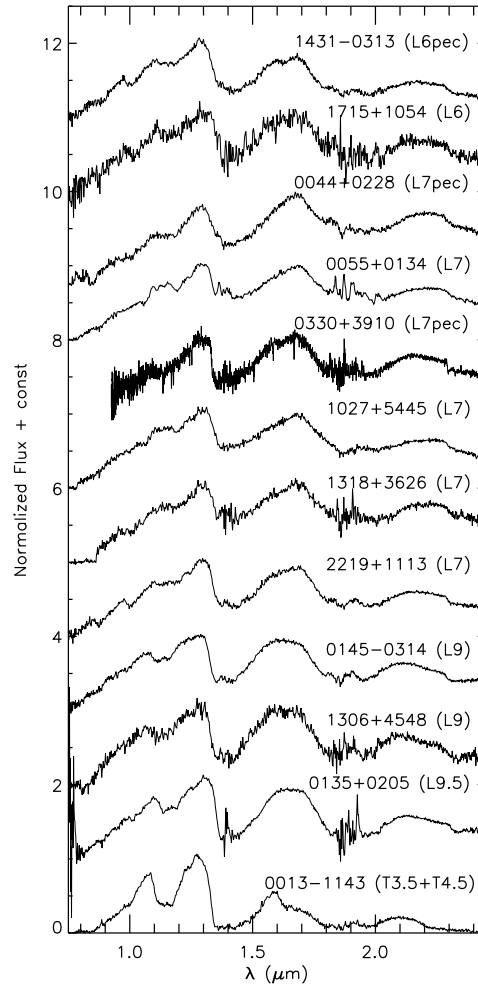


Figure 3.6: Spectra continued

the gravity-sensitive features will differ from those in older objects (e.g. Allers et al., 2007, 2013; Gorlova et al., 2003; Lodieu et al., 2008; Lucas et al., 2001; McGovern et al., 2004; Rice et al., 2010). The Na I (1.138 and 1.141  $\mu\text{m}$ ) and K I (1.169 and 1.178  $\mu\text{m}$ , 1.244 and 1.253  $\mu\text{m}$ ) doublets are weaker because of decreased pressure broadening. The FeH features (bandheads at 0.990  $\mu\text{m}$  and 1.194  $\mu\text{m}$ ) are weaker because of decreased opacity of the refractory species. Collision-induced absorption from molecular hydrogen also changes as a func-

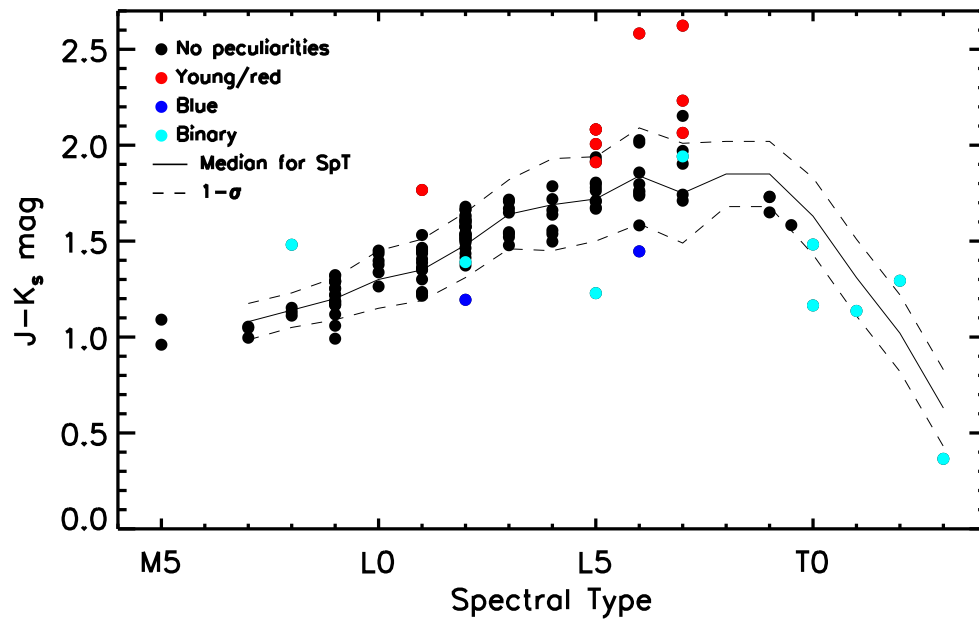


Figure 3.7: Synthetic colours of the 144 new objects discovered in our survey (P1 and present results). The solid line represents the median  $J - K_s$  colours for each spectral type from Faherty et al., 2009 and Faherty et al., 2013 and the dashed line represents the  $1\sigma$  limits. The correspondence is very good, and indicates that our synthetic colours are reliable for seeking candidate peculiar dwarfs as colour outliers.

tion of gravity, with lower collision rates in low-gravity objects imparting a triangular shape to the  $H$ -band.

As discussed in P1, the indices developed by Allers et al., 2013, Canty et al., 2013 and Schneider et al., 2014 have the potential to offer a quantitative gravity classification. However, our spectra have significantly lower spectral resolution, so the index measurements are more uncertain than in those studies. In addition, most of the indices do not extend into the late-L dwarfs, and so are inadequate to classify some of our most interesting objects. Therefore, we do not adopt spectral indices as a default gravity classification scheme. However, we do check for consistency with applicable spectral indices whenever we find peculiarities in the spectra of our L and T candidates.

We note that unusually red objects that lack some signatures of youth can still exhibit some of the spectroscopic characteristics of young objects, in particular weaker FeH bands and a triangular  $H$ -band continuum (e.g. Kirkpatrick et al., 2010; Looper et al., 2008). In these objects, such features have been attributed to high atmospheric dust content or to thicker clouds rather than to low-gravity (Allers et al., 2013; Looper et al., 2008). In the cases of unusually red objects, we rely on the strength of the gravity-sensitive alkali (K I and Na I) lines to distinguish between young objects and field-age ( $\gtrsim 0.5$  Gyr) objects with unusually high dust content.

For objects with blue near-infrared colours, we seek to determine whether the blue colours may result from low cloud opacity, low-metallicity or unresolved binarity. In order to check the possibility of them being binaries, we consider the  $\text{CH}_4$  in the  $K$ - and  $H$ -bands. If there is a higher abundance of  $\text{CH}_4$  in the  $H$ -band relative to the  $K$ -band, the object is most likely a binary as the onset of methane absorption in cooler, older objects is apparent in the  $K$ -band before the  $H$ -band (e.g. Bardalez Gagliuffi et al., 2014; Burgasser et al., 2010; Cruz et al., 2004). If we determine that the objects are not binaries, then we can also check whether or not they are metal-poor by analyzing the FeH feature in the  $Y$ - and  $J$ -bands. Although an object may be metal-poor, it may have a stronger FeH feature due to the larger relative amounts of hydrogen present and the decreased absorption by oxides such as TiO and VO (e.g. Kirkpatrick et al.,

2010). If, however, an object's blue colours come from a low cloud opacity, the overall dust continuum will simply be much weaker, leaving CO and CH<sub>4</sub> as the dominant opacity sources (Kirkpatrick, 2005).

We discuss individual objects and their defining characteristics in the next sections.

Table 3.3: Results from Spectroscopic Classification and Synthetic Photometry

2MASS ID (J2000)	IR SpT	Interpretation (from spectrum)	$z - J$ (mag)	$J - H$ (mag)	$J - K_s$ (mag)	$>1\sigma$ Colour Outlier	$>2\sigma$ Colour Outlier
Peculiarly Red							
2MASS J00065552+0236376	L3		2.80 ± 0.05	1.01 ± 0.08	1.65 ± 0.08		
2MASS J00150673+3006004	L2		2.86 ± 0.05	0.98 ± 0.09	1.62 ± 0.07		
2MASS J00440332+0228112	L7pec	red/young	3.21 ± 0.10	1.33 ± 0.17	2.23 ± 0.10	+	
2MASS J00501561+1012431	L2		2.88 ± 0.10	1.00 ± 0.12	1.66 ± 0.13		
2MASS J00550564+0134365	L7		2.98 ± 0.06	1.15 ± 0.07	1.90 ± 0.07		
2MASS J01165802+4333081	L6		2.83 ± 0.06	1.12 ± 0.12	1.86 ± 0.10		
2MASS J01183399+1810542	L2		2.86 ± 0.05	1.01 ± 0.09	1.68 ± 0.07		
2MASS J01341675-0546530	L2		2.78 ± 0.04	0.94 ± 0.07	1.51 ± 0.08		
2MASS J01392388-1845029	L6		2.87 ± 0.06	1.08 ± 0.08	1.74 ± 0.08		
2MASS J01394906+3427226	L1		2.61 ± 0.11	0.94 ± 0.12	1.53 ± 0.12		
2MASS J01453520-0314117	L9		2.55 ± 0.10	1.09 ± 0.14	1.73 ± 0.11		
2MASS J02022917+2305141	L6		... <sup>a</sup>	1.18 ± 0.13	2.01 ± 0.15		
2MASS J02151451+0453179	L2		2.77 ± 0.07	1.02 ± 0.12	1.66 ± 0.12		
2MASS J03530419+0418193	L6pec	very red	3.61 ± 0.06	1.59 ± 0.10	2.58 ± 0.11		+
2MASS J04214620-0025072	L2		2.65 ± 0.06	0.92 ± 0.09	1.51 ± 0.08		
2MASS J04234652+0843211	L2		2.69 ± 0.04	0.95 ± 0.09	1.46 ± 0.05		
2MASS J07244848+2506143	L4		2.82 ± 0.05	0.96 ± 0.11	1.54 ± 0.10		
2MASS J07552723+1138485	L2		2.91 ± 0.13	0.97 ± 0.23	1.64 ± 0.15		
2MASS J08443811+2226161	L2		2.78 ± 0.07	0.99 ± 0.21	1.61 ± 0.13		
2MASS J09053247+1339138	L1		2.64 ± 0.12	0.86 ± 0.24	1.41 ± 0.23		
2MASS J09325053+1836485	L6		2.80 ± 0.08	1.05 ± 0.13	1.76 ± 0.20		
2MASS J09393078+0653098	L3		2.74 ± 0.10	1.02 ± 0.10	1.67 ± 0.11		
2MASS J10271549+5445175	L7		2.86 ± 0.04	1.05 ± 0.06	1.74 ± 0.06		
2MASS J10524963+1858151	L5pec	red	... <sup>a</sup>	1.22 ± 0.23	2.08 ± 0.15	+	
2MASS J11220855+0343193	L5		3.10 ± 0.05	1.04 ± 0.06	1.71 ± 0.06		
2MASS J11285958+5110202	L6		2.85 ± 0.03	0.99 ± 0.08	1.58 ± 0.07		
2MASS J12023885+5345384	L2		2.80 ± 0.12	0.98 ± 0.21	1.60 ± 0.16		
2MASS J12352675+4124310	L5		2.62 ± 0.08	1.01 ± 0.08	1.65 ± 0.08		

Continued on Next Page...

Table 3.3 – Continued

2MASS ID (J2000)	IR SpT	Interpretation (from spectrum)	$z - J$ (mag)	$J - H$ (mag)	$J - K_s$ (mag)	$>1\sigma$ Colour Outlier	$>2\sigma$ Colour Outlier
2MASS J13042886-0032410	L6		2.80 ± 0.08	1.08 ± 0.11	1.80 ± 0.15		
2MASS J13184567+3626138	L7		3.18 ± 0.09	1.18 ± 0.13	1.97 ± 0.12		
2MASS J13451417+4757231	L3		2.88 ± 0.06	1.05 ± 0.11	1.71 ± 0.10		
2MASS J14554511+3843329	L2		2.55 ± 0.06	0.90 ± 0.15	1.52 ± 0.16		
2MASS J15102256-1147125	L2		2.68 ± 0.04	0.88 ± 0.05	1.44 ± 0.07		
2MASS J15163838+3333576	L1		2.63 ± 0.09	0.89 ± 0.12	1.46 ± 0.09		
2MASS J15442544+0750572	L2		2.59 ± 0.09	0.98 ± 0.10	1.57 ± 0.15		
2MASS J15500191+4500451	L5		2.92 ± 0.10	1.10 ± 0.13	1.80 ± 0.10		
2MASS J15543602+2724487	L5		2.91 ± 0.04	1.05 ± 0.09	1.71 ± 0.07		
2MASS J15565004+1449081	L5		2.87 ± 0.10	1.02 ± 0.16	1.67 ± 0.15		
2MASS J17120142+3108217	L3		2.84 ± 0.04	1.04 ± 0.07	1.72 ± 0.07		
2MASS J17153111+1054108	L6		2.80 ± 0.11	1.09 ± 0.15	1.76 ± 0.13		
2MASS J17164469+2302220	L2		...	0.88 ± 0.15	1.57 ± 0.15		
2MASS J1740969+5135032	L1		2.62 ± 0.07	0.80 ± 0.14	1.44 ± 0.12		
2MASS J22035781+0713492	L1		2.80 ± 0.05	0.72 ± 0.12	1.23 ± 0.11		
2MASS J22191282+1113405	L7		2.84 ± 0.08	1.05 ± 0.10	1.71 ± 0.10		
2MASS J22295358+1556180	L2		2.82 ± 0.06	0.96 ± 0.09	1.60 ± 0.10		
2MASS J22355244+0418563	L3		2.76 ± 0.03	0.92 ± 0.03	1.48 ± 0.04		
2MASS J23313131+2041273	L4		2.78 ± 0.05	0.97 ± 0.08	1.56 ± 0.09		
Candidate Binary							
2MASS J00100480-0930519	M9		2.40 ± 0.05	0.67 ± 0.22	1.12 ± 0.16		
2MASS J01114355+2820024	M9		2.38 ± 0.06	0.72 ± 0.17	1.22 ± 0.18		
2MASS J01141304+4354287	M5		1.74 ± 0.09	0.65 ± 0.17	0.96 ± 0.19		
2MASS J0144428+2227409	L3		2.72 ± 0.11	0.95 ± 0.13	1.55 ± 0.24		
2MASS J09194512+5135149	M9		2.40 ± 0.05	0.71 ± 0.13	1.18 ± 0.16		
2MASS J10592523+5659596	L1		2.66 ± 0.05	0.84 ± 0.15	1.35 ± 0.12		
2MASS J12453705+4028456	L1		2.59 ± 0.04	0.72 ± 0.17	1.22 ± 0.18		
2MASS J13170488+3447513	L0		2.53 ± 0.04	0.80 ± 0.15	1.26 ± 0.18		
2MASS J14124574+3403074	L0		2.54 ± 0.06	0.80 ± 0.12	1.34 ± 0.15		

Continued on Next Page...

Table 3.3 – Continued

2MASS ID (J2000)	IR SpT	Interpretation (from spectrum)	$z - J$ (mag)	$J - H$ (mag)	$J - K_s$ (mag)	$>1\sigma$ Colour Outlier	$>2\sigma$ Colour Outlier
2MASS J14313545-0313117	L6pec	blue	$2.78 \pm 0.04$	$0.88 \pm 0.10$	$1.45 \pm 0.12$	–	–
2MASS J15525579+1123523	M9		$2.48 \pm 0.04$	$0.79 \pm 0.10$	$1.29 \pm 0.13$		
2MASS J21123034+0758505	M9		$2.53 \pm 0.04$	$0.78 \pm 0.16$	$1.29 \pm 0.16$		
2MASS J22582325+2906484	M8		$2.22 \pm 0.05$	$0.67 \pm 0.19$	$1.11 \pm 0.22$		
Peculiarly Red and Candidate Binary							
2MASS J00082822+3125581	M7		$2.18 \pm 0.14$	$0.63 \pm 0.08$	$1.00 \pm 0.08$		
2MASS J00132229-1143006	T3pec	T3.5 + T4.5?	$3.31 \pm 0.10$	$0.34 \pm 0.11$	$0.37 \pm 0.22$	–	–
2MASS J00133470+1109403	L1pec	red/young	$2.94 \pm 0.04$	$1.06 \pm 0.06$	$1.77 \pm 0.07$	+	+
2MASS J00452972+4237438	L2pec	M8 + L7?	$2.71 \pm 0.13$	$0.96 \pm 0.17$	$1.48 \pm 0.14$		
2MASS J01145788+4318561	M9		$2.44 \pm 0.11$	$0.64 \pm 0.03$	$1.06 \pm 0.04$		
2MASS J01194279+1122427	M8		$2.23 \pm 0.08$	$0.69 \pm 0.10$	$1.13 \pm 0.12$		
2MASS J01412651+1001339	L5		... <sup>a</sup>	$0.93 \pm 0.17$	$1.92 \pm 0.21$		
2MASS J01442482-0430031	L4		$2.86 \pm 0.16$	$1.07 \pm 0.20$	$1.79 \pm 0.19$		
2MASS J02314893+4521059	M9		$2.46 \pm 0.14$	$0.74 \pm 0.12$	$0.99 \pm 0.10$	–	–
2MASS J03302948+3910242	L7pec	red	... <sup>a</sup>	$1.25 \pm 0.20$	$2.06 \pm 0.16$	+	+
2MASS J03315828+4130486	M5		$1.79 \pm 0.15$	$0.74 \pm 0.21$	$1.09 \pm 0.26$		
2MASS J09240328+3653444	L2pec	L2 + T3?	... <sup>a</sup>	$0.79 \pm 0.20$	$1.39 \pm 0.24$	–	–
2MASS J10265851+2515262	L5pec	red	... <sup>a</sup>	$1.15 \pm 0.20$	$2.01 \pm 0.19$	+	+
2MASS J11060459-1907025	L5		$2.93 \pm 0.12$	$1.10 \pm 0.17$	$1.78 \pm 0.13$		
2MASS J12232570+0448277	L6		$2.86 \pm 0.05$	$1.09 \pm 0.11$	$1.74 \pm 0.13$		
2MASS J13064517+4548552	L9		$2.90 \pm 0.14$	$1.14 \pm 0.20$	$1.73 \pm 0.16$		
2MASS J14193789+3333326	L3		... <sup>a</sup>	$1.07 \pm 0.10$	$1.52 \pm 0.10$		
2MASS J17570962+4325139	L2		$2.77 \pm 0.08$	$0.93 \pm 0.21$	$1.57 \pm 0.13$		
2MASS J23004298+0200145	L2		$2.89 \pm 0.05$	$0.98 \pm 0.11$	$1.63 \pm 0.13$		
2MASS J23053808+0524070	L2		$2.74 \pm 0.08$	$0.95 \pm 0.14$	$1.58 \pm 0.10$		
General Ultra-cool Dwarf Candidates							
2MASS J00062250+1300451	L2		$2.71 \pm 0.06$	$0.95 \pm 0.12$	$1.53 \pm 0.18$		

Continued on Next Page...

Table 3.3 – Continued

2MASS ID (J2000)	IR SpT	Interpretation (from spectrum)	$z - J$ (mag)	$J - H$ (mag)	$J - K_s$ (mag)	$>1\sigma$ Colour Outlier	$>2\sigma$ Colour Outlier
2MASS J00435012+0928429	L2		2.83 ± 0.03	1.00 ± 0.15	1.59 ± 0.12		
2MASS J01001471-0301494	L1		2.64 ± 0.05	0.85 ± 0.12	1.45 ± 0.12		
2MASS J01343635-0145444	L0		2.56 ± 0.05	0.86 ± 0.10	1.40 ± 0.14		
2MASS J01352531+0205232	L9.5		2.81 ± 0.05	1.01 ± 0.10	1.58 ± 0.12		
2MASS J03511847-1149326	L2		2.68 ± 0.05	0.92 ± 0.09	1.54 ± 0.11		
2MASS J04234652-0803051	L0		2.33 ± 0.04	0.85 ± 0.09	1.45 ± 0.13		
2MASS J04510592+0014394	M9		2.57 ± 0.08	0.74 ± 0.17	1.25 ± 0.17		
2MASS J08270185+4129191	L1		2.67 ± 0.03	0.86 ± 0.10	1.39 ± 0.08		
2MASS J09083688+5526401	L1		2.71 ± 0.05	0.88 ± 0.13	1.46 ± 0.09		
2MASS J09481259+5300387	L2		2.71 ± 0.04	0.85 ± 0.07	1.37 ± 0.06		
2MASS J10551343+2504028	L2		2.68 ± 0.08	0.96 ± 0.11	1.61 ± 0.15		
2MASS J11213919-1053269	L1		2.77 ± 0.04	0.86 ± 0.09	1.44 ± 0.14		
2MASS J11282763+5934003	L0		2.48 ± 0.05	0.84 ± 0.16	1.38 ± 0.13		
2MASS J12260640+1756293	L2		... <sup>a</sup>	0.80 ± 0.19	1.41 ± 0.21		
2MASS J12492272+0310255	L2		2.74 ± 0.04	0.93 ± 0.12	1.54 ± 0.13		
2MASS J13264464+3627407	L2		2.56 ± 0.06	0.93 ± 0.10	1.52 ± 0.10		
2MASS J14154242+2635040	L0		2.68 ± 0.05	0.85 ± 0.15	1.43 ± 0.11		
2MASS J15025475+5044252	L2		... <sup>a</sup>	0.97 ± 0.13	1.50 ± 0.15		
2MASS J15202471+2208340	L1		... <sup>a</sup>	0.78 ± 0.17	1.36 ± 0.20		
2MASS J15552840+5918155	L4		... <sup>a</sup>	1.05 ± 0.10	1.72 ± 0.12		
2MASS J16123860+3126489	L2		2.64 ± 0.05	0.94 ± 0.16	1.54 ± 0.13		
2MASS J16194822-0425366	L1		... <sup>a</sup>	0.76 ± 0.14	1.23 ± 0.18		
2MASS J22545900-0330590	M9		2.41 ± 0.08	0.70 ± 0.16	1.17 ± 0.17		
False-positives							
2MASS J01581172+3232013	?		1.03 ± 0.04	0.50 ± 0.07	0.59 ± 0.05		
2MASS J02555058+1926476	?		... <sup>a</sup>	2.62 ± 0.10	3.69 ± 0.10		
2MASS J02553101+1929356	?		... <sup>a</sup>	1.66 ± 0.13	2.46 ± 0.12		
2MASS J04084337+5120524	?		3.49 ± 0.06	1.87 ± 0.04	3.13 ± 0.04		
2MASS J05484895+0014367	?		3.62 ± 0.06	1.95 ± 0.03	2.79 ± 0.03		

Continued on Next Page...

Table 3.3 – Continued

2MASS ID (J2000)	IR SpT	Interpretation (from spectrum)	$z - J$ (mag)	$J - H$ (mag)	$J - K_s$ (mag)	$>1\sigma$ Colour Outlier	$>2\sigma$ Colour Outlier
2MASS J05480405+0029264	?		$3.27 \pm 0.10$	$1.75 \pm 0.06$	$2.48 \pm 0.08$		
2MASS J05584262+2150121	?		$\dots^b$	$2.01 \pm 0.04$	$2.97 \pm 0.02$		
2MASS J06380876+0940084	?		$3.20 \pm 0.16$	$1.95 \pm 0.06$	$3.30 \pm 0.04$		
2MASS J06415196+0916111	?		$3.65 \pm 0.08$	$1.87 \pm 0.07$	$2.71 \pm 0.05$		
2MASS J09232257+5208598	?		$0.97 \pm 0.05$	$0.43 \pm 0.28$	$0.49 \pm 0.20$		
2MASS J16472470-0935294	?		$4.34 \pm 0.14$	$2.34 \pm 0.12$	$3.48 \pm 0.10$		
2MASS J16484099+2231397	?		$4.34 \pm 0.05$	$2.35 \pm 0.08$	$3.48 \pm 0.09$		

We identify colour outliers by comparing the synthetic  $J - K_s$  colour of each object to the median  $J - K_s$  colours of M7–M9 and T0–T8 dwarfs from Faherty et al., 2009 and for L0–L9 dwarfs from Faherty et al., 2013. The + and – signs indicate whether the object is above or below the average, respectively. The objects were divided into the different categories based on their photometric colours. The objects in the “Peculiarly Red and Candidate Binary” category passed both the peculiarly red and candidate L+T binary selection criteria.

<sup>a</sup> The spectra of these objects are from GNIRS. The GNIRS spectra do not cover the entire SDSS  $z$ -band so we are unable to calculate the  $z - J$  colours.

<sup>b</sup> The spectra of these objects are from Magellan/FIRE. The FIRE prism spectra do not cover the entire SDSS  $z$ -band so we are unable to calculate the  $z - J$  colours.

#### 3.4.1.1 2MASS J00133470+1109403 (L1)

This object is a young L1 dwarf. Compared to a normal L1.5 dwarf, 2M J0013+1109 has much weaker FeH and K I absorption lines and a triangular  $H$ -band (Fig. 3.8). The Allers et al., 2013 spectral indices say that this object is an INT-G object. This object is very similar to the L1  $\beta$  brown dwarf 2MASS J01174748–3403258 (Burgasser et al., 2008), however, it has even weaker K I absorption lines and a redder continuum. Based on these characteristics, 2M 0013+1109 likely has lower gravity than 2M 0117–3403 and so could potentially be a  $\sim 10$  Myr-old free-floating planetary-mass object.

However, according to BANYAN II (Gagné et al., 2014; Malo et al., 2013) and the Convergent Point tool (Rodriguez et al., 2013), 2M 0013+1109 does not have a likelihood of being a part of any of the young associations and moving groups used in those works. Instead, BANYAN II calculates a 98% probability of being part of the young field when using a young prior, and 60% probability of being part of the young field when no priors are set.

#### 3.4.1.2 2MASS J00440332+0228112 (L7)

This object is a young L7 brown dwarf based on weak K I and FeH absorption, stronger  $J$ -band absorption of H<sub>2</sub>O and a more triangular shaped  $H$ -band compared to the normal L7 dwarf 2MASS J0028208+224905 (Burgasser et al., 2010; Fig. 3.8). The gravity-sensitive features in the  $J$ -band and the shape of the  $H$ -band are similar to those in the young L7 dwarf 2MASSI J0103320+193536 (Cruz et al., 2004), although the observed spectrum is slightly redder than the comparison spectrum in Fig. 3.8. The only spectral index available for such a late spectra type from Allers et al., 2013 and Schneider et al., 2014 is the  $H$ -cont index which indicates a VL-G brown dwarf. However, as noted by Allers et al., 2013, very red L dwarfs with no youth signatures can also exhibit triangular  $H$ -band shapes. In this case we can only say that the spectral index is consistent with the result from the spectral comparison.

This object was also independently reported as a young L7 dwarf in Schneider et al., 2017. They determine that there is a high probability that it belongs to

the  $\beta$  Pictorus Moving Group according to BANYAN II (Gagné et al., 2014; Malo et al., 2013;  $\sim 78\%$ ) and the Convergent Point tool (Rodriguez et al., 2013;  $\sim 97\%$ ). They also report that based on its photometric distance ( $31 \pm 3$  pc), age ( $24 \pm 3$  Myr), and bolometric luminosity, it has a mass range of 7–11  $M_{Jup}$ .

#### 3.4.1.3 2MASS J03302948+3910242 (L7)

This object is a peculiarly red L7 dwarf. The spectrum of 2M 0330+3910 is similar to both L6 and L7 dwarfs in the  $J$ - and  $H$ -bands but the shape of the  $K$ -band is more similar to an L7 dwarf. The gravity-sensitive K I features are not weaker than that of a normal L7 object and the  $H$ -band does not have the characteristic triangular shape (Fig. 3.8) so this object is not young. This object more closely resembles the peculiarly red L6 brown dwarf 2MASS J21481633+4003594 (Kirkpatrick et al., 2010) even though 2M J0330+3910 is not as red. The  $J$ -band absorption features also do not quite match but that could be attributed to the difference in spectral type and the slope of the continuum. The spectral indices are also consistent with this object being a FLD-G object.

#### 3.4.1.4 2MASS J03530419+0418193 (L6)

Not only is this one of the reddest objects observed to date ( $z - J = 3.61 \pm 0.06$  mag;  $J - K_s = 2.58 \pm 0.11$  mag), it is also one of the reddest known objects that does not have any signatures of youth. The strength of the gravity-sensitive K I absorption lines are comparable to those of a peculiarly red L6 dwarf (Fig. 3.8). The  $H$ -band continuum also does not have the characteristic sharp triangular shape of a young object. The strength of the  $0.99\mu\text{m}$  FeH feature appears to be decreased, however, this could be a result of the extremely red continuum slope as it is more comparable to the FeH strength of the peculiarly red L6 object 2MASS J21481633+4003594 (Kirkpatrick et al., 2010). The strength of the other diagnostic absorption features and the shape of the  $H$ -band continuum are also consistent with those of the peculiarly red L6 dwarf. As with 2M J0044+0228, the only spectral index available for this object is the  $H$ -cont index so we cannot use spectral indices to help us determine surface gravity in this case.

Previously, the reddest observed object that had been confirmed with no signatures of youth was the L7 dwarf WISE J233527.07+451140.9, at  $J - K_s = 2.54 \pm 0.05$  mag (Liu et al., 2016). This object was discovered by Thompson et al., 2013 in a search for ultra-cool dwarf members of the solar neighbourhood using photometry from 2MASS and the WISE All-Sky Source Catalog. The late-L/early-T dwarf WISE J173859.27+614242.1 also has an extremely red colour (2MASS  $J - K_s = 2.55 \pm 0.16$  mag; Mace et al., 2013) which has been speculated to be caused from something other than youth but its spectral type and relative surface gravity are still not known.

#### 3.4.1.5 2MASS J10265851+2515262 (L5)

This object is a peculiarly red L5 dwarf. The GNIRS spectrum in Figure 3.8 has been smoothed to the same resolution as the SpeX spectra for more direct comparison. We note that the GNIRS spectrum has a low SNR ( $\sim 7-15$ ) so definitive determination of the absorption strengths cannot be attained. We can see, however, that the K I absorption lines appear to have the same or greater strength than those of the normal L5 comparison object and the peculiarly red L5 (2MASS J23512200+3010540; Kirkpatrick et al., 2010) and that the  $H$ -band doesn't appear to be triangular in shape (Fig. 3.8). Overall, the spectrum of 2M 1026+2515 is more similar to the red L5 dwarf. The Allers et al., 2013 indices say that this object is a FLD-G object but the low SNR makes this determination unreliable. However, this object is clearly red so together with the lack of reduced absorption strength of the gravity-sensitive features, the spectroscopic features point to this object being a peculiarly red L5 dwarf.

#### 3.4.1.6 2MASS J10524963+1858151 (L5)

This object is also a peculiarly red L5 dwarf. The GNIRS spectrum in Figure 3.8 has been smoothed to the same resolution as the SpeX spectra for more direct comparison. The spectral indices classify this object as an INT-G object most likely because of its very red colour, however, the comparison to other L5 objects is inconsistent with this classification. The K I and FeH absorption features are similar in strength to those of a normal L5 object and the peculiarly

red L5 2MASS J23512200+3010540 (Kirkpatrick et al., 2010). The  $H$ -band continuum also does not resemble that of a young object. We note that the GNIRS spectrum has relatively low signal-to-noise ( $\text{SNR} \sim 10\text{--}20$ ) which makes the index values highly uncertain.

#### 3.4.1.7 2MASS J14313545–0313117 (L6)

This object is an unusually blue L6 dwarf. The spectrum is much bluer than a normal L6 dwarf and the continuum slope is more similar to the blue L6 dwarf 2MASS J11181292–0856106 (Kirkpatrick et al., 2010; Fig. 3.8). However, the absorption features do not match 2M J1118–0856. In particular, the K I absorption features are extremely weak in 2M J1431–0313 and the  $2.3\mu\text{m}$   $\text{CH}_4$  feature is much less sharp. The FeH absorption is not noticeably stronger than that of a normal object as might be expected in a low-metallicity object. Kirkpatrick et al., 2010 discuss a category of objects in which 2M J1118–0856 may fall, that are potentially slightly metal-poor but not so much that they are categorized as subdwarfs. These objects do not show signs of significantly reduced metal content but have a higher transverse velocity than the field L dwarf population indicating that they are slightly older. We do not know the transverse velocity of 2M J1431–0313 but since its spectral characteristics are similar to those of 2M J1118–0856, we tentatively adopt the slightly metal-poor classification for this object as well.

#### 3.4.2 BROWN DWARFS WITH COMPOSITE SPECTRAL TYPES

Three of the objects show peculiarities that do not readily match those found in other individual objects. Instead, they more closely resemble combination spectra of L and T dwarfs. Burgasser, 2007 and Burgasser et al., 2010 developed a technique that enables one to infer the spectral types of the individual components of a candidate unresolved binary by a goodness-of-fit comparison to a library of spectral template combinations. We adopt this technique by creating combination templates from the set of single L and T dwarfs from the SpeX Prism Library. In P1 we created templates by using only the near-infrared stan-

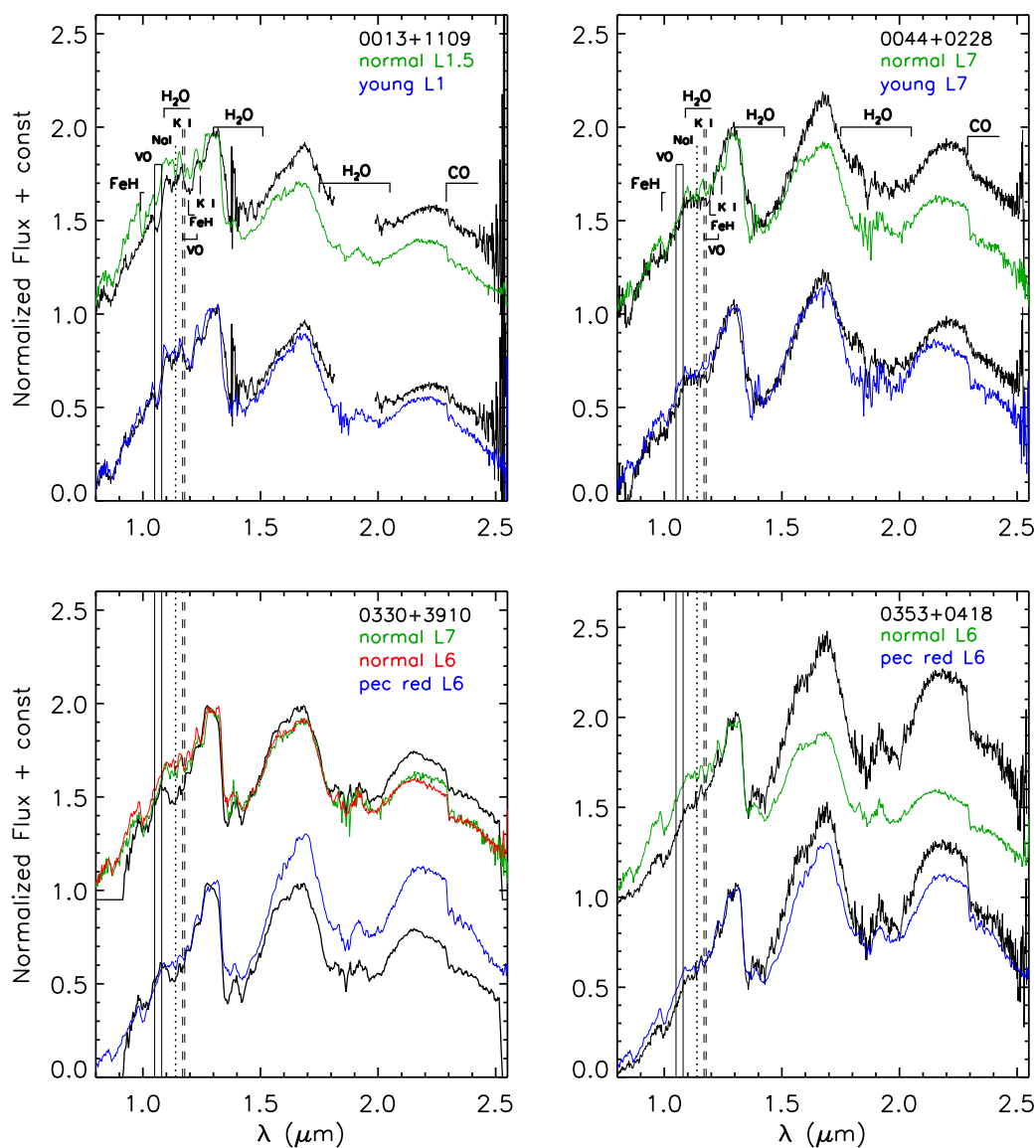


Figure 3.8: Spectra of the peculiar single objects identified in this work. The spectra are compared to spectra of both a normal object of the same spectral type and of a peculiar object of the nearest spectral type. The comparison spectra from left to right and top to bottom are: L1.5 (2MASS J07415784+0531568; Kirkpatrick et al., 2010) and young L1 (2MASS J0117474–340325; Burgasser et al., 2008); L7 (2MASS J0028208+224905; Burgasser et al., 2010) and young L7 (2MASS J0103320+193536; Cruz et al., 2004); L7 (2MASS J0028208+224905; Burgasser et al., 2010), L6 (2MASS J1010148–040649; Reid et al., 2006) and red L6 (2MASS J21481633+4003594; Kirkpatrick et al., 2010); L6 (2MASS J1010148–040649; Reid et al., 2006) and red L6 (2MASS J21481633+4003594; Kirkpatrick et al., 2010).

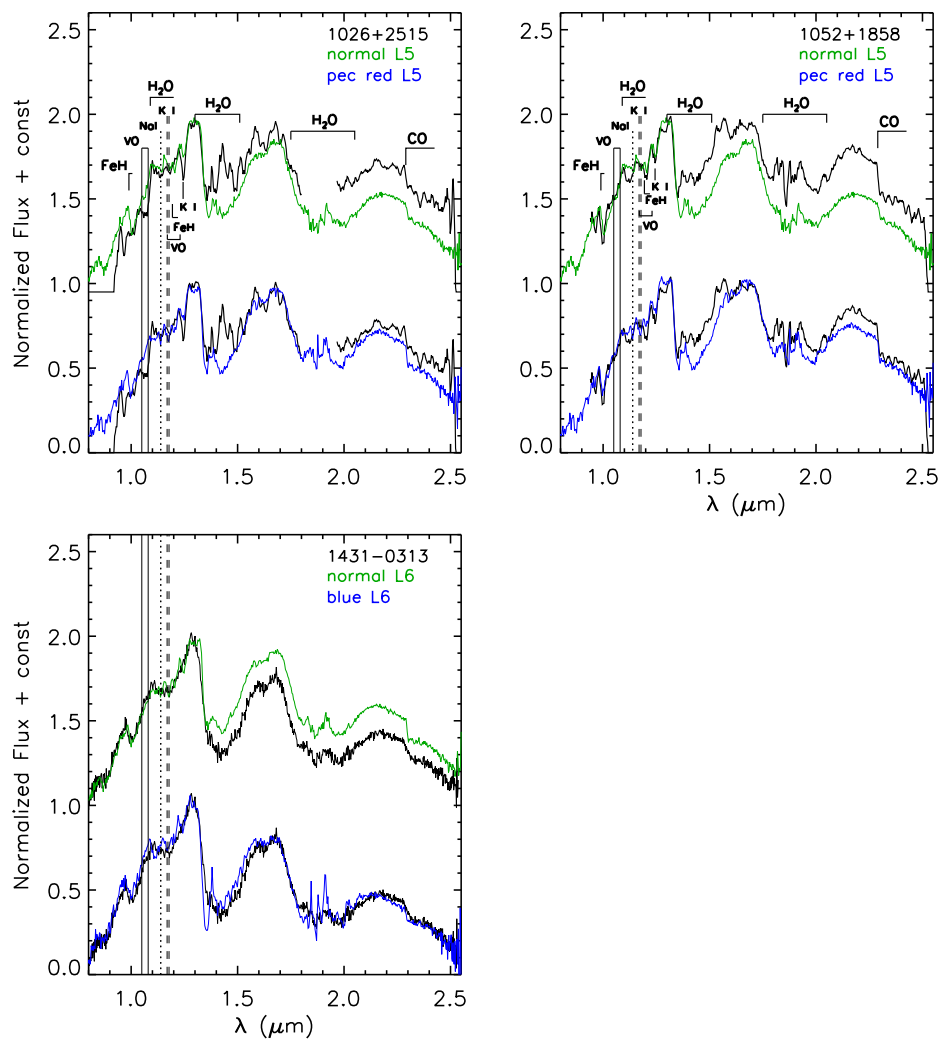


Figure 3.9: The comparison spectra from left to right and top to bottom are: L5 (2MASS J01550354+0950003; Burgasser et al., 2010) and red L5 (2MASS J23512200+3010540; Kirkpatrick et al., 2010); L5 (2MASS J01550354+0950003; Burgasser et al., 2010) and red L5 (2MASS J23512200+3010540; Kirkpatrick et al., 2010); L6 (2MASS J1010148-040640; Reid et al., 2006) and blue L6 (2MASS J11181292-0856106; Kirkpatrick et al., 2010).

dard objects. We have now expanded our templates to include objects from the entire SpeX Prism Library as done in Bardalez Gagliuffi et al., 2014.

We constructed our composite template spectra in the same way as P1 but we have now used the updated absolute spectral-type dependent magnitude polynomials given in Table 10 of Filippazzo et al., 2015. We classified an object as a likely spectral type composite — a potential unresolved binary — if the  $\chi^2$  (calculated over the entire 0.8–2.5  $\mu\text{m}$  region, minus the water absorption bands) of the dual-template spectral fit is significantly lower than the  $\chi^2$  of the single-template fit.

In addition to template fitting, where applicable, we analyzed the spectral indices defined specifically for SpeX prism spectra in Burgasser et al. (2010; for L+T binaries) and Bardalez Gagliuffi et al. (2014; for M+T and L+T binaries).

#### 3.4.2.1 2MASS J00132229–1143006 (T3.5+T4.5?)

While this object has a *J*-band spectrum consistent with that of a T3 dwarf (Fig. 3.10), it is better fit by a composite template of a T3.5 + T4.5 dwarf. However, this object could instead be a blue T3 dwarf as all the features are similar to those of the T3 dwarf except the blue colour. A third explanation is that this object is a variable T dwarf that displays two distinct temperature components. An example is 2MASS J21392676+0220226 which was originally thought to be a candidate L8.5+T3.5 unresolved binary (Burgasser et al., 2010) but was later identified as a high-amplitude variable (Radigan et al., 2012). This may also be the case with 2M J0013–1143. This object only satisfies two of the six binary index selection criteria from Table 5 of Burgasser et al., 2010. Overall because of the much better binary template fit, we treat 2M J0013–1143 as a likely unresolved binary but note that it can instead be a blue T3 dwarf.

#### 3.4.2.2 2MASS J00452972+4237438 (M8+L7?)

This object’s spectrum is quite unusual and is best fit by a composite template of an M8 and an L7 dwarf (Fig. 3.10). The overall spectral slope is quite red but there are none of the typical spectral features found in a normal ultra-cool dwarf. The spectrum appears to be more similar to a late M dwarf apart from

the red slope. However, it does not match any of the late M comparison spectra. The composite template in Figure 3.10 more closely matches the spectrum of 2M J0045+4237 but still does not reproduce all of the features. We note that in the raw data, the profile of the spectra appear to be double-peaked, indicating that this object may be resolvable at higher angular resolution or that there is a contaminating foreground or background object. We did not attempt to deconvolve the traces as the spectra are too blended in our data set. The spectra presented here have been extracted using a wider aperture than all the other objects to ensure we included all the flux from both components. More observations of this object are needed to reliably determine the presence of a binary companion.

#### 3.4.2.3 2MASS J09240328+3653444 (L2+T3)

This object is a likely unresolved binary with an L2 primary component and a T3 secondary component. Figure 3.10 shows that an L2 object fits the  $J$ -band of 2M J0924+3653 relatively well but fails to properly match the  $\text{CH}_4$  features in the  $H$ - and  $K$ -bands and the water feature between the  $Y$ - and  $J$ -bands. A composite template of an L2 and a T3 dwarf more closely matches the spectrum of this object. This object satisfies four of the twelve binary index selection criteria given in Table 4 of Bardalez Gagliuffi et al., 2014 making it a weak binary candidate, according to that classification scheme.

#### 3.4.3 NORMAL ULTRA-COOL DWARFS

We classify 80 of our candidates as normal L dwarfs, i.e., they do not have any readily apparent peculiarities based on their comparison to SpeX spectral standards. We also identified 14 candidates as normal M dwarfs. These were included in our program likely because the  $i-z$  and  $z-J$  colours of late-M dwarfs are close to the limits of our colour selection criteria (Section 3.2), and because they may have been subject to flux-overestimation bias at  $J$ -band (Section 3.3 of P1). The spectra of all these objects are included in Figure 3.2.

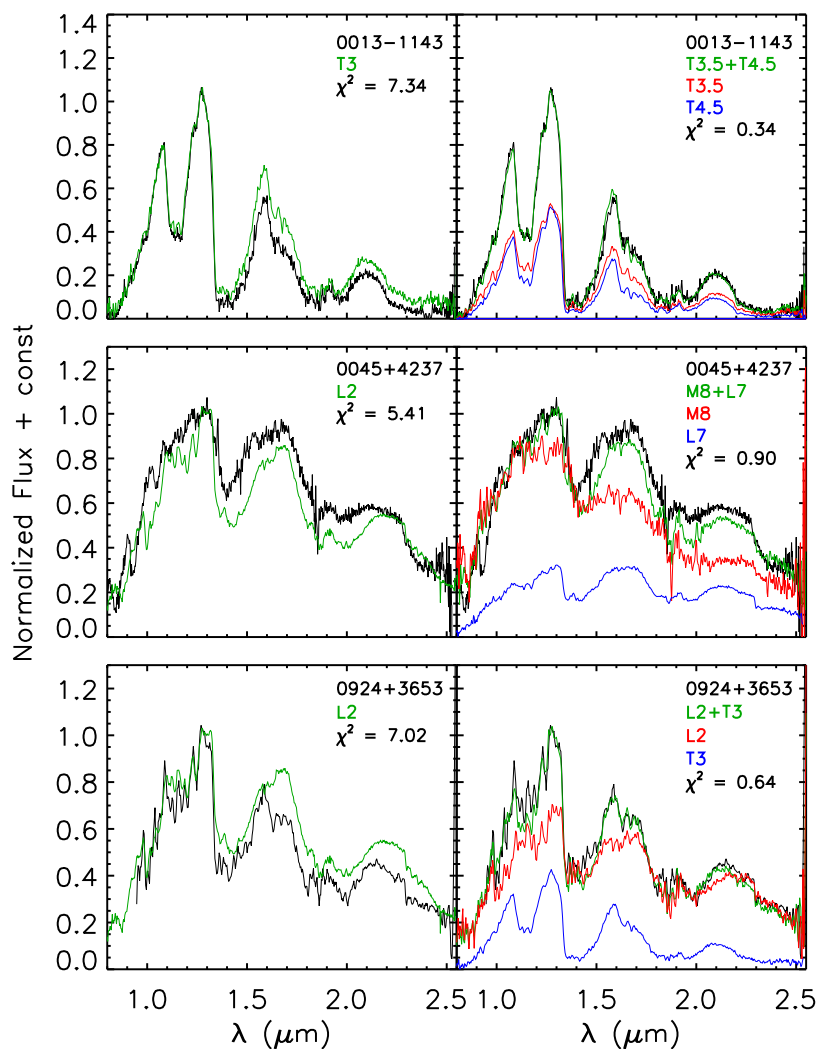


Figure 3.10: Spectra of all objects identified as candidate unresolved binaries. The left panels show comparisons to spectra (in green) that fit the 0.95-1.35  $\mu\text{m}$  continuum best. The right panels show two-component templates (also in green) that fit best over 0.8-2.5  $\mu\text{m}$ ; the individual component contributions are shown in red and blue and are scaled by their relative contributions. The quoted  $\chi^2$  values are the smallest ones for, respectively, single- and binary-template fits over the entire 0.8-2.5  $\mu\text{m}$  range. The comparison spectra from left to right and top to bottom are: T3 (2MASS J12095613-1004008; Burgasser, 2004), T3.5 (SDSSp J175032.96+175903.9; Burgasser, 2004) and T4.5 (2MASS J05591914-1404488; Burgasser et al., 2006a); L2 (2MASS J13054019-2541059; Burgasser, 2007), M8 (2MASS J02481204+2445141; Kirkpatrick et al., 2010) and L7 (SDSS J140023.12+433822.3; Burgasser et al., 2010); L2 (2MASS J13054019-2541059; Burgasser, 2007), L2 (2MASS J12304602+2827515; Sheppard et al., 2009) and T3 (2MASS J12095613-1004008; Burgasser, 2004).

#### 3.4.4 FALSE-POSITIVE ULTRA-COOL DWARFS

We identified 5 false-positives in P1 and 7 in the concluding portion of the survey presented here. The spectra of these objects were taken with SpeX, GNIRS and FIRE (see P1 for instrument set up and extraction details for the Magellan/FIRE data). The spectra are presented in Figure 3.11 and are grouped by spectral similarity. Their synthetic colours and photometric magnitudes are presented in Tables 3.3 and 3.4, respectively. As can be seen in Figure 3.11, the spectra of these objects do not appear to be those of ultra-cool dwarfs. The first two of these objects in Figure 3.11 look like they might be warmer stars and were most likely nearby stars that were targeted by mistake. We treat these objects as false-positives for the purpose of the survey statistics even though the candidates may indeed be ultra-cool dwarfs. All of the other objects have steep red slopes in the  $z$ - and  $J$ -bands, peak in the  $H$ -band, and are either relatively flat or taper off into the  $K$ -band. The  $z - J$  and  $J - K_s$  colours of these objects are similar to those of ultra-cool dwarfs and would have passed the selection criteria quite easily. We also notice a large discrepancy between the photometric and synthetic colours for these red objects (Tables 3.3 and 3.4). This suggests that the photometric magnitudes for these objects are not accurate. We believe that all of the latter objects are extragalactic in origin.

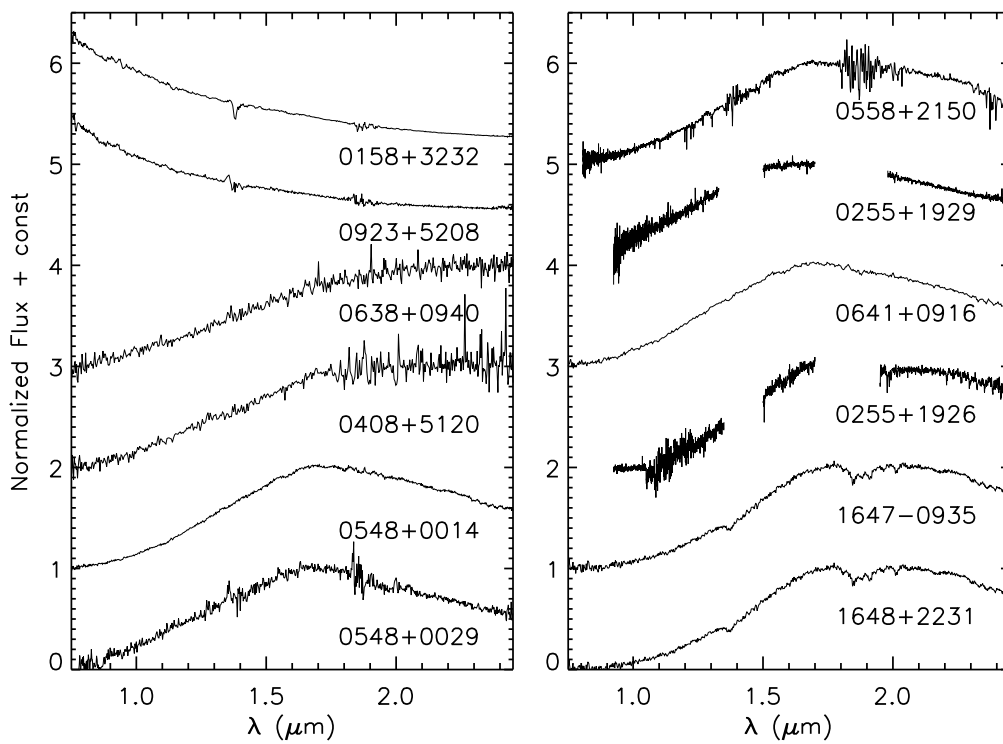


Figure 3.11: SpeX prism, GNIRS cross-dispersed and Magellan/FIRE prism spectra of the 12 unknown objects that mistakenly passed our candidate selection criteria.

Table 3.4: Unknown Object Photometry

2MASS ID (J2000)	Telescope/ Instrument	Survey <sup>a</sup> Portion	$z$ (mag)	$J$ (mag)	$H$ (mag)	$K_s$ (mag)	$W1$ (mag)	$W2$ (mag)
2MASS J01581172+3232013	IRTF/SpeX	P1	18.80 ± 0.04	16.04 ± 0.07	14.89 ± 0.07	14.16 ± 0.05	13.69 ± 0.03	13.39 ± 0.03
2MASS J02555058+1926476	Gemini/GNIRS	P2	20.03 ± 0.10	17.33 ± 0.10	16.42 ± 0.24	15.20 ± 0.15	14.93 ± 0.04	14.54 ± 0.05
2MASS J02553101+1929356	Gemini/GNIRS	P2	20.40 ± 0.16	17.48 ± 0.28	15.34 ± 0.09	14.44 ± 0.08	14.30 ± 0.03	13.91 ± 0.04
2MASS J04084337+5120524	IRTF/SpeX	P1	19.48 ± 0.06	16.65 ± 0.15	14.64 ± 0.04	13.42 ± 0.04	12.09 ± 0.02	11.10 ± 0.02
2MASS J05484895+0014367	IRTF/SpeX	P2	19.21 ± 0.06	15.84 ± 0.08	13.98 ± 0.03	13.17 ± 0.03	12.87 ± 0.03	12.60 ± 0.03
2MASS J05480405+0029264	IRTF/SpeX	P2	20.11 ± 0.10	16.61 ± 0.15	15.00 ± 0.06	14.40 ± 0.08	14.03 ± 0.03	13.73 ± 0.04
2MASS J05584262+2150121	Magellan/FIRE	P1	19.19 ± 0.05	15.80 ± 0.07	14.00 ± 0.04	13.07 ± 0.02	12.53 ± 0.02	12.30 ± 0.03
2MASS J06380876+0940084	IRTF/SpeX	P1	20.44 ± 0.16	16.93 ± 0.20	15.08 ± 0.06	13.62 ± 0.04	12.24 ± 0.02	11.27 ± 0.02
2MASS J06415196+0916111	IRTF/SpeX	P1	19.63 ± 0.08	16.00 ± 0.09	14.18 ± 0.07	13.29 ± 0.05	12.65 ± 0.02	12.35 ± 0.03
2MASS J09232257+5208598	IRTF/SpeX	P2	19.13 ± 0.05	16.51 ± 0.12	16.38 ± 0.28	15.55 ± 0.20	15.32 ± 0.04	15.00 ± 0.07
2MASS J16472470-0935294	IRTF/SpeX	P2	20.44 ± 0.14	17.45 ± 0.30	15.57 ± 0.12	14.80 ± 0.10	14.49 ± 0.03	14.32 ± 0.05
2MASS J16484099+2231397	IRTF/SpeX	P2	19.18 ± 0.05	16.26 ± 0.09	15.20 ± 0.08	14.54 ± 0.09	13.91 ± 0.03	13.48 ± 0.03

<sup>a</sup> We indicate in which portion of the survey these objects were identified: P1 — Kellogg et al., 2015, P2 — this work.

### 3.5 POPULATION STATISTICS

We have completed a survey to identify unusual brown dwarfs in the SDSS and 2MASS catalogs. In the first portion of the survey (P1) we identified 4 peculiar ultra-cool dwarfs, 5 candidate L+T binaries, 17 normal L dwarfs, 13 normal M dwarfs, and one T dwarf candidate binary. In the concluding portion of the survey presented here, we have identified 7 additional peculiar ultra-cool dwarfs, 1 candidate L+T binary, 1 candidate M+L binary, 80 normal L dwarfs, 14 normal M dwarfs, and one more T dwarf candidate binary. Table 3.3 summarizes the peculiarities of each object, as gleaned from analysis of their spectra. From the 144 new ultra-cool dwarfs discovered in the whole survey (including results from P1), we have identified 9 peculiarly red, 2 peculiarly blue, 7 candidate M+L and L+T dwarf binaries, two candidate T+T dwarf binaries, 97 normal L dwarfs, and 27 M dwarfs.

Our goal is to assess the relative population of peculiar L and T dwarfs with  $z - J > 2.5$  mag, therefore, we also include the 276 previously known objects that our selection criteria recovered and use the classifications reported in the literature. There were additional ultra-cool dwarfs from SDSS reported in the J. Gagné database<sup>†</sup> that did not pass our full set of selection criteria outlined in P1. Namely, these were objects detected in the shorter-wavelength bands (i.e.  $r < 23$  mag), had  $z - J$  colours  $< 2.5$  mag, or had  $H - W2$  colours  $< 1.2$  mag — all typically L0 dwarfs. From the sample of previously known objects that we recovered, there are 8 unusually red objects, 5 unusually blue objects, and 21 candidate binary objects. There are also 186 normal L, 51 normal T, and 5 normal M dwarfs. All recovered objects are shown in Figure 3.12. In this figure, we distinguish between late- and early-type objects where late-L type objects are  $\geq L7$  and late-T objects are  $\geq T6$ . We also differentiate between binaries in which both components are L or T objects and binaries that have one component of each type. A summary of the types of objects found in our entire survey is presented in Table 3.5. Assessing the relative occurrence rates of the various peculiarities in our full sample of 420 ultra-cool dwarfs (144 new and 276 recov-

---

<sup>†</sup><https://jgagneastro.wordpress.com/list-of-ultracool-dwarfs/>

ered) allows us to ascertain timescales of the associated phenomena.

Table 3.5: Summary of Object Types

Type	New	Recovered	Total
M	27	5	32
L0–L6	84	163	247
L7–L9	9	23	32
T0–T5	0	38	38
T6–T9	0	13	13
Young L	4	5	9
Red L	5	3	8
Blue L	2	5	7
L+L binary	0	3	3
T+T binary	2	7	9
L+T binary	6	11	17
M+L binary	1	0	1
Total	144	276	420

### 3.5.1 EFFICACY OF THE SURVEY

We had a false positive rate of 11% from the first portion of our survey (5 unknown objects out of 45 total candidates). We refined our visual selection for the second portion based on these false positives and reduced our rate to 6.2% (7 unknown objects out of 113 total remaining candidates). We exclude these objects when discussing the statistics of our full survey and only consider the 144 confirmed new and 276 previously known ultra-cool dwarfs.

From the total 420 objects that our colour criteria selected and that we confirmed to be ultra-cool dwarfs, 17 (4.0%) are peculiarly red, 7 (1.7%) are peculiarly blue and 30 (7.1%) are candidate binaries. The number of peculiarly red objects in our sample is statistically equivalent with that of the 4.6% of red objects found in an unbiased sample of L and T dwarfs from Faherty et al., 2009. Our peculiarly red selection criterion, however, identified 9 new red objects among the sample of 92 candidates (9.8%). None are peculiarly red out of the 31 general ultra-cool dwarf candidate sample so our selection technique successfully identified all of the peculiarly red objects in the sample. Including the previously known ultra-cool dwarfs, 6.2% of objects were red among the sample

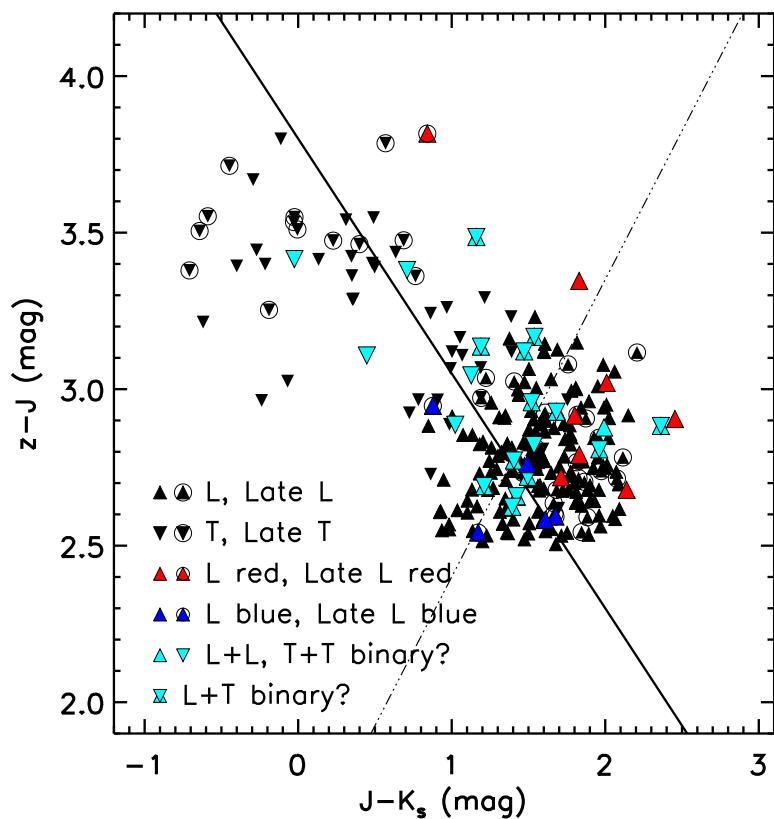


Figure 3.12: colour-colour diagram of all known L and T dwarfs recovered in our SDSS-2MASS-WISE cross-match. All symbols (upwards triangles - L dwarfs; downwards triangle - T dwarf) represent the photometric colours of the objects. The black symbols are “normal” objects and the red and blue symbols are objects that have been identified as peculiar or binary. Late-L ( $\geq L7$ ) and Late-T ( $\geq T6$ ) dwarfs are denoted with circles. Our selection criteria from §3.2 are denoted by the solid and dashed lines.

of objects that satisfied the peculiarly red criterion (17 of 274).

We had a better success rate for objects that satisfied the candidate binary criterion. Of the 51 new binary candidates, 10 (20%) were either peculiarly blue (2) or are potential binaries (8). Including the previously known ultra-cool dwarfs, 13% were unusually blue (3) or candidate binaries (20) among the sample of objects that satisfied the candidate binary criterion (173).

When we compare our newly discovered peculiarly red brown dwarfs (9) to the number of red L and T dwarfs that were already known and were recovered with our selection criterion (8), we see that we increased the sample in this colour space by a factor of 2. Similarly, we see that we increased the sample of candidate binaries by a factor of 1.4. With only 2 new unusually blue discoveries, we did not significantly impact the statistics of these types of objects. This is unsurprising as we were not targeting these objects.

We also did not uncover many L+L or T+T binaries. Binaries where both components have similar spectral morphologies are harder to discern from single low to moderate resolution spectra so are more difficult to identify. An example of this is the planetary-mass object, 2MASS J11193254–1137466, that we discovered in the first portion of the survey (L7; P1) that was later resolved into a binary system (L7+L7; Best et al., 2017b). We identified this object as peculiar based on its extremely red near-infrared colours and weak alkali absorption features but did not suspect unresolved binarity from our spectra.

### 3.5.2 UNUSUALLY RED OBJECTS

Among the 17 unusually red objects from the whole survey of 420 ultra-cool dwarfs, 9 (2.1%) are young and 8 (1.9%) are red with no signatures of youth. The  $\sim 2\%$  fraction of low-gravity ultra-cool L dwarfs is consistent with a  $\lesssim 200$  Myr age for these objects under the assumption of a constant star-formation history for the Milky Way (e.g. Burrows et al., 1993; Marley et al., 1996). This is also consistent with evolutionary models such as those in Burrows et al., 2001 and Baraffe et al., 2015 that say the radii of ultra-cool dwarfs becomes constant after  $\sim 200$  Myr and studies of objects in young stellar associations such as Allers et al., 2013 and Liu et al., 2016 which show that associations older than

$\sim 200$  Myr have a much smaller fraction of objects that show signatures of youth than younger associations.

For the 1.9% of objects that are unusually red with no signatures of youth, there has thus far not been a satisfactory explanation of their redness. We suggest that these objects may have reached a point where their surface gravities are not low enough to have distinguishing alkali line strengths from field objects in low resolution spectra, but are still young enough that their dust has not completely settled. This dust could be the sub-micron particles that potentially play a significant role in the reddening of ultra-cool dwarf spectra and settle less efficiently than the 1-100  $\mu\text{m}$  grains (Hiranaka et al., 2016). If this is the case, then the peculiarly red colour that is detectable in their optical to near-infrared SEDs is a better indicator of moderate youth than individual absorption features. Another possible explanation is that these objects were formed in environments with higher metallicity. If this is the case, then  $\sim 2\%$  of objects within the sensitivity limit of the SDSS, 2MASS and WISE surveys were born in these conditions.

Kirkpatrick et al., 2010 offer a further speculation on the nature of these unusually red objects. They find that the space velocities of these objects are similar to those of unusually blue L dwarfs that do not have any signatures of low-metallicity. They suggest that these two kinds of objects could be related and their spectral appearance could be the result of different viewing angles. If clouds are not homogeneously distributed in latitude or if cloud properties such as grain size and thickness vary in latitude, then viewing an object pole-on versus equator-on would change the spectral morphology. However, if this were the case, then we would expect the number of objects with these properties to be higher because such conditions would be ubiquitous for all brown dwarfs.

### 3.5.3 CANDIDATE BINARIES

Our binary selection criterion was designed to identify L+T binaries. In these objects, both components contribute equally to the flux in the  $J$ -band but unequally in the  $z$ - and  $K$ -bands, making the  $z - J$  colours red and the  $J - K_s$  colours blue. We identified and recovered 30 objects that are candidate binaries

out of the 420 objects in the full survey, 17 of which are binaries with one L and one T component. We did not find any new L+L binary candidates and only two new T+T binary candidates: likely because they are difficult to identify even from their spectra as the two components would be more similar in spectral morphology than the components in an L+T binary. These objects would look more like single objects and could only be identified as binaries through other means.

Our survey also recovered 51 known single T dwarfs and 9 candidate T+T binaries, 2 of which were new. These represent the entire population of T dwarfs in SDSS. The vast majority were already known from previous searches for T dwarfs in SDSS. Both of the newly discovered objects we categorized as candidate binaries, although they could also be highly variable T dwarfs.

#### 3.5.4 WISE COLOURS

As done in P1, we investigated whether the  $J - K_s$  colour outliers also have unusual colours in the  $W1$  and  $W2$  WISE bands. We have compared the objects that we discovered in this survey to known ultra-cool dwarfs in the AllWISE catalog published in Kirkpatrick et al., 2011. We determined the red and blue outliers from this data set using the median  $J - K_s$  colours and standard deviations for each spectral type from Faherty et al., 2009 and Faherty et al., 2013. We confirm the results of P1 that L dwarfs with the very reddest  $J - K_s$  colours are clearly distinguishable from the locus of L dwarfs on a  $J - K_s$  vs.  $H - W2$  and  $J - K_s$  vs.  $W1 - W2$  diagram (Fig. 3.13) mainly because of their red  $J - K_s$  colours. T dwarfs with peculiarly red  $J - K_s$  colours are slightly redder in both  $H - W2$  and  $W1 - W2$ , and the peculiarly blue L or T dwarfs and candidate binaries are not distinguishable from the normal population.

### 3.6 CONCLUSIONS

We have completed a survey to identify ultra-cool dwarfs with peculiar photometric colours in the SDSS, 2MASS and WISE catalogs. In the concluding portion of our survey, we have found two new candidate very low-gravity, planetary-

mass objects: 2MASS J00133470+1109403 (L1) and 2MASS J00440332+0228112 (L7). The latter was independently found to be a planetary-mass object with a high probability of  $\beta$  Pic membership (Schneider et al., 2017). Our survey also identified one of the reddest objects with no signatures of youth known to date: the L6 dwarf 2MASS J03530419+0418193. A detailed study of this object may give clues as to the nature of its extreme red colour as no satisfactory answer has been found to explain such objects so far.

With spectroscopic observations of the candidates from the first portion of the survey (P1) and from this work, we confirmed that 20 of our new 144 ultra-cool dwarfs are unusually red, unusually blue, or are candidate binaries. Including the 276 previously known objects that we recovered with our selection criteria and the 144 objects discovered in this survey (420 objects total), 4.0% (17) are unusually red, 1.7% (7) are unusually blue and 7.1% (30) are candidate binaries. We find that there are roughly as many L+T binaries in our sample as binaries of any other kind combined, likely because L+L or T+T binaries would be difficult to identify from low to moderate resolution spectra alone.

We also find that there are almost equal numbers of red L dwarfs that are young based on weak potassium absorption strengths (2.1%, 9/420) and red L dwarfs with normal potassium absorption (1.9%, 8/420). The first population are likely younger than 200 Myr: the approximate age where contraction mostly halts in  $\gtrsim 13 M_{\text{Jup}}$  brown dwarfs. The latter population may be only slightly older — by up to a factor of 2 — or may alternatively be more metal-rich.

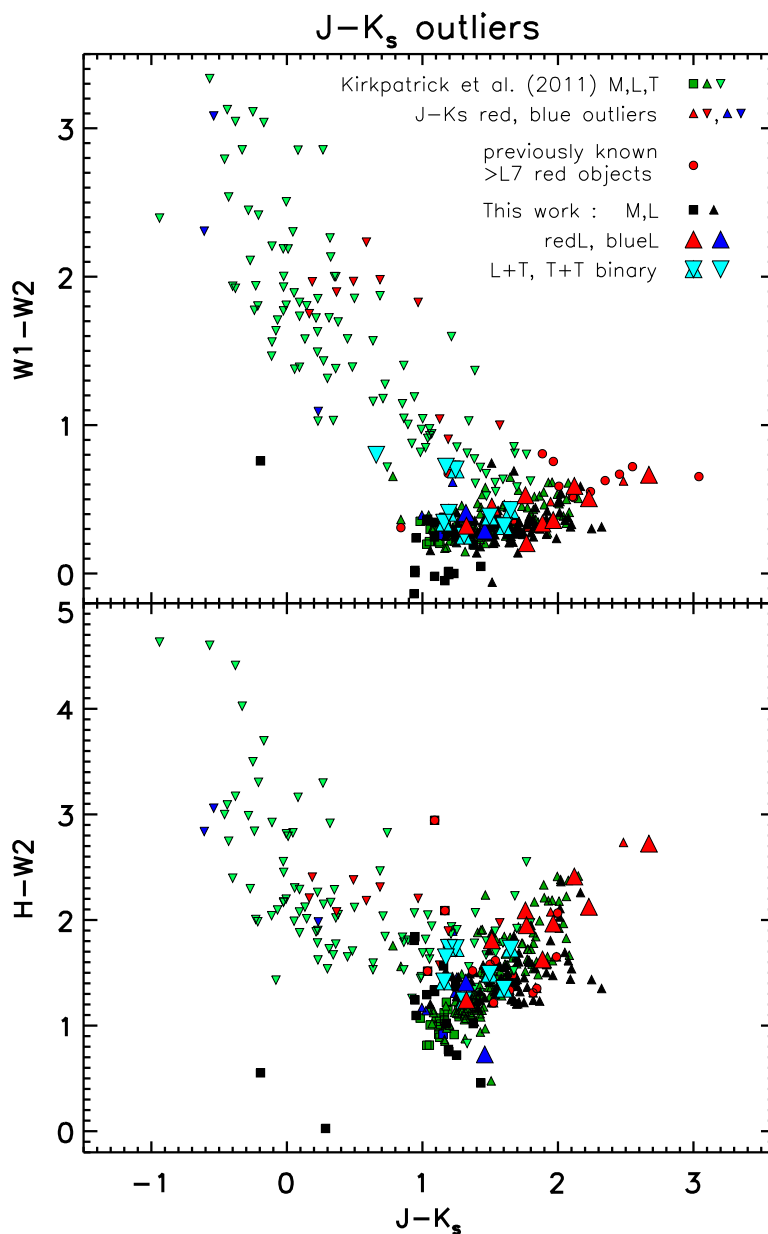


Figure 3.13: Photometric colour-colour diagrams of objects from Kirkpatrick et al., 2011. Upwards and downwards triangles denote L and T dwarfs, respectively. Red symbols denote objects with  $J - K_s$  colours  $>2\sigma$  redder than the mean for their spectral type Faherty et al., 2009, 2013. Blue symbols denote objects that are  $>2\sigma$  bluer. Large symbols represent peculiar objects identified in this work and normal symbols represent the normal objects. Red circles indicate other previously known red ultra-cool dwarfs not in Kirkpatrick et al., 2011 with spectral types of L7 and later.

## REFERENCES

- Ackerman, A. S. and Marley, M. S. (2001). *ApJ* 556, pp. 872–884. DOI: [10 . 1086/321540](https://doi.org/10.1086/321540).
- Allers, K. N., Jaffe, D. T., Luhman, K. L., et al. (2007). *ApJ* 657, pp. 511–520. DOI: [10.1086/510845](https://doi.org/10.1086/510845).
- Allers, K. N. and Liu, M. C. (2013). *ApJ* 772, 79, p. 79. DOI: [10 . 1088/0004-637X/772/2/79](https://doi.org/10.1088/0004-637X/772/2/79).
- Apai, D., Radigan, J., Buenzli, E., et al. (2013). *ApJ* 768, 121, p. 121. DOI: [10 . 1088/0004-637X/768/2/121](https://doi.org/10.1088/0004-637X/768/2/121).
- Baraffe, I., Homeier, D., Allard, F., et al. (2015). *A&A* 577, A42, A42. DOI: [10 . 1051/0004-6361/201425481](https://doi.org/10.1051/0004-6361/201425481).
- Bardalez Gagliuffi, D. C., Burgasser, A. J., Gelino, C. R., et al. (2014). *ApJ* 794, 143, p. 143. DOI: [10.1088/0004-637X/794/2/143](https://doi.org/10.1088/0004-637X/794/2/143).
- Best, W. M. J., Magnier, E. A., Liu, M. C., et al. (2017a). *ArXiv e-prints*.
- Best, W. M. J., Liu, M. C., Dupuy, T. J., et al. (2017b). *ArXiv e-prints*.
- Burgasser, A. J. (2002). PhD thesis. California Institute of Technology.
- (2004). *ApJS* 155, pp. 191–207. DOI: [10.1086/424386](https://doi.org/10.1086/424386).
- (2007). *ApJ* 659, pp. 655–674.
- Burgasser, A. J., Marley, M. S., Ackerman, A. S., et al. (2002). *ApJ* 571, pp. L151–L154. DOI: [10.1086/341343](https://doi.org/10.1086/341343).
- Burgasser, A. J., Geballe, T. R., Leggett, S. K., et al. (2006a). *ApJ* 637, pp. 1067–1093. DOI: [10.1086/498563](https://doi.org/10.1086/498563).
- Burgasser, A. J. and McElwain, M. W. (2006b). *AJ* 131, pp. 1007–1014. DOI: [10.1086/499042](https://doi.org/10.1086/499042).
- Burgasser, A. J.,Looper, D. L., Kirkpatrick, J. D., et al. (2007). *ApJ* 658, pp. 557–568. DOI: [10.1086/511518](https://doi.org/10.1086/511518).
- Burgasser, A. J., Liu, M. C., Ireland, M. J., et al. (2008). *ApJ* 681, pp. 579–593. DOI: [10.1086/588379](https://doi.org/10.1086/588379).
- Burgasser, A. J., Cruz, K. L., Cushing, M., et al. (2010). *ApJ* 710, pp. 1142–1169. DOI: [10.1088/0004-637X/710/2/1142](https://doi.org/10.1088/0004-637X/710/2/1142).

- Burrows, A., Hubbard, W. B., Saumon, D., et al. (1993). *ApJ* 406, pp. 158–171. DOI: [10.1086/172427](https://doi.org/10.1086/172427).
- Burrows, A., Hubbard, W. B., Lunine, J. I., et al. (2001). *Reviews of Modern Physics* 73, pp. 719–765. DOI: [10.1103/RevModPhys.73.719](https://doi.org/10.1103/RevModPhys.73.719).
- Burrows, A., Sudarsky, D., and Hubeny, I. (2006). *ApJ* 640, pp. 1063–1077. DOI: [10.1086/500293](https://doi.org/10.1086/500293).
- Canty, J. I., Lucas, P. W., Roche, P. F., et al. (2013). *MNRAS* 435, pp. 2650–2664. DOI: [10.1093/mnras/stt1477](https://doi.org/10.1093/mnras/stt1477).
- Chiu, K., Fan, X., Leggett, S. K., et al. (2006). *AJ* 131, pp. 2722–2736. DOI: [10.1086/501431](https://doi.org/10.1086/501431).
- Cooke, A. and Rodgers, B. (2005). *Astronomical Data Analysis Software and Systems XIV*. Ed. by P. Shopbell, M. Britton, and R. Ebert. Vol. 347. Astronomical Society of the Pacific Conference Series, p. 514.
- Cruz, K. L., Burgasser, A. J., Reid, I. N., et al. (2004). *ApJ* 604, pp. L61–L64. DOI: [10.1086/383415](https://doi.org/10.1086/383415).
- Cruz, K. L., Kirkpatrick, J. D., and Burgasser, A. J. (2009). *AJ* 137, pp. 3345–3357. DOI: [10.1088/0004-6256/137/2/3345](https://doi.org/10.1088/0004-6256/137/2/3345).
- Elias, J. H., Joyce, R. R., Liang, M., et al. (2006). *Society of Photo-Optical Instrumentation Engineers (SPIE) Conference Series*. Vol. 6269. Proc. SPIE, p. 62694C. DOI: [10.1117/12.671817](https://doi.org/10.1117/12.671817).
- Faherty, J. K., Burgasser, A. J., Cruz, K. L., et al. (2009). *AJ* 137, pp. 1–18. DOI: [10.1088/0004-6256/137/1/1](https://doi.org/10.1088/0004-6256/137/1/1).
- Faherty, J. K., Burgasser, A. J., Walter, F. M., et al. (2012). *ApJ* 752, 56, p. 56. DOI: [10.1088/0004-637X/752/1/56](https://doi.org/10.1088/0004-637X/752/1/56).
- Faherty, J. K., Rice, E. L., Cruz, K. L., et al. (2013). *AJ* 145, 2, p. 2. DOI: [10.1088/0004-6256/145/1/2](https://doi.org/10.1088/0004-6256/145/1/2).
- Faherty, J. K., Riedel, A. R., Cruz, K. L., et al. (2016). *ApJS* 225, 10, p. 10. DOI: [10.3847/0067-0049/225/1/10](https://doi.org/10.3847/0067-0049/225/1/10).
- Filippazzo, J. C., Rice, E. L., Faherty, J., et al. (2015). *ApJ* 810, 158, p. 158. DOI: [10.1088/0004-637X/810/2/158](https://doi.org/10.1088/0004-637X/810/2/158).
- Gagné, J., Lafrenière, D., Doyon, R., et al. (2014). *ApJ* 783, 121, p. 121. DOI: [10.1088/0004-637X/783/2/121](https://doi.org/10.1088/0004-637X/783/2/121).

- Golimowski, D. A., Leggett, S. K., Marley, M. S., et al. (2004). *AJ* 127, pp. 3516–3536. DOI: [10.1086/420709](https://doi.org/10.1086/420709).
- Gorlova, N. I., Meyer, M. R., Rieke, G. H., et al. (2003). *ApJ* 593, pp. 1074–1092. DOI: [10.1086/376730](https://doi.org/10.1086/376730).
- Hiranaka, K., Cruz, K. L., Douglas, S. T., et al. (2016). *ApJ* 830, 96, p. 96. DOI: [10.3847/0004-637X/830/2/96](https://doi.org/10.3847/0004-637X/830/2/96).
- Kellogg, K., Metchev, S., Geißler, K., et al. (2015). *AJ* 150, 182, p. 182. DOI: [10.1088/0004-6256/150/6/182](https://doi.org/10.1088/0004-6256/150/6/182).
- Kellogg, K., Metchev, S., Gagné, J., et al. (2016). *ApJ* 821, L15, p. L15. DOI: [10.3847/2041-8205/821/1/L15](https://doi.org/10.3847/2041-8205/821/1/L15).
- Kirkpatrick, J. D. (2005). *ARA&A* 43, pp. 195–245.
- Kirkpatrick, J. D., Reid, I. N., Liebert, J., et al. (2000). *AJ* 120, pp. 447–472. DOI: [10.1086/301427](https://doi.org/10.1086/301427).
- Kirkpatrick, J. D., Looper, D. L., Burgasser, A. J., et al. (2010). *ApJS* 190, pp. 100–146. DOI: [10.1088/0067-0049/190/1/100](https://doi.org/10.1088/0067-0049/190/1/100).
- Kirkpatrick, J. D., Cushing, M. C., Gelino, C. R., et al. (2011). *ApJS* 197, 19, p. 19. DOI: [10.1088/0067-0049/197/2/19](https://doi.org/10.1088/0067-0049/197/2/19).
- Knapp, G. R., Leggett, S. K., Fan, X., et al. (2004). *AJ* 127, pp. 3553–3578. DOI: [10.1086/420707](https://doi.org/10.1086/420707).
- Liu, M. C., Leggett, S. K., Golimowski, D. A., et al. (2006). *ApJ* 647, pp. 1393–1404. DOI: [10.1086/505561](https://doi.org/10.1086/505561).
- Liu, M. C., Dupuy, T. J., and Allers, K. N. (2016). *ApJ* 833, 96, p. 96. DOI: [10.3847/1538-4357/833/1/96](https://doi.org/10.3847/1538-4357/833/1/96).
- Lodieu, N., Hambly, N. C., Jameson, R. F., et al. (2008). *MNRAS* 383, pp. 1385–1396. DOI: [10.1111/j.1365-2966.2007.12676.x](https://doi.org/10.1111/j.1365-2966.2007.12676.x).
- Looper, D. L., Kirkpatrick, J. D., Cutri, R. M., et al. (2008). *ApJ* 686, pp. 528–541. DOI: [10.1086/591025](https://doi.org/10.1086/591025).
- Lucas, P. W., Roche, P. F., Allard, F., et al. (2001). *MNRAS* 326, pp. 695–721. DOI: [10.1046/j.1365-8711.2001.04666.x](https://doi.org/10.1046/j.1365-8711.2001.04666.x).
- Mace, G. N., Kirkpatrick, J. D., Cushing, M. C., et al. (2013). *ApJ* 777, 36, p. 36. DOI: [10.1088/0004-637X/777/1/36](https://doi.org/10.1088/0004-637X/777/1/36).

- Malo, L., Doyon, R., Lafrenière, D., et al. (2013). *ApJ* 762, 88, p. 88. DOI: [10.1088/0004-637X/762/2/88](https://doi.org/10.1088/0004-637X/762/2/88).
- Marley, M. S., Saumon, D., Guillot, T., et al. (1996). *Science* 272, pp. 1919–1921. DOI: [10.1126/science.272.5270.1919](https://doi.org/10.1126/science.272.5270.1919).
- Marley, M. S., Seager, S., Saumon, D., et al. (2002). *ApJ* 568, pp. 335–342. DOI: [10.1086/338800](https://doi.org/10.1086/338800).
- McGovern, M. R., Kirkpatrick, J. D., McLean, I. S., et al. (2004). *ApJ* 600, pp. 1020–1024. DOI: [10.1086/379849](https://doi.org/10.1086/379849).
- Radigan, J., Jayawardhana, R., Lafrenière, D., et al. (2012). *ApJ* 750, 105, p. 105. DOI: [10.1088/0004-637X/750/2/105](https://doi.org/10.1088/0004-637X/750/2/105).
- Rayner, J. T., Toomey, D. W., Onaka, P. M., et al. (2003). *PASP* 115, pp. 362–382. DOI: [10.1086/367745](https://doi.org/10.1086/367745).
- Reid, I. N., Lewitus, E., Burgasser, A. J., et al. (2006). *ApJ* 639, pp. 1114–1119. DOI: [10.1086/499484](https://doi.org/10.1086/499484).
- Rice, E. L., Barman, T., Mclean, I. S., et al. (2010). *ApJS* 186, pp. 63–84. DOI: [10.1088/0067-0049/186/1/63](https://doi.org/10.1088/0067-0049/186/1/63).
- Rodriguez, D. R., Zuckerman, B., Kastner, J. H., et al. (2013). *ApJ* 774, 101, p. 101. DOI: [10.1088/0004-637X/774/2/101](https://doi.org/10.1088/0004-637X/774/2/101).
- Schneider, A. C., Cushing, M. C., Kirkpatrick, J. D., et al. (2014). *AJ* 147, 34, p. 34. DOI: [10.1088/0004-6256/147/2/34](https://doi.org/10.1088/0004-6256/147/2/34).
- Schneider, A. C., Windsor, J., Cushing, M. C., et al. (2017). *ArXiv e-prints*.
- Sheppard, S. S. and Cushing, M. C. (2009). *AJ* 137, pp. 304–314. DOI: [10.1088/0004-6256/137/1/304](https://doi.org/10.1088/0004-6256/137/1/304).
- Thompson, M. A., Kirkpatrick, J. D., Mace, G. N., et al. (2013). *PASP* 125, p. 809. DOI: [10.1086/671426](https://doi.org/10.1086/671426).
- Tsuji, T. (2002). *ApJ* 575, pp. 264–290.

# 4

## The Nearest Isolated Member of the TW Hydrae Association is a Giant Planet Analog

### 4.1 INTRODUCTION

Young brown dwarfs, especially at the latest spectral types, have masses and atmospheres similar to those of directly imaged gas giant exoplanets. Isolated young brown dwarfs offer a way to study cool, low-pressure atmospheres of exoplanets without the inherent difficulties of isolating the planet flux from that of a brighter host star. Most of the known isolated planetary-mass brown dwarfs have been found through their unusually red optical and near-infrared colours, often in the regions of young stellar associations (e.g., [Aller et al., 2013](#); [Liu et al., 2013](#); [Luhman et al., 2005](#); [Marsh et al., 2010](#); [Schneider et al., 2014](#)). Over the past few years, targeted searches have also encompassed the position-velocity phase spaces of nearby young stellar associations (e.g., [Gagné et al., 2015a,b](#); [Gagné et al., 2014a](#)), most notably with the Bayesian Analysis for

---

A version of this chapter has been published ([Kellogg et al., 2016](#)).

Nearby Young AssociatioNs (BANYAN) tool (Malo et al., 2013). These have helped recognize or discover the lowest-mass isolated brown dwarfs in the solar neighbourhood (Delorme et al., 2012; Gagné et al., 2014b, 2015; Liu et al., 2013).

In Kellogg et al., 2015 we conducted a comprehensive program to purposefully seek L and T dwarfs with unusual optical/infrared colours in the combined set of SDSS, 2MASS, and WISE data. We did not impose positional or space velocity constraints, in order to obtain an unbiased assessment of ultra-cool dwarfs with peculiar spectral energy distributions (SEDs). One of the newly discovered objects was the extremely red ( $J - K_s = 2.58 \pm 0.03$  mag) L7 candidate low-gravity dwarf 2MASS J11193254–1137466 (henceforth, 2MASS J1119–1137). At  $K_s = 14.75 \pm 0.01$  mag in the VISTA Hemisphere Survey (VHS; PI McMahon, Cambridge, UK), a confirmation of its youth would place it among the brightest isolated planetary-mass objects, making it exceptionally suitable for investigating exoplanetary atmospheres in detail.

Herein we report the spectroscopic confirmation of the low surface gravity of 2MASS J1119–1137, its kinematic association with the TW Hydrae association (TWA; Webb et al., 1999), and hence its planetary mass.

## 4.2 OBSERVATIONS AND DATA REDUCTION

To confirm the youth of 2MASS J1119–1137, we obtained low-resolution spectra with FLAMINGOS-2 (Eikenberry et al., 2004) on the Gemini-South telescope through Fast Turnaround program GS-2015B-FT-5. The spectrum revealed weaker gravity-sensitive K I absorption lines than in a typical field-age late-L dwarf indicating that 2MASS J1119–1137 is young (e.g. Cruz et al., 2009; Rice et al., 2010). Because of unresolved spectrophotometric systematics, namely an extremely red spectral slope and unexpectedly deep OH absorption bands inconsistent with our SpeX spectrum (Kellogg et al., 2015), we do not present the F-2 spectrum here. We subsequently obtained an  $R \sim 6000$ , 0.8–2.45  $\mu\text{m}$  spectrum with the Folded-port InfraRed Echellette (FIRE; Simcoe et al., 2008; Simcoe et al., 2013) at the Magellan Baade telescope on 2016 January 21. It is this

spectrum that we use for the surface gravity and radial velocity analysis presented herein. We observed the target at the parallactic angle (PA)  $\sim 226^\circ$ , at an airmass of 1.17–1.05 with good weather conditions and a seeing of  $\sim 0''.5$ . The echelle disperser was used in conjunction with the Sample Up the Ramp (SUTR) readout and high-gain (1.3 e-/DN) modes. A single 900 s exposure and six 600 s exposures were obtained for a total integration time of 1.25 hr, which yielded signal-to-noise ratios of  $\sim 10$ –70 per pixel in the 1.1–2.2  $\mu\text{m}$  range. We observed the A0 standard HD 85056 immediately afterwards at a similar airmass (1.08–1.09).

We used ThAr calibration lamps (10 s exposure times), observed in the middle and at the end of the science sequence, and again after the telluric standard, to ensure a proper wavelength calibration. A total of eleven internal high-signal flats (1 s exposures with high-voltage lamps) and eleven low-signal flats (10 s exposures with low-voltage lamps) were obtained at the beginning of the night: high-signal flats provide a good pixel response calibration in the blue orders, whereas low-signal flats are used for the red orders. Five 4 s dome flats were also obtained to characterize the slit illumination function.

We reduced the data using the Interactive Data Language (IDL) pipeline FIREHOSE, which is based on the MASE (Bochanski et al., 2009) and SpeX-Tool (Cushing et al., 2004; Vacca et al., 2003) packages. The pipeline was modified to achieve a better rejection of bad pixels (i.e., see Gagné et al., 2015b; Gagné et al., 2015\*). This reduction package includes a barycentric velocity correction and converts the wavelength solution to vacuum.

### 4.3 CONFIRMATION OF YOUTH

To determine if 2MASS J1119–1137 is young, we focused our analysis on the gravity-sensitive K I absorption lines (1.1692 and 1.1778  $\mu\text{m}$ , 1.2437 and 1.2529  $\mu\text{m}$ ). Our FIRE spectrum has 40 times the resolution of our previous SpeX prism spectrum (Kellogg et al., 2015), allowing us to directly compare the strength

---

\*The modified FireHose 2.0 data reduction package can be found at [https://github.com/jgagneastro/FireHose\\_v2/tree/v2.0](https://github.com/jgagneastro/FireHose_v2/tree/v2.0)

of the spectral features to those of young and field-age late-L dwarfs. The top panels of Figure 4.1 show sections of our FIRE spectrum (black) compared to FIRE spectra of the young L7 dwarf PSO J318.5338–22.8603 (green; hereafter PSO J318.5–22; Faherty et al., 2016) and the field-aged L7.5 dwarf Luhman 16A (blue; Faherty et al., 2014) centred on the K I lines. The K I lines in the 2MASS J1119–1137 spectrum are weaker than in Luhman 16A, indicating low surface gravity and hence a young age ( $\lesssim 200$  Myr; Allers et al., 2013). Conversely, the K I line strengths of 2MASS J1119–1137 and PSO J318.5–22 are indistinguishable from each other. The two objects are among the reddest isolated L dwarfs known to date. The equivalent widths of the K I lines as defined by McLean et al., 2003 for 2MASS J1119–1137 ( $1.21 \pm 0.66$  at  $1.1168 \mu\text{m}$ ;  $3.84 \pm 0.64$  at  $1.1177 \mu\text{m}$ ;  $1.89 \pm 0.29$  at  $1.1243 \mu\text{m}$ ; and  $3.12 \pm 0.31$  at  $1.1254 \mu\text{m}$ ) are systematically lower than those of field L7 dwarfs (e.g., see McLean et al., 2003, Figure 15). The complete  $R \sim 6000$ ,  $0.7\text{--}2.4 \mu\text{m}$  FIRE spectrum of 2MASS J1119–1137 is shown in the bottom panel of Figure 4.1, where it is seen to be significantly redder than the near-IR spectrum of the field-aged L7.5 dwarf Luhman 16A.

The combined evidence leads us to conclude that 2MASS J1119–1137 is indeed young, and comparable in age to the 23 Myr-old  $\beta$  Pictoris association member PSO J318.5–22. At the current signal-to-noise ratios and resolutions, we cannot determine if one object is younger than the other from the spectra alone. From this comparison, together with the very red colour and the consistency of various spectral features and indices with other young, late-L dwarfs (Kellogg et al., 2015), we conclude that 2MASS J1119–1137 has low surface gravity and is likely  $\lesssim 120$  Myr old.

#### 4.4 KINEMATICS

We used single-exposure, single-order and telluric-corrected FIRE spectra to measure the radial velocity of 2MASS J1119–1137. We used a forward modelling approach that relies on the zero-velocity BT-Settl atmosphere models (Allard et al., 2013; Baraffe et al., 2003) to reproduce our observations. Our for-

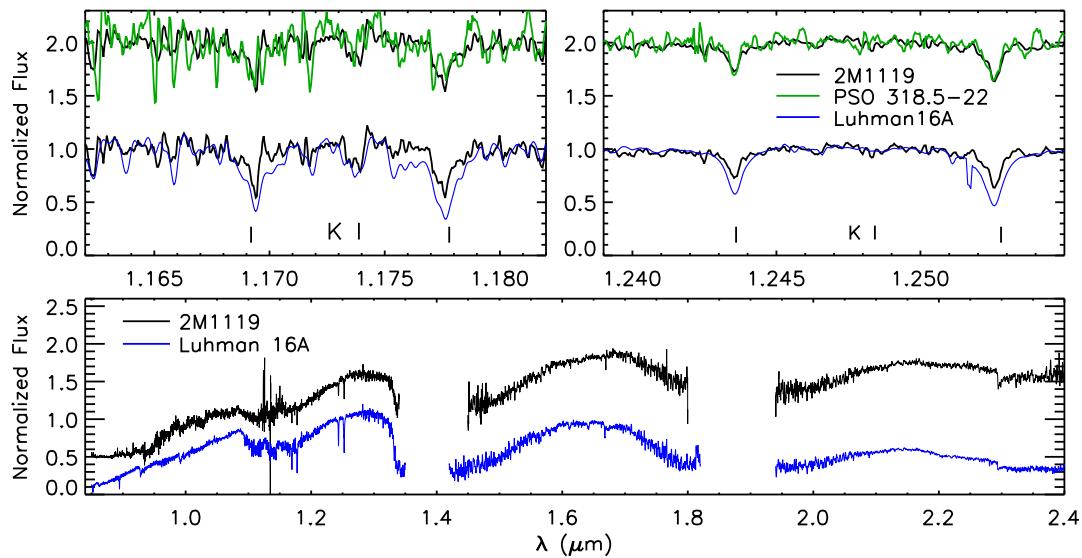


Figure 4.1: Comparison of the  $R \sim 6000$  FIRE spectra of 2MASS J1119–1137 (black), the young L7 dwarf PSO J318.5–22 (green; Faherty et al., 2016) and the old L7.5 dwarf Luhman 16A (blue; Faherty et al., 2014). *Top*: Comparison of the two K I doublet FIRE orders, showing that 2MASS J1119–1137 and PSO J318.5–22 have comparably low surface gravities. *Bottom*: Full FIRE spectra, normalized to unity between 1.25–1.30  $\mu\text{m}$  and offset vertically by 0.5 units for clarity. The  $\lambda < 1.1 \mu\text{m}$  region in the spectrum of 2MASS J1119–1137 has low SNR and the FIRE order stitching is unreliable. The high-order continuum change at 1.55  $\mu\text{m}$  and the CO band head at 2.30  $\mu\text{m}$  fall at FIRE order boundaries, so the strength of these features is also unreliable. The complete spectrum of PSO J318.5–22 (not shown) is presented in Faherty et al., 2016.

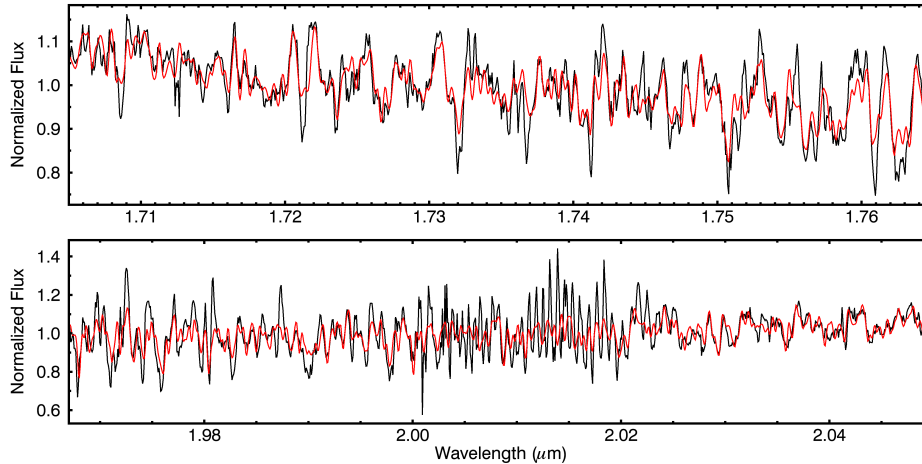


Figure 4.2: Forward model fitting (red line) to the observed spectra (black line) in echelle orders 15 and 13, in order to determine the radial velocity of 2MASS J1119–1137.

ward model employs 4 free parameters: a radial velocity shift, an instrumental line spread function (LSF) width where the LSF is modelled as a Gaussian function, and a two-parameters linear slope multiplicative correction to account for instrumental effects.

We used the IDL implementation of AMOEBA to identify the set of parameters that minimize the reduced  $\chi^2$  between the forward model and the observed spectrum. This is similar to the algorithm described by Allers et al., 2016 except that telluric absorption was corrected a priori and we did not attempt to measure  $v \sin i$  with the limited resolution of our data. This optimization was carried out on the 7 individual exposures, in a selected set of wavelength ranges that are located away from order boundaries and in regions where the S/N is high and sufficient radial velocity information is present in the science spectrum. We selected specific wavelength regions in orders 24 (1.092–1.120  $\mu\text{m}$ ), 17 (1.510–1.554  $\mu\text{m}$ ), 15 (1.680–1.790  $\mu\text{m}$ ), and 13 (1.960–2.050  $\mu\text{m}$ ), that satisfied these criteria. We used the BT-Settl model with  $T_{\text{eff}} = 1600$  K and  $\log g = 4.0$ , which yielded the smallest reduced  $\chi^2$  in these orders with no velocity shift. This temperature and surface gravity are in agreement with those found for PSO J318.5–22 (Liu et al., 2013). We display two example model fits that we obtained in Figure 4.2.

In each order, the useful wavelength range was split in 15 individual segments of width  $0.02 \mu\text{m}$  to account for sub-pixel systematic effects in the wavelength calibration (e.g., see Gagné et al. 2015). This yielded a total of 420 individual radial velocity measurements (7 exposures, 4 orders and 15 order segments). The single-exposure radial velocities were first combined at every wavelength range using an SNR-squared weighted mean. A weighted standard deviation was used to obtain measurement errors on each of these radial velocity measurements.

This method yielded a weighted-average radial velocity of  $8.5 \pm 1.3 \text{ km s}^{-1}$ . Similar radial velocity measurements with FIRE have been demonstrated to bear a  $3 \text{ km s}^{-1}$  systematic uncertainty (e.g., see Zapatero Osorio et al. 2007), which we add in quadrature to our measurement to obtain  $8.5 \pm 3.3 \text{ km s}^{-1}$ .

In order to calibrate our method, we applied it to FIRE data obtained for PSO J318.5–22, for the young T5.5 SDSS J111010.01+011613.1 (Gagné et al., 2015), and for three young M9.5–L2 brown dwarfs with Keck NIRSPEC radial velocity measurements (2MASS J02340093–6442068, 2MASS J02103857–3015313, 2MASS J23225299–6151275; Faherty et al., 2016). We found measurement discrepancies between  $0.5 \text{ km s}^{-1}$  and  $4.4 \text{ km s}^{-1}$  with a standard deviation of  $1.5 \text{ km s}^{-1}$ , well within our measurement errors. These data will be detailed in a future publication.

We solved for the proper motion from the 14-year baseline spanned by 2MASS, SDSS, WISE, WISE 3-Band Post-Cryo, and NEOWISE-R images, using relative astrometry as prescribed in Kirkpatrick et al., 2014. The total proper motion differs slightly from the measurement in Kellogg et al., 2015 which was obtained only from the difference between the 2MASS and AllWISE positions.

#### 4.5 TWA MEMBERSHIP

We used our radial velocity measurement along with the sky position and proper motion of 2MASS J1119–1137 (Table 1) to calculate a young moving group membership probability with the BANYAN II tool<sup>†</sup> (Gagné et al., 2014a). The

---

<sup>†</sup>Publicly available at <http://www.astro.umontreal.ca/~gagne/banyanII.php>

BANYAN II tool assumes gaussian ellipsoid models adjusted to fit the XYZ and UVW distributions of known bona fide members of different moving groups, or the Besançon galactic model (Robin et al., 2012) for the field hypothesis. Bayes’ theorem is used to derive a probability density from the comparison of the measurements to the models, and the probability is obtained by marginalizing the probability density function over all possible distances.

Table 4.1: Characteristics of 2MASS J11193254–1137466

Right Ascension	$11^h 19^m 32.543^s$
Declination	$-11^\circ 37' 46.70''$
Radial Velocity	$8.5 \pm 3.3 \text{ km s}^{-1}$
$\mu_\alpha \cos \delta$	$-145.1 \pm 14.9 \text{ mas yr}^{-1}$
$\mu_\delta$	$-72.4 \pm 16.0 \text{ mas yr}^{-1}$
<i>Y</i>	$19.045 \pm 0.093 \text{ mag}$
<i>J</i>	$17.330 \pm 0.029 \text{ mag}$
<i>H</i>	$15.844 \pm 0.017 \text{ mag}$
<i>K<sub>s</sub></i>	$14.751 \pm 0.012 \text{ mag}$
<i>W1</i>	$13.548 \pm 0.026 \text{ mag}$
<i>W2</i>	$12.883 \pm 0.027 \text{ mag}$
$\log L/L_\odot$	$-4.39 \pm 0.14$
Age	$10 \pm 3 \text{ Myr}$
Kinematic Distance	$28.9 \pm 3.6 \text{ pc}$
Estimated Mass	$4.3\text{--}7.6 M_{\text{Jup}}$

*YJHK<sub>s</sub>* magnitudes from the VHS<sup>†</sup>.

We obtained an 88% probability that 2MASS J1119–1137 is a TWA member, with a calibrated field contamination probability of 0.003% equivalent to a statistical significance of  $4.15\sigma$ . The coordinate that puts the most stringent constraint on the membership of 2MASS J1119–1137 is *Z*, which only matches the distribution of TWA members. The statistical kinematic distance is  $28.9 \pm 3.6 \text{ pc}$ , consistent with our earlier photometric estimate of  $27 \pm 7.2 \text{ pc}$  (Kellogg et al., 2015) which was calculated from the apparent *K<sub>s</sub>* magnitude and the expected absolute *K<sub>s</sub>* magnitude of a young L7 dwarf (Filippazzo et al., 2015). The distance is also consistent with the absolute magnitude relations for other young, late-type L dwarfs (e.g. WISEP J004701.06+680352.1 and PSO J318.5–22; Faherty et al., 2016), which take into account all young L dwarfs. When we include the photometric distance estimate as an input to the BANYAN II algorithm, the TWA membership probability increases to 92% and the field

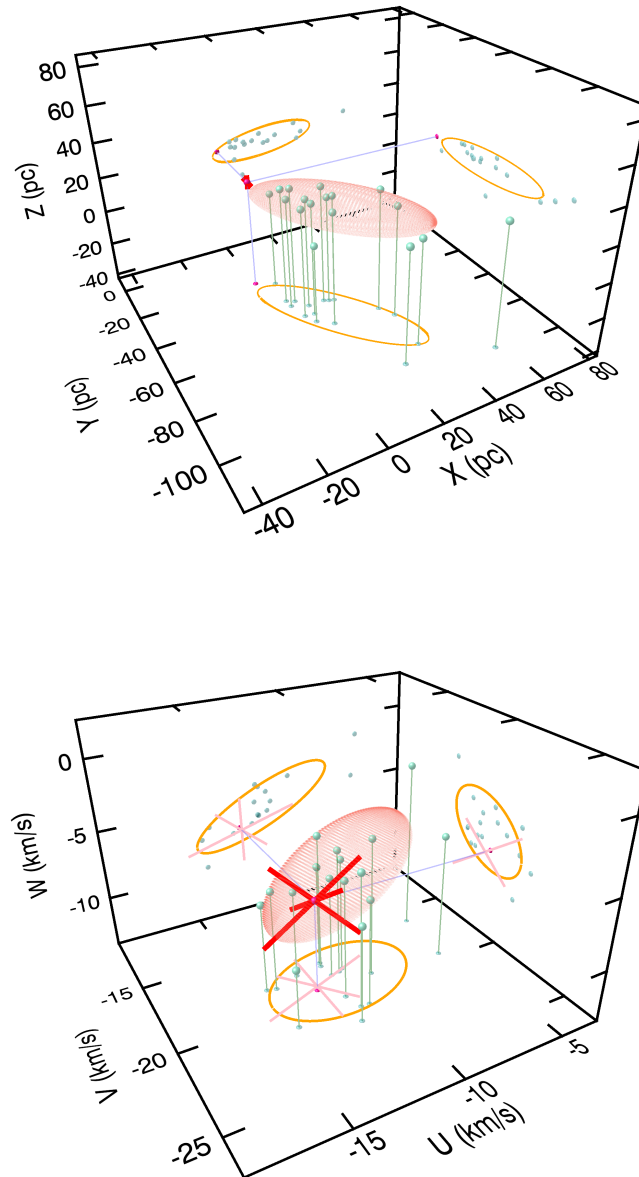


Figure 4.3: Galactic position and space velocity of 2MASS J1119–1137 (red sphere and red error bars) compared to known TW Hydrae bona fide members (green spheres) and the  $1\sigma$  Gaussian ellipsoid spatial and kinematic models used in BANYAN II (orange ellipses). The data are projected to the three 2D planes for an easier visualization.

contamination probability significantly decreases to 0.0005%, meaning that 2MASS J1119–1137 is consistent with being a TWA member at a statistical significance of  $4.55\sigma$ .

In Figure 4.3 we display the galactic position  $XYZ$  and space velocity  $UVW$  of 2MASS J1119–1137 at its statistical distance, compared to known bona fide TWA members, and to the  $1\sigma$  contours of the 3D Gaussian ellipsoid models used in BANYAN II. Although the current model of TWA extends its  $1\sigma$  contour to only  $\sim 33$  pc, this  $\sim 25$  pc object appears to have been drawn from the same gaussian random distribution in  $XYZUVW$  space. The  $XYZ$  position of 2MASS J1119–1137 reveals it to be the nearest TWA member and extends the observed distance distribution of currently known objects. While other closer candidate TWA members have been reported in the literature (TWA 22; Song et al., 2003), their space positions and velocities fall well outside of the TWA ellipsoid (Mamajek, 2005; Teixeira et al., 2009; Weinberger et al., 2013). Our own calculation with BANYAN II yields an association probability of  $10^{-7}$  for TWA 22.

At the age of TWA ( $10 \pm 3$  Myr; Bell et al. 2015), we estimate that the mass of 2MASS J1119–1137 is  $4.3\text{--}7.6 M_{\text{Jup}}$ , where we have compared the bolometric luminosity derived from the  $K_s$  magnitude at its TW Hydrae kinematic distance and age to model predictions from Saumon et al., 2008 and directly compared the absolute  $K_s$  magnitude to the predictions from Baraffe et al., 2015.

The mass makes 2MASS J1119–1137 comparable to the early-L companion object, 2M1207b (Chauvin et al., 2004, 2005), which is also a member of TW Hydrae (Gizis, 2002). The two objects have similar  $H - K_s$  colours ( $1.16 \pm 0.24$  mag for 2M1207b; Chauvin et al., 2004) to within the uncertainties, although 2M1207b is overall redder in the  $1\text{--}4 \mu\text{m}$  region (Chauvin et al., 2004; Song et al., 2006). The 0.4 dex lower luminosity of 2M1207b (Filippazzo et al., 2015) reveals that it is likely lower in mass, regardless of model assumptions. Comparing to the cooling tracks of Saumon et al., 2008 and Baraffe et al., 2015, 2M1207b has an estimated mass of  $3.3\text{--}5.4 M_{\text{Jup}}$ . Our mass estimate for 2MASS J1119–1137 is slightly higher,  $4.3\text{--}7.6 M_{\text{Jup}}$ , which still leaves it as the least massive isolated member of TWA. Both objects are at or above the

theoretical opacity-limited turbulent fragmentation limit of  $3\text{--}5 M_{\text{Jup}}$  (Boyd et al., 2005), so both could have formed through star-like gravo-turbulent collapse. However, both have masses comparable to or smaller than the  $5\text{--}7 M_{\text{Jup}}$  masses of the HR 8799 planets (Marois et al., 2008, 2010). Hence both 2MASS J1119–1137 and 2M1207b could have in principle formed via a planet-like mechanism, and in the case of 2MASS J1119–1137, subsequently been ejected.

We sought bright common proper motion companions to 2MASS J1119–1137 by calculating the 2MASS–AllWISE proper motions of all 2MASS entries within  $60'$ , corresponding to a maximum physical separation of 22,500 AU at 25 pc. None of the 368 2MASS sources within this radius had a proper motion within  $76 \text{ mas yr}^{-1}$  of that of 2MASS J1119–1137, indicating no potential stellar host to this young planetary-mass object.

#### 4.6 CONCLUSION

We have spectroscopically confirmed the low surface gravity, and hence youth, of the L7 dwarf 2MASS J1119–1137. Its radial velocity, proper motion, and galactic position are consistent with that of the  $10 \pm 3$  Myr-old TWA. From the object's near-infrared absolute magnitudes we determine a mass of  $4.3\text{--}7.6 M_{\text{Jup}}$ . It is the nearest member of TWA, and the second-brightest isolated  $<10 M_{\text{Jup}}$  object discovered to date. Hence, 2MASS J1119–1137 is an excellent benchmark for young, directly imaged extrasolar planets.

#### REFERENCES

- Allard, France, Homeier, D, Freytag, B, et al. (2013). *Mem. Soc. Astron. Ital.* 24, p. 128.
- Aller, K. M., Kraus, A. L., Liu, M. C., et al. (2013). *ApJ* 773, 63, p. 63. DOI: [10.1088/0004-637X/773/1/63](https://doi.org/10.1088/0004-637X/773/1/63).
- Allers, K. N. and Liu, M. C. (2013). *ApJ* 772, 79, p. 79. DOI: [10.1088/0004-637X/772/2/79](https://doi.org/10.1088/0004-637X/772/2/79).
- Allers, K N, Gallimore, J F, Liu, Michael C, et al. (2016). *arXiv.org*, arXiv:1601.04717.

- Baraffe, I., Homeier, D., Allard, F., et al. (2015). *A&A* 577, A42, A42. DOI: [10.1051/0004-6361/201425481](https://doi.org/10.1051/0004-6361/201425481).
- Baraffe, Isabelle, Chabrier, G, Barman, Travis S, et al. (2003). *A&A* 402.2, pp. 701–712.
- Bell, Cameron P M, Mamajek, Eric E, and Naylor, Tim (2015). English. *Monthly Notices of the Royal Astronomical Society* 454.1, pp. 593–614. DOI: [10.1093/mnras/stv1981](https://doi.org/10.1093/mnras/stv1981).
- Bochanski, John J, Hennawi, Joseph F, Simcoe, Robert A., et al. (2009). *PASP* 121, pp. 1409–1418.
- Boyd, D. F. A. and Whitworth, A. P. (2005). *A&A* 430, pp. 1059–1066. DOI: [10.1051/0004-6361:20041703](https://doi.org/10.1051/0004-6361:20041703).
- Chauvin, G., Lagrange, A.-M., Dumas, C., et al. (2004). *A&A* 425, pp. L29–L32. DOI: [10.1051/0004-6361:200400056](https://doi.org/10.1051/0004-6361:200400056).
- (2005). *A&A* 438, pp. L25–L28. DOI: [10.1051/0004-6361:200500116](https://doi.org/10.1051/0004-6361:200500116).
- Cruz, K. L., Kirkpatrick, J. D., and Burgasser, A. J. (2009). *AJ* 137, pp. 3345–3357. DOI: [10.1088/0004-6256/137/2/3345](https://doi.org/10.1088/0004-6256/137/2/3345).
- Cushing, Michael C, Vacca, William D, and Rayner, John T (2004). *PASP* 116.8, pp. 362–376.
- Delorme, P., Gagné, J., Malo, L., et al. (2012). *A&A* 548, A26, A26. DOI: [10.1051/0004-6361/201219984](https://doi.org/10.1051/0004-6361/201219984).
- Eikenberry, S. S., Elston, R., Raines, S. N., et al. (2004). *Ground-based Instrumentation for Astronomy*. Ed. by A. F. M. Moorwood and M. Iye. Vol. 5492. Proc. SPIE, pp. 1196–1207. DOI: [10.1117/12.549796](https://doi.org/10.1117/12.549796).
- Faherty, J. K., Beletsky, Y., Burgasser, A. J., et al. (2014). *ApJ* 790, 90, p. 90. DOI: [10.1088/0004-637X/790/2/90](https://doi.org/10.1088/0004-637X/790/2/90).
- Faherty, J. K., Riedel, A. R., Cruz, K. L., et al. (2016). *ApJS* 225, 10, p. 10. DOI: [10.3847/0067-0049/225/1/10](https://doi.org/10.3847/0067-0049/225/1/10).
- Filippazzo, J. C., Rice, E. L., Faherty, J., et al. (2015). *ApJ* 810, 158, p. 158. DOI: [10.1088/0004-637X/810/2/158](https://doi.org/10.1088/0004-637X/810/2/158).
- Gagné, J., Lafrenière, D., Doyon, R., et al. (2015a). *ApJ* 798, 73, p. 73. DOI: [10.1088/0004-637X/798/2/73](https://doi.org/10.1088/0004-637X/798/2/73).

- Gagné, J., Faherty, J. K., Cruz, K. L., et al. (2015b). *ApJS* 219, 33, p. 33. DOI: [10.1088/0067-0049/219/2/33](https://doi.org/10.1088/0067-0049/219/2/33).
- Gagné, Jonathan, Lafrenière, David, Doyon, René, et al. (2014a). *ApJ* 783.2, p. 121.
- Gagné, Jonathan, Faherty, Jacqueline K., Cruz, Kelle K., et al. (2014b). *ApJL* 785.1, p. L14.
- Gagné, Jonathan, Lambrides, Erini, Faherty, Jacqueline K, et al. (2015).
- Gagné, Jonathan, Burgasser, Adam J, Faherty, Jacqueline K, et al. (2015). *The Astrophysical Journal Letters* 808.1, p. L20. DOI: [10.1088/2041-8205/808/1/L20](https://doi.org/10.1088/2041-8205/808/1/L20).
- Gizis, J. E. (2002). *ApJ* 575, pp. 484–492. DOI: [10.1086/341259](https://doi.org/10.1086/341259).
- Kellogg, K., Metchev, S., Gagné, J., et al. (2016). *ApJ* 821, L15, p. L15. DOI: [10.3847/2041-8205/821/1/L15](https://doi.org/10.3847/2041-8205/821/1/L15).
- Kellogg, Kendra, Metchev, Stanimir, Geißler, Kerstin, et al. (2015). *The Astrophysical Journal* 150.6, p. 182. DOI: [10.1088/0004-6256/150/6/182](https://doi.org/10.1088/0004-6256/150/6/182).
- Kirkpatrick, J. D., Schneider, A., Fajardo-Acosta, S., et al. (2014). *ApJ* 783, 122, p. 122. DOI: [10.1088/0004-637X/783/2/122](https://doi.org/10.1088/0004-637X/783/2/122).
- Liu, Michael C., Magnier, Eugene A, Deacon, Niall R, et al. (2013). *ApJL* 777.2, p. L20.
- Luhman, K. L., Adame, L., D’Alessio, P., et al. (2005). *ApJ* 635, pp. L93–L96. DOI: [10.1086/498868](https://doi.org/10.1086/498868).
- Malo, L., Doyon, R., Lafrenière, D., et al. (2013). *ApJ* 762, 88, p. 88. DOI: [10.1088/0004-637X/762/2/88](https://doi.org/10.1088/0004-637X/762/2/88).
- Mamajek, E. E. (2005). *ApJ* 634, pp. 1385–1394. DOI: [10.1086/468181](https://doi.org/10.1086/468181).
- Marois, C., Macintosh, B., Barman, T., et al. (2008). *Science* 322, p. 1348. DOI: [10.1126/science.1166585](https://doi.org/10.1126/science.1166585).
- Marois, C., Zuckerman, B., Konopacky, Q. M., et al. (2010). *Nature* 468, pp. 1080–1083. DOI: [10.1038/nature09684](https://doi.org/10.1038/nature09684).
- Marsh, K. A., Kirkpatrick, J. D., and Plavchan, P. (2010). *ApJ* 709, pp. L158–L162. DOI: [10.1088/2041-8205/709/2/L158](https://doi.org/10.1088/2041-8205/709/2/L158).
- McLean, I. S., McGovern, M. R., Burgasser, A. J., et al. (2003). *ApJ* 596, pp. 561–586. DOI: [10.1086/377636](https://doi.org/10.1086/377636).

- Rice, E. L., Barman, T., Mclean, I. S., et al. (2010). *ApJS* 186, pp. 63–84. DOI: [10.1088/0067-0049/186/1/63](https://doi.org/10.1088/0067-0049/186/1/63).
- Robin, A. C., Marshall, D. J., Schultheis, M., et al. (2012). *A&A* 538, A106, A106. DOI: [10.1051/0004-6361/201116512](https://doi.org/10.1051/0004-6361/201116512).
- Saumon, D. and Marley, M. S. (2008). *ApJ* 689, 1327–1344, pp. 1327–1344. DOI: [10.1086/592734](https://doi.org/10.1086/592734).
- Schneider, A. C., Cushing, M. C., Kirkpatrick, J. D., et al. (2014). *AJ* 147, 34, p. 34. DOI: [10.1088/0004-6256/147/2/34](https://doi.org/10.1088/0004-6256/147/2/34).
- Simcoe, Robert A, Burgasser, Adam J, Bernstein, Rebecca A, et al. (2008). *Ground-based and Airborne Instrumentation for Astronomy II. Edited by McLean* 7014, 70140U–70140U–10. DOI: [10.1117/12.790414](https://doi.org/10.1117/12.790414).
- Simcoe, Robert A., Burgasser, Adam J., Schechter, Paul L, et al. (2013). *PASP* 125.925, pp. 270–286.
- Song, I., Zuckerman, B., and Bessell, M. S. (2003). *ApJ* 599, pp. 342–350. DOI: [10.1086/379194](https://doi.org/10.1086/379194).
- Song, I., Schneider, G., Zuckerman, B., et al. (2006). *ApJ* 652, pp. 724–729. DOI: [10.1086/507831](https://doi.org/10.1086/507831).
- Teixeira, R., Ducourant, C., Chauvin, G., et al. (2009). *A&A* 503, pp. 281–285. DOI: [10.1051/0004-6361/200912173](https://doi.org/10.1051/0004-6361/200912173).
- Vacca, William D, Cushing, Michael C, and Rayner, John T (2003). *PASP* 115.8, pp. 389–409.
- Webb, R. A., Zuckerman, B., Platais, I., et al. (1999). *ApJ* 512, pp. L63–L67.
- Weinberger, A. J., Anglada-Escudé, G., and Boss, A. P. (2013). *ApJ* 762, 118, p. 118. DOI: [10.1088/0004-637X/762/2/118](https://doi.org/10.1088/0004-637X/762/2/118).
- Zapatero Osorio, M R, Martín, E L, Béjar, V J S, et al. (2007). English. *The Astrophysical Journal* 666.2, pp. 1205–1218. DOI: [10.1086/520673](https://doi.org/10.1086/520673).

# 5

## Characterizing The Cloud Decks of Luhman 16AB with Medium-Resolution Spectroscopic Monitoring

### 5.1 INTRODUCTION

The spectral morphology of brown dwarfs changes drastically ( $\sim 6$  subtypes) over a relatively narrow range of effective temperatures ( $\sim 1200$ – $1300$  K) at the transition from spectral type L to T. During this transition, clouds in the atmospheres of mid-L objects disappear and by mid-T spectral types the visible atmospheres are cloud-free. It is not yet well understood how these clouds disappear or if it is possible that objects skip spectral types rather than evolve through all intervening spectral morphologies.

A characteristic of ultracool atmospheres in this spectral type range is flux variability on the rotation period of the object (Radigan et al., 2014; Radigan, 2013). Summarizing the evidence from ground-based photometric monitoring campaigns in the  $J$  band, Radigan, 2014 finds that large-amplitude ( $>2\%$ ) vari-

---

A version of this chapter has been submitted to The Astrophysical Journal.

ability is common for brown dwarfs spanning the L-to-T transition. Among L9–T3.5 dwarfs  $24\%_{-9\%}^{+11\%}$  are large-amplitude variables, vs. only  $3\%_{-2\%}^{+3\%}$  among L0–L8.5 and T4–T9.5 dwarfs. The near-infrared (NIR) 1–2.4  $\mu\text{m}$  variability has been attributed to clear holes in a prevailing cloud deck that reveal deeper, hotter parts of the atmosphere (e.g., Artigau et al., 2009) or, more generally, to multiple patchy cloud layers that lead to net changes in the observed photospheric level as a brown dwarf rotates (Apai et al., 2013). The picture of dissipating cloud decks across the L-to-T transition is consistent with the rainout of condensates invoked in the progression from dusty L-type to clear T-type atmospheres (Ackerman et al., 2001; Burgasser, 2002).

Longer-wavelength 3–5  $\mu\text{m}$  monitoring during the *Weather on Other Worlds* program with the *Spitzer Space Telescope* has now revealed that smaller-amplitude variations are likely ubiquitous in L and T dwarfs across all spectral types (Metchev et al., 2015). That study finds that  $80\%_{-27\%}^{+20\%}$  of L3–L9.5 dwarfs vary by  $>0.2\%$  and  $36\%_{-17\%}^{+26\%}$  of T0–T8 dwarfs vary by  $>0.4\%$  in the *Spitzer* [3.6] and [4.5] bands. Unlike Radigan, 2014, Metchev et al., 2015 find no evidence for enhancement in either frequency or amplitude of variability at the L/T transition, but instead observe that the maximum detected amplitudes increase throughout the L3–T8 range. The different dependence of variability on spectral type measured at *JHK* (1–2.4  $\mu\text{m}$ ) relative to the *Spitzer* IRAC bands (3–5  $\mu\text{m}$ ) is likely rooted in the difference among the atmospheric pressure levels—and correspondingly, sources of opacity—observed at these wavelengths. NIR observations, especially in the *J* band, can be sensitive to deep condensate clouds at  $\sim 10$  bar pressures, while 3–5  $\mu\text{m}$  photometry probes mostly upper-atmosphere carbon monoxide and methane gas opacity at 0.1–1 bar (e.g., Ackerman et al., 2001).

To test this hypothesis, we need simultaneous observations with a broad wavelength range that probe multiple pressure levels. Precise low-dispersion ( $R \sim 130$ ) 1.1–1.6  $\mu\text{m}$  spectrophotometric monitoring with WFC3 on the *Hubble Space Telescope* of Luhman 16AB (Luhman, 2013) shows that there are multiple photospheric regions involved in the flux variations (Apai et al., 2013; Buenzli et al., 2015a), possibly with different brightness temperatures (Karalidi et al., 2016). Apai et al., 2013 demonstrate that the photospheric inhomogeneities can

be attributed to regions with various contributions from cool thick clouds and warmer, brighter, and thinner clouds. A similar conclusion is reached by Burgasser et al., 2014 from a  $R \sim 120$  resolved spectroscopic sequence on a binary from ground-based observations with SpeX on the IRTF. Multiple spots can also produce phase lags among the light curves at different wavelengths, as have already been reported from simultaneous 1–5  $\mu\text{m}$  *Hubble* and *Spitzer* observations of L and T dwarfs (Apai et al., 2013; Yang et al., 2016).

Higher-dispersion ( $R > 1000$ ) monitoring can be used to accurately estimate the altitudes of the various cloud decks. Given sufficient spectral resolution, the line profiles of gravity-sensitive absorbers, such as alkali elements, can be resolved throughout the optical and the NIR. Variations in the strengths of these lines, corresponding to holes in the upper cloud deck rotating in and out of view, can thus reveal the pressure levels where cloud condensates form.

The nearest pair of brown dwarfs—the L7.5 + T0.5 binary WISE J104915.57–531906.1AB (a.k.a., Luhman 16AB; Luhman, 2013)—offers one of the best opportunities for high dispersion spectroscopy of substellar objects. Both components are bright (MKO  $J$  magnitudes of 11.5 and 11.2 for the A and B components, respectively; Burgasser et al., 2013), and spatially well resolved ( $1''.5$  at the time of discovery; Luhman, 2013). Photometric monitoring has shown that the secondary T0.5 component can vary by upwards of 10% peak-to-peak in the optical through NIR (Biller et al., 2013; Buenzli et al., 2015a; Burgasser et al., 2014; Gillon et al., 2013). Biller et al., 2013 found that the variations of Luhman 16B in the bandpasses that probe the lower atmosphere ( $z'$ ,  $J$ , and  $H$ ) are in phase while the variations in the bands that probe the upper atmosphere ( $r'$ ,  $i'$  and  $K$ ) are out of phase by  $\geq 100^\circ$  with respect to the  $z'$  band. Since then, WFC3/*HST* observations by Buenzli et al., 2015b have shown that the primary L7.5 component also varies, with a peak-to-peak amplitude of up to 4.5%. The variability periods of the components are 5.05 h for component B, and either 5 h or 8 h for component A (Karalidi et al., 2016). The periodic variations in the binary components can thus be conveniently studied over the course of a single observing night.

Luhman 16AB has already been intensively investigated at high spectral res-

olution. Most notably, Crossfield, 2014 used very high dispersion ( $R = 50,000$ ) spectroscopy to invert the time-dependence in the Doppler broadening of the molecular line profiles to produce a spatially resolved map of brightness variations of Luhman 16B. A comparative medium resolution ( $R \sim 4000$ ) 0.8–2.4  $\mu\text{m}$  analysis of the binary by Faherty et al., 2014 found that the T0.5-type B component shows stronger absorption in the gravity-sensitive 1.168, 1.177, 1.243, and 1.254  $\mu\text{m}$  K I lines than the L7.5-type A component, while having a brighter continuum in the 1.17  $\mu\text{m}$  and 1.25  $\mu\text{m}$  region. They interpret this as a verification of the cloud dissipation hypothesis across the L/T transition: the cooler component has a patchy upper cloud layer that reveals the hotter, higher-pressure inner parts of the atmosphere. Where the molecular opacity is low, such as in the  $J$  band, these make the B component brighter than the hotter L7.5-type A component of the binary. The Faherty et al., 2014 analysis does not address the variability of the Luhman 16 components, as it combines altogether only 40 min of exposure on each component.

Here we present a two night-long  $R \sim 4000$ , 0.9–2.5  $\mu\text{m}$  spectroscopic monitoring study of Luhman 16AB. We analyze the behaviour of the K I,  $\text{CH}_4$ , FeH, and  $\text{H}_2\text{O}$  absorption strengths in order to determine the nature of the variability phenomenon. A companion study (Heinze et al. 2017, in preparation) will describe a complementary and contemporaneous set of  $R \sim 300$  optical spectra, and will investigate the variability of the much stronger K I 0.77  $\mu\text{m}$  absorption doublet.

## 5.2 OBSERVATIONS AND DATA REDUCTION

We obtained simultaneous observations of Luhman 16AB with the Folded-port InfraRed Echellette spectrograph (FIRE; Simcoe et al., 2008, 2013) on the Magellan, Baade telescope and the Gemini Multi-Object Spectrometer (GMOS) on the Gemini-South telescope on 2014, February 23 and 24. Both nights were clear with a stable seeing between 0.8 and 1 arcsec. We used the 1''0 slit on FIRE in cross-dispersed mode ( $R \sim 4000$ ) covering 0.9–2.5  $\mu\text{m}$ . Observations were taken over two nights for a monitoring of  $\sim 2$  rotations of Luhman 16B per

night. We only report the results from the NIR observations here. The results from the optical observations will be discussed in Heinze et al. (2017). Because we monitored Luhman 16AB over complete nights, our observations likely inherit cyclic correlations with seeing and airmass. We discuss methods to mitigate these effects in the calibration of our spectra in §5.3.1.

A total of forty-six 600s exposures were taken with an ABBA nodding sequence with the slit aligned on both components for simultaneous observations of Luhman 16 A and B. Several observations of a telluric standard, HD 98042, were taken throughout the observing sequence on both nights. We used gain settings of  $3.8 \text{ e}^-/\text{DN}$  for the science and the standard observations. Illumination and appropriate pixel flats were observed either at the beginning or the end of the night and a neon-argon lamp was observed immediately after each set of target and standard star observations for use in instrumental calibrations. All science and telluric observations were taken using the sample-up-the-ramp (SUTR) readout mode.

We reduced the data using the Interactive Data Language (IDL) pipeline FIREHOSE, which is based on the MASE (Bochanski et al., 2009) and SpeX-Tool (Cushing et al., 2004; Vacca et al., 2003) packages. A majority of the bad pixels were removed initially using a bad pixel mask. The pipeline was modified to subsequently achieve a better rejection of bad pixels and includes a barycentric velocity correction and converts the wavelength solution to vacuum. The extraction profiles built by FIREHOSE cannot account for traces of both objects at once, hence it is only an approximate profile that covers both traces in the case of science exposures. The profiles were used only for the purpose of straightening the 2D traces in a first step using a custom Interactive Data Language (IDL) routine. In a second step, the two-dimensional wavelength solutions were used to un-shear the two-dimensional raw exposures in the wavelength direction. These steps resulted in a straight horizontal spectral trace with a uniform wavelength solution on every row for every exposure and order.

A custom IDL pipeline was then used to extract the spectral traces of the two Luhman 16 AB components separately. At each column of the two-dimensional exposures, two Moffat functions (Moffat, 1969) were fit simultaneously to the

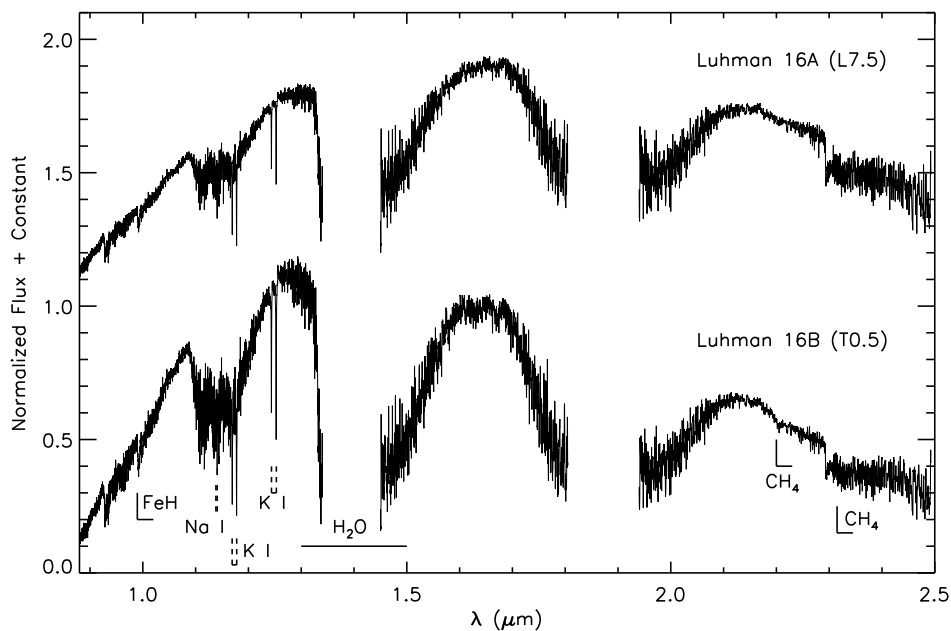


Figure 5.1: The  $R \sim 4000$  Magellan FIRE spectra of the Luhman 16A and B components from 2014, February 23 and 24. The spectra for each object were median-combined order by order and the orders were subsequently stitched.

data using the MPFITFUN.PRO routine, which performs a Levenberg-Marquardt least-squares fit. The resulting area under the curve of the individual best-fitting Moffat profiles then provide the separate raw spectral flux densities of Luhman 16 A and B. We calculate that an average of  $\sim 10\%$  of the measurement error is attributed to systematic flux contamination from the opposite component. A similar one-profile algorithm was used to extract the telluric standard, which was then used to correct telluric absorption from the Earth's atmosphere using the FIRE\_XTELLCOR.PRO IDL routine.

Figure 5.1 shows spectra of the two components—Luhman 16A (L7.5) and Luhman 16B (T0.5)—median-combined from both nights of observations (6 hr total exposure).

### 5.3 ANALYSIS AND RESULTS

Our goal was to understand how the strengths of spectroscopic features, particularly pressure-sensitive lines, change as Luhman 16B varies. We first discuss how we calibrated the light curves of Luhman 16B with Luhman 16A to remove systematic effects. Then we discuss how we created spectra that represented the bright and faint states of Luhman 16B to assess changes in the strengths of the absorption features between states. Finally, we discuss the variations and changes we observed in the spectra.

#### 5.3.1 LIGHT CURVE CALIBRATION

Figure 5.2 shows the sum of the continuum flux in the orders of the pressure-sensitive alkali doublets ( $1.145\text{--}1.155\mu\text{m}$ ,  $1.155\text{--}1.165\mu\text{m}$ , and  $1.230\text{--}1.240\mu\text{m}$ ) for each spectrum taken over the span of two nights. It is immediately evident that the fluxes in the respective orders of A and B correlate strongly, which we attribute to seeing and slit-loss variations during the monitoring sequence. Because components A and B were aligned along the slit, these variations are correlated. We eliminated these relative systematics and obtained a corrected light curve of the variability of the T0.5 dwarf B component by dividing the spectra of component B by those of component A.

Although the L7.5 dwarf A component is also known to vary with a  $\gtrsim 2$  times smaller amplitude (Buenzli et al., 2015b), our primary concern was the elimination of the much larger-amplitude variations caused by the seeing. Relative calibration with respect to A was the only option to achieve this with a long-slit spectrograph. The GMOS optical spectra of component B were also normalized by the A component (Heinze et al. 2017), therefore, using a ratio of the FIRE spectra of the components allows a direct comparison between the variability in the NIR and in the optical.

We show the thus-normalized continuum flux variations in three of the panels of Figure 5.3. We have also applied the same technique to other wavelength regions of interest: namely the continua around FeH ( $0.975\text{--}0.985\mu\text{m}$ ),  $\text{H}_2\text{O}$  ( $1.280\text{--}1.320\mu\text{m}$ ) and  $\text{CH}_4$  ( $2.190\text{--}2.200\mu\text{m}$  and  $2.300\text{--}2.310\mu\text{m}$ ), and show these

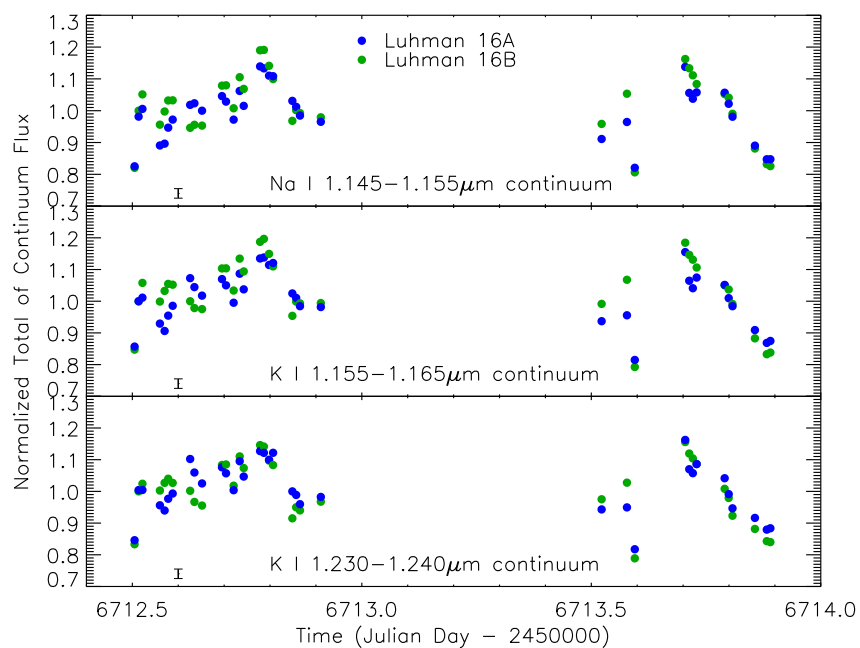


Figure 5.2: Continuum variations of Luhman 16A and B (blue and green circles, respectively) around the Na I and K I NIR lines from the two nights of FIRE observations. The data have been normalized to the respective mean values of the entire observing period. Wavelength regions for the summation of the continuum fluxes are 1.145–1.155 $\mu\text{m}$  for the Na I doublet and 1.155–1.165 $\mu\text{m}$ , 1.230–1.240 $\mu\text{m}$  for the K I doublets; i.e., excluding the doublets themselves. The average random uncertainties are shown in the bottom left corner.

in the other panels of Figure 5.3. We see from this Figure that the exposures of the optical and NIR data are not entirely synchronized because of the logistics of the individual observations. In particular, time was lost at the beginning of the first night of GMOS observations because of a technical fault. The most prominent peak and trough of the light curve and the clearest trend of variability occur at the beginning of the two-night observing period for both the NIR and optical data.

### 5.3.2 CREATION OF REPRESENTATIVE BRIGHT AND FAINT STATE SPECTRA

We are particularly interested in how the relative strengths of the absorption features change over the course of the observations as this offers insight into the pressure level where the variability arises. To assess this, we identified the observations that were taken at the maxima and minima of the light curve (Figure 5.3). We used the continuum around the  $J$ -band K I doublets to identify the minima and maxima, and selected the same sets of spectra for all other wavelength regions for consistency. While we used the light curve of the B/A ratios to identify the bright- and faint-state spectra, we only used the telluric-corrected spectra of the B component when median-combining to create representative bright and faint spectra. We thus avoided contaminating our results with any effects from the variation in the primary A component.

The variations during the second night appeared less organized than during the first night. Consequently, we were unable to select moments when the conditions contributing to either the bright or to the faint state were clearly expressed. Such changes in the light curve are not unexpected. Long-term monitoring of SIMP J013656.5+093347 shows that the light curve becomes irregular at some epochs (e.g., Artigau et al., 2009; Metchev et al., 2013). For this reason, we excluded night two from our analysis.

To assess the amplitudes of the absorption feature variations in the T0.5 dwarf B component, we formed the ratio of the spectra representing the bright and faint states. The representative maximum and minimum spectra were created by using the three spectra of Luhman 16B that cluster around each of the two peaks of the light curve (bright state) and the three spectra that clustered around

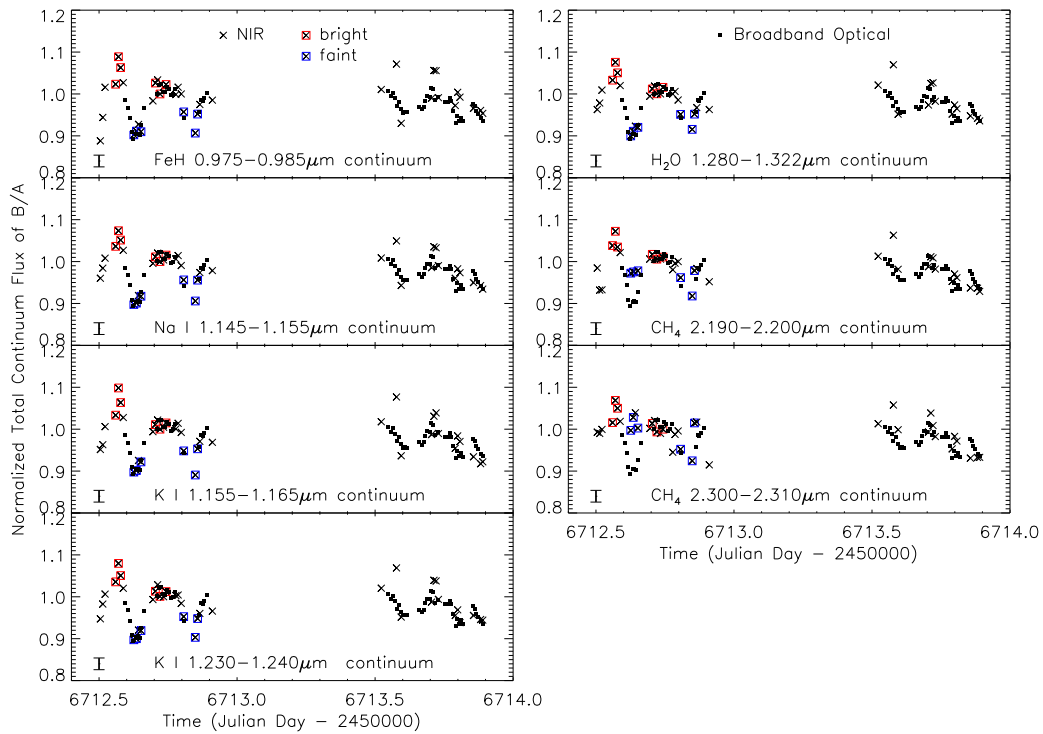


Figure 5.3: Luhman 16B continuum variations

Variations in the continuum around the various absorption features of the ratio of Luhman 16B/A from the two nights of FIRE observations. The GMOS 0.8–1.0  $\mu\text{m}$  light curve is also shown for comparison. The data are normalized to the respective mean values of the observations that overlapped in time. The crosses are the NIR data and the squares are the optical data (Heinze et al. 2017). The points corresponding to each of the six spectra used for the bright and faint states are indicated in red and blue, respectively. The average total uncertainties are shown in the bottom left corners.

each of the two troughs (faint state): for a total of six spectra for each state. We did not normalize these spectra by the corresponding spectra of Luhman 16A: to avoid incurring an unknown correlation with the spectroscopic variability of the primary component. However, this meant that our selected maximum- and minimum-light spectra of Luhman 16B were again subject to slit losses and changing atmospheric conditions, and so had systematic slope discrepancies. To mitigate this, we removed any slopes in the continua by filtering out the lowest frequency from a Fast Fourier Transform. We thus remove sensitivity to overall colour changes but retain sensitivity to changes in the higher order features such as absorption lines. We then scaled the corrected spectra to the average continuum level of the six in each of the maximum- and minimum-light sets.

We also noticed a slight shift in the wavelength solution for the spectra over the course of the observations which resulted from a lack of frequent observations of an arc lamp. Before combining the spectra, we cross-correlated all the spectra with respect to the first and shifted them by the appropriate amount. Finally, we median-combined and re-normalized the six scaled spectra for each set to unity in the continua, which resulted in two representative spectra: one for the bright and one for the faint state. While the two representative spectra lack absolute flux calibration, the relative flux information within each of the two spectra is precisely calibrated. The top panels in Figure 5.4 show the median-combined representative spectra for the bright (black) and faint (red) states for night one in all of the spectral regions of interest. We formed ratios of the bright and faint states to assess the relative changes in line strengths: shown in the bottom sets of panels in Figure 5.4.

To verify that the changes in the line strengths between minimum and maximum light are not caused by residual telluric effects, we also investigated changes in the telluric spectra. The top panels of Figure 5.5 show the six spectra of the same telluric standard (HD 98042) observed on the first night (23 February 2014) for the orders that contain the  $1.24\text{--}1.25\mu\text{m}$  K I doublet and the  $1.32\mu\text{m}$  H<sub>2</sub>O band head. We see that the overall flux was indeed changing over the course of the night. Because we divide Luhman 16B by Luhman 16A in our assessment of the flux variability, this telluric variability is removed. Fur-

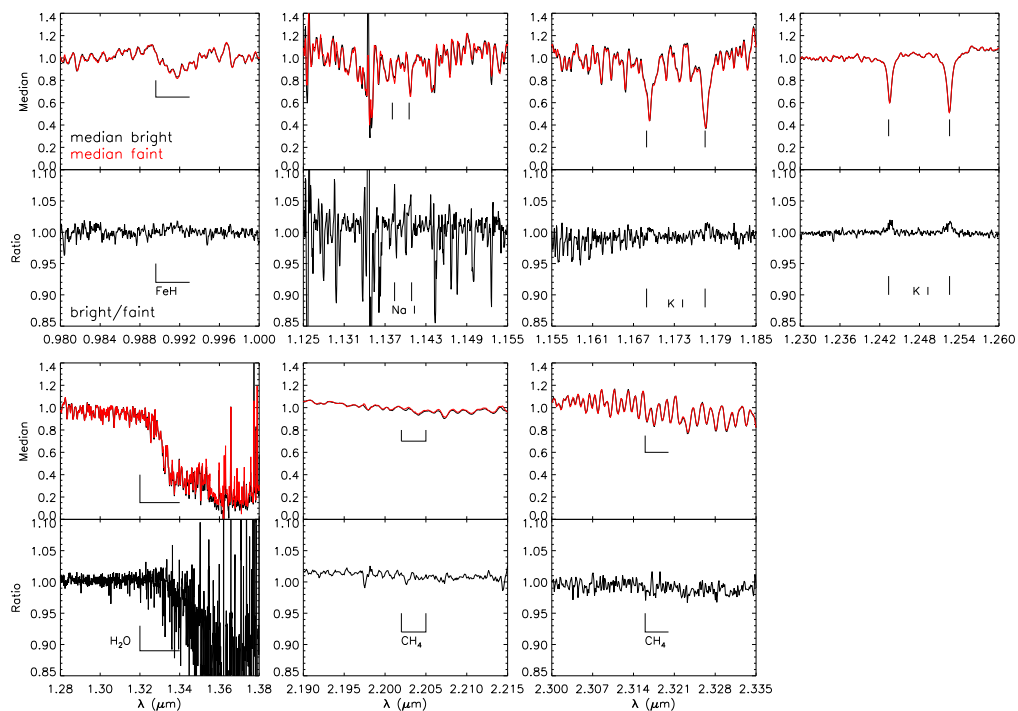


Figure 5.4: Relative absorption strength changes in the spectral regions of interest: around the FeH, Na I, K I, H<sub>2</sub>O, and CH<sub>4</sub> absorbers. The top sets of panels show the representative spectra of Luhman 16B at maximum (black) and minimum (red) light. The bottom sets of panels show the maximum-to-minimum light spectral ratios. We see a change in absorption strength of the two K I doublets and the water band but not of the other absorption features.

thermore, we see that the ratios of the brightest to the faintest telluric standard spectra in either order are relatively flat, with no high-frequency features above the noise level at the wavelengths of the K I doublet or the H<sub>2</sub>O band head (lower panels of Figure 5.5). We do notice changes in the telluric Na I feature at 1.268 $\mu$ m, but these do not affect other absorption features intrinsic to the brown dwarf. We conclude that although the recorded flux from the telluric standard was changing throughout the night, it did not affect our results.

### 5.3.3 VARIABILITY AND ABSORPTION STRENGTH CHANGES

Because our spectra span a relatively wide wavelength range (0.9–2.5 $\mu$ m), we are able to assess the flux variability over a broad range of atmospheric levels (e.g. Karalidi et al., 2016; Morley et al., 2014). The resolution of our spectra ( $R \sim 4000$ ) also allows us to accurately determine how each of the absorption features changes as the emergent flux varies.

Based on the first trough and peak of the first night of data in Figure 5.3, it appears that the variability amplitude for the continuum next to the K I absorption lines is larger in the NIR than it is in the optical. The NIR amplitude is  $\sim 16\%$  peak-to-trough while the optical amplitude is  $\sim 12\%$  peak-to-trough. Uncertainties in the amplitude are on average  $\pm 1\%$ . The continuum flux changes by similar amounts next to the other dominant absorbers—FeH (0.975–0.985 $\mu$ m continuum), Na I (1.145–1.155 $\mu$ m continuum) and water (1.280–1.322 $\mu$ m) continuum—by 15%, 15% and 13%, respectively. The variation appears to decrease in the *K*-band continuum next to the CH<sub>4</sub> features. The 2.190–2.200 $\mu$ m continuum next to the 2.20 $\mu$ m CH<sub>4</sub> band varies by 6% and the 2.300–2.310 $\mu$ m continuum next to the 2.31 $\mu$ m CH<sub>4</sub> band head has a large scatter rather than a clear periodic signature.

From the ratio of the bright and faint states (Fig. 5.4), we find that the amplitude of the variability within the water band is only about 88% of the amplitude of the continuum next to it. This is as expected, since gas-phase water absorption occurs at altitudes above the cloud deck in early T dwarfs (Apai et al., 2013; Yang et al., 2015). Conversely, the strengths of most other absorbers do not change by measurable amounts, except for small changes in the

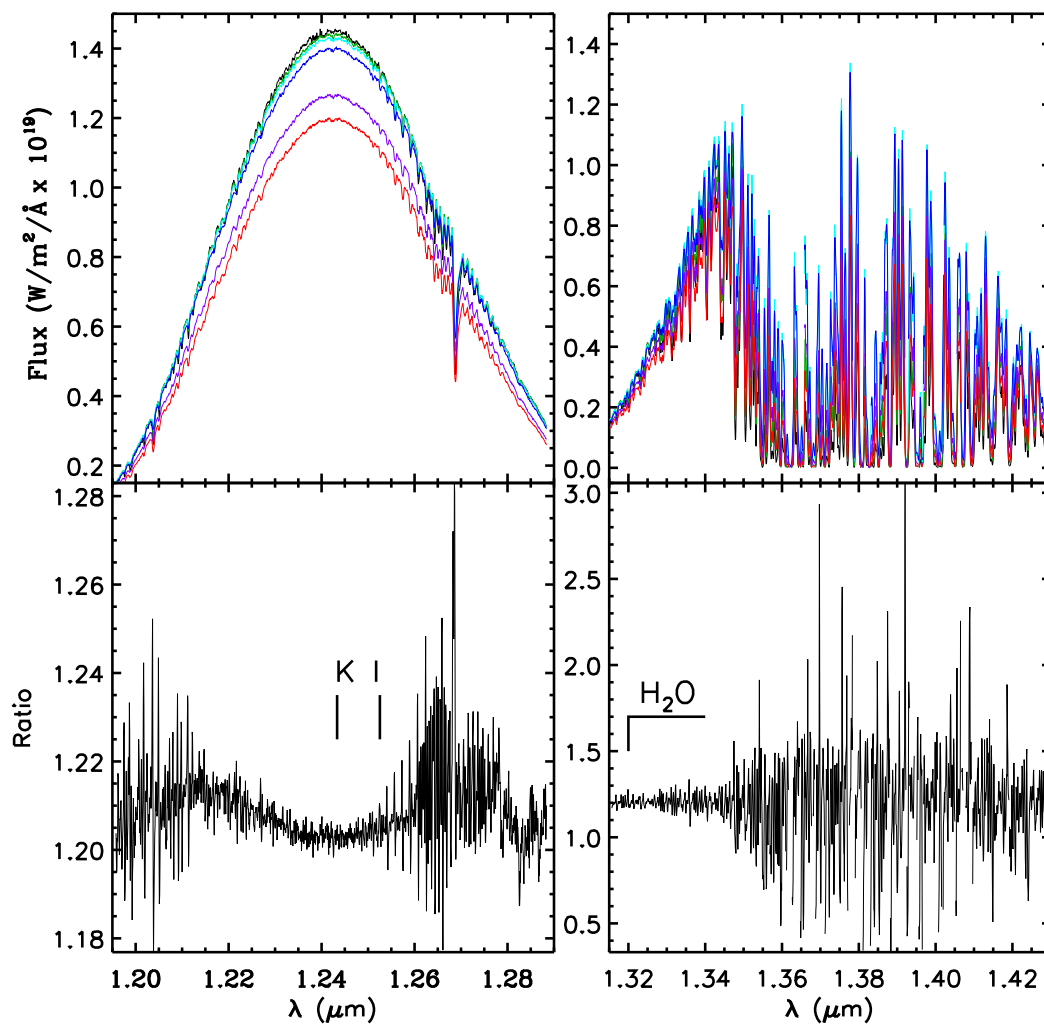


Figure 5.5: *Top panels:* Extractions from the six spectra of the HD 98042 telluric standard observed on 23 February 2014 for the orders that contain the 1.24–1.25  $\mu\text{m}$  K I doublet and the 1.32  $\mu\text{m}$  H<sub>2</sub>O band head. *Bottom panels:* Ratios of the brightest to faintest telluric standard spectra show no above-noise systematics near the K I lines and the H<sub>2</sub>O band head.

equivalent widths of K I doublets. The shorter-wavelength doublet changes by  $0.18 \pm 0.08 \text{ \AA}$  and  $0.15 \pm 0.07 \text{ \AA}$ , and the longer-wavelength doublet by  $0.21 \pm 0.06 \text{ \AA}$  and  $0.28 \pm 0.06 \text{ \AA}$ . These variations are 1–2% stronger than in the surrounding continuum: for an overall variability amplitude of 17–18% in the lines. Relative to the surrounding continuum, the K I lines are weaker in the bright state than in the faint state. We discuss the meaning of these results in the next section.

We sought to confirm the changes in the K I lines by means of Principal Component Analysis (PCA), as done for time-resolved HST/WFC3 grism spectroscopy of L and T dwarfs by Apai et al., 2013 and Buenzli et al., 2015b. PCA can isolate the main contributing factors in the wavelength-dependent light curve, and can potentially pinpoint the effect in the K I lines as a separate component. However, because the changes in the K I line strengths are well below the noise level in the individual spectra, this approach did not result in useful information. In addition, because we analyze all spectral orders after flattening the continuum—to avoid slit loss and telluric systematics—the PCA does not even reveal colour changes in the continuum: seen as a wavelength dependence in the variability amplitude of the first principal component in the HST/WFC3 spectra of Buenzli et al., 2015b. Hence, we do not use PCA further.

#### 5.4 DISCUSSION

Many ideas have been put forth for the cause of the variability in brown dwarfs, Luhman 16B in particular. Buenzli et al., 2015a,b and Karalidi et al., 2016 invoke clouds to explain the change in flux in Luhman 16B, which is the favored mechanism for variability at the L/T transition (Ackerman et al., 2001; Burgasser, 2002). Robinson et al., 2014 suggest that brightness temperature variations can also be produced by temperature perturbations introduced at the base of the atmosphere. Separately, Tremblin et al., 2016 suggest that in L/T transition objects, a reduced temperature gradient and temperature fluctuations caused by a thermochemical instability can reproduce the observed red colours and variable fluxes. The empirical evidence favors a joint effect of changing cloudiness and temperature at the L/T transition. Thus, Apai et al.,

2013 note that the NIR photometric and colour variations of the two early-T dwarfs 2MASS J21392676+0220226 (2M2139) and SIMP J013656.5+093347 (SIMP0136) can be explained as linear combinations of cloud thickness variations and effective temperature.

We note that any change in temperature or cloudiness of a single object may also be potentially reproducible as a spectral type change. Such a supposition offers an attractive premise for explaining the complex spectroscopic signature of what are often referred to as spectral binary ultra-cool dwarfs: candidate unresolved doubles with components of different spectral types that show the combined spectroscopic signature of both components (Burgasser, 2007). Indeed, 2M2139 is the best known example of an object that was initially suggested to be a strong spectral binary candidate (Burgasser et al., 2010), and was subsequently identified as a high-amplitude variable without evidence for a companion (Radigan et al., 2012). We also note that the Apai et al., 2013 conclusions about effective temperature and cloudiness changes as drivers for variability are not inconsistent with excursions along the spectral type sequence.

We explore the phenomenological characterization of variability in the context of spectral type changes in the following sections.

#### 5.4.1 SPECTRAL TYPE CHANGES

If the observed variations were the result of changing spectral morphology, one would expect the changes in absorption strengths to follow a spectral sequence. The ratio of an earlier spectral type representing the bright state and a later spectral type representing the faint state might be able to explain the wavelength-dependent differences in Figure 5.4. The spectral type change would be a small one considering that the changes in absorption strengths between spectral subtypes can be as small as only a few percent.

We investigated the amount of spectral type change necessary to reproduce the bright-to-faint ratios for Luhman 16B for some of the main absorption features in Figure 5.4. We created template spectra for the bright and faint states by combining pairs of L8 to T2 standard spectra from the BDSS survey (McLean et al., 2003), with weights in increments of 0.1. The spectrum for a bright state

would be, e.g.,  $0.9 \times \text{L8} + 0.1 \times \text{T2}$ , indicating proportional contributions from an L8 type and a T2 type atmosphere. We analyzed these template spectra in the same manner as we have our observed spectra, namely by forming ratios that represent bright and faint states. The spectra from the BDSS survey do not span the full NIR wavelength range—only  $1.14\text{--}2.30\mu\text{m}$ —so we were only able to assess the behaviour of the *J*-band K I,  $1.34\mu\text{m}$  H<sub>2</sub>O, and  $2.2\mu\text{m}$  CH<sub>4</sub> features.

We used a reduced  $\chi^2$  statistic to assess the quality of the template fits to the bright-to-faint ratios in each of the four testable wavelength regions. The errors in our reduced  $\chi^2$  calculation were estimated from the scatter in the continuum regions of the bright-to-faint ratio spectra. In Figure 5.6 we show the best-fit combinations of spectral templates, along with the distribution of the reduced  $\chi^2$  values up to twice the minimum  $\chi^2$ . From the top two panels of Figure 5.6, we see that the majority of the best fitting templates in the K I regions are made of similar components in the bright and faint states that differ in their leading coefficients by only 0.1 to 0.2. This means that only a small change in spectral types is needed to reproduce the change in K I absorption strength. The best fitting templates in the H<sub>2</sub>O region are also comprised of similar spectral types in the bright and faint states. However, while the dominant components tend to be the same, the secondary components in the best fitting templates often differ by one spectral subtype. That is, in comparison to the K I regions, the change in the H<sub>2</sub>O band head represents a larger change in spectral morphology. The CH<sub>4</sub> region provides fewer constraints than the other three regions. While the majority of the best fitting templates lie along the diagonal of the diagram—meaning the bright and faint states have similar dominating components—this region has a larger range of templates that fit well. This is mostly due to the fact that the bright-to-faint ratio of the CH<sub>4</sub> band head is relatively flat and is quite easy to replicate.

Overall, we see that the majority of best-fit templates cluster towards the top right of the diagram in all wavelength regions. This means that most of the best fitting templates are dominated by relatively warm L8 or L9 spectra with a smaller contribution from the cooler T1 or T2 spectra. There are a few tem-

plates that fit relatively well that are dominated by cooler T1 or T2 spectra but they do not fit well in all wavelength regions. We also see that the faint state template has a greater contribution from a cooler secondary spectrum than the bright state.

The ratios of spectral template linear combinations with the minimum  $\chi^2$  values for the selected absorbers are  $(0.9 \times L8 + 0.1 \times L9) / (0.9 \times L8 + 0.1 \times T0)$  and  $(0.9 \times T2 + 0.1 \times L9) / (0.9 \times T1 + 0.1 \times T2)$  for the K I doublets,  $(0.7 \times L9 + 0.3 \times T1) / (0.9 \times L9 + 0.1 \times T2)$  for the H<sub>2</sub>O band head and  $(0.9 \times L9 + 0.1 \times L8) / (0.8 \times L9 + 0.2 \times T1)$  for the CH<sub>4</sub> band head (Figure 5.7). We find, however, that a combination of an L9 and T1 in the bright state and an L9 and T2 in the faint state also fits all wavelength regions with low reduced  $\chi^2$  values (bottom comparison spectra in Figure 5.7). We interpret this to mean that the dominant component of the atmosphere is relatively warm and can be represented by an L9 spectrum. The changing cloud structure can then be represented by the changing secondary spectrum in the templates. During the bright state a cool T1 component contributes to the spectral morphology but when the flux decreases and goes into the faint state, the secondary component cools even further to a T2 spectral morphology. We see from Figure 5.7 however, that even though these templates have relatively low reduced- $\chi^2$  values, they do not reproduce the bright-to-faint spectra as well as the best-fitting templates. Because we have only used a single spectrum from each spectral type and spectral morphology ranges even within spectral types due to a variety in atmospheric structures, the templates do not fit perfectly and we can only use these templates as estimates of what components the atmosphere is made of.

From this analysis we see that the changes in spectral features of Luhman 16B can in fact be replicated by a change in spectral types. We find that the atmosphere of Luhman 16B can be represented by a predominantly warm L8 or L9 component with a smaller contribution from a cooler T1 or T2 component. Thus, we surmise that the mechanism that governs spectral appearance across the L/T transition may be the same as the mechanism that causes apparent variability in brown dwarfs.

The preceding conclusion is borne out of the use of spectral templates as

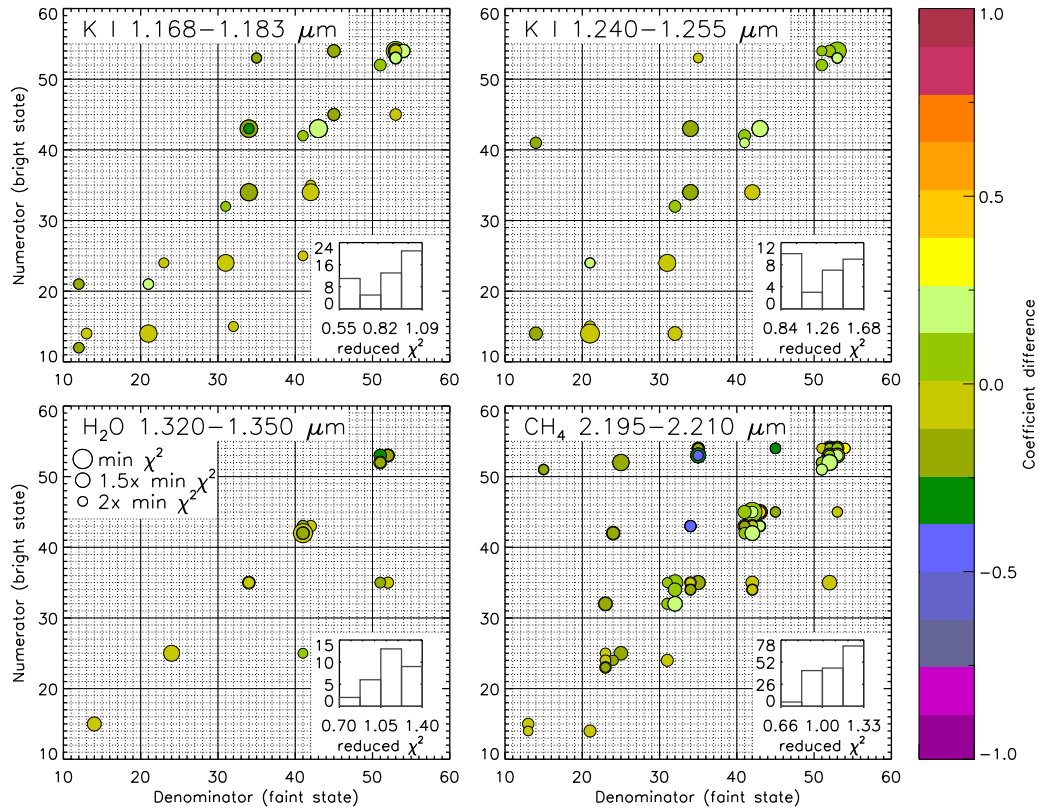


Figure 5.6: Results of fitting spectral templates to our bright-to-faint state ratios of Luhman 16B for each of the four testable wavelength regions. We include results with reduced  $\chi^2$  value up to only twice the minimum. Each spectral template combination is represented by two two-digit numbers: one for the numerator (indicated along the ordinate axes) and one for denominator (indicated along the abscissas). Each digit corresponds to a spectrum that comprises the template: the first digit to the dominant spectrum in the template (carrying a  $\geq 0.5$  weight), and the second digit to the secondary spectrum. The greater the digit, the warmer the spectrum: L8=5, L9=4, T0=3, T1=2, T2=1. A data point on any of the panels thus reflects a combination of BDSS spectral templates that represent the numerator and the denominator in the maximum-to-minimum light ratio. The colours correspond to the difference in the coefficient in front of the leading spectrum between the bright and faint states, with steps in units of 0.1. The sizes of the data points are inversely proportional to the reduced  $\chi^2$  value, so more probable fits are shown with larger symbols. As an example, the data point at (21,14) in the top left panel has a faint state that is made of a T1 + T2 template (encoded as '21'), a bright state spectrum that is made of an T2 + L9 template (encoded as '14') and the leading coefficients differ by 0. The overall ratio of this example template is  $(0.9 \times T2 + 0.1 \times L9) / (0.9 \times T1 + 0.1 \times T2)$ . The inset histograms show the distribution of the reduced  $\chi^2$  values of the best-fit templates up to twice the minimum  $\chi^2$  value.

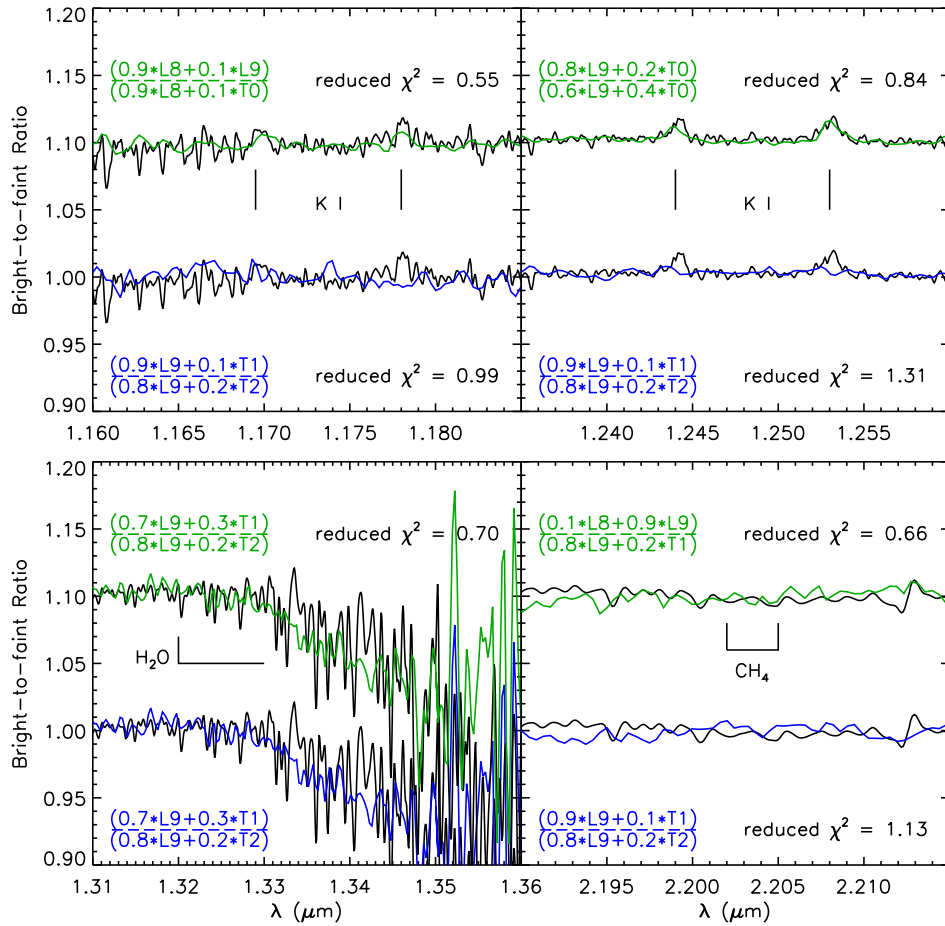


Figure 5.7: Ratio of template spectra representing the bright and faint states for the two K I doublets and the H<sub>2</sub>O and CH<sub>4</sub> band heads created using standard spectra from the BDSS survey (McLean et al., 2003). The green comparison spectra are the absolute best-fitting templates and the blue comparisons are the set of templates that have the same dominant and secondary spectra and fit well with relatively low reduced- $\chi^2$  values in all wavelength regions. In the H<sub>2</sub>O region, both templates are the same. The standard spectra used to create the templates are: 2MASS J16322911+1904407 (L8), DENIS-P J025503.3-470049.0 (L9), 2MASS J0423485-041403 (T0), SDSS J08371721-0000180 (T1) and SDSSp J125453.90-012247.4 (T2).

principal components. However, the result is unusual in that while the fainter state is slightly cloudier, it is best represented by a combination of subtypes that has a greater weighting on the early-T component (Fig. 5.7). This is contrary to the current understanding of spectroscopic sequencing across the L/T transition, where early T dwarfs are considered to be less cloudy than late L dwarfs. Hence, we speculate that the ordering of the L9–T1 spectral subtypes, while monotonic in CH<sub>4</sub> absorption strength, is not monotonic in effective temperature and fractional cloud coverage. This hypothesis is independently corroborated by two other facts. First, the L9–T1 spectral subtypes are missing from the optical late-L and T spectroscopic sequence, which jumps from L8 to T2 (Kirkpatrick, 2005), and indicates that the change in physical properties is too small to affect the red optical spectroscopic appearance. And second, the near-IR K I line strengths, which are sensitive to temperature and clouds in addition to surface gravity, follow a random progression in the L7–T2 range (Faherty et al., 2014). We therefore surmise that individual subtypes in the L9–T1 range represent random realizations of cloud fraction and effective temperature—even if only over a narrow range—and that the ordering by methane absorption strength obscures these effects.

#### 5.4.2 CLOUD TOMOGRAPHY

The spectroscopic differences in the variability can be combined with radiative transfer and condensation models to infer the pressure levels of the cloud decks. If a cloud deck resides at a lower pressure level than (i.e., above) the atmospheric regions contributing mostly to the source function at a certain wavelength, e.g., in the 1.25–1.32 $\mu\text{m}$  continuum, then the clouds will attenuate the detected flux at this wavelength. Conversely, if in a neighbouring wavelength region the source function originates at lower pressure levels, as in the 1.33–1.5 $\mu\text{m}$  water band, then the same cloud will have little influence on the detected flux. The combined effect across the 1.25–1.5 $\mu\text{m}$  region will be that of higher-amplitude variability in the continuum and the lower-amplitude variability in the water band: as found in Apai et al. (2013), and as we confirm in Figure 5.3.

With spectroscopic monitoring across the NIR, and at sufficiently high dis-

persion to resolve the pressure-sensitive alkali line profiles, we now have ample information to accurately map the vertical cloud structure in Luhman 16B. We conduct a preliminary analysis of the wavelength-dependence of the variability here, with more detailed inverse modeling deferred to a later publication.

We first consider the continuum variations, away from dominant atomic or molecular absorbers. From Figure 5.3, we see that the continuum variations decrease roughly monotonically with decreasing pressure level or increasing altitude (cf. Figure 12 in Karalidi et al., 2016). In order of decreasing pressure, the flux varies by 15% (FeH continuum), 15% (Na I continuum), 16% (NIR K I continua), 13% (H<sub>2</sub>O continuum), 12% (optical K I continuum), 6% (2.2 $\mu$ m CH<sub>4</sub> continuum), and  $\sim$ 2% (2.31 $\mu$ m CH<sub>4</sub> continuum). The decreasing variation with increasing altitude suggests that the optically thick clouds are located deep in the atmosphere and only directly affect the flux originating in the lower atmosphere. The peak in amplitude at the 1.23 $\mu$ m continuum (near K I) indicates that the clouds reside nearest this pressure level and have a decreasing affect on the flux originating above it.

We are the most interested in how the absorption features change over the course of the observations. From the bright-to-faint ratio of Luhman 16B, we see that there is no discernible change in strength of the FeH, Na I or CH<sub>4</sub> absorption. The only features which have a measurable change in strength relative to the surrounding continuum are the H<sub>2</sub>O and K I features. In the case of the H<sub>2</sub>O absorption, we observe a similar behaviour as seen by Apai et al. (2013) and Yang et al. (2015) in early T dwarfs. Namely, the strength of the water absorption is greater relative to the continuum in the bright state compared to the faint state. Yang et al. (2015) explain this by a high-altitude water haze, which resides above the inhomogeneous cloud layer driving variability in early T dwarfs.

Unexpectedly, the bright-to-faint ratios of the K I absorption features are greater than unity. This means that the absorption strength relative to the continuum in the faint state is greater than it is in the bright state. If we assume the most intuitive scenario of a cloud obscuring the deeper layers in the faint state, then with part of the K I column density removed, we would expect the

lines to decrease in strength. Instead, we observe the opposite. That is, when the cloud comes in and obscures the flux coming from the deeper atmosphere, the NIR K I absorption increases.

We consider two possible explanations for this phenomenon. On one hand, we may be observing a layer of enhanced neutral potassium haze that exists only above the cloud deck. Alkali cloud hazes have successfully been created in Earth’s upper stratosphere by injecting sodium atoms with rockets (e.g., Blamont, 2001). In the stable layers of Earth’s upper stratosphere these clouds have relatively long lifetimes. The conditions of a stratosphere above the dominant cloud deck in an ultra-cool atmosphere could be similarly stable. We note that at the lower end of the  $\approx 1000\text{--}1800$  K brightness temperatures probed by the  $1\text{--}6\mu\text{m}$  continuum in early T dwarfs (Morley et al., 2012), and at the 1–5 bar pressures that correspond to the peak of the  $1.0\text{--}1.3\mu\text{m}$  source function in Luhman 16B (see, e.g., Figure 12 in Karalidi et al., 2016), neutral potassium is close to equilibrium with its chloride, KCl (see Figure 14 in Burrows et al., 2001). It is conceivable that neutral potassium can therefore be locally enhanced through the dissociation of KCl. However, this runs in the opposite sense of what may be expected. The temperature above the cloud top should be lower than if the optically thick clouds were absent, as they impede the radiative heat transfer from the deeper atmosphere. Hence, we would expect enhanced formation of KCl above the cloud deck, rather than enhanced dissociation, and so depletion of neutral potassium through this mechanism.

On the other hand, rather than changing neutral potassium abundances, the varying strengths of the K I doublets could simply reflect the different states of the temperature-pressure relation in the presence vs. absence of a cloud deck. When a cloud deck is present, the observable emission from the atmosphere is cooler. As discussed in Section 5.4.1, the observed spectroscopic variability can be well represented by increasing contributions from cooler spectral templates in the faint state. Considering the NIR spectroscopic sequences of L and T dwarfs from Kirkpatrick, 2005 and Cushing et al., 2005, we see that the absorption strength of K I decreases from early- to late-L dwarfs until  $\sim\text{L}8$ . However, between the L8 and T2 spectral types, the strength increases before it decreases

again into the mid- to late-T dwarfs and disappears altogether. This agrees with the observed 1–2% stronger K I absorption in the cooler state of Luhman 16B.

Although we cannot conclusively determine the specific mechanism that causes the increased absorption strength—changing K I abundances or T-P profiles—it is evident that the effects of the variability can be reproduced by changing combinations of spectral types. Thus, the mechanism that is responsible for the NIR photometric variability and the change of the K I absorption strengths may well be identical to the one that governs the diversity of spectral morphology across the L/T transition.

## 5.5 CONCLUSIONS

We monitored Luhman 16AB for two nights at  $R \sim 4000$  over the 0.9–2.5 $\mu\text{m}$  wavelength range. This experiment has offered the unprecedented opportunity to study the atmospheric changes in the more highly variable early T-type secondary component at high SNR. Our analysis shows that:

- the variability amplitude of Luhman 16B decreases with decreasing pressure level, indicating that the variability mechanism operates at pressures at least as high as those corresponding to the 1.2 $\mu\text{m}$  continuum ( $\sim 2\text{--}3$  bars; Karalidi et al., 2016);
- the NIR K I absorption strength increases in the faint state, either because of an increased K I abundance above the cloud deck or because of changes in the temperature-pressure profile;
- the variability behaviour can be decomposed as a changing combination of late-L and early-T spectral templates.

The decreasing variability with pressure confirms the results of Apai et al., 2013 which demonstrates that the variability causes the  $J$ -band flux to vary more than the  $J - K_s$  colour. This gives the L/T transition a wide range in  $M_J$  magnitudes on a colour-magnitude diagram. We have been able to reproduce the bright-to-faint ratio of Luhman 16B with a template which is predominantly a relatively warm L8 or L9 with a smaller contribution from a cooler T1

or T2 component. The faint state also has a cooler secondary component than the bright state meaning that during the faint state, part of the atmosphere is slightly cooler than in the bright state.

We interpret the ability to reproduce the ratios with changing spectral templates as an indication that the governing mechanism of brown dwarf variability is the same as the one responsible for the diversity in spectral morphology across the L/T transition. We also find that since the fainter, cloudier state paradoxically requires greater contributions from clearer T-type photospheres, the L9–T1 portion of the spectral sequence does not follow a monotonic trend in either effective temperature or cloud coverage.

## REFERENCES

- Ackerman, A. S. and Marley, M. S. (2001). *ApJ* 556, pp. 872–884. DOI: [10 . 1086/321540](https://doi.org/10.1086/321540).
- Apai, D., Radigan, J., Buenzli, E., et al. (2013). *ApJ* 768, 121, p. 121. DOI: [10 . 1088/0004-637X/768/2/121](https://doi.org/10.1088/0004-637X/768/2/121).
- Artigau, É., Bouchard, S., Doyon, R., et al. (2009). *ApJ* 701, pp. 1534–1539. DOI: [10.1088/0004-637X/701/2/1534](https://doi.org/10.1088/0004-637X/701/2/1534).
- Billier, B. A., Crossfield, I. J. M., Mancini, L., et al. (2013). *ApJ* 778, L10, p. L10. DOI: [10.1088/2041-8205/778/1/L10](https://doi.org/10.1088/2041-8205/778/1/L10).
- Blamont, J (2001). *The Century of Space Science*. Ed. by Johan A. M. Bleeker, Johannes Geiss, and Martin C. E. Huber. Dordrecht: Springer Netherlands, pp. 189–202. ISBN: 978-94-010-0320-9. DOI: [10.1007/978-94-010-0320-9\\_7](https://doi.org/10.1007/978-94-010-0320-9_7).
- Bochanski, J. J., Hennawi, J. F., Simcoe, R. A., et al. (2009). *PASP* 121, pp. 1409–1418. DOI: [10.1086/648597](https://doi.org/10.1086/648597).
- Buenzli, E., Saumon, D., Marley, M. S., et al. (2015a). *ApJ* 798, 127, p. 127. DOI: [10.1088/0004-637X/798/2/127](https://doi.org/10.1088/0004-637X/798/2/127).
- (2015b). *ApJ* 798, 127, p. 127. DOI: [10.1088/0004-637X/798/2/127](https://doi.org/10.1088/0004-637X/798/2/127).
- Burgasser, A. J. (2002). PhD thesis. California Institute of Technology.
- (2007). *ApJ* 659, pp. 655–674.

- Burgasser, A. J., Cruz, K. L., Cushing, M., et al. (2010). *ApJ* 710, pp. 1142–1169. DOI: [10.1088/0004-637X/710/2/1142](https://doi.org/10.1088/0004-637X/710/2/1142).
- Burgasser, A. J., Sheppard, S. S., and Luhman, K. L. (2013). *ApJ* 772, 129, p. 129. DOI: [10.1088/0004-637X/772/2/129](https://doi.org/10.1088/0004-637X/772/2/129).
- Burgasser, A. J., Gillon, M., Faherty, J. K., et al. (2014). *ApJ* 785, 48, p. 48. DOI: [10.1088/0004-637X/785/1/48](https://doi.org/10.1088/0004-637X/785/1/48).
- Burrows, A., Hubbard, W. B., Lunine, J. I., et al. (2001). *Reviews of Modern Physics* 73, pp. 719–765. DOI: [10.1103/RevModPhys.73.719](https://doi.org/10.1103/RevModPhys.73.719).
- Crossfield, I. J. M. (2014). *A&A* 566, A130, A130. DOI: [10.1051/0004-6361/201423750](https://doi.org/10.1051/0004-6361/201423750).
- Cushing, M. C., Vacca, W. D., and Rayner, J. T. (2004). *PASP* 116, pp. 362–376. DOI: [10.1086/382907](https://doi.org/10.1086/382907).
- Cushing, M. C., Rayner, J. T., and Vacca, W. D. (2005). *ApJ* 623, pp. 1115–1140. DOI: [10.1086/428040](https://doi.org/10.1086/428040).
- Faherty, J. K., Beletsky, Y., Burgasser, A. J., et al. (2014). *ApJ* 790, 90, p. 90. DOI: [10.1088/0004-637X/790/2/90](https://doi.org/10.1088/0004-637X/790/2/90).
- Gillon, M., Triaud, A. H. M. J., Jehin, E., et al. (2013). *A&A* 555, L5, p. L5. DOI: [10.1051/0004-6361/201321620](https://doi.org/10.1051/0004-6361/201321620).
- Karalidi, T., Apai, D., Marley, M. S., et al. (2016). *ApJ* 825, 90, p. 90. DOI: [10.3847/0004-637X/825/2/90](https://doi.org/10.3847/0004-637X/825/2/90).
- Kirkpatrick, J. D. (2005). *ARA&A* 43, pp. 195–245.
- Luhman, K. L. (2013). *ApJ* 767, L1, p. L1. DOI: [10.1088/2041-8205/767/1/L1](https://doi.org/10.1088/2041-8205/767/1/L1).
- McLean, I. S., McGovern, M. R., Burgasser, A. J., et al. (2003). *ApJ* 596, pp. 561–586. DOI: [10.1086/377636](https://doi.org/10.1086/377636).
- Metchev, S., Apai, D., Radigan, J., et al. (2013). *Astronomische Nachrichten* 334, pp. 40–43. DOI: [10.1002/asna.201211776](https://doi.org/10.1002/asna.201211776).
- Metchev, S. A., Heinze, A., Apai, D., et al. (2015). *ApJ* 799, 154, p. 154. DOI: [10.1088/0004-637X/799/2/154](https://doi.org/10.1088/0004-637X/799/2/154).
- Moffat, A. F. J. (1969). *A&A* 3, p. 455.
- Morley, C. V., Fortney, J. J., Marley, M. S., et al. (2012). *ApJ* 756, 172, p. 172. DOI: [10.1088/0004-637X/756/2/172](https://doi.org/10.1088/0004-637X/756/2/172).

- Morley, C. V., Marley, M. S., Fortney, J. J., et al. (2014). *ApJ* 789, L14, p. L14.  
DOI: [10.1088/2041-8205/789/1/L14](https://doi.org/10.1088/2041-8205/789/1/L14).
- Radigan, J. (2014). *ApJ*, in press, <http://arxiv.org/abs/1408.5919>.
- Radigan, J., Jayawardhana, R., Lafrenière, D., et al. (2012). *ApJ* 750, 105, p. 105.  
DOI: [10.1088/0004-637X/750/2/105](https://doi.org/10.1088/0004-637X/750/2/105).
- Radigan, J., Lafrenière, D., Jayawardhana, R., et al. (2014). *ApJ* 793, 75, p. 75.  
DOI: [10.1088/0004-637X/793/2/75](https://doi.org/10.1088/0004-637X/793/2/75).
- Radigan, J. M. (2013). *Ph.D. Thesis, The University of Toronto, Toronto, Ontario, Canada*. Available at <http://www.astro.utoronto.ca/theses/thesis13.radigan.pdf>.
- Robinson, T. D. and Marley, M. S. (2014). *ApJ* 785, 158, p. 158. DOI: [10.1088/0004-637X/785/2/158](https://doi.org/10.1088/0004-637X/785/2/158).
- Simcoe, R. A., Burgasser, A. J., Bernstein, R. A., et al. (2008). *Society of Photo-Optical Instrumentation Engineers (SPIE) Conference Series*. Vol. 7014. Society of Photo-Optical Instrumentation Engineers (SPIE) Conference Series.  
DOI: [10.1117/12.790414](https://doi.org/10.1117/12.790414).
- Simcoe, R. A., Burgasser, A. J., Schechter, P. L., et al. (2013). *PASP* 125, p. 270.  
DOI: [10.1086/670241](https://doi.org/10.1086/670241).
- Tremblin, P., Amundsen, D. S., Chabrier, G., et al. (2016). *ApJ* 817, L19, p. L19.  
DOI: [10.3847/2041-8205/817/2/L19](https://doi.org/10.3847/2041-8205/817/2/L19).
- Vacca, W. D., Cushing, M. C., and Rayner, J. T. (2003). *PASP* 115, pp. 389–409. DOI: [10.1086/346193](https://doi.org/10.1086/346193).
- Yang, H., Apai, D., Marley, M. S., et al. (2015). *ApJ* 798, L13, p. L13. DOI: [10.1088/2041-8205/798/1/L13](https://doi.org/10.1088/2041-8205/798/1/L13).
- Yang, H., Apai, D., Marley, M. S., et al. (2016). *ApJ* 826, 8, p. 8. DOI: [10.3847/0004-637X/826/1/8](https://doi.org/10.3847/0004-637X/826/1/8).

# 6

## Discovery of a Possible Early-T Thick-Disk/Halo Subdwarf from the AllWISE 2 Motion Survey

### 6.1 INTRODUCTION

Brown dwarfs are the lowest mass products of star formation. With masses that are below the hydrogen burning minimum mass (HBMM;  $<75M_{\text{Jup}}$ ), they cannot undergo sustained nucleosynthesis like their higher mass brethren. As such, their compositions stay essentially unchanged from when they formed (e.g. Burrows et al., 1993; Marley et al., 1996). Metal-poor brown dwarfs and very low-mass stars offer unique insights into the young Milky Way as they are objects that formed in the early galaxy and their compositions have not changed much since that time.

Recently, dedicated searches for the old, low-mass population of objects in our galaxy have been carried out using the Wide-field Infrared Survey Explorer (WISE; Kirkpatrick et al., 2014, 2016; Pinfield et al., 2014), UKIDSS Large-

---

A version of this chapter has been submitted to The Astronomical Journal.

Area Survey (ULAS; Zhang et al., 2017a), Two-Micron All Sky Survey (2MASS; Kirkpatrick et al., 2010), and Sloan Digital Sky Survey (SDSS; Sivarani et al., 2009). The totality of the results of these surveys reveals that these objects are relatively rare. The very lowest metallicity objects belong to the galactic halo of the Milky Way and are the oldest objects in the galaxy. At a slightly younger age and higher metallicity are the members of the thick-disk. Both populations have high space velocities and are very uncommon in the solar neighbourhood. Only  $\sim 6\%$  and  $<1\%$  of the brown dwarfs in the vicinity of the sun are expected to be part of either the thick-disk or halo populations, respectively (Gazzano et al., 2013). These objects have primordial compositions and are excellent testing grounds for models at low metallicities.

L/T transition subdwarfs, in particular, are of key interest in studying the effects of metallicity on cloud physics in atmospheric models. The transition between L and T dwarfs, in the case of solar-metallicity brown dwarfs, is a rapid evolution from cloudy to clear atmospheres (e.g. Ackerman et al., 2001; Burgasser et al., 2002; Burrows et al., 2001; Marley et al., 2002) and takes place over a narrow effective temperature range of only 200–300K (e.g. Kirkpatrick, 2005). Late-L and early-T subdwarfs, then, are excellent objects to study the role that metallicity plays in the evolution of brown dwarfs and their atmospheres. Due to the nature of the L/T transition, however, this spectral range is comparatively devoid of objects, even more so than the late-T subdwarfs which are not readily detected due to their intrinsically faint near-infrared magnitudes.

There has also been evidence that there is a “subdwarf gap” which divides stellar and sub-stellar objects at late ages on a colour-magnitude diagram. Stellar theory predicts that at  $\sim 10$  Gyr, the lowest mass stars and brown dwarfs diverge in their observable properties due to the different energy production process above and below the hydrogen-burning minimum mass (e.g. Burgasser, 2004a; Burrows et al., 2001; Chabrier et al., 1997). Low-mass stars and brown dwarfs are more difficult to distinguish at younger ages but evolution models predict the stellar/substellar boundary occurs at higher temperatures for solar metallicity objects and brown dwarfs have spectral types as early as M6 (e.g. Baraffe et al., 2015; Burrows et al., 2001; Dupuy et al., 2017). Searches for low-

metallicity objects reveal that the subdwarf gap appears to be between mid- and late-L dwarfs (Kirkpatrick et al., 2016; Zhang et al., 2017b). Late-L/early-T subdwarfs, then, would be on the substellar side of this region. The exact extension of the gap, however, has yet to be determined and locating the edges is of keen interest in the study of low-metallicity objects.

Given the rarity of halo/thick-disk brown dwarfs, finding even one new object to study is a significant step forward in understanding this population. An even more important step to understanding old, low-metallicity objects and their atmospheres is filling in the gap between late-L and late-T subdwarfs. As part of the AllWISE2 Motion Survey (hereafter AllWISE2; Kirkpatrick et al., 2016), we have possibly identified the second object in this spectral range that also has kinematics consistent with the population of thick-disk/halo objects — WISE J071121.36–573634.2.

In §6.2 we discuss how we identified this object and in §6.3 we outline our observations and data reduction. We discuss the spectral classification of WISE J0711–5736 in §6.4 and put it in context of the population of halo/thick-disk objects in §6.5.

## 6.2 CANDIDATE SELECTION

The AllWISE1 and AllWISE2 Motion Surveys (Kirkpatrick et al., 2014, 2016) were searches designed to leverage the multi-epoch mid-infrared observations of the entire sky and identify objects with proper motions detectable over the 1-year period of the AllWISE mission. Objects with such high apparent motions are either located in the solar neighbourhood or have inherently large space velocities. The AllWISE1 Motion Survey imposed an  $rchi2/rchi2\_pm > 1.03$ , selecting objects where the  $\chi^2$  value of the stationary fit was at least 3% higher than the  $\chi^2$  of the motion fit. This criteria was removed for the AllWISE2 Motion Survey allowing objects with smaller motions to potentially be recovered in the second iteration of the survey. An interesting subset of the motion sources are ones that do not have counterparts in surveys at shorter wavelengths (e.g SDSS and 2MASS) — typically late-T and Y dwarfs. The model

predictions for the spectral energy distributions of such objects peak at  $\sim 4\text{--}12\mu\text{m}$  ( $700\text{K} > T_{\text{eff}} > 250\text{K}$ ) so they are very often undetected in optical and near-IR surveys. We, therefore, created a devoted search for similar objects.

We published 58 WISE-only candidates from AllWISE1 in Kirkpatrick et al., 2014. We implemented the same type of selection criterion for WISE-only sources in AllWISE2, selecting objects that did not have counterparts in 2MASS or SDSS. After visual verifications (details in section 2 of Kirkpatrick et al., 2016), we ended up with 11 WISE-only objects from AllWISE2, for a total of 69 candidate late-T and Y dwarfs from both AllWISE1 and AllWISE2. The WISE magnitudes and proper motions of the 11 new WISE-only AllWISE2 candidates are presented in Table 6.1. One AllWISE1 object turned out to be an important new discovery: the Y dwarf WISEA J085510.74–071442.5 (Luhman, 2014). Four of the candidates from AllWISE2 were also already known T and Y dwarfs: WISE J223617.60+510551.8 (T5), WISE J104752.35+212417.2 (T6.5), WISE J115013.85+630241.5 (T8), and WISE J140518.39+553421.3 (Y0pec?). Two of the known ultra-cool dwarfs — WISE J104752.35+212417.2 and WISE J223617.60+510551.8 — actually did have 2MASS counterparts but their motions are high enough that they were not recognized in the 2MASS images. For the rest of the analysis, we only consider the 64 new candidate ultra-cool dwarfs.

Table 6.1: AllWISE2 Motion Candidates Lacking 2MASS Counterparts

Designation	W1 (mag)	W2 (mag)	AllWISE (R.A. Motion) (mas yr <sup>-1</sup> )	AllWISE (Decl. Motion) (mas yr <sup>-1</sup> )	Calculated $\mu_{\alpha} \cos(\delta)$ (mas yr <sup>-1</sup> )	Calculated $\mu_{\delta}$ (mas yr <sup>-1</sup> )	Spectral Type	Discovery Publication
WISE J003428.12+393153.7	15.910 ± 0.046	14.666 ± 0.050	663 ± 224	-1033 ± 233	-3 ± 25	-48 ± 80		1
WISE J071121.36-573634.2	15.092 ± 0.029	14.627 ± 0.038	507 ± 137	998 ± 145	18 ± 10	990 ± 90		1
WISE J081031.30-475602.8	15.741 ± 0.039	14.398 ± 0.041	-1215 ± 272	-902 ± 274	6 ± 25	63 ± 80		1
WISE J082811.56-443738.1 <sup>a</sup>	14.751 ± 0.031	12.650 ± 0.024	512 ± 83	643 ± 88	2 ± 28	18 ± 85		1
WISE J102055.17+530859.4	15.666 ± 0.042	14.526 ± 0.047	1247 ± 304	1287 ± 326	-2 ± 25	31 ± 80		1
WISE J104752.35+212417.2	15.377 ± 0.036	13.004 ± 0.030	-908 ± 171	-682 ± 186	-112 ± 25	-516 ± 80	T6.5	2
WISE J115013.85+630241.5	16.958 ± 0.089	13.405 ± 0.028	330 ± 198	-1194 ± 202	63 ± 25	-540 ± 80	T8	3
WISE J122738.12-232819.6	16.102 ± 0.058	14.692 ± 0.061	1897 ± 317	221 ± 352	7 ± 27	33 ± 85		1
WISE J140518.39+553421.3	18.765 ± 0.396	14.097 ± 0.037	-1862 ± 326	-324 ± 334	-265 ± 25	187 ± 80	Y0(pec?)	3
WISE J153747.73+181151.3	14.198 ± 0.025	12.220 ± 0.022	-228 ± 64	-367 ± 69	5 ± 25	48 ± 80		1
WISE J223617.60+510551.8	13.827 ± 0.025	12.499 ± 0.025	573 ± 99	-118 ± 89	70 ± 27	358 ± 85	T5	4

Discovery papers are: <sup>1</sup> This work, <sup>2</sup>Burgasser et al., 1999, <sup>3</sup>Kirkpatrick et al., 2011, <sup>4</sup>Mace et al., 2013a.

<sup>a</sup> WISE J081031.30-475602.8 is a flux transient rather than a motion object.

All of the new objects had motions that were quite small and at the limit of bye-eye detection. Since the longest baseline for any of the objects was only 0.5 yr, we turned to the new data from the NEOWISE Reactivation mission (Mainzer et al., 2011) to provide a longer baseline. We used the WISE co-add tool\* developed at IPAC to combine images for each of the 64 new candidates for comparison. We created two co-added images: one from the observations during the first observational epoch (early 2010; WISE All-Sky) and one from observations during the last epoch (late 2015; NEOWISE-R). This gave a baseline of  $>5$  years for most candidates, sufficient to authenticate their motion. Calculated proper motions based on the longer baseline co-added images are presented in Table 6.1. One object, WISE J082811.56–443738.1, turned out to increase in brightness rather than have any motion so we did not follow this object up.

One candidate showed clear motion — WISE J071121.36–573634.2 (hereafter WISE J0711–5736). The co-added W2 images of WISE J0711–5736 from the first and last observational epoch are shown in Figure 6.1. From these images, we calculated a more accurate proper motion of WISE J0711–5736 (Table 6.2) compared to the AllWISE proper motion estimates (Table 6.1).

This object, however, does not have the characteristic infrared colours of a late-T or Y dwarf. Instead, the colours appeared to be that of a late-L or early-T dwarf based on the  $W1$ – $W2$  vs spectral type relation from Kirkpatrick et al., 2011. With this assumption and an estimated absolute  $W2$  magnitude for this spectral range from Faherty et al., 2016, we calculated a photometric distance (36–39 pc) and tangential velocity (165–200 km s<sup>−1</sup>) consistent with the population of galactic halo/thick-disk objects. We also calculated the reduced proper motion ( $H_{W2} = W2 + 5\log(\mu) + 5$ ) of this object to be  $\approx 19.6$  mag. From Figure 11 of Pinfield et al., 2014, we see that the  $H_{W2}$  and  $W1 - W2$  values put this object far outside the 100 km s<sup>−1</sup> curve — also consistent with being part of at least the thick-disk population. For verification of the spectral type of WISE J0711–5736 we obtained near-IR spectra. The details are outlined in the next section.

---

\*<http://irsa.ipac.caltech.edu/applications/ICORE/>

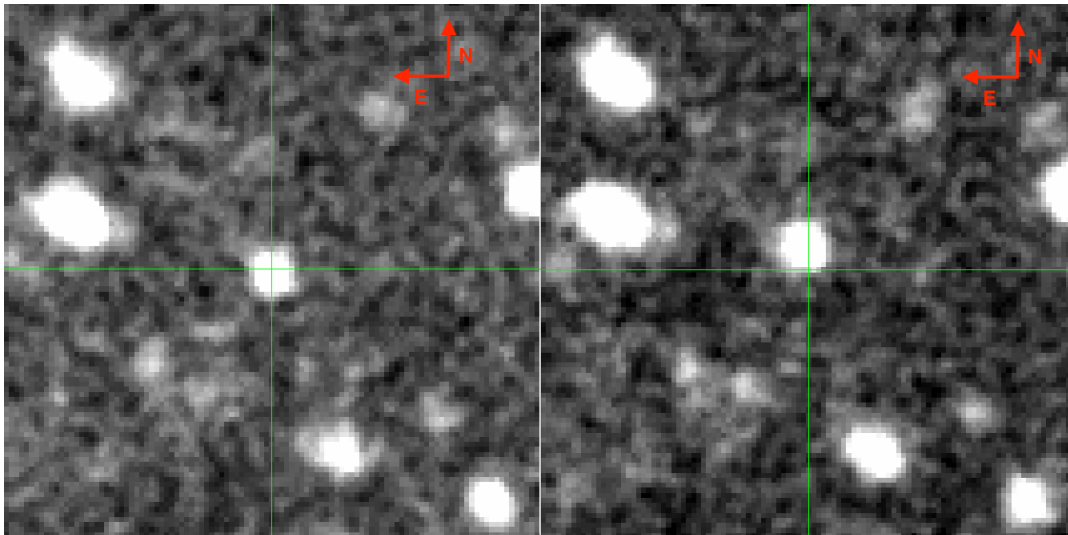


Figure 6.1: Co-added  $2' \times 2'$  images from WISE in W2. The first image is from UT 2010 May 4 (WISE All-Sky), the second is from UT 2015 Nov 16 (NEOWISE-R).

Table 6.2: Object Properties

Identifier	WISE J071121.36–573634.2
RA	07:11:21.36
Dec	–57:36:34.20
W1	$15.092 \pm 0.029$ mag
W2	$14.627 \pm 0.038$ mag
W3	$12.504 \pm 0.500$ mag
W4	$9.558 \pm 0.500$ mag
Calculated $\mu_\alpha \cos(\delta)$	$18 \pm 10$ mas yr $^{-1}$
Calculated $\mu_\delta$	$990 \pm 90$ mas yr $^{-1}$
$H_{W2}$	$19.61 \pm 0.02$ mag

### 6.3 SPECTROSCOPIC OBSERVATIONS AND DATA REDUCTION

We observed WISE J0711–5736 on UT 2016 December 14 with the Folded-port InfraRed Echellette (FIRE; Simcoe et al., 2008, 2013) at the *Magellan*/Baade telescope in the high-throughput prism mode. The weather was clear with a seeing of  $\sim 0''.3$ . We used the  $0''.6$  slit, yielding a resolving power of  $R \sim 450$  in the 0.8–2.45  $\mu\text{m}$  wavelength range. We obtained four 120 s exposures in a nodding ABBA pattern along the slit at airmasses of 1.262–1.275, yielding a signal-to-noise ratio of  $\sim 50$  per pixel in the 1.5–1.8  $\mu\text{m}$  range. The telluric exposures which were obtained immediately before WISE J0711–5736 were saturated and therefore not usable. The A0-type star HD 35265 observed on UT 2016 January 22 with six 1 s exposures under clear weather conditions, a seeing of  $\sim 0''.6$ , and an airmass of 1.210–1.231 was therefore used to perform the telluric correction

package (Bochanski et al., 2009; Gagné et al., 2015<sup>†</sup>; see Gagné et al., 2015 for more details on the reduction package). We extracted the spectra using an optimal extraction approach. The local background was modeled using a basis spline fit to the masked aperture profile and subtracted it from the spectra. We subsequently extracted the spectra using a weighted profile extraction approach. We wavelength-calibrated and median-combined the resulting spectra using a modified version of the Spextool routine `xcombspec` (Cushing et al., 2004). Finally, we corrected for telluric absorption and flux-calibrated the spectra with `tellcor_general.pro` using the A0 calibration star.

Since our telluric standard was observed 11 months prior to WISE J0711–5736 and the precipitable water content in the atmosphere was likely not the same on the two nights, we performed the same type of telluric correction using two additional standards. Observed at an airmass of  $\sim 1.07$  on 2016 January 22, HD 102338 was located in a region of sky with lower water content than HD 35265 (airmass  $\approx 1.22$ ) and HD 149818, observed at an airmass of  $\sim 1.83$  on 2016 January 22, was located in a region of sky with higher water content. Figure 6.2 shows the comparison of WISE J0711–5736 corrected with all three telluric standards and smoothed for clarity. As we can see, the depths of all the water bands ( $1.10\text{--}1.18\mu\text{m}$ ,  $1.30\text{--}1.45\mu\text{m}$ , and  $1.70\text{--}1.95\mu\text{m}$ ) are similar between the spectra corrected with two standards at low and moderate airmasses (HD 102338 and HD 35265). The spectrum that was corrected with the standard at a higher airmass (HD 149818) has less water absorption. However, the residual telluric features at  $2.0\text{--}2.1\mu\text{m}$  indicate that the spectrum corrected with HD 149818 was over-corrected and too much water absorption was removed. We conclude that performing a correction with HD 35265 was sufficient to remove all of the telluric absorption. We also conclude that the depths of the water bands are intrinsic to WISE J0711–5736 and are not a consequence of correcting with a telluric standard that was observed on a night with different precipitable water content.

---

<sup>†</sup>Available at [https://github.com/jgagneastro/FireHose\\_v2/tree/v2.0](https://github.com/jgagneastro/FireHose_v2/tree/v2.0)

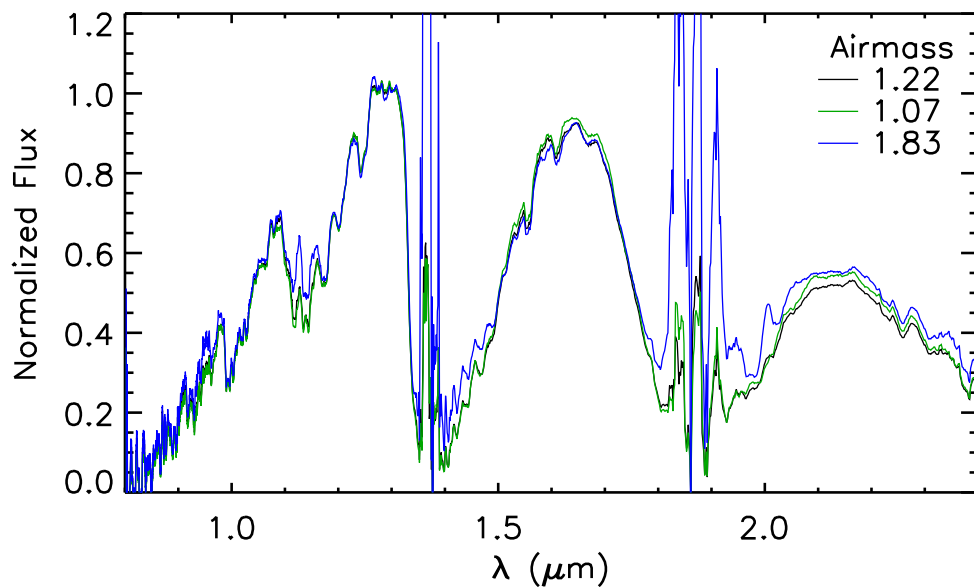


Figure 6.2: Comparison of smoothed spectra of WISE J0711–5736 telluric corrected with HD 35265 (airmass  $\approx 1.22$ ; black), HD 102338 (airmass  $\approx 1.07$ ; green) and HD 149818 (airmass  $\approx 1.83$ ; red).

## 6.4 SPECTRAL CLASSIFICATION AND KINEMATICS

In order to classify WISE J0711–5736, we compare our FIRE spectrum to spectra of published objects and to theoretical spectra. When comparing to published spectra, we smooth our medium-resolution spectrum to the resolution of the comparison object using a least-squares quadratic interpolation. All spectra are normalized to the median flux value in the  $1.25\text{--}1.30\mu\text{m}$  region.

### 6.4.1 LATE-L/EARLY-T SUBDWARF

In Figure 6.3 we compare our FIRE spectrum of WISE J0711–5736 to the closest matching spectra of each type of L9–T1 dwarf from the SpeX Prism Library. From this comparison, we see that WISE J0711–5736 has more FeH and K I absorption than all of the comparison objects and very little CO absorption at  $\sim 2.3\mu\text{m}$ . We also see that WISE J0711–5736 has deeper water bands.

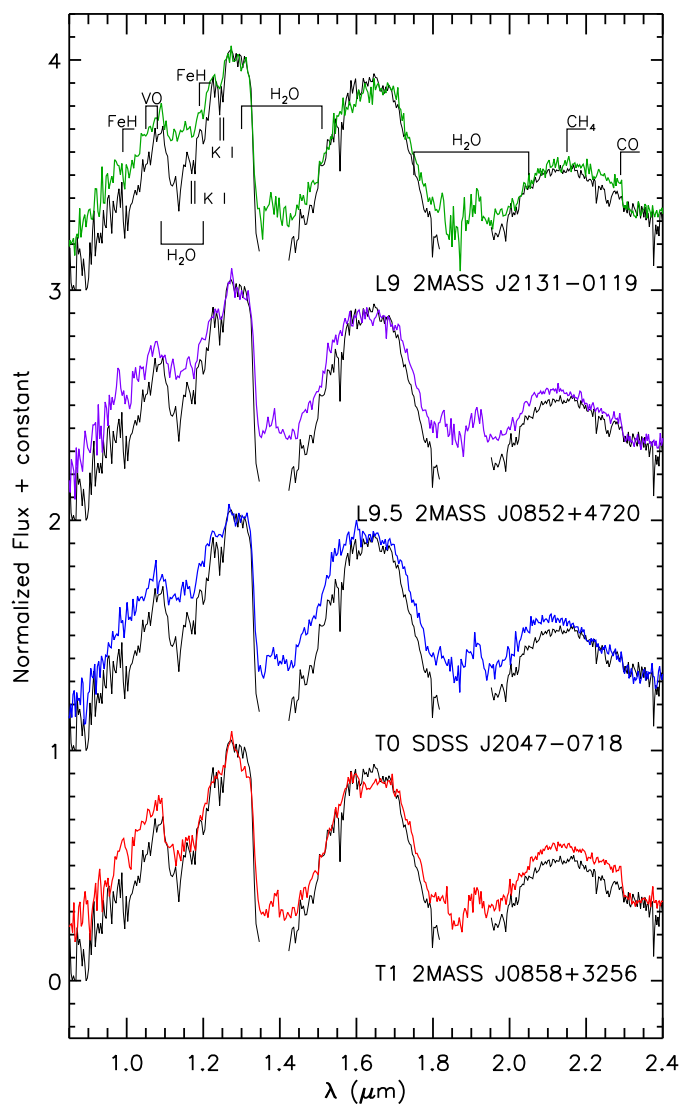


Figure 6.3: Our FIRE spectrum of WISE J0711–5736 (black) compared to SpeX Prism Library spectra of L9–T1 dwarfs. The FIRE spectrum has been smoothed to the resolution of the SpeX spectra. Comparison spectra are: L9 (2MASS J21315444–0119374; Chiu et al., 2006); L9.5 (2MASS J08523490+4720359; Burgasser et al., 2010); T0 (SDSS J204749.61–071818.3; Burgasser et al., 2010); T1 (2MASS J08583467+3256275; Burgasser et al., 2010).

All of these features are characteristic of an old, metal-poor ultracool dwarf (Burgasser et al., 2008a). Low-metallicity brown dwarfs typically have increased

FeH absorption and weak signatures of CO. These metal poor objects are also old with high surface gravities which leads to greater line strengths of the pressure-sensitive alkali species, namely K I. As Burgasser et al., 2008a details, however, these characteristics cannot explain all of the features in the spectra of subdwarfs, particularly the strong H<sub>2</sub>O bands. For that, thin and/or large-grain condensate clouds are needed to reduce the contrast between the *J*-band peak and 1.4 $\mu$ m water band.

Although these are typical characteristics of low-metallicity L dwarfs, we assume they are also the features of late-L/early-T subdwarfs. One defining characteristic of subdwarfs that we cannot match is the blue *J* – *K* colour — our NIR spectrum does not show enhanced collision-induced H<sub>2</sub> absorption (CIA H<sub>2</sub>) in the *H*- and *K*-bands. However, we are uncertain if the the FIRE prism spectral slope can be trusted as previous experience has shown that the slopes can sometimes be redder than they truly are. The derived colour can be checked via future follow-up either by obtaining another spectrum or by obtaining *J* and *K* photometry. We have reason to believe, however, that the slope is correct. If WISE J0711–5736 had enhanced CIA H<sub>2</sub> absorption, the *H*- and *K*-bands would appear flatter. Since this is not the case we conclude that this object truly does not have a blue *J* – *K* colour.

We have also compared our spectrum of WISE J0711–5736 to two L7 subdwarfs (SDSS J141624.08+134826.7, Schmidt et al., 2010; ULAS J133836.97–022910.7, Zhang et al., 2017a) and a suspected T1.5 subdwarf (WISE J210529.08–623558.7, Luhman et al., 2014) in Figure 6.4. These are a few of the only late-L/early-T subdwarfs known to date. From Figure 6.4, we see that the strengths of the K I and FeH features of WISE J0711–5736 match those of the sdL7 dwarf ULAS J1338–0229 as well as the lack of CO absorption. Both SDSS J1416+1348 and ULAS J1338–0229 have bluer *J* – *K* colours and shallower H<sub>2</sub>O bands but this could be a consequence of the different spectral types. The depths of the H<sub>2</sub>O bands of WISE J0711–5736 are more comparable to those of WISE J2105–6235 but the K I and FeH features are stronger. The long-wavelength side of the *H*-band appears to be suppressed by CIA H<sub>2</sub> but the effects on the *K*-band are unknown since the F2 spectrum of WISE J2105–6235 only covers the *J*- and

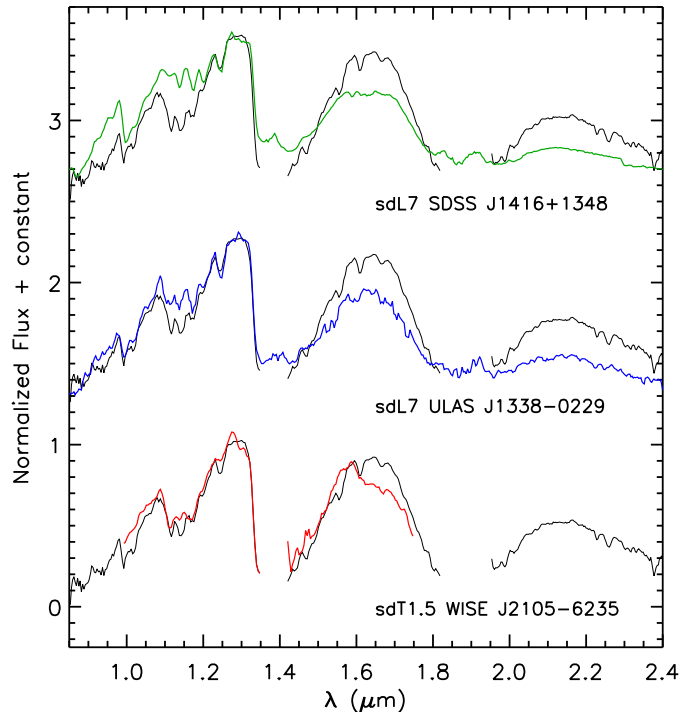


Figure 6.4: Our FIRE spectrum of WISE J0711–5736 (black) compared to the SpeX Prism spectrum of SDSS J141624.08+134826.7 (sdL7; Schmidt et al., 2010), the FIRE Prism spectrum of ULAS J133836.97–022910.7 (sdL7; Zhang et al., 2017a), and the Gemini Flamingos-2 spectrum of WISE J210529.08–623558.7 (sdT1.5; Luhman et al., 2014). All spectra have been smoothed to the resolution of the SpeX spectrum for a more direct comparison.

*H*-bands.

Although WISE J0711–5736 lacks the characteristic blue NIR colour of a typical low-metallicity object, all other signs point to it being part of the old galactic population. Thus, we tentatively conclude that this is a  $T_{0\pm 1}$  subdwarf.

We have also compared our spectrum to theoretical spectra. The set of models that most comprehensively cover the temperature, gravity and metallicity parameters are the spectra from Burrows et al., 2006. We have compared our FIRE spectrum of WISE J0711–5736 to model spectra that have  $T_{\text{eff}}=1300\text{--}1500\text{K}$ ,  $\log g=4.5\text{--}5.5$  and metallicities between 0.3 and 3 times solar (Figure 6.5). We can see from Figure 6.5 that when the models are compared to each other,

the low-metallicity models have deeper FeH and K I features and a lack of CO absorption compared to the higher metallicity models. Since this is similar to what we observe when we compare WISE J0711–5736 to other L and T dwarfs, we conclude that this object likely also has a low metallicity, despite the poor model fits and apparent lack of enhanced CIA H<sub>2</sub> absorption. The lower surface gravity models appear to provide better comparisons but the fits are still quite poor. The fact that the best fits appear to have both a low surface gravity and a low metallicity is puzzling as we would expect a low-metallicity object to be older, and hence, have higher surface gravity.

#### 6.4.2 UNRESOLVED BINARY?

We also compared the spectrum of WISE J0711–5736 to objects that were classified as peculiar in the SpeX Prism Library and to templates of spectral binaries. We created our templates by normalizing all single L and T dwarfs in the SpeX Prism Library to the flux in the 1.25–1.3 $\mu$ m region, scaling them to their spectral-type dependent absolute magnitudes given in Filippazzo et al., 2015, and summing the pairs of resulting spectra. The best matches are shown in Figure 6.6, however, none of the spectra can reproduce all of the features in the spectrum of WISE J0711–5736, in particular the slopes in the *H*-band. Interestingly, the best matching peculiar spectra in the *J*-band are 2MASS J04234858–0414035 (Burgasser, 2004b), 2MASS J15111466+0607431 (Chiu et al., 2006) and SDSS J151642.97+305344.5 (Burgasser et al., 2010), all of which are confirmed or suspected binaries (Bardalez Gagliuffi et al., 2015; Burgasser et al., 2006, 2010). The L7.5 + T0 spectrum of 2M J0423–0414 fits the *H*- and *K*-band quite well but matches the *J*-band only marginally better than the single spectra of Figure 6.3. The L7.5 + T2 spectrum of SDSS J1516+3053 matches the depth of the water absorption bands but fails to match the FeH and K I absorption features and the overall slope of WISE J0711–5736. The L5 + T5 spectrum of 2M J1511+0607 fits the *J*-band of WISE J0711–5736 extremely well but fails to match the *H*- and *K*-bands, mostly due to the contribution of the T5 in 2M J1511+0607.

From these comparisons, we see that as the fit in the *J*-band improves with

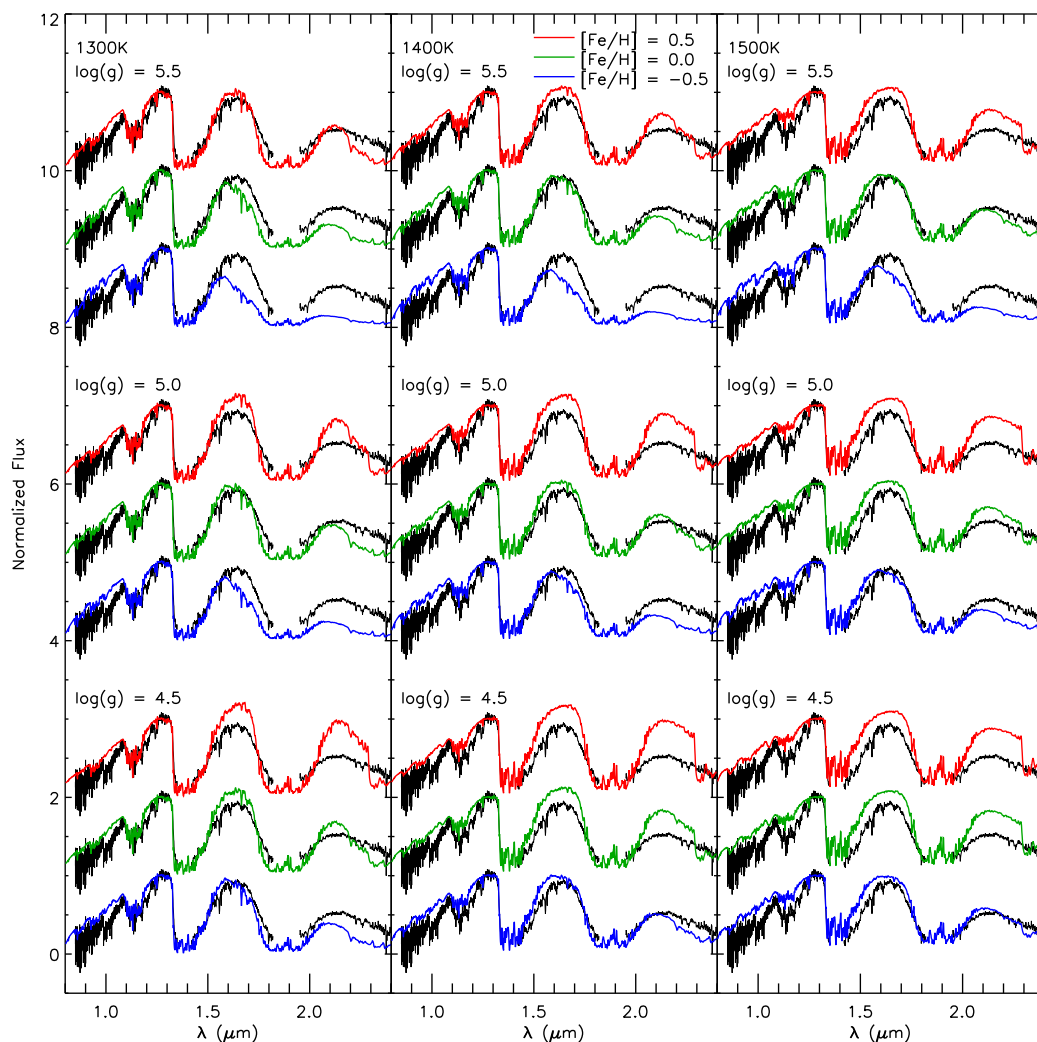


Figure 6.5: The FIRE spectrum of WISE J0711–5736 (black) compared to theoretical spectra from Burrows et al., 2006. The low-metallicity models (blue) and low-gravity models (lowest sets) seem to fit the spectrum of WISE J0711–5736 best, however, the fits are quite poor.

combinations of earlier L dwarfs and later T dwarfs, the fit in the  $H$ - and  $K$ -bands becomes worse. This, along with the apparent lack of  $\text{CH}_4$  absorption disfavors the possibility that this object is a spectral binary.

The best fits from the spectral binary template fitting seem to produce better matches (right panel of Figure 6.6), however, the templates still cannot match the strength of the K I and FeH features. Quantitative measurements show these templates provide no, or not a significant, improvement over the fit to the sdT1.5 dwarf WISE 2105–6235 (reduced  $\chi^2 = 0.30, 0.17$  and  $0.17$ , respectively, versus  $0.19$  for WISE 2105–6235). We also note that at least one spectrum in each of the templates is itself a suspected binary or other peculiar object: the T3.5 dwarf SDSS J153417.05+161546.1 (Chiu et al., 2006) is a T1.5+T5.5 binary (Liu et al., 2006); the L4.5 dwarf 2MASSI J0652307+471034 (Burgasser et al., 2010) is potentially young (Cruz et al., 2007); the T2 dwarf SDSS J024749.90–163112.6 (Chiu et al., 2006) is a candidate T0+T7 binary (Burgasser et al., 2010); and the L5 dwarf 2MASSW J1239272+551537 (Burgasser et al., 2010) is an L5+L6 binary (Radigan, 2013). Because one spectrum in each template is itself a suspected binary, the spectra are in fact triple templates. Since the scenario of a young or thin-disk triple system moving with such large proper motion is unlikely, we also tentatively rule out this possibility. However, we cannot altogether dismiss the possibility of unresolved multiplicity.

#### 6.4.3 KINEMATICS

Using the absolute magnitude vs. spectral type polynomial from Faherty et al., 2016 for a  $T0 \pm 1$  dwarf, we estimate that WISE J0711–5736 has an absolute  $W2$  magnitude of  $\sim 11.8$  mag, giving a photometric distance of 37 pc. The proper motion of this object at the photometric distance corresponds to a tangential velocity of  $\sim 170$  km s $^{-1}$ . The relations of Faherty et al., 2016, however, were calibrated using normal field objects and we expect the absolute  $W2$  magnitudes of late-L/early-T subdwarfs to be slightly fainter than those of normal objects of the same spectral type. This would mean our distance and velocity values are slightly overestimated. Using the absolute magnitude vs. spectral type relations from Gonzales et al. (2017; in prep) for subdwarfs up to L5 and doing a naive extension to T0 spectral types, WISE J0711–5736 should have an absolute magnitude of  $\sim 12.3$  mag, giving a photometric distance of 29 pc. The proper motion then corresponds to  $\sim 150$  km s $^{-1}$ ; a much smaller value.

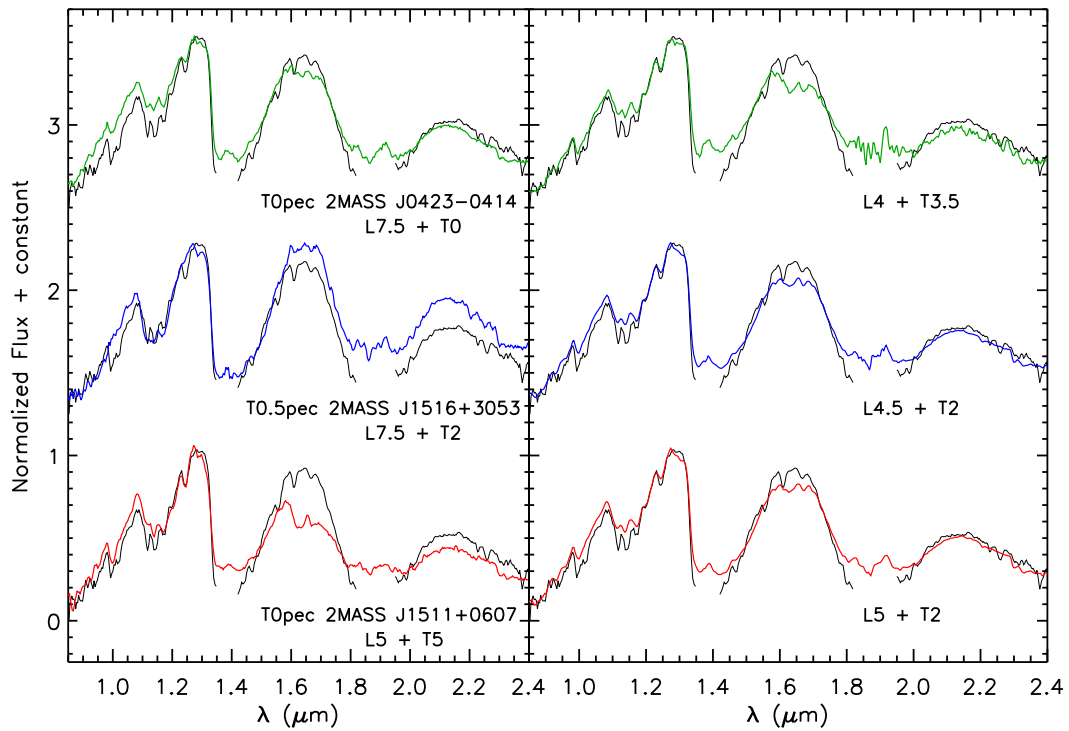


Figure 6.6: Our FIRE spectrum of WISE J0711–5736 (black) compared to SpeX Prism peculiar spectra (left) and spectral binary templates (right). The FIRE spectrum has been smoothed to the resolution of the SpeX spectra. Comparison spectra for the peculiar objects are: T0pec (2MASS J04234858–0414035; Burgasser, 2004b); T0.5pec (SDSS J151642.97+305344.5; Burgasser et al., 2010); T0pec (2MASS J15111466+0607431; Chiu et al., 2006). The spectra used in the spectral binary templates are: L4 (2MASS J04070752+1546456; Burgasser et al., 2008b) and T3.5 (SDSS J153417.05+161546.1; Chiu et al., 2006); L4.5 (2MASS J0652307+471034; Burgasser et al., 2010) and T2 (SDSS J024749.90–163112.6; Chiu et al., 2006); L5 (2MASSW J1239272+551537; Burgasser et al., 2010) and T2 (SDSS J024749.90–163112.6; Chiu et al., 2006).

Table 6.3: Inferred Properties of WISE J0711–5736

Spectral Type	sdT0 $\pm$ 1
From Faherty et al., 2016	
$M_{W2}$	$11.8 \pm 0.5$ mag
Photometric Distance	$36.8 \pm 4.2$ pc
Tangential Velocity	$173 \pm 22$ km s $^{-1}$
From Gonzales et al. (2017; in prep)	
$M_{W2}$	$12.3 \pm 0.5$ mag
Photometric Distance	$28.9 \pm 4.2$ pc
Tangential Velocity	$149 \pm 22$ km s $^{-1}$

Uncertainties represent the values for the range of possible spectral types — L9–T1.

## 6.5 HALO/THICK-DISK BROWN DWARFS

From studies of stars, tangential velocities of objects in the thick-disk have been found to be  $\sim 85$ – $180$  km s $^{-1}$  (e.g. Feltzing et al., 2003; Fuhrmann, 1998; Soubiran et al., 2003) and  $\sim 200$ – $300$  km s $^{-1}$  in the halo (e.g. Chiba et al., 2000; Mace et al., 2013b; Schilbach et al., 2009). With a tangential velocity of  $\sim 170$  km s $^{-1}$ , WISE J0711–5736 lies right on the cusp between these populations. Based on the membership probability distributions calculated by Dupuy et al., 2012, WISE J0711–5736 has a  $>90\%$  probability of being part of the thick-disk and  $<10\%$  probability of being a member of either the halo or thin-disk populations. Using the tangential velocity calculated using the relation from Gonzales et al. (2017; in prep), WISE J0711–5736 has a membership probability of 50–90% for the thick-disk,  $<10$ – $10\%$  for the thin-disk, and  $<10\%$  for the halo. If WISE J0711–5736 were an unresolved binary, it would be a factor of  $\sim 30$ – $40\%$  further away, and so will have a proportionately higher tangential velocity: putting it further into the thick-disk kinematics.

The comparison of WISE J0711–5736 with solar-metallicity objects and theoretical spectra with  $[\text{Fe}/\text{H}]$  values between 0.0 and  $-0.5$  indicates a low metallicity, making it consistent with either the thick-disk or halo populations (Lépine

et al., 2007; Reddy et al., 2006; Zhang et al., 2017b). However, this is only tentative as the model fits are quite poor.

Only a handful of T dwarfs have been confirmed to be a part of the thick-disk or halo populations, most of which are late T dwarfs — WISE J200520.38+542433.9 (T8;  $v_{tan} \approx 110 \text{ km s}^{-1}$ ; Mace et al., 2013b), WISE J001354.39+063448.2 (T8;  $v_{tan}^\ddagger \approx 107\text{--}190 \text{ km s}^{-1}$ ) and WISE J083337.83+005214.2 (T9;  $v_{tan}^\ddagger \approx 126\text{--}231 \text{ km s}^{-1}$ ; Pinfield et al., 2014), and ULAS J131610.28+075553.0 (T6.5;  $v_{tan} \approx 240\text{--}340 \text{ km s}^{-1}$ ; Burningham et al., 2014). The latest L-type brown dwarfs that are part of the thick-disk or halo populations are L7 dwarfs (e.g. Burgasser et al., 2003; Zhang et al., 2017a). There has, so far, been a lack of discoveries of low-metallicity late-L and early-T brown dwarfs. Only one early-T dwarf, WISE J210529.08–623558.7 (T1.5;  $v_{tan} = 176 \pm 25 \text{ km s}^{-1}$ ; (Luhman et al., 2014), has been found to potentially have kinematics and a metallicity consistent with these populations. The discovery of WISE J0711–5736 potentially brings the number of objects in this observational gap up to two.

More detailed metallicity measurements and kinematics are needed to confidently determine to which population this object belongs: halo or thick-disk.

## 6.6 CONCLUSIONS

We have determined that our candidate object, WISE J071121.36–573634.2, is potentially a sdT0  $\pm 1$  dwarf. The estimated absolute  $W2$  magnitude of this object puts it at  $\sim 37$  pc with a tangential velocity of  $\sim 170 \text{ km s}^{-1}$ , or  $\sim 29$  pc with a tangential velocity of  $\sim 150 \text{ km s}^{-1}$ . The properties of WISE J0711–5736 are generally consistent with those of the thick-disk population. Using either of the distance estimates, this object is relatively close to the sun and so obtaining a parallax measurement should be relatively easy. Provided this object is indeed an sdT0 dwarf, the discovery of WISE J0711–5736 would only be the second low-metallicity late-L/early-T dwarf discovered to date. Further spectroscopic observations will allow us to be able to definitively determine the metallicity, thus the membership, of this object. New observations will also allow us to rule

---

<sup>‡</sup>Assuming a photometric distance using mid-infrared magnitudes as we do in this work.

out (or confirm) multiplicity.

#### REFERENCES

- Ackerman, A. S. and Marley, M. S. (2001). *ApJ* 556, pp. 872–884. DOI: [10.1086/321540](https://doi.org/10.1086/321540).
- Baraffe, I., Homeier, D., Allard, F., et al. (2015). *A&A* 577, A42, A42. DOI: [10.1051/0004-6361/201425481](https://doi.org/10.1051/0004-6361/201425481).
- Bardalez Gagliuffi, D. C., Gelino, C. R., and Burgasser, A. J. (2015). *AJ* 150, 163, p. 163. DOI: [10.1088/0004-6256/150/5/163](https://doi.org/10.1088/0004-6256/150/5/163).
- Bochanski, J. J., Hennawi, J. F., Simcoe, R. A., et al. (2009). *PASP* 121, pp. 1409–1418. DOI: [10.1086/648597](https://doi.org/10.1086/648597).
- Burgasser, A. J. (2004a). *ApJS* 155, pp. 191–207. DOI: [10.1086/424386](https://doi.org/10.1086/424386).
- (2004b). *ApJS* 155, pp. 191–207. DOI: [10.1086/424386](https://doi.org/10.1086/424386).
- Burgasser, A. J., Kirkpatrick, J. D., Brown, M. E., et al. (1999). *ApJ* 522, pp. L65–L68. DOI: [10.1086/312221](https://doi.org/10.1086/312221).
- Burgasser, A. J., Marley, M. S., Ackerman, A. S., et al. (2002). *ApJ* 571, pp. L151–L154. DOI: [10.1086/341343](https://doi.org/10.1086/341343).
- Burgasser, A. J., Kirkpatrick, J. D., Burrows, A., et al. (2003). *ApJ* 592, pp. 1186–1192. DOI: [10.1086/375813](https://doi.org/10.1086/375813).
- Burgasser, A. J., Geballe, T. R., Leggett, S. K., et al. (2006). *ApJ* 637, pp. 1067–1093. DOI: [10.1086/498563](https://doi.org/10.1086/498563).
- Burgasser, A. J.,Looper, D. L., Kirkpatrick, J. D., et al. (2008a). *ApJ* 674, 451–465, pp. 451–465. DOI: [10.1086/524726](https://doi.org/10.1086/524726).
- Burgasser, A. J., Liu, M. C., Ireland, M. J., et al. (2008b). *ApJ* 681, pp. 579–593. DOI: [10.1086/588379](https://doi.org/10.1086/588379).
- Burgasser, A. J., Cruz, K. L., Cushing, M., et al. (2010). *ApJ* 710, pp. 1142–1169. DOI: [10.1088/0004-637X/710/2/1142](https://doi.org/10.1088/0004-637X/710/2/1142).
- Burningham, B., Smith, L., Cardoso, C. V., et al. (2014). *MNRAS* 440, pp. 359–364. DOI: [10.1093/mnras/stu184](https://doi.org/10.1093/mnras/stu184).
- Burrows, A., Hubbard, W. B., Saumon, D., et al. (1993). *ApJ* 406, pp. 158–171. DOI: [10.1086/172427](https://doi.org/10.1086/172427).

- Burrows, A., Hubbard, W. B., Lunine, J. I., et al. (2001). *Reviews of Modern Physics* 73, pp. 719–765. DOI: [10.1103/RevModPhys.73.719](https://doi.org/10.1103/RevModPhys.73.719).
- Burrows, A., Sudarsky, D., and Hubeny, I. (2006). *ApJ* 640, pp. 1063–1077. DOI: [10.1086/500293](https://doi.org/10.1086/500293).
- Chabrier, G. and Baraffe, I. (1997). *A&A* 327, pp. 1039–1053.
- Chiba, M. and Beers, T. C. (2000). *AJ* 119, pp. 2843–2865. DOI: [10.1086/301409](https://doi.org/10.1086/301409).
- Chiu, K., Fan, X., Leggett, S. K., et al. (2006). *AJ* 131, pp. 2722–2736. DOI: [10.1086/501431](https://doi.org/10.1086/501431).
- Cruz, K. L., Reid, I. N., Kirkpatrick, J. D., et al. (2007). *AJ* 133, pp. 439–467. DOI: [10.1086/510132](https://doi.org/10.1086/510132).
- Cushing, M. C., Vacca, W. D., and Rayner, J. T. (2004). *PASP* 116, pp. 362–376. DOI: [10.1086/382907](https://doi.org/10.1086/382907).
- Dupuy, T. J. and Liu, M. C. (2012). *ApJS* 201, 19, p. 19. DOI: [10.1088/0067-0049/201/2/19](https://doi.org/10.1088/0067-0049/201/2/19).
- (2017). *ApJS* 231, 15, p. 15. DOI: [10.3847/1538-4365/aa5e4c](https://doi.org/10.3847/1538-4365/aa5e4c).
- Faherty, J. K., Riedel, A. R., Cruz, K. L., et al. (2016). *ApJS* 225, 10, p. 10. DOI: [10.3847/0067-0049/225/1/10](https://doi.org/10.3847/0067-0049/225/1/10).
- Feltzing, S., Bensby, T., and Lundström, I. (2003). *A&A* 397, pp. L1–L4. DOI: [10.1051/0004-6361:20021661](https://doi.org/10.1051/0004-6361:20021661).
- Filippazzo, J. C., Rice, E. L., Faherty, J., et al. (2015). *ApJ* 810, 158, p. 158. DOI: [10.1088/0004-637X/810/2/158](https://doi.org/10.1088/0004-637X/810/2/158).
- Fuhrmann, K. (1998). *A&A* 338, pp. 161–183.
- Gagné, J., Burgasser, A. J., Faherty, J. K., et al. (2015). *ApJ* 808, L20, p. L20. DOI: [10.1088/2041-8205/808/1/L20](https://doi.org/10.1088/2041-8205/808/1/L20).
- Gagné, Jonathan, Lambrides, Erini, Faherty, Jacqueline K, et al. (2015).
- Gazzano, J.-C., Kordopatis, G., Deleuil, M., et al. (2013). *A&A* 550, A125, A125. DOI: [10.1051/0004-6361/201117747](https://doi.org/10.1051/0004-6361/201117747).
- Kirkpatrick, J. D. (2005). *ARA&A* 43, pp. 195–245.
- Kirkpatrick, J. D., Looper, D. L., Burgasser, A. J., et al. (2010). *ApJS* 190, pp. 100–146. DOI: [10.1088/0067-0049/190/1/100](https://doi.org/10.1088/0067-0049/190/1/100).

- Kirkpatrick, J. D., Cushing, M. C., Gelino, C. R., et al. (2011). *ApJS* 197, 19, p. 19. DOI: [10.1088/0067-0049/197/2/19](https://doi.org/10.1088/0067-0049/197/2/19).
- Kirkpatrick, J. D., Schneider, A., Fajardo-Acosta, S., et al. (2014). *ApJ* 783, 122, p. 122. DOI: [10.1088/0004-637X/783/2/122](https://doi.org/10.1088/0004-637X/783/2/122).
- Kirkpatrick, J. D., Kellogg, K., Schneider, A. C., et al. (2016). *ApJS* 224, 36, p. 36. DOI: [10.3847/0067-0049/224/2/36](https://doi.org/10.3847/0067-0049/224/2/36).
- Lépine, S., Rich, R. M., and Shara, M. M. (2007). *ApJ* 669, pp. 1235–1247. DOI: [10.1086/521614](https://doi.org/10.1086/521614).
- Liu, M. C., Leggett, S. K., Golimowski, D. A., et al. (2006). *ApJ* 647, pp. 1393–1404. DOI: [10.1086/505561](https://doi.org/10.1086/505561).
- Luhman, K. L. (2014). *ApJ* 786, L18, p. L18. DOI: [10.1088/2041-8205/786/2/L18](https://doi.org/10.1088/2041-8205/786/2/L18).
- Luhman, K. L. and Sheppard, S. S. (2014). *ApJ* 787, 126, p. 126. DOI: [10.1088/0004-637X/787/2/126](https://doi.org/10.1088/0004-637X/787/2/126).
- Mace, G. N., Kirkpatrick, J. D., Cushing, M. C., et al. (2013a). *ApJS* 205, 6, p. 6. DOI: [10.1088/0067-0049/205/1/6](https://doi.org/10.1088/0067-0049/205/1/6).
- Mace, G. N., Kirkpatrick, J. D., Cushing, M. C., et al. (2013b). *ApJ* 777, 36, p. 36. DOI: [10.1088/0004-637X/777/1/36](https://doi.org/10.1088/0004-637X/777/1/36).
- Mainzer, A., Bauer, J., Grav, T., et al. (2011). *ApJ* 731, 53, p. 53. DOI: [10.1088/0004-637X/731/1/53](https://doi.org/10.1088/0004-637X/731/1/53).
- Marley, M. S., Saumon, D., Guillot, T., et al. (1996). *Science* 272, pp. 1919–1921. DOI: [10.1126/science.272.5270.1919](https://doi.org/10.1126/science.272.5270.1919).
- Marley, M. S., Seager, S., Saumon, D., et al. (2002). *ApJ* 568, pp. 335–342. DOI: [10.1086/338800](https://doi.org/10.1086/338800).
- Pinfield, D. J., Gomes, J., Day-Jones, A. C., et al. (2014). *MNRAS* 437, pp. 1009–1026. DOI: [10.1093/mnras/stt1437](https://doi.org/10.1093/mnras/stt1437).
- Radigan, J. M. (2013). *Ph.D. Thesis, The University of Toronto, Toronto, Ontario, Canada*. Available at <http://www.astro.utoronto.ca/theses/thesis13.radigan.pdf>.
- Reddy, B. E., Lambert, D. L., and Allende Prieto, C. (2006). *MNRAS* 367, pp. 1329–1366. DOI: [10.1111/j.1365-2966.2006.10148.x](https://doi.org/10.1111/j.1365-2966.2006.10148.x).
- Schilbach, E., Röser, S., and Scholz, R.-D. (2009). *A&A* 493, pp. L27–L30. DOI: [10.1051/0004-6361:200811281](https://doi.org/10.1051/0004-6361:200811281).

- Schmidt, S. J., West, A. A., Hawley, S. L., et al. (2010). *AJ* 139, pp. 1808–1821.  
DOI: [10.1088/0004-6256/139/5/1808](https://doi.org/10.1088/0004-6256/139/5/1808).
- Simcoe, R. A., Burgasser, A. J., Bernstein, R. A., et al. (2008). *Society of Photo-Optical Instrumentation Engineers (SPIE) Conference Series*. Vol. 7014. Society of Photo-Optical Instrumentation Engineers (SPIE) Conference Series.  
DOI: [10.1117/12.790414](https://doi.org/10.1117/12.790414).
- Simcoe, R. A., Burgasser, A. J., Schechter, P. L., et al. (2013). *PASP* 125, p. 270.  
DOI: [10.1086/670241](https://doi.org/10.1086/670241).
- Sivarani, T., Lépine, S., Kembhavi, A. K., et al. (2009). *ApJ* 694, pp. L140–L143. DOI: [10.1088/0004-637X/694/2/L140](https://doi.org/10.1088/0004-637X/694/2/L140).
- Soubiran, C., Bienaymé, O., and Siebert, A. (2003). *A&A* 398, pp. 141–151.  
DOI: [10.1051/0004-6361:20021615](https://doi.org/10.1051/0004-6361:20021615).
- Zhang, Z. H., Pinfield, D. J., Gálvez-Ortiz, M. C., et al. (2017a). *MNRAS* 464, pp. 3040–3059. DOI: [10.1093/mnras/stw2438](https://doi.org/10.1093/mnras/stw2438).
- Zhang, Z. H., Homeier, D., Pinfield, D. J., et al. (2017b). *MNRAS* 468, pp. 261–271. DOI: [10.1093/mnras/stx350](https://doi.org/10.1093/mnras/stx350).

# 7

## Conclusion

Brown dwarfs are the lowest mass products of star formation. Their masses ( $\sim 13M_{\text{Jup}}-75M_{\text{Jup}}$ ) prevent them from achieving stable hydrogen fusion in their core. Because they lack a stable internal energy and thermal pressure source, their radii, luminosities and temperatures decrease as they age. Their contraction stops when their interiors become electron degenerate at  $R \approx 1R_{\text{Jup}}$ , however, they continue to cool and fade. The spectral appearance of stellar mass objects is determined by temperature and brown dwarfs generally follow the same trend. As an object cools, its spectral type changes from L-type to T-type depending on its mass. However, the relationship between spectral type and temperature is not linear. In these cool objects ( $250\text{K} \lesssim T_{\text{eff}} \lesssim 2500\text{K}$ ), a large variety of molecule and condensate species are able to form. The results are atmospheres that are complex and spectra that are riddled with absorption features.

On top of the effects from complex chemistry, spectral appearances are influenced by factors such as cloud structure, surface gravity and metallicity. I have approached these issues from both a statistical and an individual object point of view. Understanding the population statistics of each type of atmospheric phenomenon lets us determine how frequently they occur, thus, the evolutionary timescales over which they remain in such a state. Studying individual ob-

jects gives us insight into the effects that specific conditions have on their atmospheres. Both viewpoints are necessary to build a comprehensive picture of brown dwarf atmospheres.

### 7.1 TIMESCALES OF ATMOSPHERIC PHENOMENA

When brown dwarfs are young and have not yet collapsed to the point where they are supported only by degeneracy pressure, their radii are relatively large and surface gravities are relatively low. This low gravity causes dust to be located in the upper altitudes in the atmosphere rather than settled in the lower atmosphere, leading to redder infrared colours than they would normally have after this evolutionary phase. The youth of these objects can easily be determined through spectroscopic observations. The low gravities lead to less broadening of absorption features that are pressure sensitive. There are also objects with unusually red infrared colours that do not show any signs of youth in their spectra. The red colours undoubtedly come from excess dust in their upper atmospheres but the cause of the increased dust content at these altitudes hasn't yet been explained satisfactorily. The frequency of this atmospheric phenomenon may be the key to understanding its underlying cause.

By performing a colour-selected search for these peculiarly red L and T dwarfs, I have now been able to determine the frequency of both the young and unusually dusty objects. In the statistical survey, I also have been able to identify unresolved L + T binary candidates. With spectroscopic observations, I confirmed that 21 of the new 104 ultra-cool dwarfs discovered in this survey are unusually red, unusually blue, or are candidate binaries. Including the 276 previously known objects that I recovered with my selection criteria (420 objects total), 4.0% (17) are unusually red, 1.7% (7) are unusually blue and 7.1% (30) are candidate binaries. I find that there are roughly as many L + T binaries in my sample as binaries of any other kind combined, likely because I was not targeting any other binary combination.

I also find that there are almost equal numbers of young objects as brown dwarfs with unusually high dust content that do not appear young. Within my

sample, 2.1% of objects show signs of youth which corresponds to  $\sim 200$  Myr of an object's lifetime that is spent contracting until the signs of the early stages of evolution can no longer be seen in near-infrared spectra. Another 1.9% of the objects are unusually red with no signs of youth. These objects could have dust in the atmosphere that has not yet settled after contraction. If this is the case, this phase would then correspond to the next  $\sim 200$  Myr of the object's life. The red infrared colours could also potentially be explained by high metallicity. If this is the case, 1.9% of objects in the sensitivity limit of SDSS, 2MASS and WISE could have formed in molecular clouds with high metallicities.

With my colour-selected search for peculiar L and T dwarfs, I have demonstrated that with the proper selection criteria, we can identify unusual L and T dwarf candidates in large photometric surveys in the absence of spectral type information. With follow-up spectroscopy, we can verify the unusual properties and begin to discern their underlying cause. This is particularly advantageous for finding isolated objects that are analogous to the typically very red directly imaged extrasolar planets in order to study their atmospheric characteristics at higher fidelity. These discoveries attest to the power of simultaneous positional and colour cross-correlations across photometric databases over colour-only searches on individual databases that are then positionally compared to other databases.

## 7.2 ATMOSPHERES OF INDIVIDUAL OBJECTS

Through detailed analysis of several individual objects, I have shed light on the effects of gravity, cloud structure and metallicity on brown dwarf atmospheres.

From my statistical survey, I have found the reddest object with no signatures of youth known to date — the L6 dwarf 2MASS J03530419+0418193. A detailed study of this object may give clues as to the nature of its extreme red colour as no satisfactory answer has been found to explain such objects so far. I have also found one of the brightest, planetary-mass free-floating objects known to date — the L7 dwarf 2MASS J11193254–1137466. With moderate resolution ( $R \sim 6000$ ) spectra, I have confirmed the low surface gravity, and hence youth, of

the L7 dwarf 2MASS 1119–1137. Its radial velocity, proper motion, and galactic position are consistent with that of the  $10 \pm 3$  Myr-old TW Hydrae Association (TWA). From the object’s near-infrared absolute magnitudes I determine a mass of  $4.3\text{--}7.6 M_{\text{Jup}}$ , making it one of the lowest mass free-floating brown dwarfs known. It is the nearest member of TWA at  $\sim 27$  pc, and the second-brightest isolated  $< 10 M_{\text{Jup}}$  object discovered to date. Its relatively bright near-infrared luminosity makes it one of the best candidates to study in detail the atmosphere of a very young, very low-mass object. Hence, 2MASS 1119–1137 is an excellent benchmark for young, directly imaged extrasolar planets.

Determining how clouds affect the spectra of brown dwarfs is crucial in understanding the underlying structure and physics in their atmospheres. With this goal in mind, we monitored the nearby L/T transition binary Luhman 16AB for two nights at  $R \sim 4000$  over the  $0.9\text{--}2.5\mu\text{m}$  wavelength range. This experiment has offered the unprecedented opportunity to study the atmospheric changes in the more highly variable early T-type secondary component at high SNR. My analysis shows that the variability amplitude of Luhman 16B decreases with decreasing pressure level, indicating that the variability mechanism operates at pressures at least as high as those corresponding to the  $1.2\mu\text{m}$  continuum ( $\sim 2\text{--}3$  bars). The decreasing variability with pressure demonstrates that the variability causes the  $J$ -band flux to vary more than the  $J - K_s$  colour. This gives the L/T transition a wide range in  $M_J$  magnitudes on a colour-magnitude diagram. I have also determined that the NIR K I absorption strength increases in the faint state, either because of an increased K I abundance above the cloud deck or because of changes in the temperature-pressure profile. I have been able to reproduce the bright-to-faint ratio of Luhman 16B with a spectral template which is predominantly a relatively warm L8 or L9 with a smaller contribution from a cooler T1 or T2 component. The faint state also has a cooler secondary component than the bright state meaning that during the faint state, part of the atmosphere is slightly cooler than in the bright state. I interpret the ability to reproduce the ratios with changing spectral templates as an indication that the governing mechanism of brown dwarf variability is the same as the one responsible for the diversity in spectral morphology across the L/T transition.

Metallicity also has a profound affect on the chemical composition and evolution of brown dwarf atmospheres. However, most work done on low metallicity objects has been theoretical so far. So-called subdwarfs are relatively rare, making model testing incomplete. Identifying and studying brown dwarfs with low metallicity content, hence old age, will allow us to reliably test atmospheric and evolutionary models and understand exactly what role metallicity plays in brown dwarf atmospheres. Not only are subdwarfs rare, but late-L and early-T subdwarfs are almost non-existent in the solar neighbourhood due to the nature of the L/T transition. I have discovered an object — the sdT0 dwarf WISE J071121.36–573634.2 — that is potentially part of the old thick-disk or halo. The estimated absolute  $W2$  magnitude of this object puts it at  $\sim 37$  pc with a tangential velocity of  $\sim 170$  km s $^{-1}$ . Although there are very few late-L/early-T subdwarfs to compare our object to, it appears that the characteristics of L subdwarfs are also those of a T0 subdwarf. The kinematic and spectroscopic properties of WISE 0711–5736 are consistent with the population of thick-disk or halo objects. With the discovery of this object, I have set the stage for the study of one of the rarest kinds of brown dwarfs in the solar neighbourhood.

### 7.3 SUMMARY

One of the main goals of my work has been to identify objects with unusual characteristics such as decreased gravity, high atmospheric dust content, and unresolved binarity in large all-sky surveys. By comparing the population of objects with “peculiar” properties to the population of “normal” objects, I have been able to determine the timescales of each atmospheric phenomenon and how they play into the evolution of ultra-cool dwarfs. From this study, I have also discovered one of the brightest and lowest mass free-floating brown dwarfs. Another piece of the puzzle is understanding how conditions on individual objects affect their structure and composition. With this goal in mind, I have studied in detail one of the closest objects to the sun and that is known to have large degrees of varying cloud structure — Luhman 16B. Finally, old, low-metallicity objects in the Milky Way are remnants from the early galactic environment and

I have found one such potential object. By studying these objects we can gain a better understanding of conditions in the young Milky Way and figure out the role that metallicity plays on the atmospheric evolution of these lowest mass objects.



## Permissions

*Background Material:* All figures in the background material section published in any American Astronomical Society Journal have been reproduced by permission of the AAS. No permission was required for the other figures.

*Chapter 1:* Chapter 1 is a version of Kellogg et al. (2015) and has been reproduced by permission of the AAS.

*Chapter 3:* Chapter 3 is a version of Kellogg et al. (2016) and has been reproduced by permission of the AAS.

# Curriculum Vitae

# Kendra Kellogg

## **Education:**

---

2013-2017      PhD: Astrophysics, The University of Western Ontario  
2011-2013      MA: Physics, Stony Brook University  
2007-2011      BS: Physics and Astronomy, Northern Arizona University

## **Research Experience:**

---

2015 Winter      IPAC Fellow/Research Assistant: Infrared Processing and  
Analysis Center/Caltech  
Identifying peculiar brown dwarfs in a mid-infrared proper  
motion survey  
Advisor: Dr. J. Davy Kirkpatrick

2013-2017      Research Assistant/PhD candidate: University of Western  
Ontario  
Identifying peculiar brown dwarfs in a cross-match of large  
optical/near-infrared surveys  
Advisor: Dr. Stanimir Metchev

2011-2013      Research Assistant: Stony Brook University  
Identifying peculiar brown dwarfs in a cross-match of large  
optical/near-infrared surveys (extended into a PhD thesis)  
Advisor: Dr. Stanimir Metchev

2010-2011      Research Assistant: Lowell Observatory  
Characterizing various orbital parameters of a complex  
multi-object stellar system via spectroscopy  
Advisor: Dr. Lisa Prato

2010 Summer      REU: National Solar Observatory  
Identifying effects of solar flares on acoustic oscillations  
Advisors: Drs. Sushant Tripathy and Kiran Jain

2009-2010      NASA/NAU Space Grant: Lowell Observatory  
Identifying correlations between various photometric  
characteristics of circumstellar disks  
Advisor: Dr. Lisa Prato

## **Publications:**

---

- Kellogg, K., Metchev, S., Miles Paez, P., Tannock, M. 2017 (accepted): *A Statistical Survey of Peculiar L and T Dwarfs in SDSS, 2MASS, and WISE*
- Kellogg, K., Metchev, S., Heinze, A., Gagne, J., Kurtev, R. 2017 (submitted): *Characterizing the Cloud Decks of Luhman 16AB with Medium-Resolution Spectroscopic Monitoring*
- Kellogg, K., Kirkpatrick, J. D., Gagne, J., Faherty, J. 2017 (submitted): *Discovery of a Possible Early-T Thick-Disk Subdwarf from the AllWISE 2 Motion Survey*
- Kellogg, K., Prato, L., Torres, G., Schaefer, G., et al. 2017, ApJ, 844, 168: *The TWA 3A Young Triple System: Orbits, Disks, Evolution*
- Kellogg, K., Metchev, S., Gagne, J., Faherty, J. 2016, ApJL, 821, L15: *The Nearest Isolated Member of the TW Hydrae Association is a Giant Planet Analog*
- Kirkpatrick, J. D., Kellogg, K., Schneider, A., Fajardo-Acosta, S., et al. 2016, ApJS, 224, 36: *The AllWISE Motion Survey, Part 2*
- Kellogg, K., Metchev, S., Geissler, K., Hicks, S., Kirkpatrick, J. D., Kurtev, R. 2015, AJ, 150, 182: *A Targeted Search for Peculiarly Red L and T Dwarfs in SDSS, 2MASS and WISE*
- Heinze, A., Metchev, S., Kellogg, K. 2015, ApJ, 801, 104: *Weather on Other Worlds. III. A Survey for T Dwarfs with High-amplitude Optical Variability*

## **Meetings and Presentations:**

---

- |               |  |
|---------------|--|
| 2017 January  | American Astronomical Society<br>Talk: <i>A Statistical Study of Brown Dwarf Peculiarity</i>                             |
| 2016 June     | Cool Stars 19 2016<br>Poster: <i>The Nearest Isolated Member of the TW Hydrae Association is a Giant Planet Analogue</i> |
| 2015 April    | Greater IPAC Science Symposium<br>Talk: <i>AllWISE1 the Sequel: AllWISE2</i>   |
| 2015 February | WISE @ 5<br>Talk: <i>AllWISE1 the Sequel: AllWISE2</i>   |
| 2014 June     | Cool Stars 18 2014<br>Poster: <i>A Substellar Companion to ScoPMS 214 in the Young Upper Scorpius Association</i>        |

- 2014 March Sustainability and Environment Showcase  
Three Minute Thesis Presentation: *A Search for Brown Dwarfs with Unusual Atmospheres*
- 2014 January American Astronomical Society  
Poster: *A Survey of L/T-transition and Peculiar Brown Dwarfs from an SDSS/2MASS/WISE Cross-match*
- 2013 August Mind the Gap  
Poster: *A Survey of L/T-transition and Peculiar Brown Dwarfs from an SDSS/2MASS/WISE Cross-match*
- 2013 January American Astronomical Society  
Poster: *A Survey of Substellar Atmospheric Properties in L/T-transition and Peculiar Brown Dwarfs from an SDSS/2MASS Cross-match*
- 2012 March Astronomical Society of New York,  
Poster: *Spectroscopic Study of New L- and T-type Brown Dwarfs*
- 2011 January American Astronomical Society  
Poster: *Effect of Solar Flares on Acoustic Oscillations Within the Sun*

**Observing Experience:**

---

- 28 nights NASA Infrared Telescope Facility: SpeX spectrograph
- 2 nights Magellan: FIRE spectrograph
- 18 nights Kitt Peak 2.1 metre telescope: CCD imager

**Programming experience:**

---

IDL  
Python  
IRAF

**Teaching Experience:**

---

- 2013-2017 Graduate Teaching Assistant: Western University
- 2014 March Guest Lecturer: Western University  
Introductory Physics II

**Awards:**

---

2014 May                      Award of Excellence in Teaching

**Professional Memberships:**

---

American Astronomical Society Junior Member

**Outreach and Leadership:**

---

2015-2017    Exploring the Stars: The University of Western Ontario  
Ran events throughout the year for various groups of people that included giving presentations and demonstrations of a variety of astronomical topics and observing through the university's historical Cronyn Observatory telescope.

2010-2011    Treasurer, Society of Physics Students: Northern Arizona University  
Along with running weekly meetings and planning club activities, had the opportunity to educate middle school and high school students on various aspects of physics using table-top demonstrations

2007-2011    Public Program Docent: Lowell Observatory  
Volunteered as a docent in the evening program using eye-piece observing to educate the public on astronomical phenomena